Particle-in-Cell Simulations of Electron Dynamics in Low Pressure Discharges with Magnetic Fields

A Thesis Submitted to the
College of Graduate Studies and Research
in Partial Fulfillment of the Requirements
for the degree of Doctor of Philosophy
in the Department of Physics and Engineering Physics
University of Saskatchewan
Saskatoon

By
Dmytro Sydorenko

Permission to Use

In presenting this thesis in partial fulfilment of the requirements for a Postgraduate degree from the University of Saskatchewan, I agree that the Libraries of this University may make it freely available for inspection. I further agree that permission for copying of this thesis in any manner, in whole or in part, for scholarly purposes may be granted by the professor or professors who supervised my thesis work or, in their absence, by the Head of the Department or the Dean of the College in which my thesis work was done. It is understood that any copying or publication or use of this thesis or parts thereof for financial gain shall not be allowed without my written permission. It is also understood that due recognition shall be given to me and to the University of Saskatchewan in any scholarly use which may be made of any material in my thesis.

Requests for permission to copy or to make other use of material in this thesis in whole or part should be addressed to:

Head of the Department of Physics and Engineering Physics
163 Physics Building
116 Science Place
University of Saskatchewan
Saskatoon, Saskatchewan
Canada
S7N 5E2

Abstract

In modern low pressure plasma discharges, the electron mean free path often exceeds the device dimensions. Under such conditions the electron velocity distribution function may significantly deviate from Maxwellian, which strongly affects the discharge properties. The description of such plasmas has to be kinetic and often requires the use of numerical methods. This thesis presents the study of kinetic effects in inductively coupled plasmas and Hall thrusters carried out by means of particle-in-cell simulations. The important result and the essential part of the research is the development of particle-in-cell codes.

An advective electromagnetic 1d3v particle-in-cell code is developed for modelling the inductively coupled plasmas. An electrostatic direct implicit 1d3v particle-in-cell code EDIPIC is developed for plane geometry simulations of Hall thruster plasmas. The EDIPIC code includes several physical effects important for Hall thrusters: collisions with neutral atoms, turbulence, and secondary electron emission. In addition, the narrow sheath regions crucial for plasma-wall interaction are resolved in simulations. The code is parallelized to achieve fast run times.

Inductively coupled plasmas sustained by the external RF electromagnetic field are widely used in material processing reactors and electrodeless lighting sources. In a low pressure inductive discharge, the collisionless electron motion strongly affects the absorption of the external electromagnetic waves and, via the ponderomotive force, the density profile. The linear theory of the anomalous skin effect based on the linear electron trajectories predicts a strong decrease of the ponderomotive force for warm plasmas. Particle-in-cell simulations show that the nonlinear modification of electron trajectories by the RF magnetic field partially compensates the effects of electron thermal motion. As a result, the ponderomotive force in warm collisionless plasmas is stronger than predicted by linear kinetic theory.

Hall thrusters, where plasma is maintained by the DC electric field crossed with

the stationary magnetic field, are efficient low-thrust devices for spacecraft propulsion. The energy exchange between the plasma and the wall in Hall thrusters is enhanced by the secondary electron emission, which strongly affects electron temperature and, subsequently, thruster operation. Particle-in-cell simulations show that the effect of secondary electron emission on electron cooling in Hall thrusters is quite different from predictions of previous fluid studies. Collisionless electron motion results in a strongly anisotropic, nonmonotonic electron velocity distribution function, which is depleted in the loss cone, subsequently reducing the electron wall losses compared to Maxwellian plasmas. Secondary electrons form two beams propagating between the walls of a thruster channel in opposite radial directions. The secondary electron beams acquire additional energy in the crossed external electric and magnetic fields. The energy increment depends on both the field magnitudes and the electron flight time between the walls.

A new model of secondary electron emission in a bounded plasma slab, allowing for emission due to the counter-propagating secondary electron beams, is developed. It is shown that in bounded plasmas the average energy of plasma bulk electrons is far less important for the space charge saturation of the sheath than it is in purely Maxwellian plasmas. A new regime with relaxation oscillations of the sheath has been identified in simulations. Recent experimental studies of Hall thrusters indirectly support the simulation results with respect to the electron temperature saturation and the channel width effect on the thruster discharge.

Acknowledgements

I am grateful to my research advisor Andrei Smolyakov for his continual guidance, help, financial support, his interest in my career, and for the numerous opportunities he gave to me.

I heartily thank Igor Kaganovich and Yevgeny Raitses from the Princeton Plasma Physics laboratory, who introduced me to the exciting problem of Hall thrusters, for their advice and interest in my work, their time spent in numerous discussions, and warm welcome during my visits to the Princeton Plasma Physics Laboratory.

I express my gratitude to Artem Smirnov, Edward Startsev, and Nathaniel J. Fisch from the Princeton Plasma Physics Laboratory for helpful discussions.

I am thankful to Kaori Tanaka for providing the opportunity to use the 128-CPU Beowulf-class PC cluster at the University of Saskatchewan, funded by the Canada Foundation for Innovation.

Simulations were partially carried out using the WestGrid facilities at the University of British Columbia and the University of Calgary.

This study could not have been possible without the financial support of the University of Saskatchewan. I am grateful to the Herzberg Fund at the University of Saskatchewan for awarding me the Gerhard Herzberg Memorial Scholarship and travel grants. I thank Dr. Robert Summers-Gill, whose generous donation allowed the University of Saskatchewan to award me the Harold E. Johns Scholarship in Physics. The financial assistance for travel provided by the President/Student Fund and by the College of Graduate Studies and Research is greatly appreciated.

I deeply appreciate the warm and friendly atmosphere created by my friends: Yuriy Tyshetskiy, Tatyana Chshyolkova, Leonid Benkevich, Elena Krestova, Ivan Khalzov, Tatyana Novoselova, Sergei Ivanov, and Aaron Froese.

Many thanks to my family for their patience, support, and understanding.

Contents

List of Tables

List of Figures

List of Abbreviations

AC	Alternating Current
AR	Acceleration Region
DC	Direct Current
ECR	Electron Cyclotron Resonance
EDIPIC	Electrostatic Direct Implicit Particle-in-Cell
EM	Electromagnetic
EEDF	Electron Energy Distribution Function
EVDF	Electron Velocity Distribution Function
ICP	Inductively Coupled Plasma
MFP	Mean Free Path
MPI	Message Passing Interface
NWC	Near-Wall Conductivity
PIC	Particle-in-Cell
PMF	Ponderomotive Force
RF	Radio Frequency
RSO	Relaxation Sheath Oscillations
SEE	Secondary Electron Emission
SCL	Space Charge Limited
1d3v	one-dimensional in configuration space and three-dimensional in velocity space

Chapter 1

Introduction

The electron mean free path (MFP) is an important plasma characteristic. The MFP is the distance l an electron travels between collisions, determined as $l = v\tau$, where v is the electron velocity, and τ is the effective time between collisions. If the MFP is small compared to the plasma size L, $l \ll L$, the plasma is in thermal equilibrium and may be considered as a mixture of conducting electron and ion fluids. In the fluid approach, thermal motion of individual particles is not considered; the plasma properties are completely determined by a few macroscopic values: density n, temperature T, and flow velocity $\mathbf{u}$ [1]. The fluid equations [1]

$$\frac{\partial n}{\partial t} + \nabla \cdot (n\mathbf{u}) = 0 \ ,$$
$$mn\left[\frac{\partial \mathbf{u}}{\partial t} + (\mathbf{u} \cdot \nabla)\mathbf{u}\right] = -ne(\mathbf{E} + \mathbf{u} \times \mathbf{B}) - \nabla p$$

well describe processes with spatial and time scales much larger than the MFP and the time between collisions, such as diffusion, Ohm's law, etc. Here $\mathbf{E}$ and $\mathbf{B}$ are the electric and magnetic fields, $-e$ and m are the electron charge and mass, and p is the electron pressure.

If the size of the plasma is small compared to the MFP, $L \ll l$, the plasma is no longer in thermal equilibrium and the description of such plasma must be kinetic. In the kinetic approach, the plasma properties are defined by the electron velocity distribution function (EVDF) $f(\mathbf{v}, \mathbf{r}, t)$. The value $f(\mathbf{v}, \mathbf{r}, t)$ is the number of particles per unit of elementary volume $d^3r d^3v$ in six-dimensional phase space $\{\mathbf{r}, \mathbf{v}\}$

[1] Here the continuity and the momentum balance equations for electrons are presented. The latter equation is given in a simplified form without the drag force due to relative motion of electrons and ions. Equations for ions are similar.

at time t [2]. A collisional plasma in thermal equilibrium, which is well described by the fluid approximation, has a Maxwellian EVDF:

$$f_M(v_x, v_y, v_z) = n \left(\frac{m}{2\pi T}\right)^{3/2} \exp\left[-\frac{m(v_x^2 + v_y^2 + v_z^2)}{2T}\right] ,$$

where the electron temperature T is in energy units. In the kinetic, collisionless regime the EVDF may deviate significantly from the Maxwellian EVDF [3, 4, 5, 6, 7]. In the absence of collisions, the main equation of kinetic theory is the Vlasov equation:[2]

$$\frac{\partial f}{\partial t} + (\mathbf{v} \cdot \nabla) f - \frac{e}{m}(\mathbf{E} + \mathbf{v} \times \mathbf{B}) \frac{\partial f}{\partial \mathbf{v}} = 0 \ .$$

This equation expresses the conservation of the number of particles in the phase space.

Solution of the kinetic equation is usually cumbersome and often can only be obtained numerically. The most widely used methods are the Vlasov and particle-in-cell (PIC) algorithms. The Vlasov method directly solves the kinetic equation using a multi-dimensional grid in configuration and velocity phase space. This method is free of numerical noise persistent in PIC simulations, however, it requires many more numerical resources [8]. The PIC methods represent the plasma as a large number of charged particles and follow the motion of each particle [9, 10]. Because of the finite number of particles, PIC methods suffer high statistical noise and have difficulties in reproducing the tails of distribution functions. However, PIC algorithms are relatively simple, they use very few approximations and retain most of the nonlinear effects [11], can be applied to three-dimensional simulations on state-of-the-art computational facilities [12], and allow numerous collisional processes to be easily implemented [13].

The work described in this thesis includes the development of particle-in-cell codes and their application to the study of kinetic effects in two types of low-pressure discharges, namely inductively coupled discharges and Hall thrusters.

[2]The Vlasov equation is the specific case of the general Boltzmann equation without the collision term $(\partial f/\partial t)_c$ on the right hand side.

1.1 Kinetic and nonlinear effects in inductively coupled plasmas

1.1.1 Description of the design of an inductive discharge

The inductively coupled discharge was observed for the first time by Hittorf in 1884 [14]. Inductive discharges are capable of producing plasmas of high density, which are uniform over large scales, with low ion energy and low contamination by sputtering products from the discharge chamber walls. Nowadays inductively coupled plasmas (ICP) are widely used in industry for material processing [15] and lighting sources [16].

A typical inductive discharge device consists of a cylindrically symmetric discharge chamber and a driving antenna, which is usually a coil wrapped around the chamber (see Fig. 1.1a) or a plane coil attached to one end of the chamber (see Fig. 1.1b). A radio frequency (RF) current flows in the antenna and creates an RF electromagnetic (EM) field which sustains the plasma. The range of operating parameters for ICPs that manufacture integrated circuits is as follows: the electron temperature is $1 - 10$ eV, the driving current frequency is $1 - 10$ MHz, the plasma density is $10^{16} - 10^{18}$ m^{-3}. Note that in ICP the RF frequency $\omega \sim 10^7$ s^{-1} is much lower than the electron plasma frequency $\omega_{pe} \sim 10^9 - 10^{10}$ s^{-1}, where $\omega_{pe}^2 = ne^2/\varepsilon_0 m$, and $\varepsilon_0 = 8.85 \cdot 10^{-12}$ F $\cdot$ m^{-1} is the vacuum permittivity.

1.1.2 Classical and anomalous skin effects

An electromagnetic wave cannot propagate inside a plasma if $\omega < \omega_{pe}$. Consider a uniform plasma of density n, with frequency of electron collisions ν, occupying a half-space $z > 0$. Let the electric field at the boundary $z = 0$ be $E_y(0, t) = E_0 \exp(i\omega t)$. Neglect the electron thermal motion and the effects of the RF magnetic field. With these assumptions the motion of the electron due to collisions and the RF electric

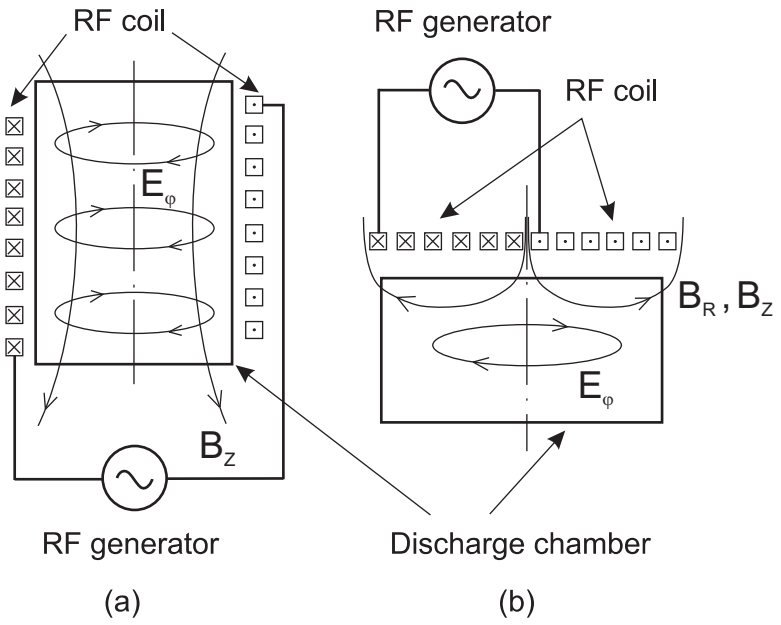

Figure 1.1: Schematic diagrams of ICP discharges. Figure (a) – side coil design; figure (b) – top coil (pancake) design.

field is described by

$$i\omega v_y = -\frac{e}{m}E_y - \nu v_y \ . \tag{1.1}$$

Equation of motion (1.1) corresponds to the case when the electric current is a local function of the electric field, *i.e.*, the current satisfies Ohm's law

$$j_y(z,t) = \sigma(\omega,\nu)E_y(z,t) \ , \tag{1.2}$$

where j_y is the electric current density and σ is the conductivity

$$\sigma(\omega,\nu) = \frac{\varepsilon_0\omega_{pe}^2}{i\omega+\nu} = \frac{\varepsilon_0\omega_{pe}^2}{\sqrt{\omega^2+\nu^2}}\exp\left(i\phi_\sigma\right) \ , \tag{1.3}$$

with $\tan\phi_\sigma = -\omega/\nu$. Assuming that the plasma is dense enough to ensure $\omega_{pe}^2 \gg \omega\sqrt{\omega^2+\nu^2}$, the displacement current $\partial\varepsilon_0 E_y/\partial t \ll j_y(z,t)$ can be omitted in Maxwell's equations, and the dispersion relation of the low frequency EM wave inside the plasma is

$$k^2 = -\frac{i\omega\sigma}{c^2\varepsilon_0} \ ,$$

where k is the complex wave number and c is the speed of light in vacuum. Here it is assumed that $E_y(z,t) = E_0 \exp(-ikz + i\omega t)$. The amplitude of the electric field

$$E_y(z) = E_0 \exp(-i(i\mathrm{Im}k)z) = E_0 \exp(\mathrm{Im}k\ z) \equiv E_0 \exp\left(-\frac{z}{\delta}\right)$$

is an exponentially decreasing function of coordinate z, $\delta > 0$. The spatial scale of the exponential decay is

$$\delta^{-1} = -\mathrm{Im}k = \mathrm{Re}\left(\frac{i\omega\sigma}{c^2\varepsilon_0}\right)^{1/2} . \tag{1.4}$$

For a collisionless plasma, $\nu \ll \omega \ll \omega_{pe}$, one obtains $\delta = c/\omega_{pe} \equiv \delta_c$. The exponential decay of a low frequency EM wave in conducting media (*e.g.*, plasma or metal) with the local relation (1.2) between electric current and electric field is called the *classical* skin effect, the region of intense field adjacent to the boundary, $0 < z \leq \delta$, is called the skin layer, and the scale δ is called the skin depth.

In ICP, most interaction between the plasma electrons and the RF EM field occurs in the skin layer. The different regimes of ICP operation are determined by the speed of electron flight through the skin layer, which is characterized by the nonlocality parameter λ, defined as [6]

$$\lambda = \frac{v_{th}}{\delta\sqrt{\omega^2 + \nu^2}} ,$$

where v_{th} is the electron thermal velocity. If the driving frequency is high, $\omega > v_{th}/\delta$, or if the collisions are frequent, $\nu > v_{th}/\delta$, then the nonlocality parameter is small, $\lambda \ll 1$, the current is a local function of the electric field, the skin effect is classical, and the plasma acquires energy from the RF field due to collisional Joule heating [6].

At the present time, inductive discharges tend to operate at low neutral gas pressure ($1 - 10$ mTorr) and low driving frequencies (< 1 MHz). Transition to lower operating frequencies reduces the effects of capacitive coupling, simplifies and decreases the cost of the RF power source and RF circuit, decreases transmission line effects in ICP inductors, and simplifies scaling the ICP to a larger size [17]. In warm plasmas most of the electrons fly quickly through the skin layer and the nonlocality parameter is large, $\lambda \gg 1$. In this regime, the electron velocity is determined by the

profile of the EM field along the whole electron trajectory and the local Ohm's law (1.2) is no longer valid [18]. The skin effect under the condition of nonlocal induced current is called the *anomalous* or *nonlocal* skin effect.

The anomalous skin effect was observed for the first time in metal by London [19] and in a xenon plasma by Demirkhanov *et al.* [20]. To qualitatively explain the anomalous skin effect in metals, Pippard [21] suggested that the major contribution to the induced current is due to the electrons that enter the skin layer almost parallel to the walls and thus spend a lot of time in the skin layer. The number of these electrons is small, about the ratio of the skin depth to the electron MFP, *i.e.*, the inverse nonlocality parameter $\lambda^{-1} \ll 1$. As an approximation, the anomalous skin depth can be obtained from (1.4) with conductivity multiplied by the aforementioned ratio [22], as follows:

$$\delta^{-1} = \mathrm{Re}\left(\frac{i\omega\sigma}{c^2\varepsilon_0}\frac{\delta\sqrt{\omega^2+\nu^2}}{v_{th}}\right)^{1/2} .$$

Then the anomalous skin depth is

$$\delta \sim \left(\frac{c^2 v_{th}}{\omega_{pe}^2\omega}\right)^{1/3} \sim \frac{c}{\omega_{pe}}\left(\frac{v_{th}\omega_{pe}}{c\omega}\right)^{1/3} \gg \frac{c}{\omega_{pe}} . \tag{1.5}$$

In the anomalous regime, the depth of field penetration (1.5) increases with plasma temperature.

Rigorous description of the anomalous skin effect assumes that the electric current at a given point is calculated by taking into account the RF EM field profile in a neighborhood the size of an electron MFP around this point. For metal this problem was solved for the first time by Reuter and Sondheimer [23]. The first work on the anomalous skin effect in plasma was done by Weibel [18]. The exact value of the skin depth in the anomalous regime [18] differs from the estimated value (1.5) by a factor of order unity:

$$\delta = \frac{8}{9\pi^{1/6}} \times \left(\frac{c^2 v_{th}}{\omega_p^2\omega}\right)^{1/3} .$$

In Ref. [18], it was shown analytically that in the anomalous regime the field decays nonmonotonically due to the current carried deep into the plasma by thermal electrons, which acquire additional momentum in the skin layer. The nonmonotonic

amplitude is a distinctive feature of the anomalous skin effect observed in numerous experiments [20, 24]. Another important property of the anomalous skin effect is the collisionless plasma heating due to the resonant absorption of damping electromagnetic wave by thermal electrons [18, 25, 26, 27]. Experimental confirmation of collisionless power absorption is described in [28, 29].

1.1.3 Nonlinear force and the ponderomotive effect

Equation of motion (1.1) does not account for the RF magnetic field and describes a linear motion. However, the amplitude of the RF magnetic field increases for the low frequency EM wave, $|\mathbf{B}| \sim (|k|/\omega)|\mathbf{E}|$, eventually becoming non-negligible. When the RF magnetic field is included, the electron equation of motion becomes

$$m\frac{d\mathbf{v}}{dt} = -e(\mathbf{E} + \mathbf{v} \times \mathbf{B}) - m\nu\mathbf{v} \ ,$$

and the equation of momentum balance for the Maxwellian electron liquid is nonlinear:

$$mn\frac{\partial \mathbf{u}}{\partial t} = -en\mathbf{E} - mn\nu\mathbf{u} - \nabla p + \mathbf{F}_{NL} \ , \tag{1.6}$$

where the nonlinear force $\mathbf{F}_{NL}$ is

$$\mathbf{F}_{NL} = -en\mathbf{u} \times \mathbf{B} - mn(\mathbf{u} \cdot \nabla)\mathbf{u} \ . \tag{1.7}$$

The first term of $\mathbf{F}_{NL}$ is the Lorentz force, the second term is the contribution from the electron inertia. The nonlinear force acts on the electrons, resulting in polarization of the plasma and excitation of the nonlinear polarization potential and electron current [30]. The polarization potential contains a DC component and the second harmonic, *i.e.*, the oscillatory component with the frequency 2ω [30]. The ions respond to the DC part of the potential $\Phi_{dc} = \langle\Phi\rangle$, so the plasma density profile forms according to the equilibrium condition $en\nabla\Phi_{dc} + \langle\mathbf{F}_{NL}\rangle - \nabla p = 0$, see Ref. [31]. Thus, the average part of the nonlinear force, $\langle\mathbf{F}_{NL}\rangle$, leads to the modification of the plasma density profile. This is the ponderomotive effect in fluid formulation.

In a nonuniform, time-varying EM field, the plasma motion separates into a "fast" motion and a "slow" motion compared to the oscillation period. The slow motion

occurs as if the plasma is affected by an external force $\mathbf{F}_p$, called the ponderomotive force (PMF) [32]. In the fluid formulation presented above, the PMF is the averaged nonlinear force, $\mathbf{F}_p = \langle \mathbf{F}_{NL} \rangle$. Alternatively, the PMF can be derived considering the nonlinear motion of a single particle. For an electron moving in the field of an EM-wave with spatially varying amplitude

$$\mathbf{E}(\mathbf{r},t) = \mathbf{E}_s(\mathbf{r}) \cos \omega t \ , \quad \mathbf{B}(\mathbf{r},t) = -\frac{1}{\omega} \nabla \times \mathbf{E}_s \sin \omega t \ ,$$

the PMF appears as a second order correction [33]:

$$m \langle \frac{d\mathbf{v}_2}{dt} \rangle = -\frac{e^2}{4m\omega^2} \nabla \left(\mathbf{E}_s \right)^2 \ ,$$

where $\mathbf{v}_2$ is the velocity of the electron guiding center, time-averaging $\langle\rangle$ is done over the wave period $2\pi/\omega$. In a cold plasma, the PMF acting on a unit volume is

$$\mathbf{F}_p = -\frac{\varepsilon_0 \omega_{pe}^2}{4\omega^2} \nabla E_s^2 \ . \tag{1.8}$$

The PMF describes a number of phenomena. It is responsible for the self-focusing and filamentation of laser beams in plasmas, density profile steepening, formation of cavitons, parametric instabilities, and magnetic field excitation in laser-produced plasmas (see the review [34] and numerous references therein).

The value of the PMF in a low frequency ICP can be larger than the force from the RF electric field. At low driving frequencies, the PMF is strongly affected by the nonlocal electron dynamics. In Ref. [35], the PMF was obtained as the average part of the Lorentz force by allowing for the nonlocal effects in approximation of exponentially decaying RF field. It was shown that in a strongly nonlocal regime, $\lambda \gg 1$, the PMF is

$$F_p = \frac{\varepsilon_0 \omega_{pe}^2}{2\omega^2} E_0^2 \frac{\sqrt{\pi}\omega}{v_{th}} \ , \tag{1.9}$$

where E_0 is the amplitude of the electric field of the evanescent EM wave at the plasma boundary. Note that expression (1.9) is meaningful only for a strongly decaying RF field with $\delta \ll v_{th}/\omega$. Comparing (1.9) with (1.8) one obtains

$$F_{p,\ \mathrm{NLC}} \sim \sqrt{\pi} \frac{1}{\lambda} F_{p,\ \mathrm{LC}} \ll F_{p,\ \mathrm{LC}} \ ,$$

where $F_{p,\ \mathrm{NLC}}$ is the nonlocal PMF calculated by (1.9) and $F_{p,\ \mathrm{LC}}$ is the local PMF calculated by (1.8). In the regime of the anomalous skin effect, the PMF (1.9) decreases with electron temperature due to the nonlocal effects.

1.1.4 Studies of ponderomotive and nonlinear effects in inductively coupled plasmas

Cohen and Rognlien [36] considered theoretically the dynamics of plasma electrons in ICP in the transverse electric E_y and magnetic B_x fields with an exponentially decaying spatial profile. They showed that some electrons can be trapped in the skin layer and others can be reflected back into the plasma before they even reach the plasma boundary. Electron heating by Lorentz force produces much more isotropic EVDF than the case with omitted magnetic field effects. The nonlinear force causes oscillations of the electron density in the skin region with a frequency double that of the induced field. The electron density reduction excites a strong longitudinal electrostatic field. In Ref. [37], both the transverse (electric and magnetic) and nonlinear longitudinal electric fields are taken into account. The latter field restores immediate quasineutrality. Its averaged part pushes the ions from the plasma boundary, modifying the plasma density profile.

Godyak *et al.* [24], in their studies of top coil ICP with relatively high operating frequency ($3.39 - 13.56$ MHz) found that the second harmonic of the RF plasma potential is higher at low gas pressure and low driving frequency when the RF magnetic field is large. An axial RF current oscillating at 2ω was also observed and measured. This current appears because of the interaction of the azimuthal RF current and the radial component of the magnetic field. Because of cylindrical geometry and two components of the magnetic field (B_r and B_z), the current formed a closed path in the plane $r - z$ within the plasma volume. As it was predicted in [37], the asymmetry of the plasma density profile due to the PMF was observed with a larger plasma gradient on the skin layer side.

The nonlinear effects in the low frequency low pressure ICP (0.45 MHz, 1 mTorr)

were also studied in [38]. Intensive second harmonics of plasma potential, radial and axial currents were registered. The decrease of the PMF in the warm low frequency ICP caused by the electron thermal motion was observed.

In Ref. [31], the experimental observation of a significant decrease of the PMF in the warm plasma of a cylindrical inductive discharge is described in detail. The discharge parameters are: a driving RF frequency of 0.45 MHz, an electron temperature of about 7 eV, a skin depth of 2.24 cm, and an effective collision frequency of $4 \cdot 10^6$ s^{-1}. Since $v_{th}/\delta \gg \omega, \nu$, this experiment falls within the typical anomalous skin effect regime. The PMF measured near the field maximum was about 10 times smaller than the value calculated by Eq. (1.8).

Furthermore, the influence of the PMF on the electron energy distribution function (EEDF) in a cylindrical inductive discharge with a flat coil at low frequency and low neutral gas pressure was observed experimentally [6]. Measurements of the EEDF showed significant depletion at low energies in the skin layer. Because of the reduction of the RF current in the skin layer due to thermal electron motion [38], the major part of the current is created by low energy electrons. As a result, the PMF mainly acts on the low energy electrons, thereby removing them from the skin layer. Qualitatively similar anisotropic EEDF was obtained theoretically in [36].

The nonlinear skin effect was discussed in [39] for cylindrical ICP within the magnetohydrodynamic framework. For a one-dimensional cylindrical ICP (side coil, with azimuthal symmetry and infinite along the axis) it is shown that the axial magnetic field (constant or RF) does not affect the field penetration because the modification of the azimuthal electric current due to the magnetic field is cancelled by the Hall current from the induced radial polarization field [39, 40]. However, in a planar ICP, the curvature of the magnetic field and the electron inertia result in nonlinear currents in $r-z$ plane, and, thus, a nonlinear azimuthal magnetic field B_φ is produced. This field may lead to the enhanced penetration of the RF field.

Experimental observation of the deep RF field penetration in a side coil ICP discharge is described by Tuszewski in [41, 42, 43]. He has found that the induced RF magnetic field essentially lowers the plasma electron thermal conductivity, resulting

in a much more uniform deposition of RF power. However, in experiments the EM field distribution is strongly influenced not only by the plasma screening, but by the chamber geometry as well. Additionally, the plasma density is usually nonuniform, decreasing towards the boundaries. Therefore, it is hard to relate the available observations of the changing of RF field penetration exclusively to nonlinear effects. At the same time the nonlinear skin effect is well known in metals, producing a decrease of the field penetration in the nonlinear regime (see [44] and the references therein).

1.1.5 Simulations of inductively coupled plasmas and motivation for the present work

The physics of low frequency ICP is rich in nonlocal and nonlinear effects. The analytical description of these effects requires significant simplifications. For example, the anomalous skin effect theory [18] and the calculation of the PMF in warm ICP [35] assume that the electrons move through the skin layer with constant velocity in the direction normal to the plasma boundary. However, in low frequency ICP the electron trajectories are strongly modified by the RF magnetic field, which could affect the excited electron flow and, thus, the PMF. The only way to investigate the nonlocal effects modified by the nonlinear force is through the use of numerical simulations.

Simulations of discharge devices for industry purposes are often based on fluid models [45] because of the great numerical cost of kinetic simulations. The performance of both types of simulations can be increased by using advanced physical models. Kortshagen *et al.* [46] proposed a kinetic model of ICP based on the nonlocal EVDF obtained from the Boltzmann equation averaged over the fast electron motion. Turner considered viscosity in the fluid model to add the effect of nonlocal current spreading in fluid simulations [47].

A straightforward method of simulating a kinetic system is the use of PIC algorithms [9, 10]. Impressive two-dimensional hybrid simulations of realistic discharge

configurations with kinetic representation of electrons and fluid representation of ions were carried out in Refs. [7, 48]. Turner [49] and Yoon *et al.* [50] studied the collisionless heating in ICP with PIC simulations based on the advective EM algorithm of Langdon and Dawson [10]. These simulations were carried out for high RF frequency 13.56 MHz, where the nonlinear effects are negligible.

The ponderomotive effect in the strongly nonlinear, nonlocal, collisionless regime typical for modern ICPs has not been previously considered, which motivates the present study [51, 52, 53]. To investigate the effects of electron thermal motion on the PMF in nonlinear low frequency ICP, a fully electromagnetic, quasineutral PIC code was developed. The code resolves one spatial dimension and three velocity components for every particle (1d3v). The code is applied to the calculation of the PMF (i) in the nonlinear regime, when the electron trajectories are modified by the RF magnetic field, and (ii) in the regime with linear electron trajectories, so comparison with the linear theoretical results of Refs. [25] and [35] may be carried out.

1.2 Kinetic effects in Hall thrusters

Hall thrusters [54] are low-thrust electric propulsion devices for orbital maneuvering of spacecrafts. The operation of a Hall thruster relies on the large electron MFP in the region where the accelerating electric field forms. In this region the electron motion is nearly collisionless, and the plasma properties significantly deviate from those of a Maxwellian plasma.

1.2.1 Hall thruster design and principles of operation

The development of Hall thrusters started in the middle of the 1960's independently in both the USSR and the US. The first satellite equipped with a Hall thruster was launched into orbit at the end of 1971. It was the Russian satellite "Meteor-18". Since that time Hall thrusters were installed on about 100 spacecraft, mostly Russian [55]. In November 2004 the European spacecraft "SMART-1" entered lunar

orbit using a Hall thruster as its main propulsion system.

The design of a Hall thruster is presented in Fig. 1.2. Inside the thruster, the plasma is contained in a coaxial ceramic channel. Between the cathode and the anode a voltage of several hundred Volts is applied, producing an axial electric field E_z. The magnetic core creates a magnetic field B_r, which is maximal near the exit plane of a thruster, see the blue curve in the graph in the bottom of Fig. 1.2. The direction of the magnetic field is almost completely radial, thus, the magnetic field is crossed with the axial electric field. The amplitude of the magnetic field is hundreds of Gauss. In the region of maximal magnetic field the radius of electron cyclotron rotation $R_{Le} = v_{th}m/eB_r - 10^{-3} \div 10^{-4}$ m, where B_r is the magnetic field amplitude, is much smaller than the electron MFP $l = v_{th}/\nu \sim 1$ m, and the width of the maximal magnetic field region $\Delta z_B \sim 10^{-2}$ m, *i.e.*, $R_{Le}/\Delta z_B \ll 1$ and $R_{Le}/l \ll 1$. The ions are heavy, the propellant is xenon with an ion mass $M = 131$ amu, and the radius of the ion cyclotron orbit R_{Li} is large, $R_{Li}/\Delta z_B \gg 1$. This mass difference results in qualitatively different motion of electrons and ions in the maximal magnetic field region. The electrons drift only in the azimuthal direction due to the crossed electric and magnetic fields, along the axis the electrons can move only due to collisions, while the ions are accelerated by the axial electric field and move freely across the magnetic field.

In Hall thrusters single charge ions are accelerated to $2 \cdot 10^4$ m/s, *i.e.*, about ten times faster than the jet velocity of a typical thermochemical rocket engine. The outgoing ion stream is neutralized by electrons ejected from the cathode. The power of operating Hall thrusters is within the range $0.5 - 5$ kW, the thrust is about 60 mN/kW, the propellant mass flow rate is $\dot{m} \sim 10^{-3}$ g/s, the lifetime is thousands of hours [56].

In fluid formulation, the electron flow velocity is related to the applied electric field via the electron mobility μ_e, $\mathbf{u} = \mu_e \mathbf{E}$. Near the exit of a Hall thruster the axial electron mobility is essentially suppressed by the strong magnetic field:

$$\mu_e = \frac{e}{m\nu} \frac{1}{1 + \omega_c^2/\nu^2} \ , \tag{1.10}$$

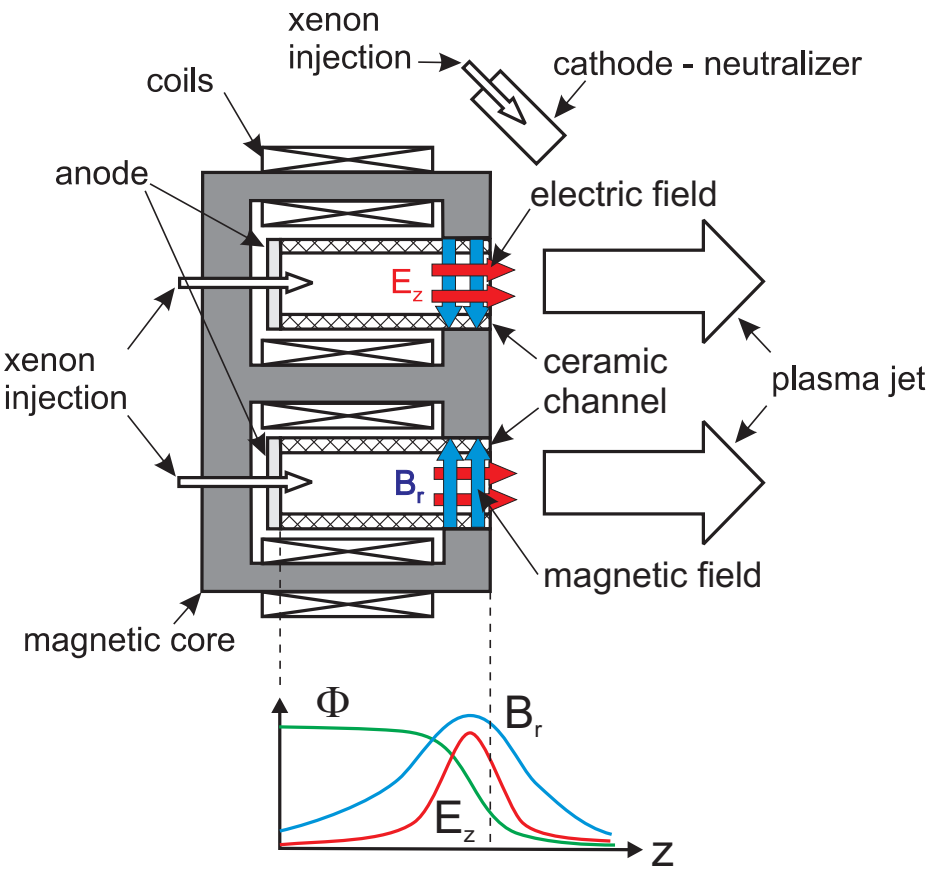

Figure 1.2: Schematic diagram of a Hall thruster and axial profiles of the electrostatic potential Φ, accelerating electric field E_z, and radial magnetic field B_r.

where $\omega_c = eB_r/m$ is the electron cyclotron frequency. In this region, the major drop of the potential occurs and the largest longitudinal electric field is excited (see green and red curves at bottom of Fig. 1.2). This region is called the acceleration region (AR). It is interesting that in the AR of a Hall thruster the actual electron mobility is significantly higher than the classical value (1.10) if the collision frequency is determined by the scattering of electrons on neutral atoms only [57]. Possible theoretical explanations of this anomalously high conductivity involve the anomalous Bohm diffusion due to magnetic field turbulence [58] and fluctuations of the azimuthal electric field [57, 59]. These fluctuations can arise due to various instabilities of electron current across the magnetic field [60, 61, 62]. There are a number of experimental evidences of the microturbulence in Hall thrusters [57, 63]. Azimuthal oscillations of electric field and electron density in Hall thrusters as well as the increase of axial electron mobility due to these oscillations were obtained in two-dimensional simulations in [64, 65, 66]. The other possible mechanism explaining high electron mobility is considered in the theory of near-wall conductivity (NWC), which suggests that the scattering of electrons in electron-wall collisions can increase the electron mobility across the magnetic field [67, 68]. The exact mechanism of anomalous electron mobility in Hall thrusters has not been established yet. Various analytical and numerical models usually introduce some effective collisions in addition to electron-neutral collisions in order to account for the anomalous electron mobility [69, 70].

The formation of a gradual drop in potential over the length of about $1 - 2$ cm in the AR crucially depends on electron energy. The condition $R_{Le}/\Delta z_B \ll 1$ must be satisfied, which requires electron energies in the range of tens of electronvolts, much smaller than the applied discharge voltage. The important role in limiting the electron temperature is played by the ceramic walls of the thruster channel. The wall material produces secondary electrons in response to bombardment by energetic plasma electrons. This phenomenon is called secondary electron emission (SEE) [71]. The hot plasma electrons are substituted by cold secondary electrons, which continually decrease the electron temperature. Cooling of the electron component via

interaction with the wall is largely determined by the processes that occur within the narrow non-neutral region near the wall.

1.2.2 Plasma-wall interaction with secondary electron emission

In bounded plasmas a thin space charge layer (sheath) is formed at the plasma-material interface [72, 73]. The drop of the potential across the sheath creates an electric field that reflects most of electrons back to the plasma, thus limiting the electron current and partially insulating the plasma from the wall. Total current to the dielectric wall is zero, so the electron flux to the wall Γ_1 must be equal to the ion flux Γ_i, $\Gamma_1 = \Gamma_i$. According to the Bohm condition [74], the ion flux is $\Gamma_i = n_s\sqrt{T_e/M}$, where T_e is the electron temperature, and n_s is the plasma density at the sheath boundary; Γ_i is relatively small because of the large ion mass.

If the wall emits electrons (*e.g.*, due to the SEE), the emitted electron flux Γ_2 (the secondary electron flux) partially compensates the electron flux Γ_1 coming to the wall from the plasma (the primary electron flux), and the flux balance equation is $\Gamma_1 - \Gamma_2 = \Gamma_i$. The intensity of SEE is characterized by the emission coefficient γ defined as the ratio of emitted and incident electron currents, $\gamma = \Gamma_2/\Gamma_1$. The sheath with SEE was examined for the first time and the approximate expression for the plasma potential Φ was found in Ref. [75]:

$$e\Phi \simeq T_e \ln\left[(1-\gamma)\left(\frac{M}{2\pi m}\right)^{1/2}\right]. \tag{1.11}$$

With SEE the plasma potential relative to the wall decreases.

Expression (1.11) is valid for small emission coefficients, $\gamma \ll 1$, and corresponds to a monotonic potential profile. When the emission coefficient approaches to unity, $\gamma \to 1$, the primary electron flux drastically increases, $\Gamma_1 = \Gamma_i/(1-\gamma) \to \infty$. In fact, if the emission coefficient exceeds some threshold γ_{cr}, $\gamma > \gamma_{cr}$, a double charged layer with nonmonotonic potential profile forms in the sheath region, and part of the emitted current is returned back to the wall, thus limiting the secondary electron

current that penetrates through the potential barrier adjacent to the wall. This SEE regime is called the space charge limited (SCL) regime. The resulting emission coefficient in the SCL regime does not exceed unity, $\gamma < 1$. In Ref. [75], the value of the emission coefficient that corresponds to the transition to the SCL SEE, the so-called critical emission coefficient, is found to be

$$\gamma_{cr} = 1 - 8.3 \left(\frac{m}{M}\right)^{1/2}. \tag{1.12}$$

For many materials the emission coefficient increases with the energy of incident electrons, as a result, plasmas with higher electron temperature produce emission characterized by higher γ. Transition to the SCL regime occurs at $\gamma = \gamma_{cr}$ and is accompanied by an exponential growth of the plasma electron flux to the wall. For plasmas with Maxwellian EVDF, the threshold value of the electron temperature T_{cr} corresponding to the transition to the SCL regime is called the critical electron temperature. This temperature is often considered to be the upper limit for the electron temperature in plasmas bounded by the walls with SEE. In particular, for boron nitride ceramic walls the critical electron temperature is only $T_{cr} \approx 18$ eV [76]. However, in Hall thrusters significantly higher values of the electron temperature can be achieved, which presents a significant theoretical problem.

1.2.3 Experimentally found properties of Hall thruster operation

Experimental study of the 2 kW Hall thruster with boron nitride ceramic channel carried out at the Princeton Plasma Physics Laboratory [77, 78, 79, 80] reveals the following discharge properties. There is a threshold value U_* of the discharge voltage U_d, about 400 V, which separates two regimes of electron temperature in Hall thrusters. Below the threshold, the electron temperature is maximal inside the thruster channel and increases linearly with the discharge voltage. Above the threshold, the electron temperature saturates at the level of $50-60$ eV and the temperature maximum is outside of the thruster channel, in the near-plume region [79]. The maximal electron temperature observed *inside* the channel is about 40 eV [78, 79], which

is more than two times larger than the critical electron temperature. The electron temperature *inside* the thruster channel does not exceed the value 40 eV even if the discharge voltage exceeds the threshold U_*.

It is reasonable to attribute the electron temperature saturation at $U_d > U_*$ to the plasma-wall interaction enhanced by intense SEE, as it is predicted by several fluid theories [81, 82]. This assumption is supported by the fact that for voltages above this threshold, the relation between the local values of the electron temperature and the plasma potential changes. In [83], the linear relation between the temperature and the potential was introduced, $T_e \sim \beta\Phi$. This law was later confirmed by many researchers, with a proportionality coefficient in the range $\beta = 0.09 - 0.14$ (see [78] and numerous references therein). For $U_d < U_*$, the relation $T_e \sim \beta\Phi$ is fulfilled both in the AR inside the channel and outside the channel in the near plume region, while for $U_d > U_*$, this relation is violated inside the thruster channel. However, for voltages around $U_d = 450$ V $\approx U_*$ the fluid theories [81, 82] predict a transition to the SCL regime, which is not confirmed by the experimental data.

The possibility of the transition to the SCL regime at different discharge voltages was analyzed in Ref. [79] by comparing the frequencies of electron-wall collisions with those for Maxwellian plasmas with corresponding temperatures. The electron-wall collision frequencies are estimated from the experimental data as follows. It is assumed that the electron energy loss at the walls is balanced by the Joule heating

$$\nu_w w_e = \frac{j_z}{n_e}\frac{\partial\Phi(z)}{\partial z} \ , \tag{1.13}$$

where ν_w is the frequency of electron-wall collisions, w_e is the average energy carried away by each collision, j_z is the axial electron current density, and n_e is the average electron density. For plasmas with isotropic Maxwellian EVDF of temperature T_e, one obtains $w_e \approx 2T_e$. The value of ν_w is determined from (1.13). It is found [79] that even for high discharge voltages $U_d = 400 - 700$ V, the experimental value of the electron-wall collision frequency is far less than the frequency of electron-wall collisions for a Maxwellian plasma in the SCL regime. Therefore, the SCL regime is likely not realized even though the electron temperature significantly exceeds the

critical value.

The aforementioned outward shift of the temperature maximum for $U_d > U_*$ is accompanied with a shift of the electric field maximum in the same direction, thus, the electric field inside the thruster channel decreases. In Ref. [79], the conclusion is made that the saturation of electron temperature inside the thruster channel is related to the decrease of the Joule heating $j_z E_z$ rather than to the electron wall losses enhanced by SEE.

For discharge voltages above the threshold U_*, the axial electron current and the electron mobility increase [79]. This increase may be related with the NWC effect [68]. The NWC is considered to be important if the SEE is close to the SCL regime [82]. It is interesting that in a Hall thruster with a narrow channel the AR forms almost completely outside of the thruster channel [80]. In a thruster with a narrow channel, the electron-wall collisions are more important, and the observed shift of AR may be related to the NWC as well. However, in narrow thrusters there is no experimental evidence of a correlation between the energy of electrons and the increased electron mobility inside the thruster channel, which is expected if the additional mobility appears due to the SEE effects.

1.2.4 Hall thruster fluid theories

In modern fluid theories of Hall thrusters, sheath models are used to provide self-consistent boundary conditions for the bulk plasma. In Ref. [69], the two-dimensional (r, z) fluid model describing the plasma volume inside the channel of a Hall thruster is based on the following system of equations:

$$
\begin{aligned}
nM(\mathbf{v}_i \cdot \nabla)\mathbf{v}_i &= ne\mathbf{E} - \nabla p_i - \beta n M n_a \mathbf{v}_a \ , \\
\nabla \cdot (\mathbf{v}_i n) &= \beta n n_a \ , \\
\nabla \cdot (\mathbf{v}_a n_a) &= -\beta n n_a \ , \\
0 &= -en(\mathbf{E} + \mathbf{v} \times \mathbf{B}) - \nabla p_e - n\nu m \mathbf{v}_e \ , \\
\frac{3}{2}\frac{\partial (j_e T_e)}{\partial z} &= Q_j - Q_w - Q_{ion} \ ,
\end{aligned}
$$

where n is the plasma density, n_a is the neutral atom density, β is the ionization rate, $Q_j = j_e E$ is the Joule heat, E is the axial component of the electric field, j_e is the electron current density, $Q_w = \nu_w n[2T_e + (1-\gamma)e\Delta\Phi_w]$ represents the wall losses, $\nu_w = (v_{th,e}/h)\exp(-\Delta\Phi_w/T_e)$ is the frequency of electron-wall collisions with $h = R_2 - R_1$ as the channel width, R_1 and R_2 being the inner and outer radii of the channel, $v_{th,e}$ is the electron thermal velocity, Q_{ion} represents ionization losses and $\Delta\Phi_w$ is the potential drop in the sheath. The value of $\Delta\Phi_w$ is found from the one-dimensional sheath model similar to [75], see equation (1.11) above. The total electron collision frequency ν consists of the electron-wall collisions ν_w, the electron-neutral collisions ν_{en}, and the anomalous collisions ν_B related to the Bohm diffusion. It was found that the SEE significantly affects the electron temperature distribution along the channel. Changing γ from 0.95 to 0.8 resulted in an almost two-fold increase in the maximum T_e value: from 16 eV to 30 eV. The T_e peak is attained inside the channel near the exhaust. In Ref. [69], only the non-SCL regime is considered.

In Ref. [84], the sheath/presheath model of a plasma flowing along annular dielectric walls with SEE was developed. The effects of the axial flow on the radial motion were included by adding the corresponding source terms in the radial equations. In Ref. [81], this model was combined with the one-dimensional macroscopic model of the steady-state axial discharge, which reproduces the channel of a Hall thruster and the near-plume region. The temperature in the acceleration region was determined by the balance between the Joule heating, the wall losses, and the heat conduction. It is shown that the temperature inside the thruster channel is limited by high losses of electron energy at the walls. Transition to the SCL regime occurs for discharge voltage $U_d = 450$ V.

The one-dimensional transit fluid model that allows for the electron temperature anisotropy was developed in [82]. The sheath model similar to that of Ref. [75] was used. A wide range of the discharge voltage U_d was considered. In simulations, the SCL regime was obtained for $U_d > 450$ V. In this regime, the increase of the discharge voltage results in rapid growth of the electron temperature. The average electron

energy exhibits strong anisotropy $T_{e\perp} \gg T_{e\parallel}$, where $T_{e\perp}$ is the electron temperature in the direction perpendicular to the magnetic field and $T_{e\parallel}$ is the electron temperature in the direction parallel to the magnetic field.

Fluid theories predict the saturation of the electron temperature when the discharge voltage is below the SCL regime [82], $U_d = 400 - 450$V, and occurs due to the intense wall losses enhanced by SEE [81]. Experiments [79] show that the temperature saturation is not simultaneous with the SCL regime, that the saturation occurs at much higher discharge voltages, and the reason for it is the decrease in the Joule heating. The difference between the results of fluid theories and the experiments appears to be because the fluid theories use the Maxwellian EVDF with pronounced high energy tails and intense wall fluxes, which are not present in Hall thrusters.

1.2.5 Kinetic studies of Hall thrusters and motivation for the present research

In confined plasmas, the electron flux to the wall is determined by the EVFD and by the sheath potential. In Hall thrusters, the electron MFP significantly exceeds the dimensions of the device. Under such conditions, the EVDF may deviate from Maxwellian, and the use of a Maxwellian EVDF for calculation of the electron fluxes may result in significant overestimation of the losses of electron energy at the walls.

It is shown, mostly numerically but also experimentally, that numerous kinds of low-pressure discharges, such as electron cyclotron resonance (ECR) discharges [5], capacitively [85] and inductively coupled plasmas [6, 7, 46], DC discharges [4], do indeed have non-Maxwellian electron velocity distribution functions. Modifications to the EVDF of collisionless plasmas can include depletion in the high energy range [4], depletion in the low energy range [6], anisotropy [5], *etc.*

Similarly, measurements of the electron energy distribution function (EEDF) inside Hall thrusters reveal that there are several groups of electrons with different average energies and that the total EEDF is non-Maxwellian [86]. Numerical analysis of kinetic equations reveal depletion of the high energy tail of the EEDF in Hall

thrusters and a reduction of electron losses to the wall compared to fluid theories [87]. Three-dimensional Monte-Carlo simulations of Hall thrusters [88] found that the EEDF exhibited a beam-like shape in high energy region.

Most available models of Hall thrusters are fluid, based on the Maxwellian EVDF; the number of kinetic models is much smaller. Full kinetic simulation of a Hall thruster has extremely high numerical cost because of several significantly different spatial and temporal scales that must be resolved. For example, the typical time of ion flight through the system is $t_i \sim 10^{-5}$ s, while the typical time of electron flight through the sheath is $t_e \sim \omega_{pe}^{-1} \sim 10^{-10}$ s; the dimensions of a thruster are $L \sim 10^{-1} - 10^{-2}$ m, while the width of the sheath is of the order of electron Debye length $\lambda_D \sim 10^{-3} - 10^{-4}$ m. The electron scales have to be resolved at least in the near-wall region in order to reproduce correctly the structure of the sheath and, therefore, the plasma-wall interaction in simulations.

Available kinetic studies of Hall thrusters consider electron distribution over energy [87, 88], and thus are limited to isotropic distributions, while the advanced fluid models [82] show that the velocity distribution in Hall thrusters may be anisotropic. The sheath is represented by a potential drop at the boundary, obtained analytically from some model [87] or simply set to some constant value [88]. PIC simulations of plasma-wall interactions carried out in Ref. [89] consider only the sheath region and assume that the EVDF of the bulk plasma remains Maxwellian. Thus, there is a need to study the plasma-wall interaction in Hall thrusters with self-consistent potential and EVDF.

For the purpose of a kinetic investigation of the effects of SEE on plasma-wall interaction in Hall thrusters, a one-dimensional plane geometry model was developed [90, 91, 92, 93, 94, 95]. The considered plasma is a slab, bounded by secondary electron emitting dielectric walls, immersed in a constant external strong magnetic field directed normal to the plasma boundaries and an electric field directed parallel to the plasma boundaries. The electrons collide with neutral atoms, ions, and other electrons, and perform additional "turbulent" collisions to reproduce the anomalous axial electron mobility. The model considered is a plane geometry

approximation of the AR of a Hall thruster. This model was originally proposed by Dr. Igor Kaganovich from the Princeton Plasma Physics Laboratory. The 1d3v electrostatic direct implicit PIC code (EDIPIC) was developed for simulations of this system. The code resolves both the sheath regions and the plasma bulk. To increase the simulation performance, the code has been parallelized. The code was extensively applied to plasma simulations with experimental parameters, as well as with parameters quite different from those observed in Hall thrusters. A whole set of new properties and possible regimes of plasma-wall interaction in Hall thrusters was discovered in simulations.

1.3 Thesis outline

In Chapter 2, the plane geometry model of ICP is studied by means of PIC simulations. A description of the model and the details of the developed 1d3v advective electromagnetic PIC code are given. The results of simulations with linear and nonlinear electron trajectories are compared with each other. The effect of nonlinear electron trajectories on the PMF in nonlocal regime is analyzed.

Chapter 3 contains the detailed description of the models and algorithms implemented in the EDIPIC code. The results of testing of the EDIPIC code are presented in Chapter 4. Chapters 5-7 are devoted to the study of the plane geometry model of the AR of a Hall thruster, carried out with the EDIPIC code.

In Chapter 5, the non-Maxwellian EVDF obtained in PIC simulations of the Hall thruster model is presented. The effects of different plasma parameters, namely, the frequencies of electron collisions with neutral atoms and "turbulent" collisions, external electric and magnetic fields, and Coulomb collisions on the shape of the EVDF are discussed. The counter-propagating beams of secondary electrons are introduced. The electron flux to the wall in a Hall thruster plasma is compared with that for a Maxwellian plasma.

In Chapter 6, the new model of SEE in a bounded plasma slab with counter-propagating secondary electron beams is described. This model allows for the emis-

sion produced by the secondary electron beams. The new criterion for the SCL SEE regime is derived, which essentially decouples the SCL regime from the temperature of the plasma bulk electrons. The energy gain of secondary electrons in crossed external electric and magnetic fields is described. The effect of the non-Maxwellian EVDF on the beam propagation through the plasma slab is discussed.

In Chapter 7, the new regime of the SEE, with strongly nonlinear quasi-periodic relaxation-type oscillations, is described. The detailed sequence of processes during one period of such oscillations is presented. The nonmonotonic current-voltage characteristic of the sheath with the region of negative conductivity is obtained. The system becomes unstable when its state corresponds to the negative conductivity of the sheath, which may be the reason for the relaxation-type oscillations. The effects of the ion mass, collision frequency, and width of the plasma gap on the oscillations are discussed.

In Chapter 8 the major results of the kinetic study of ICP and Hall thrusters are listed. The directions of the future work are described.

Appendix A describes energy conservation in simulations with EDIPIC code with large number of particles.

In Appendix B some parameters of Hall thruster simulations are presented.

Appendix C contains details of derivation of SEE characteristics in a bounded plasma slab.

Chapter 2

Particle-in-cell simulations of ponderomotive effects in inductively coupled plasmas

Oscillations of plasma particles in a time-varying inhomogeneous EM field result in a net force applied to the plasma, which is called the ponderomotive force or Miller force [32]. For cold plasmas, the PMF per unit volume is given by Eq. (1.8). The PMF is significant for low frequency ICP. Cohen and Rognlien [36, 37] predicted theoretically and Godyak *et al.* [31] found experimentally that the PMF modifies the plasma density profile in ICP.

The PMF is strongly affected by nonlocal effects due to electron thermal motion. In a number of works [96, 97, 98], thermal effects were considered as small corrections (of the order of the nonlocality parameter $\lambda \sim v_{th}/\omega\delta \ll 1$) to the classical expression (1.8). However, in the anomalous skin effect regime [18, 22, 49, 99], the nonlocality parameter λ is large, and thermal corrections of the PMF are no longer small. Experimental measurements have revealed that the PMF is significantly decreased in the warm plasma of a cylindrical inductive discharge [31].

The discrepancy between the Miller PMF (1.8) and the experiment may be attributed to the effects of thermal motion of electrons, which are crucial for the anomalous skin effect regime [18, 25], but are neglected in the classical cold plasma approach. Kinetic treatment of the PMF [35] shows that in the nonlocal regime the PMF (1.9) is strongly reduced due to finite electron temperature, in qualitative agreement with [31].

Calculations of the PMF in [35] were carried out with the assumption of linear electron trajectories, where the electrons moved with constant speed in the direction normal to the plasma boundary. However, in ICP the electron trajectories are strongly modified by the RF magnetic field, which affects the excited electron flow and, thus, the PMF. To further investigate the effects of the electron thermal motion on the PMF in the ICP, a 1d3v electromagnetic quasineutral PIC code was developed.

This Chapter discusses the results of numerical calculations of the PMF in a warm ICP. Section 2.1 describes the simulated plasma system and the details of the 1d3v EM PIC code. In Section 2.2, the analytical expressions for the nonlocal PMF calculated with self-consistent EM fields [25] and prescribed exponentially decaying EM fields [35] are presented. Section 2.3 compares the PMF calculated in linear electron trajectory PIC simulations with the theoretical PMF values of Refs. [25, 35]. Section 2.4 contains the results of nonlinear PIC simulations, where the electron trajectories are modified by the driving EM field. Conclusions are given in the Summary Section.

2.1 Description of the 1d3v PIC model

The simulated plasma has the form of a slab with thickness $L_{\rm pl}$, which is uniform and infinite along the x and y directions. The electromagnetic algorithm used in these simulations requires vacuum regions on both sides of the plasma (see Fig. 2.1). The whole system has length $L_{\rm sys}$ along the z direction, $L_{\rm sys} > L_{\rm pl}$. The plane EM-wave (E_y, B_x) propagates through the left vacuum region in the positive z direction, impinges normally on the plasma and propagates back in the negative z direction after the reflection. The plasma electrons are presented as macroparticles. In the present study, the ions form the immobile uniform background. No collisions between particles are considered. The initial velocity distribution is isotropic Maxwellian and the plasma density is uniform.

The developed PIC code uses the advective EM algorithm of Langdon and Daw-

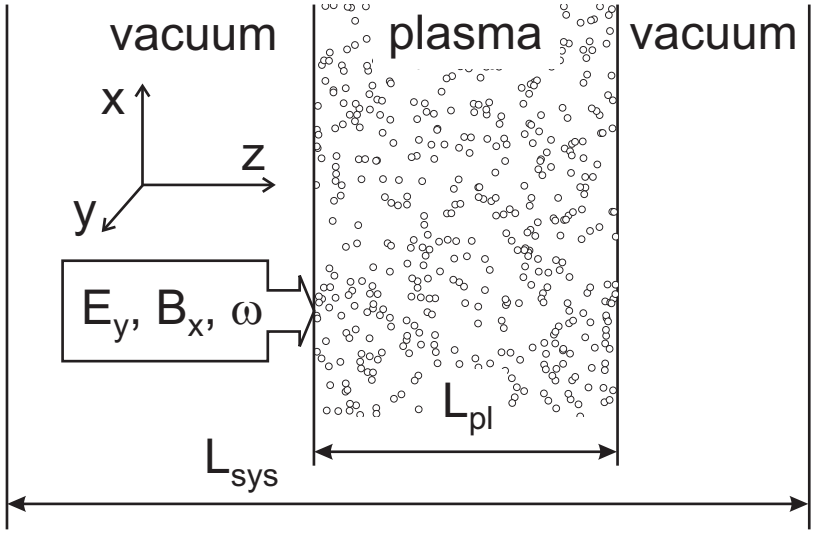

Figure 2.1: Schematic diagram of an inductively coupled plasma for PIC simulations.

son [10, 100, 101] to calculate the transverse field components. Assuming that there are no perturbations along the x and y directions, the Maxwell equations can be written in the form

$$\left(\frac{\partial}{\partial t} \pm c\frac{\partial}{\partial z}\right) {}^{\pm}F = -\frac{J_y}{\varepsilon_0} \ ,$$

where $c = 1/\sqrt{\varepsilon_0\mu_0}$ is the speed of light in vacuum, the left $(-)$ and the right $(+)$ propagating field combinations are

$${}^{\pm}F = E_x \pm Z_0 H_y \ ,$$

$Z_0 = (\mu_0/\varepsilon_0)^{1/2}$, and $\mu_0 = 4\pi \cdot 10^{-7}$ H $\cdot$ m^{-1} is the magnetic permeability. The transverse fields are recovered from ${}^{\pm}F$ as

$$E_y = \frac{1}{2}\left({}^{+}F + {}^{-}F\right) \ ,$$
$$H_x = \frac{1}{2Z_0}\left({}^{+}F - {}^{-}F\right) \ .$$

The combination $(\partial/\partial t) \pm c(\partial/\partial z)$ is the total derivative d/dt for the observer moving with the velocity $\pm c$. The finite difference form of the equations is

$$\frac{{}^{\pm}F_{j\pm1}^{n+1} - {}^{\pm}F_{j}^{n}}{\Delta t} = -\frac{1}{\varepsilon_0} {}^{\pm}J_{j\pm1/2}^{n+1/2} \ ,$$

where

$$ {}^{+}J^{n+1/2}_{j-1/2} = \sum_i v^{n+1/2}_{i,y} q_i \frac{1}{2} \left[S(Z_j - z^{n+1}_i) + S(Z_{j-1} - z^n_i) \right] \ , $$

$$ {}^{-}J^{n+1/2}_{j+1/2} = \sum_i v^{n+1/2}_{i,y} q_i \frac{1}{2} \left[S(Z_j - z^{n+1}_i) + S(Z_{j+1} - z^n_i) \right] \ . $$

Index n denotes time step number, index j denotes the spatial node with the coordinate Z_j, sum over i is the sum over particles with velocity component $v_{i,y}$, coordinate z_i, and charge q_i, and function S is the profile function of charge distribution over the neighbor nodes.

The advantages of the algorithm are, first, that such a time-centered scheme is stable against the numerical Cerenkov instability [102]. Second, that the fields are calculated at integer positions j and time steps n, which is convenient for the particle mover. Third, that the boundary conditions can be easily formulated.

One can show that ${}^{+}F = 2E^{+}_y$, where E^{+}_y is the electric field amplitude of the wave propagating in the positive z direction. Similarly, ${}^{-}F = 2E^{-}_y$ corresponds to the wave propagating in the negative z direction. For the wave (E_y, B_x) propagating in the positive z direction, the boundary condition at the left system boundary (not the left plasma boundary!) is

$$ {}^{+}F(z = 0, t) = E_{\text{wave}} \sin(\omega t) \ , \tag{2.1} $$

where E_{wave} is the amplitude of the incident EM-wave. In the right vacuum region there is only the wave propagating to the right. Therefore, the boundary condition at the right system boundary is

$$ {}^{-}F(z = L_{\text{sys}}, t) = 0 \ . $$

The main disadvantage of the described algorithm is a small time step Δt defined by the condition $\Delta z / \Delta t = c$ where Δz is the distance between two neighboring nodes.

The longitudinal electric field was calculated from the quasineutrality condition. Such an approach was used in Ref. [103]. On a long time scale, which is of interest for the PMF studies, deviations from quasineutrality are small, since it is restored within a time scale of several plasma oscillation periods. The longitudinal electric

field that maintains equal electron and ion densities $n_e = n_i$ is determined from the equation

$$E_z = -\frac{1}{n_i e}\frac{\partial}{\partial z}\left(n_i T_{ez}\right) - \frac{J_{ey}B_x}{en_e} \ , \tag{2.2}$$

where T_{ez} is the longitudinal component of the electron temperature. It was found by comparison of quasineutral simulations with simulations where the Poisson's equation was involved[1] that the quasineutral algorithm decreases the noise in E_z by (roughly) a factor of 100. Note that in quasineutral simulations the longitudinal plasma oscillations disappear, while the transverse EM waves are not affected.

In PIC simulations, the PMF is calculated as follows:

$$F_p(z) = \langle -J_y(z,t)B_x(z,t)\rangle \ ,$$

where $\langle ...\rangle$ means averaging over the wave period, J_y is calculated as the sum of contributions from separate macroparticles. This is equivalent to the calculation of the electric current density in the kinetic approach as the moment of the EVDF. In general, the total nonlinear force in the electron fluid equation of motion has also a contribution from the nonlinear convective term $n_e[-m(\mathbf{u}\cdot\nabla)\mathbf{u} - e(\mathbf{u}\times\mathbf{B})]$. The convective term does not appear in the considered one-dimensional plane geometry, provided the electron flow normal to the plasma boundary is zero, $u_z = 0$, so that the PMF is due to the time-averaged Lorentz force only.

For all calculations presented in this Chapter, if not specified otherwise, the following parameters of plasma were chosen: $n_e = 10^{17}$ m^{-3}, $\omega = 3.14\cdot 10^6$ s^{-1}. All values are calculated at a distance $z = 2$ mm from the left plasma boundary. The system width is $L_{sys} = 20$ cm, the plasma slab width is $L_{pl} = 10$ cm, the width of each vacuum region is 5 cm. The uniform computational grid has 200 cells, with 100 cells inside the plasma slab. The number of electron macroparticles is $2\cdot 10^5$.

[1]The initial version of the PIC code was solving the Poisson's equation. It was the high noise of E_z in simulations with the old version of the code that motivated transition to the quasineutral approach.

2.2 Theoretical description of the ponderomotive force with thermal effects

2.2.1 Self-consistent linear ponderomotive force

In Ref. [25] the coupled Maxwell and kinetic equations are solved self-consistently for an EM wave penetrating into a uniform plasma halfspace. The following expressions for the complex amplitudes of electric field and current are obtained:

$$E_y^c(z) = -\frac{2\eta v_{th}}{\pi\omega}\int_0^\infty d\kappa \frac{\cos(\kappa\zeta)}{\kappa^2 - \beta_t^2 + g k_\xi(\kappa)} \ , \tag{2.3}$$

$$J_y^c(z) = \frac{\eta\omega_{pe}^2 v_{th}}{\pi^{5/2}\omega^2}\left(-\frac{2}{\xi}\right)\int_0^\infty d\kappa \frac{\cos(\kappa\zeta)k_\alpha(\kappa)}{\kappa^2 - \beta_t^2 + g k_\xi(\kappa)} \ , \tag{2.4}$$

where $\zeta = z\omega/v_{th}$, $\beta_t = v_{th}/c$, $\eta = \frac{d}{dz}E_y$ and η is calculated at the plasma boundary $z = 0$, $g = 2i\omega_{pe}^2\beta_t^2/\sqrt{\pi}\omega^2\xi$, $\xi = \nu/\omega + i$,

$$k_\xi(\kappa) = \left(\frac{\xi}{\kappa}\right)^3 \int_0^\infty dx x \exp(-x^2) \times \left\{\left[1 + \left(\frac{\kappa x}{\xi}\right)^2\right] i \ln\left(\frac{1 - i\kappa x/\xi}{1 + i\kappa x/\xi}\right) - 2\frac{\kappa x}{\xi}\right\} \ .$$

Substituting (2.3) into the corresponding Maxwell equation one obtains the complex amplitude of the magnetic field

$$B_x^c(z) = -i\frac{2\eta c}{\pi\omega}\int_0^\infty d\kappa \frac{\kappa \sin(\kappa\zeta)}{\kappa^2 - \beta_t^2 + g k_\xi(\kappa)} \ . \tag{2.5}$$

For the complex electric current density $J_y(z,t) = J_y^c(z)\exp(i\omega t)$ with complex amplitude $J_y^c = |J|\exp(i\phi_J)$ given by equation (2.4) and the complex magnetic field $B_x(z,t) = B_x^c(z)\exp(i\omega t)$ with complex amplitude $B_x^c = |B|\exp(i\phi_B)$ given by equation (2.5), the expression for the PMF is

$$F_p = -\frac{1}{2c}|J||B|\cos(\phi_J - \phi_B) \ . \tag{2.6}$$

2.2.2 Ponderomotive force with exponentially decaying fields

Instead of the complicated self-consistent procedure of Ref. [25], in Ref. [35] the electric and magnetic fields are taken in the form [18, 31]

$$\begin{aligned} E_y(z,t) &= E_0 \exp(-\gamma z)\exp(-i\omega t)\ , \\ B_x(z,t) &= \frac{i\gamma}{\omega} E_0 \exp(-\gamma z)\exp(-i\omega t)\ , \end{aligned} \tag{2.7}$$

where E_0 is the field amplitude at the plasma boundary, $\gamma = 1/\delta - i\kappa$ is the complex longitudinal wavenumber,[2] δ is the skin depth, and κ determines the energy flux into the plasma. Using these prescribed fields, the following expression for the PMF in a semi-infinite uniform plasma is obtained:

$$F_p = \frac{\omega_{pe}^2}{8\pi\omega} E_0^2 \exp\left(-\frac{2z}{\delta}\right) \mathrm{Re}\left\{ i\frac{\gamma^*}{\gamma v_{th}} \left[Z(-is) - \exp(\gamma z) G(\gamma z, s) \right] \right\}\ , \tag{2.8}$$

where

$$Z(p) = \frac{1}{\sqrt{\pi}} \int\limits_{-\infty}^{\infty} \frac{\exp(-x^2)}{x-p} dx$$

is the plasma dispersion function, $s = (\omega + i\nu)/\gamma v_{th}$, and

$$G(\gamma z, s) = \frac{2}{\sqrt{\pi}} \int\limits_{0}^{\infty} \frac{t \exp\left(i\gamma z s/t - t^2\right)}{t^2 + s^2} dt\ .$$

Expression (2.8) approaches (1.9) for $s \ll 1$.

Note that PMF (2.6) and (2.8) are represented in cgs units, as in the original papers [25, 35].

2.3 Thermal effects in the ponderomotive force for linear electron trajectories

In an effort to verify the PIC code by comparison with analytical solutions, the values of the theoretical PMF were calculated using Eqs. (2.4-2.6) and Eq. (2.8). An

[2] Note, in Chapters 3 – 7 notation γ is used instead for the emission coefficient.

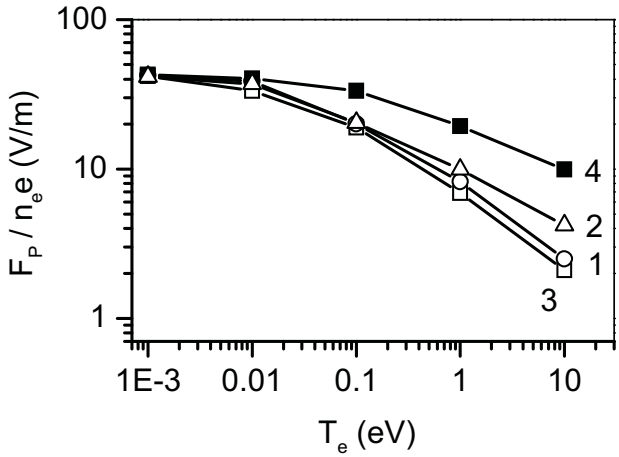

Figure 2.2: The PMF as a function of the electron temperature. Curve 1 is calculated from (2.4-2.6), curve 2 is from (2.8), curve 3 is obtained with linear PIC simulations, and curve 4 is from PIC simulations with nonlinear electron dynamics. The amplitude of the electric field at the plasma boundary is $E_0 = 10$ V/m.

electric field amplitude of $E_0 = 10$ V/m at the plasma boundary and various electron temperatures T_e (see curves 1 and 2 in Fig. 2.2) were tested. The PMF obtained with self-consistent Eqs. (2.4-2.6) is close to the prescribed-field PMF (2.8) in the whole range of considered temperatures 0.001 eV $\leq T_e \leq$ 10 eV. The PMF rapidly decreases with the increase of the electron temperature. At low temperatures the calculated magnitude of the PMF approaches the cold plasma value (1.8).

Both in the self-consistent approach [25] and in the approach of prescribed EM fields [35], the linearized kinetic equation,

$$\frac{\partial f_1}{\partial t} + v_z \frac{\partial f_1}{\partial z} + \frac{e}{m} E_y \frac{\partial f_0}{\partial v_y} = -\nu f_1 \ ,$$

where f_0 is the Maxwellian distribution function, was solved by integration along the linear electron trajectories with a constant velocity v_z along the z direction. To reproduce the linear trajectories in PIC simulations, the Lorentz force and the longitudinal electric field E_z were omitted in the equations of electron motion.

For a consistent comparison with linear theoretical results, which use an electric field amplitude of $E_0 = 10$ V/m at the left plasma boundary, the PIC simulations must have the same electric field amplitude. Note that E_0 is not the amplitude of

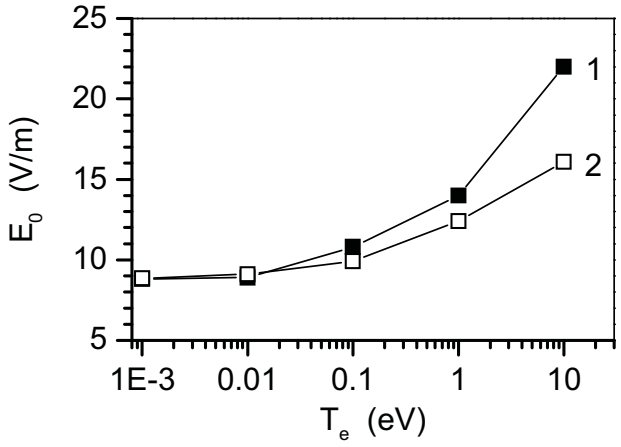

Figure 2.3: The transverse electric field amplitude at the plasma boundary E_0 versus the electron temperature T_e at constant amplitude of the incident EM-wave $E_{\rm wave} = 28800$ V/m. Curve 1 corresponds to the linear PIC simulations, curve 2 – to the nonlinear PIC simulations.

the incident wave $E_{\rm wave}$ used in the boundary condition (2.1). The EM field in the left vacuum region is the superposition of the EM fields of the incident wave and the wave reflected from plasma. Due to the strong reflection of a low frequency EM wave from a dense plasma, the incident and the reflected waves have close amplitudes and opposite phases of the electric field. Therefore, the amplitude of the total electric field at the plasma-vacuum boundary E_0 is much smaller than the amplitude of the incident wave in vacuum $E_{\rm wave}$. In the simulations, the value of $E_{\rm wave}$ was set to 28800 V/m, which produces $E_0 = 10$ V/m in cold plasma. In a plasma with higher electron temperature the absorption of the EM energy increases (the linear anomalous skin effect) and $E_0(T_e)$ becomes larger (see curve 1 in Fig. 2.3), although $E_{\rm wave}$ remains constant. The values of the PMF obtained for different amplitudes E_0 were scaled to the desired base amplitude $E_0 = 10$ V/m by using the following relation:

$$F_p(T_e, E_{0b}) = \frac{E_{0b}^2}{E_0^2(T_e)} F_p(T_e, E_0) \ , \tag{2.9}$$

where $F_p(T_e, E_{0b})$ is the PMF at a given electron temperature T_e and the base electric field amplitude $E_{0b} = 10$ V/m, $F_p(T_e, E_0)$ is the PMF produced in a plasma with the electron temperature T_e by RF field with the actual value of the electric field

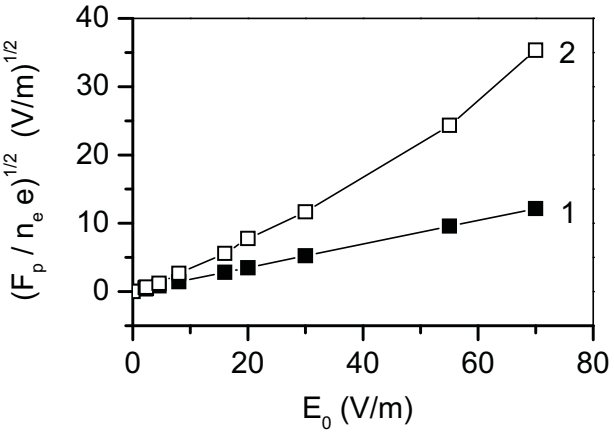

Figure 2.4: The square root of the ponderomotive force versus the transverse electric field amplitude at the left plasma boundary E_0 at constant electron temperature $T_e = 10$ eV. Curve 1 corresponds to the linear PIC simulations, curve 2 – to the nonlinear PIC simulations.

amplitude $E_0(T_e)$. The above relation is valid provided $F_p \sim E_0^2$, which is confirmed in several linear simulation tests (see curve 1 in Fig. 2.4).

The dependence of the PMF on T_e, obtained in PIC simulations with linear trajectories, is presented in Fig. 2.2 by curve 3. The PMF decreases as the electron temperature T_e increases. At low temperatures the PMF is very close to the value of the PMF in a cold plasma (1.8). The linear PIC simulations and the analytical solution to the system of kinetic and Maxwell equations (2.4-2.6) give similar values of the PMF over a wide range of electron temperatures (compare curves 3 and 1 in Fig. 2.2). The overall comparison of the linear PIC simulations with the theoretical results gives confidence that the PIC code is working properly, and allows one to understand the effect of various approximations.

2.4 Effects of the nonlinear modification of the electron trajectories

This Section presents the results of PIC simulations when the RF magnetic field and the longitudinal electric field are retained in the equations of motion of electrons.

The electron trajectories are no longer straight lines and the classical theory of the anomalous skin effect is not valid in this case.

As in linear simulations described in Section 2.3, the amplitude of the electric field at the vacuum-plasma boundary E_0 is larger in a warm plasma than in a cold one (see curve 2 in Fig. 2.2). However, this effect is less strong in nonlinear simulations than in linear ones for plasmas of the same temperature, *i.e.*, the EM wave reflection is enhanced in the nonlinear case. The scaling law $F_p \sim E_0^2$ is not valid in nonlinear simulations (curve 2 in Fig. 2.4 is not a straight line, unlike curve 1).

Curve 4 in Fig. 2.2 shows the temperature dependence of the PMF calculated in the nonlinear PIC simulations. The decrease of the PMF in warm plasmas is observed. However, the PMF in nonlinear simulations is from two to three times larger than the corresponding linear values at $T_e > 1$ eV. Therefore, the nonlinear effects of the RF magnetic field partially compensate the reduction of the ponderomotive force due to the electron thermal motion.

Compare two simulations carried out with the same initial parameters of the plasma and the incident wave: the first simulation with the electrons moving in the complete EM field (curves 1 in Fig. 2.5) and the second linear simulation with the electrons moving only under the influence of the transverse electric field (curves 2 in Fig. 2.5). The latter model corresponds to the linear electron trajectories. The RF electric field amplitude in nonlinear simulation is about 25% lower than that in simulation with linear electron dynamics (see Fig. 2.5a). The phase shift between the magnetic and the electric fields in simulation with complete fields is close to $\pi/2$, *i.e.*, wave penetration into the plasma decreases compared to the case of the linear electron dynamics. The time dependence of B_x is almost identical in both simulations (Fig. 2.5b). The most noticeable effect is the increase of the electric current density: its amplitude in the nonlinear case is 2.5 times larger than in linear simulation (see Fig. 2.5c). The increased current results in a proportional increase of the Lorentz force and its mean value – the PMF – in the nonlinear case (Fig. 2.5d).

Qualitative explanation of the increase of the electric current can be as follows. The nonlinear Lorentz force expels electrons from the strong field region near the

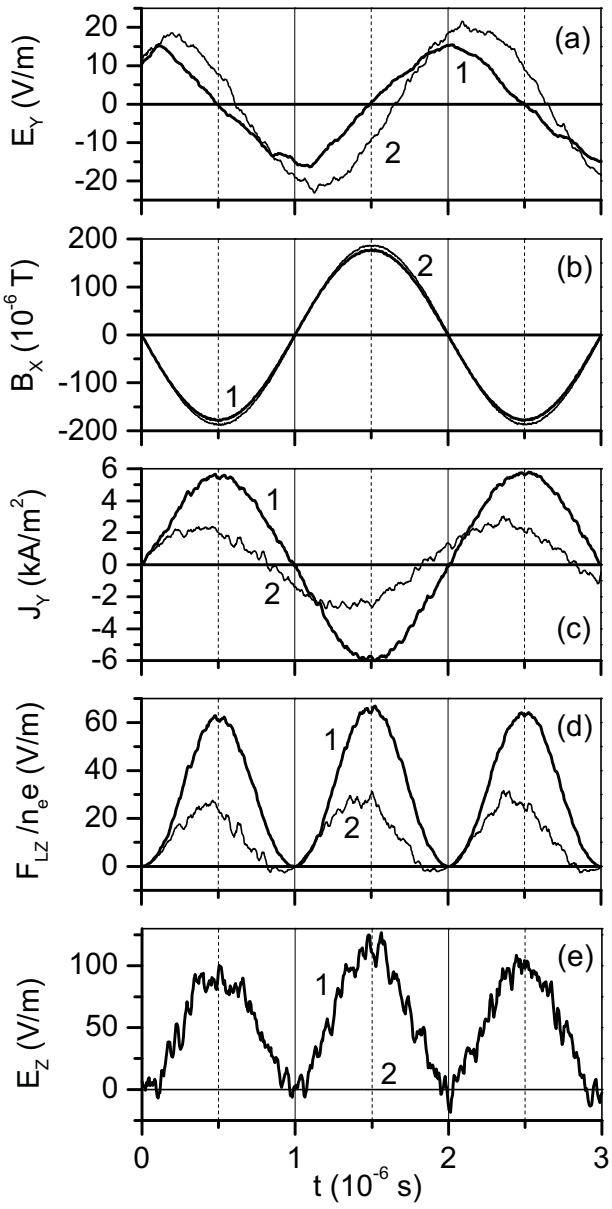

Figure 2.5: The transverse electric field (a), the magnetic field (b), the electric current density (c), the nonlinear force (d), and the longitudinal electric field (e) versus time, for nonlinear (curves 1) and linear (curves 2) PIC simulations with $T_e = 10\ eV$, $E_{wave} = 28800$ V/m.

plasma boundary [6]. Since the ion mobility is low (in fact, in present simulations, the ions are immobile), a strong longitudinal electric field (2.2) arises (see curve 1 in Fig. 2.5e), which restores the quasineutrality of the plasma in the skin layer [36, 37]. Note that in the linear PIC simulations $E_z = 0$ (curve 2 in Fig. 2.5e). When $\omega_c \gg \omega$, where ω_c is the electron cyclotron frequency, the crossed E_z and B_x fields result in an electron drift in the y direction, which increases the electron flow already caused by the E_y component of the EM wave. This effect is somewhat similar to the effect of the Hall polarization field which increases the electric current in a plasma with a constant magnetic field [39, 40].

In fact, modification of the electron trajectories by the RF magnetic field is much more complicated than just the Larmor motion and the slow drift in the crossed electric and magnetic fields. Besides the fields being nonuniform and time-dependent, the plasma is bounded. Some electrons reach the plasma boundary and are reflected there, moving along the trajectories which are close to the linear ones (curve 1 in Fig. 2.6). At other times, the electrons can be reflected by the Lorentz force back into the plasma before reaching the plasma boundary (curve 2 in Fig. 2.6) or even be trapped [44] in the skin layer (curve 3 in Fig. 2.6).

The electron paths shown in Fig. 2.6 exemplify strongly nonlinear conditions. The ratio of the width of the skin layer to the Larmor radius near the plasma boundary, where the magnetic field is the strongest, is $\rho(v) = \delta\omega_{c0}/v = 0.72 \simeq 1$, where $\omega_{c0} = eB_x(0)/m$. For faster particles with $\rho \ll 1$ the trajectories are close to the linear ones. Slower particles with $\rho \geq 1$ have strongly perturbed trajectories. There are enough such low energy particles to significantly affect the results, even though the value of ρ obtained using the thermal velocity is small.

A set of linear and nonlinear simulations with $T_e = 10$ eV has been carried out over a range of RF field amplitudes and, correspondingly, values of $\rho_{th} \equiv \rho(v_{th})$. Simulations with the electric field amplitude at the plasma boundary below 2 V/m could not be run because the numerical noise becomes comparable to the RF field. The smallest ρ_{th} achieved in this set of simulations was $\rho_{th} = 0.092$. The ratio of the PMF in nonlinear simulation to the PMF in linear simulation is 4.9 at $\rho_{th} = 1.44$,

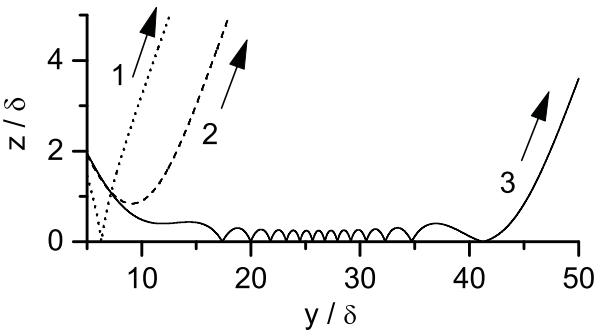

Figure 2.6: Trajectories in the y–z plane of a single electron in the exponentially decaying oscillating EM fields E_y, B_x and E_z. The transverse field components are calculated as the real part of Eqs. (2.7). The longitudinal electric field (2.2) of PIC simulations is approximated as $E_z(z,t) = E_{z0}\exp(-2\gamma z)(\sin\omega t)^2$. Curve 1 is the trajectory of an electron specularly reflected from the plasma boundary $z = 0$; curve 2 is the trajectory of an electron reflected by the Lorentz force; curve 3 is the trajectory of a trapped electron. The arrows show the direction of the electron motion. The transverse electric field has amplitude $E_y =$ 16 V/m, the longitudinal electric field has amplitude $E_{z0} = 100$ V/m, the skin depth $\delta =$ 0.043 m, $\gamma = 1/\delta$, the electron initial velocity $v = 1.88\cdot 10^6$ m/s corresponds to the thermal velocity $v_{th} = (2T_e/m)^{1/2}$ with $T_e = 10$ eV. The above parameters are close to the corresponding values of the nonlinear simulation presented in Fig. 2.5.

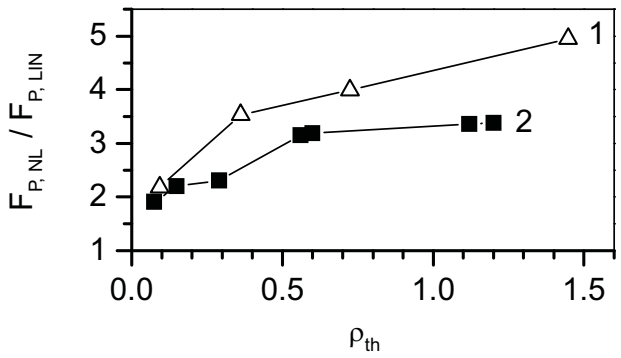

Figure 2.7: The ratio of the PMF obtained in nonlinear PIC simulations to the PMF obtained in linear PIC simulations versus the ratio of the skin layer depth to the Larmor radius of thermal electron. Curve 1 corresponds to electrons with normal mass, $m = 9.1 \cdot 10^{-31}$ kg, $T_e = 10$ eV and $n_e = 10^{17}$ m^{-3}; curve 2 corresponds to the "heavy" electrons, $m = 9.1 \cdot 10^{-30}$ kg, $T_e = 100$ eV and $n_e = 10^{18}$ m^{-3}.

and it decreases to 2.1 when $\rho_{th} = 0.092$ (see curve 1 in Fig. 2.7). The "nonlinear" PMF tends to its "linear" value in low intensity RF fields because the contribution of nonlinear electrons becomes less important.

To investigate the behavior of the PMF at even lower values of ρ_{th}, the electron mass, electron temperature, and plasma density were artificially increased in simulations by a factor of 10. Such scaling conserves the electron thermal velocity and the electron plasma frequency, thus the linear anomalous skin effect remains unchanged, while for the same RF field amplitude, the value of ρ_{th} decreases by 10 times. A set of nonlinear and linear PIC simulations was performed, similar to the one described above, with "heavy" electrons. The ratio of the "nonlinear" to the "linear" PMF decreases from 3.3 at $\rho_{th} = 1.2$ to 1.9 at $\rho_{th} = 0.075$ (see curve 2 in Fig. 2.7). Unfortunately, heavier electrons raise the noise level, so the range $\rho_{th} < 0.075$ (corresponding to the electric field amplitude $E_0 < 20$ V/m for "heavy" electrons) was impossible to study. However, the available data from both sets of PIC simulations show the strong tendency to transition from the nonlinear to the linear regime at $\rho_{th} < 0.075$. The dynamics of normal electrons at $T_e = 10$ eV could be linear if the RF electric field amplitude is less than 2 V/m, which is negligible in comparison with the intensity of the electric field ($E_0 \sim 100$ V/m) in experimental devices.

In fact, the higher "nonlinear" PMF is in better agreement with the experimental results of Ref. [31] than the "linear" PMF. In experiment [31], the ponderomotive potential U was obtained from the plasma equilibrium equation $T_e\nabla n + n\nabla V + n\nabla U = 0$, where V is the plasma potential and n is the plasma density. The PMF term $-n\nabla U$ includes the contribution from the Lorentz force $\mathbf{u}\times\mathbf{B}$ and the contribution due to the convective part of the inertia force $(\mathbf{u}\cdot\nabla)\mathbf{u}$. The DC Lorentz force measured in Ref. [31] was about three times larger than the full PMF $-n\nabla U$, therefore, the Lorentz force was partially compensated by the convective term. Since the present simulations are performed in the idealized one-dimensional geometry, the electric current flows along the plasma boundary in the y direction only, and the PMF is only the time averaged Lorentz force. In the realistic cylindrical geometry [31], the nonlinear force can be further modified by the effect of curvature of the electron flow [39, 40] when $(\mathbf{u}\cdot\nabla)\mathbf{u}\neq 0$, as well as by the effects of the particle reflections from the curved sheath at the plasma boundary [104].

2.5 Summary

The 1d3v fully electromagnetic quasineutral collisionless PIC code is developed to study the nonlinear modification of the effects of the electron thermal motion on the PMF in ICP.

The standard analytical theory of the anomalous skin effect [18, 25] is based on the assumption of the linear trajectories of electrons, which are not affected by the RF magnetic field. The PIC simulations are carried out under similar conditions to compare with linear theoretical results [25, 35]. In these simulations the magnetic field is omitted in the electron motion equations. The linear PIC simulations give the values of the PMF, which are close to the theoretical values. The strong thermal reduction of the PMF is reproduced in linear simulations.

The nonlinear simulations of the ponderomotive effect are conducted with electron trajectories modified by the RF magnetic field and the ambipolar electric field. It is found that at high electron temperatures the PMF values are several times

larger than the corresponding values obtained in linear simulations. The nonlinear increase of the PMF can be qualitatively explained as a result of the additional transverse electron current due to the drift in the crossed ambipolar electric field and the transverse magnetic field.

Trajectories of electrons, whose Larmor radius is smaller than or comparable with the skin layer depth, are strongly modified. The plasma dynamics can be nonlinear due to these low energy electrons, even when the trajectories of electrons with thermal velocity are weakly perturbed. The increased PMF (2 times larger than the linear value) is obtained, although the ratio of the Larmor radius to the skin depth for a thermal electron was $0.092 \ll 1$. The simulations show that the small linear PMF value can be achieved only at very low amplitudes of RF field, typically much smaller than the RF field amplitudes in operating ICP discharges.

Chapter 3

The electrostatic direct implicit particle-in-cell (EDIPIC) code

The fully three-dimensional PIC simulation of a Hall thruster is of extremely high numerical cost and cannot be accomplished on commonly available computational facilities within a reasonable period of time. The required computational resources are significantly smaller for one-dimensional simulations. The one-dimensional approximation of a Hall thruster is possible because of the strong radial magnetic field: the EVDF inside the AR of a Hall thruster is established on a spatial scale much smaller than the entire length of the device, which permits the consideration of only a short axial section of the AR, where the modification of the plasma properties, the axial electric field, and the radial magnetic field in axial direction can be neglected. Such a section is well described by the model of a plasma slab uniform along the directions parallel to its boundaries, which leaves only the radial direction to be resolved in simulations.

Even utilizing this one-dimensional approximation, the cost of simulations remains high because of the existence of essentially different spatial and temporal scales that must be resolved. In the sheath, the computational grid must finely resolve the Debye length $\lambda_D = v_{th}/\omega_{pe}$, which imposes a condition on the size of the grid mesh $\Delta x \ll \lambda_D$. At the same time, the width of the plasma slab is of the order of $L \sim 10^2 \lambda_D$. Assuming that the computational grid is fine and uniform, $\Delta x \sim 0.1\lambda_D$, and the number of macroparticles per cell is $N_{\text{macro}} \sim 10^3$, the total number of macroparticles of a single species must be at least $N_{\text{part}} = N_{\text{macro}}(L/\lambda_D)(\lambda_D/\Delta x) \sim 10^6$. The mesh size imposes a further limitation on the particle advance time step

Δt: to properly reproduce Debye shielding, the time step must be smaller than the typical time of electron transit across the mesh [105], $\Delta t < \Delta x/v_{th}$, a typical choice being $\Delta t \sim 10^{-1}\omega_{pe}^{-1}$.

Note that implicit schemes enable converging simulations with large time steps, $\Delta t \gg \omega_{pe}^{-1}$, and coarse spatial resolution, $\Delta x \gg \lambda_D$, to be performed [106]. However, the limitation on the electron transit time $\Delta t < \Delta x/v_{th}$ does not allow this advantage to be exploited when the spatial resolution remains fine, $\Delta x \ll \lambda_D$ [105].

The evolution of the simulated plasma must be followed during a time interval $T_{\rm sim}$ comparable to the ion time scales, $T_{\rm sim} \sim L/c_i$, where $c_i = (T_e/M)^{1/2}$ is the ion sound velocity[1]. Assuming a xenon plasma with $M/m \sim 2.4 \cdot 10^5$, and setting $\Delta t = \Delta x/v_{th}$, one obtains an estimate for the total number of time steps of $N_T = T_{\rm sim}/\Delta t \sim [L/(T_e/M)^{1/2}]/(\Delta x/v_{th}) = (L/\Delta x)(2M/m)^{1/2} \sim 10^6$.

The computer time of a simulation with the above parameters can be estimated as follows. The explicit electromagnetic simulations described in Chapter 2 were performed on a single 3 GHz Xeon processor where calculation of $3 \cdot 10^4$ time steps for $4 \cdot 10^5$ macroparticles of a single species required about 2 hours. From this test, the estimated time to run a simulation of the entire plasma slab with the sheath resolved is $(N_{\rm part}/4 \cdot 10^5) \times (N_T/3 \cdot 10^4) \times 2$ hours $\sim 2 \cdot 10^2$ hours > 8 days if one uses a single processor and an ordinary algorithm. The performance of the simulations can be increased using the multi-scale approach [107], which uses a nonuniform grid with a small mesh near the wall and large mesh in the middle regions [108], with corresponding variable time steps of particle advance. Such approach can significantly reduce the computational time. However, the multi-scale algorithm is complex and has a number of difficulties related with the possible violation of energy conservation. Another approach, essentially simpler for programming but with high hardware requirements, is the parallel execution of a simple and robust single-scale algorithm on a cluster of processors.

[1]Note that since the objective of simulations is the study of plasma-wall interaction, acceleration of ions along the thruster axis is not important in the considered model, which is why the characteristic time of simulation is the time of ion flight between the walls of the ceramic channel of a thruster.

Such powerful computers suitable for parallel calculations are available at both WestGrid[2] and the University of Saskatchewan. The availability of these computational resources strongly affected the choice of the method of high performance calculations. The PIC code was developed on the basis of a single-scale implicit algorithm with a uniform spatial grid of mesh size $\Delta x \ll \lambda_D$ and execution of the code was parallelized. The implicit scheme was chosen instead of a simpler explicit scheme because implicit schemes show much better energy conservation than the explicit ones. This is especially important when a simulation lasts for many time steps, where the numerical heating produced by explicit schemes may become intolerable [10].

This Chapter is organized as follows. Section 3.1 presents the general characteristics of the EDIPIC code and the simulated system. In Section 3.2, the equations of motion and the modified Poisson's equation are described. The modified boundary conditions for the electrostatic potential are discussed in Section 3.3. Section 3.4 contains a description of the probabilistic model of SEE with multiple components. Section 3.5 describes the Monte-Carlo model of electron collisions with neutral atoms (elastic, inelastic, ionization) and "turbulent" collisions. Finally, the Langevin model of Coulomb collisions is presented in Section 3.6.

3.1 The plane geometry model of the Hall thruster acceleration region

The EDIPIC code was developed for kinetic studies of plasmas inside the AR of a Hall thruster. The plasma is simulated as a slab of thickness L with the x axis directed normal to and the y and z axes parallel to the plasma boundaries. The slab is infinite and uniform along the y and z axes. The external constant electric field E_z and magnetic field B_x are applied as shown in Fig. 3.1. Both electrons and ions are considered as particles. The ion-to-electron mass ratio is realistic. One

[2]Western Canada Research Grid (www.westgrid.ca)

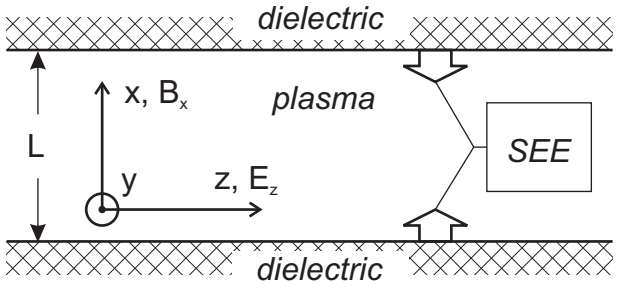

Figure 3.1: Schematic diagram of the simulated plasma system. The two dielectric walls represent the coaxial ceramic channel of a Hall thruster.

spatial dimension x and three velocity components v_x, v_y, and v_z are resolved for each particle. The electron motion is affected by the external electric and magnetic fields, and by the self-consistent electrostatic field directed normal to the walls. The motion of ions only in the direction normal to the walls is of interest, which is why in simulations it is affected by the self-consistent electrostatic field only. Acceleration of ions by the external electric and magnetic fields is omitted.

The direct implicit scheme of time integration of particles is used [105]. The modified Poisson's equation is solved using the particle positions at the intermediate stage of particle advance to obtain the longitudinal electrostatic field [109]. The code includes a model of secondary electron emission [110], which is tailored to approximate the emission properties of grade HP boron nitride ceramics – a typical material for Hall thruster channels [111]. The Monte-Carlo model of electron-neutral collisions [13] and the Langevin model of Coulomb collisions for electrons [112] are also implemented.

The code is written in Fortran 90 and parallelized with the Message Passing Interface (MPI)[3]. The parallel algorithm implemented in the code distinguishes a server process (a process with rank 0)[4] and a set of N_{proc} client processes (with ranks from 1 to N_{proc}). A single process runs on a single processor of a computational cluster. All processes initialize global variables by reading the simulation parameters

[3]MPI is the standard protocol for communication between nodes when running a parallel program on a computer system with distributed memory, *e.g.*, a Beowulf Linux cluster.

[4]Here the rank is a unique integer identifier assigned to the process by MPI.

from the common input data files. The server process performs initial distribution over velocity and coordinate for all particles, and then uniformly distributes the particles between the client processes. Every client process follows particle dynamics across the whole system. During the main cycle of simulations, each client process advances its particles and calculate charge density distribution due to these particles, as well as the diagnostic values. The server process collects the charge density distributions and the diagnostic data from all client processes, solves the Poisson's equation, sends the potential profile back to the client nodes, and performs the diagnostic output. The qualitative flowchart of the parallel execution of the code is presented in Fig. 3.2.

EDIPIC code can be run with a wide variety of boundary conditions, which allows one to simulate a plasma bounded by dielectric or metal walls, a semi-infinite plasma, and a periodic plasma-beam system. The code is equipped with numerous, diverse diagnostics.

3.2 Implicit equations of motion and Poisson's equation

The implicit finite difference equations of motion are taken in the following vector form [109]:

$$\begin{aligned} \mathbf{v}_s^{n+1/2} &= \mathbf{v}_s^{n-1/2} + \Delta t \mathbf{a}_s^n + \frac{q_s \Delta t}{m_s} \left(\mathbf{E}_{\text{ext}} + \frac{\mathbf{v}_s^{n+1/2} + \mathbf{v}_s^{n-1/2}}{2} \times \mathbf{B}_{\text{ext}} \right) , \\ \mathbf{x}_s^{n+1} &= \mathbf{x}_s^n + \Delta t \mathbf{v}_s^{n+1/2} , \\ \mathbf{a}_s^n &= \frac{1}{2} \left(\mathbf{a}_s^{n-1} + \frac{q_s}{m_s} \mathbf{E}^{n+1} \right) , \end{aligned} \tag{3.1}$$

where q_s is the charge, m_s the mass, $\mathbf{v}_s$ the velocity, $\mathbf{a}_s$ the acceleration, and $\mathbf{x}_s$ the coordinate of a particle of species s, $\mathbf{E}$ is the electrostatic field calculated from the Poisson's equation, the superscripts correspond to the time level when the value is calculated, and $\mathbf{E}_{\text{ext}}$ and $\mathbf{B}_{\text{ext}}$ are the external constant electric and magnetic fields. The acceleration $\mathbf{a}_s^n$ is an implicit value because it contains the advanced electrostatic

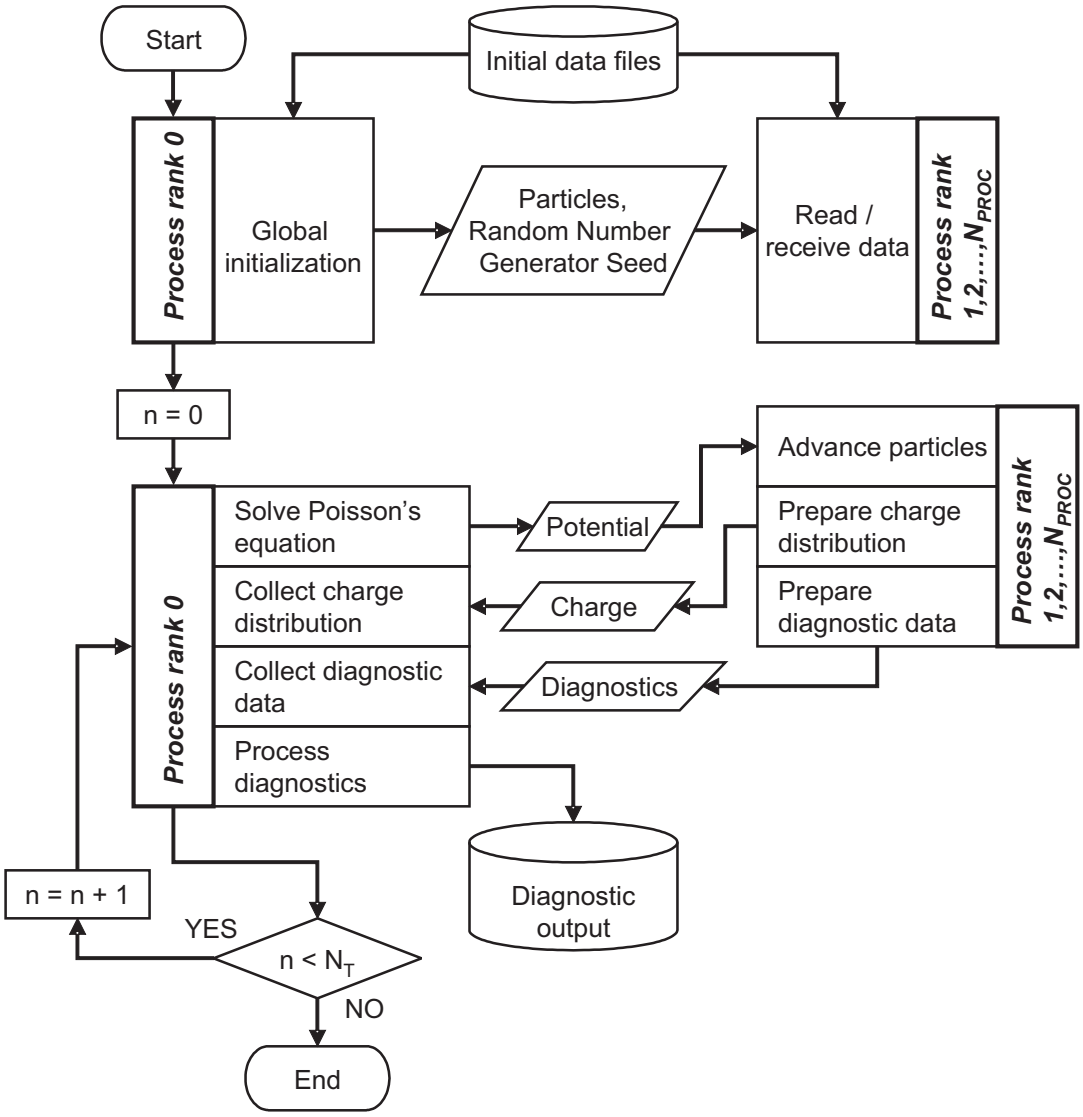

Figure 3.2: The flowchart of the parallel code execution. Here N_{PROC} is the total number of processes with nonzero rank, N_T is the required number of time steps.

field $\mathbf{E}^{n+1}$. The particle push is performed in two steps. First, the quantities known at the n-th time level are used to advance particles to the so-called "streaming" position. Then the "streaming" quantities are used to estimate the advanced field $\mathbf{E}^{n+1}$, and this field is used to finish the particle push.

The first equation of system (3.1) can be transformed to the form

$$\mathbf{v}_s^{n+1/2} = \mathbf{K}_s \mathbf{v}_s^{n-1/2} + \mathbf{A}_s^{-1} \left(\frac{\Delta t}{2} \mathbf{a}_s^{n-1} + \frac{q_s \Delta t}{2 m_s} \mathbf{E}^{n+1} + \frac{q_s \Delta t}{m_s} \mathbf{E}_{\text{ext}} \right) ,$$

where in Cartesian coordinates, matrix $\mathbf{A}_s^{-1}$ is

$$\mathbf{A}_s^{-1} = \frac{1}{1+\theta_s^2} \times \begin{pmatrix} 1+\alpha_s^2 B_{\text{ext},x}^2 & \alpha_s^2 B_{\text{ext},x} B_{\text{ext},y} + \alpha_s B_{\text{ext},z} & \alpha_s^2 B_{\text{ext},x} B_{\text{ext},z} - \alpha_s B_{\text{ext},y} \\ \alpha_s^2 B_{\text{ext},x} B_{\text{ext},y} - \alpha_s B_{\text{ext},z} & 1+\alpha_s^2 B_{\text{ext},y}^2 & \alpha_s^2 B_{\text{ext},y} B_{\text{ext},z} + \alpha_s B_{\text{ext},x} \\ \alpha_s^2 B_{\text{ext},x} B_{\text{ext},z} + \alpha_s B_{\text{ext},y} & \alpha_s^2 B_{\text{ext},y} B_{\text{ext},z} - \alpha_s B_{\text{ext},x} & 1+\alpha_s^2 B_{\text{ext},z}^2 \end{pmatrix} ,$$

matrix $\mathbf{K}_s$ is

$$\mathbf{K}_s = 2\mathbf{A}_s^{-1} - \mathbf{1} ,$$

$\mathbf{1}$ is the unity matrix, $\theta_s^2 \equiv \alpha_s^2 (B_{\text{ext},x}^2 + B_{\text{ext},y}^2 B_{\text{ext},z}^2)$, and $\alpha_s \equiv q_s \Delta t / 2 m_s$. Then the equations of particle push to the "streaming" position are

$$\begin{aligned} \widetilde{\mathbf{v}}_s &= \mathbf{K}_s \mathbf{v}_s^{n-1/2} + \mathbf{A}_s^{-1} \left(\frac{\Delta t}{2} \mathbf{a}_s^{n-1} + \frac{q_s \Delta t}{m_s} \mathbf{E}_{\text{ext}} \right) , \\ \widetilde{\mathbf{x}}_s &= \mathbf{x}_s^n + \Delta t \widetilde{\mathbf{v}}_s . \end{aligned} \tag{3.2}$$

Provided $\mathbf{E}^{n+1}$ is known, the equations of the final particle push are

$$\begin{aligned} \delta \mathbf{v}_s &= \frac{q_s \Delta t}{2 m_s} \mathbf{A}_s^{-1} \mathbf{E}^{n+1} , \\ \mathbf{v}_s^{n+1/2} &= \widetilde{\mathbf{v}}_s + \delta \mathbf{v}_s , \\ \delta \mathbf{x}_s &= \Delta t \delta \mathbf{v}_s , \\ \mathbf{x}_s^{n+1} &= \widetilde{\mathbf{x}}_s + \delta \mathbf{x}_s . \end{aligned} \tag{3.3}$$

The advanced charge density at time level $n+1$, which is necessary to define the advanced electric field $\mathbf{E}^{n+1}$, can be obtained via the Taylor expansion of the charge

density calculated using the "streaming" particle positions:

$$\begin{aligned}
\rho^{n+1}(\mathbf{x}_g) &= \sum_{s,i} \frac{q_s}{\Delta\mathbf{x}} S\left(\mathbf{x}_g - \mathbf{x}_{si}^{n+1}\right) \\
&= \sum_{s,i} \frac{q_s}{\Delta\mathbf{x}} S\left(\mathbf{x}_g - \widetilde{\mathbf{x}}_{si} - \delta\mathbf{x}_{si}\right) \\
&= \sum_{s,i} \frac{q_s}{\Delta\mathbf{x}} \left[S\left(\mathbf{x}_g - \widetilde{\mathbf{x}}_{si}\right) + \delta\mathbf{x}_{si} \frac{\partial}{\partial \widetilde{\mathbf{x}}_{si}} S\left(\mathbf{x}_g - \widetilde{\mathbf{x}}_{si}\right) + \ldots \right] \\
&\simeq \sum_{s,i} \frac{q_s}{\Delta\mathbf{x}} S\left(\mathbf{x}_g - \widetilde{\mathbf{x}}_{si}\right) - \frac{\partial}{\partial \mathbf{x}_g} \sum_{s,i} \Delta t \delta\mathbf{v}_{si} \frac{q_s}{\Delta\mathbf{x}} S\left(\mathbf{x}_g - \widetilde{\mathbf{x}}_{si}\right) \\
&= \widetilde{\rho}(\mathbf{x}_g) - \frac{\partial}{\partial \mathbf{x}_g} \sum_{s,i} \frac{q_s \Delta t^2}{2m_s} \mathbf{A}_s^{-1} \mathbf{E}_{si}^{n+1} \frac{q_s}{\Delta\mathbf{x}} S\left(\mathbf{x}_g - \widetilde{\mathbf{x}}_{si}\right) \ .
\end{aligned} \tag{3.4}$$

Here $\rho^{n+1}(\mathbf{x}_g)$ is the charge density in the node with coordinate $\mathbf{x}_g$ at time level $n+1$, $\widetilde{\rho}(\mathbf{x}_g)$ is the charge density in the node $\mathbf{x}_g$ obtained with the "streaming" coordinates, $\widetilde{\mathbf{x}}_{si}$ is the "streaming" coordinate of particle i of species s, the sum over i and s is the sum over all particles (including different species), $S\left(\mathbf{x}_g - \mathbf{x}\right)$ is the shape function, which determines the distribution of the charge from particle with coordinate $\mathbf{x}$ to the grid node $\mathbf{x}_g$, $\Delta\mathbf{x}$ is the volume of the mesh.

The field $\mathbf{E}_{si}^{n+1}$ in (3.4) is, in fact, the field at the position of a particle, which may significantly complicate calculation of the sum in the second term of the last line of (3.4). However, in Ref. [105], it has been found that the use of the grid values $\mathbf{E}^{n+1}(\mathbf{x}_g)$ instead of $\mathbf{E}_{si}^{n+1}$ is one of the most stable and least computationally expensive methods. Therefore, the grid values of the advanced charge density are

$$\rho^{n+1}(\mathbf{x}_g) = \widetilde{\rho}(\mathbf{x}_g) - \frac{\partial}{\partial \mathbf{x}_g} \left[\mathbf{X}(\mathbf{x}_g) \mathbf{E}^{n+1}(\mathbf{x}_g) \right] \ , \tag{3.5}$$

where tensor $\mathbf{X}$ is

$$\mathbf{X}(\mathbf{x}_g) = \sum_{s,i} \frac{q_s^2 \Delta t^2}{2m_s \Delta\mathbf{x}} S(\mathbf{x}_g - \widetilde{\mathbf{x}}_{si}) \mathbf{A}_s^{-1} \ .$$

The Poisson's equation for the advanced electrostatic potential Φ^{n+1} with charge density (3.5) becomes

$$\nabla \left[\left(\varepsilon_0 \mathbf{1} + \mathbf{X} \right) \nabla \Phi^{n+1} \right] = -\widetilde{\rho} \ . \tag{3.6}$$

Tensor $\mathbf{X}$ is often called the implicit susceptibility tensor [105].

The considered plasma system is nonuniform along the x direction only, so $\nabla \to (\partial/\partial x)$, the external electric field is $\mathbf{E}_{\rm ext} = (0, 0, E_z)$, and the external magnetic field is $\mathbf{B}_{\rm ext} = (B_x, 0, 0)$. Eqs. (3.2) that push a particle of species s to the "streaming" position transform to

$$\begin{aligned}
\widetilde{v}_x &= v_x^{n-1/2} + \frac{\Delta t}{2} a^{n-1}, \\
\widetilde{v}_y &= v_y^{n-1/2} \frac{1 - \alpha_s^2 B_x^2}{1 + \alpha_s^2 B_x^2} + v_z^{n-1/2} \frac{2\alpha_s B_x}{1 + \alpha_s^2 B_x^2} + \frac{2\alpha_s^2 B_x^2}{1 + \alpha_s^2 B_x^2} \frac{E_z}{B_x}, \\
\widetilde{v}_z &= -v_y^{n-1/2} \frac{2\alpha_s B_x}{1 + \alpha_s^2 B_x^2} + v_z^{n-1/2} \frac{1 - \alpha_s^2 B_x^2}{1 + \alpha_s^2 B_x^2} + \frac{2\alpha_s B_x}{1 + \alpha_s^2 B_x^2} \frac{E_z}{B_x} \ , \\
\widetilde{x} &= x^n + \Delta t \widetilde{v}_x \ .
\end{aligned} \tag{3.7}$$

Eqs. (3.3) for the final push of a particle of species s take the following form:

$$\begin{aligned}
v_x^{n+1/2} &= \widetilde{v}_x + \alpha_s E_x^{n+1}, \\
v_y^{n+1/2} &= \widetilde{v}_y, \\
v_z^{n+1/2} &= \widetilde{v}_z, \\
x^{n+1} &= x^n + \Delta t v_x^{n+1/2}, \\
a^n &= \frac{1}{2} \left(a^{n-1} + \frac{q}{m} E_x^{n+1} \right) \ .
\end{aligned} \tag{3.8}$$

Note, that in Eqs. (3.7) and (3.8) the subscript s is omitted in the particle velocities, accelerations and coordinates.

The one-dimensional finite difference form of Poisson's equation (3.6) is

$$\begin{aligned}
&\left(2 + \frac{X_{j+1}}{\varepsilon_0} + \frac{X_j}{\varepsilon_0} \right) \Phi_{j+1} - \left(4 + \frac{X_{j+1}}{\varepsilon_0} + 2\frac{X_j}{\varepsilon_0} + \frac{X_{j-1}}{\varepsilon_0} \right) \Phi_j \\
&+ \left(2 + \frac{X_j}{\varepsilon_0} + \frac{X_{j-1}}{\varepsilon_0} \right) \Phi_{j-1} = -\frac{2\Delta x^2}{\varepsilon_0} \widetilde{\rho}_j \ , \quad j = 1, ..., N_{\rm cell} - 1 \ ,
\end{aligned} \tag{3.9}$$

where $X_j \equiv X(x_j)$, $\Phi_j \equiv \Phi(x_j)$, $\widetilde{\rho}_j \equiv \widetilde{\rho}(x_j)$, x_j is the coordinate of the node with index j, and $N_{\rm cell} = L/\Delta x$. The nodes are numbered from zero at the plasma boundary $x = 0$ node to $N_{\rm cell}$ at the plasma boundary $x = L$ node.

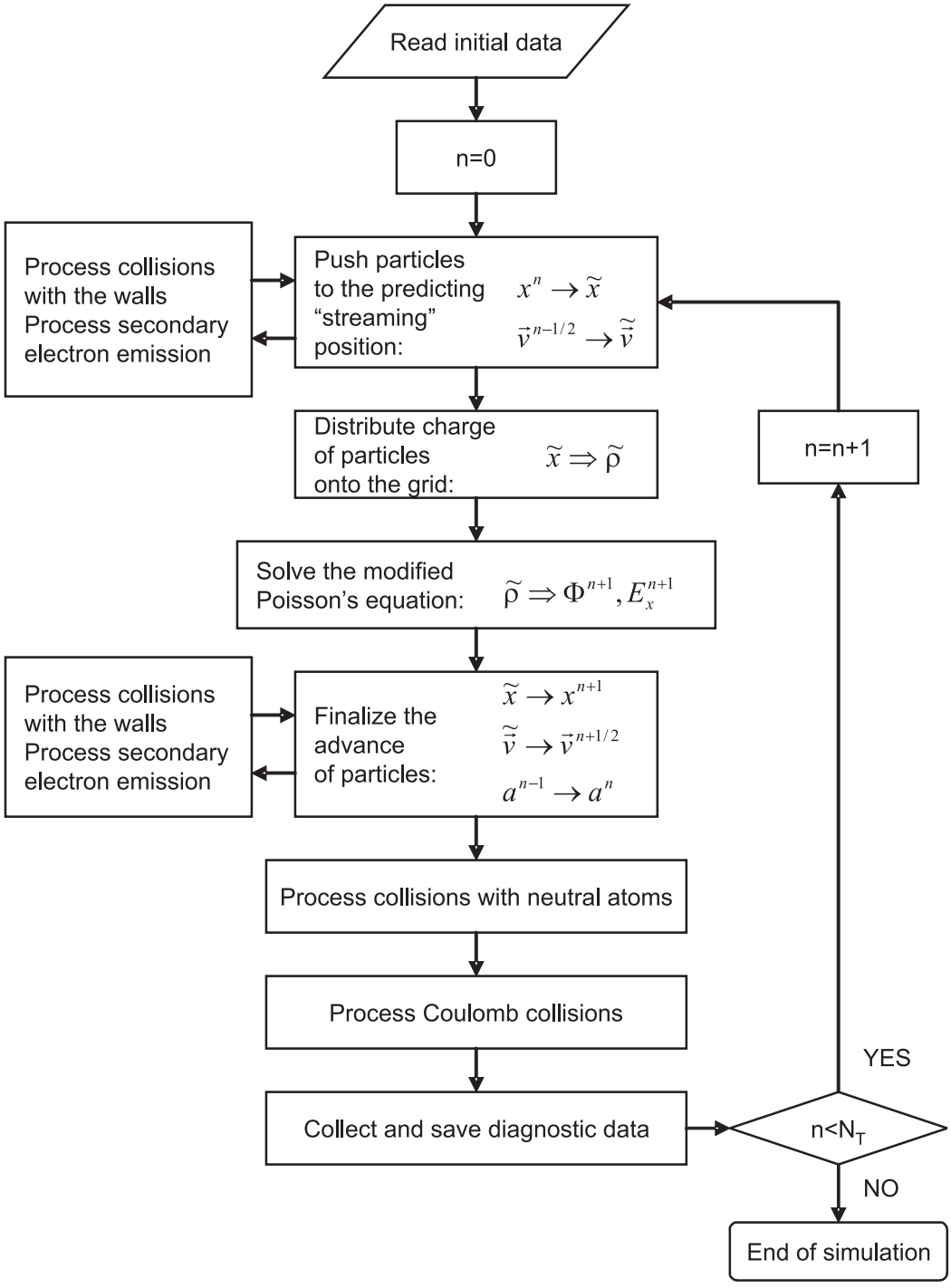

Figure 3.3: The flowchart of the main cycle of implicit simulation. Here N_T is the required number of time steps.

3.3 Boundary conditions for the electrostatic potential

The EDIPIC code allows one to apply different field boundary conditions, thus broadening the range of simulated systems.

First, the plasma can be bounded by metal walls with a given potential difference U. In this case, the values of the potential at the plasma boundaries $x = 0$ and $x = L$ have to be constant:

$$\begin{aligned} \Phi_0 \equiv \Phi(0) = U \ , \\ \Phi_{N_{\rm cell}} \equiv \Phi(L) = 0 \ . \end{aligned} \tag{3.10}$$

Condition $\Phi_0 = \Phi_{N_{\rm cell}} = 0$ is appropriate for simulations of periodic plasmas.

Second, the plasma can be bounded by dielectric walls. If the relative dielectric permittivity of the wall material is ε_d, the modified one-dimensional Poisson's equation takes the form

$$\frac{\partial}{\partial x}\left[(\varepsilon_0 + X)\varepsilon\frac{\partial\Phi}{\partial x}\right] = -\widetilde{\rho} \ , \tag{3.11}$$

where in the dielectric, *i.e.*, for $x < 0$ and $x > L$, one has $X = 0$, $\widetilde{\rho} = 0$, and $\varepsilon = \varepsilon_d$, while in plasma, $0 < x < L$, the implicit susceptibility X and the "streaming" charge density $\widetilde{\rho}$ are defined as usual with $\varepsilon = 1$. Eq. (3.11) can be integrated over a small segment including the boundary point $x = 0$ as follows:

$$\int\limits_{0-\delta x}^{\Delta x/2} dx \frac{\partial}{\partial x}\left[(\varepsilon_0 + X)\varepsilon\frac{\partial\Phi}{\partial x}\right] = -\int\limits_{0-\delta x}^{\Delta x/2} dx\widetilde{\rho} \ . \tag{3.12}$$

After transforming Eq. (3.12) and performing a similar integration at the boundary $x = L$, one obtains two additional equations:

$$\begin{aligned} \Phi_1 - \Phi_0 = \frac{\Delta x}{\varepsilon_0 + (X_0 + X_1)/2}\left[-\widetilde{\sigma}_0 - \widetilde{\rho}_0\frac{\Delta x}{2} + \varepsilon_d\varepsilon_0\left(\frac{\partial\Phi}{\partial x}\right)_{-0}\right] \ , \\ \Phi_{N_{\rm cell}} - \Phi_{N_{\rm cell}-1} = \frac{\Delta x}{\varepsilon_0 + (X_{N_{\rm cell}-1} + X_{N_{\rm cell}})/2}\left[\widetilde{\sigma}_{N_{\rm cell}} + \widetilde{\rho}_{N_{\rm cell}}\frac{\Delta x}{2} + \varepsilon_d\varepsilon_0\left(\frac{\partial\Phi}{\partial x}\right)_{L+0}\right] \ , \end{aligned} \tag{3.13}$$

where $\widetilde{\sigma}_0$ and $\widetilde{\sigma}_{N_{\rm cell}}$ are the "streaming" surface charge density at the boundaries $x = 0$ and $x = L$, respectively, and $-\left(\dfrac{\partial\Phi}{\partial x}\right)_{-0}$ and $-\left(\dfrac{\partial\Phi}{\partial x}\right)_{L+0}$ are the electric fields inside the dielectric layers $x < 0$ and $x > L$, respectively.

In simulations, the plasma is neutral as a whole with no external electric field normal to the boundaries applied, therefore, the fields inside the dielectric are zero and the potential derivatives on the right hand side of equations (3.13) vanish. In this case, one has two equations (3.13) together with the $N_{\rm cell}-1$ finite difference Poisson's equations (3.9) for $N_{\rm cell}+1$ unknown values of potential Φ_j, where $j = 0, ..., N_{\rm cell}$. One of equations (3.13) can be expressed through the other equation and equations (3.9) because of the condition of zero total plasma charge, i.e.

$$\Delta x \sum_{j=1}^{N_{\rm cell}-1} \widetilde{\rho}_j + \frac{\Delta x}{2}(\widetilde{\rho}_0 + \widetilde{\rho}_{N_{\rm cell}}) + \widetilde{\sigma}_0 + \widetilde{\sigma}_{N_{\rm cell}} = 0 \ .$$

Therefore, only the first equation of (3.13) may be considered as the boundary condition. The eliminated equation is not required, since the potential always contains an arbitrary constant, one can simply set the constant value of potential at some point.

Finally, the set of boundary conditions for the case of a plasma bounded by dielectric walls is

$$\begin{aligned} \Phi_0 - \Phi_1 &= \frac{\Delta x}{\varepsilon_0 + (X_0 + X_1)/2}\left[\widetilde{\sigma}_0 + \widetilde{\rho}_0\frac{\Delta x}{2}\right] \ , \\ \Phi_{N_{\rm cell}} &= 0 \ . \end{aligned} \tag{3.14}$$

Note, that the actual value of the relative dielectric permittivity of the wall material is not important for the boundary conditions (3.14).

The flowchart of the main cycle of simulations is presented in Fig. 3.3. Processing of electron-neutral and Coulomb collisions is carried out after the final advance of particles. Collisions with walls and possible SEE are processed during both the predicting and final pushes, every time a particle collides with the wall.

3.4 Probabilistic model of secondary electron emission

In the EDIPIC code, the following regimes of particle interaction with the walls are implemented. For ions, either complete absorption or perfect specular reflection can be selected. Electrons can (i) be absorbed, (ii) be reflected specularly or at a random direction, either elastically or inelastically, (iii) cause the emission of secondary electrons. The user can combine and tune all these processes for electrons, so as to adjust the wall properties to that of the material used in a real discharge device. The major objective of the developed model of electron-wall interaction is the creation of the boundary with SEE characteristics similar to those found in grade HP boron nitride ceramics – the typical channel material of Hall thrusters tested at the Princeton Plasma Physics Laboratory [111].

Electrons that bombard the wall surface (primary electrons) cause the emission of secondary electrons. The SEE intensity is characterized by the emission coefficient γ, defined as $\gamma = \Gamma_2/\Gamma_1$, where Γ_2 is the total secondary electron flux and Γ_1 is the total primary electron flux. When the energy of primary electrons ranges from tens to thousands of electronvolts, many materials have an emission coefficient that is described by the formula proposed by Vaughan [113]:

$$\gamma_V(w,\vartheta) = \gamma_{max}(\vartheta)\{v(w,\vartheta)\exp\left[1 - v(w,\vartheta)\right]\}^k \ , \tag{3.15}$$

where

$$v(w,\vartheta) = \frac{w - w_0}{w_{max}(\vartheta) - w_0} \ ,$$

$$w_{max}(\vartheta) = w_{max,0}\left(1 + \frac{k_s}{\pi}\vartheta^2\right) \ , \quad \gamma_{max}(\vartheta) = \gamma_{max,0}\left(1 + \frac{k_s}{2\pi}\vartheta^2\right) \ ,$$

$$k = \begin{cases} 0.62 & \text{if} \quad w < w_{max} \\ 0.25 & \text{if} \quad w > w_{max} \end{cases} \ ,$$

w and ϑ are the primary electron's energy and angle of incidence, w_0 is the emission threshold energy, k_s is the smoothness factor for the surface ($k_s = 0$ for a very rough

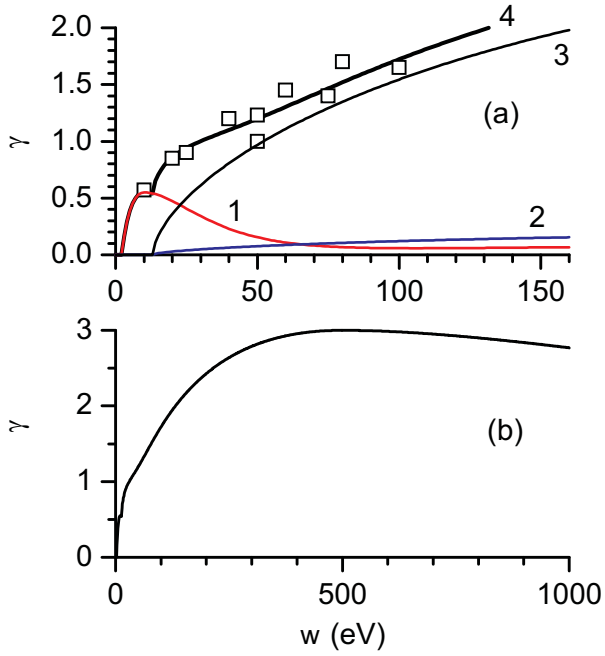

Figure 3.4: (a) The emission coefficients of the components of secondary electron emission versus the incident electron energy for normal incidence. Curve 1 is the the elastic reflection (3.16), curve 2 the inelastic backscattering (3.17), curve 3 the true secondary emission (3.18), and curve 4 the total emission coefficient (3.19). Squares mark the available experimental data for boron nitride ceramics. (b) The total emission coefficient (3.19) over a range of incident electron energies.

surface and $k_s = 2$ for a polished surface), and $w_{max,0}$ and $\gamma_{max,0}$ are the primary electron energy and the emission coefficient at the maximum of emission for normal incidence.

The general phenomenological model of SEE [71, 113] assumes that the total flux of secondary electrons consists of (i) elastically reflected primary electrons with flux Γ_{2e}, (ii) inelastically backscattered primary electrons with flux Γ_{2i}, and (iii) true secondary electrons with flux Γ_{2t}, *i.e.*, $\Gamma_2 = \Gamma_{2e} + \Gamma_{2i} + \Gamma_{2t}$. The latter component represents the electrons excited by primary electrons in the near-surface layer of the wall. Injection of these components is determined by the partial emission coefficients $\gamma_{e,i,t} = \Gamma_{2e,i,t}/\Gamma_1$.

Vaughan's emission coefficient (3.15) vanishes if $w < w_0$. However, for dielectrics, the low energy primary electrons produce significant emission because of

the increasing role of the elastic reflections [82]: γ_e has maximum $\gamma_{e,max} \simeq 0.5$ at $w = w_{e,max} = 5 - 10$ eV. Also, at high energies, elastically reflected electrons comprise about 3% of the emitted current [110]. Therefore, in simulations, the emission coefficient due to elastic reflection is approximated by a function, which has a maximum at $w = w_{e,max}$ and gives 3% of total emission (Vaughan's) at high energies:

$$\gamma_e(w,\vartheta) = r_e\gamma_V(w,\vartheta) + \gamma_{e,max}\begin{cases} v_1(w)\exp\left[1 - v_1(w)\right] & \text{if } w_{e,0} < w < w_{e,max}\ , \\ \left[1 + v_2(w)\right]\exp\left[-v_2(w)\right] & \text{if } w_{e,max} < w, \end{cases} \tag{3.16}$$

where

$$v_1(w) = \frac{w - w_{e,0}}{w_{e,max} - w_{e,0}}\ , \quad v_2(w) = \frac{w - w_{e,max}}{\Delta_e}\ ,$$

$w_{e,0}$ is the threshold energy for the elastic reflection, Δ_e is the parameter controlling the decay of the "bumping" part of γ_e for $w > w_{e,max}$, and $r_e = 0.03$ determines the portion of the total emitted current that is made of the elastically reflected electrons. The graph of the function $\gamma_e(w,\vartheta)$ for $\vartheta = 0$ is presented in Fig. 3.4a by curve 1.

The current due to the inelastically backscattered electrons is about 7% of the total secondary current Γ_2 [110]. The corresponding emission coefficient is set to be the constant fraction of the Vaughan's coefficient:

$$\gamma_i(w,\vartheta) = r_i\gamma_V(w,\vartheta)\ , \tag{3.17}$$

where $r_i = 0.07$. The graph of the function $\gamma_i(w,0)$ is presented by curve 2 in Fig. 3.4a.

The true secondary emission coefficient is

$$\gamma_t(w,\vartheta) = (1 - r_e - r_i)\gamma_V(w,\vartheta)\ . \tag{3.18}$$

The corresponding graph $\gamma_t(w,0)$ is depicted by curve 3 in Fig. 3.4a.

The total emission coefficient is the sum of the three components:

$$\gamma(\varepsilon,\vartheta) = \gamma_t(\varepsilon,\vartheta) + \gamma_e(\varepsilon,\vartheta) + \gamma_i(\varepsilon,\vartheta)\ . \tag{3.19}$$

The total γ defined by Eq. (3.19) is close to the Vaughan's coefficient (3.15) for energies $w > w_0$ (see Fig. 3.4b), while in the low energy region $w_0 > w > w_{e,0}$, it deviates

Table 3.1: Parameters of partial emission coefficients (3.16 - 3.18), which approximate the SEE properties of boron-nitride ceramics.

w_0 [eV]	k_s	$\gamma_{max,0}$	$w_{max,0}$ [eV]	r_e	$w_{e,0}$	$\gamma_{e,max}$	$w_{e,max}$ [eV]	r_i
13	1	3	500	0.03	2	0.55	10	0.07

from the Vaughan's curve to ensure better correspondence with the experimental data (compare curve 4 with the squares in Fig. 3.4a, which represent a compilation of experimental data from [111, 70] and references therein). The emission parameters are presented in Table 3.1.

The angular distribution of the intensity of secondary electron current from polycrystalline materials is isotropic over the azimuthal angle ϕ_2, proportional to the cosine law over the polar angle ϑ_2, and independent of the primary electron angle of incidence. For simulation, the angles of emission of a secondary electron are defined as follows:

$$\begin{aligned} \vartheta_2 &= \sin^{-1} R \ , \\ \varphi_2 &= R2\pi \ , \end{aligned} \tag{3.20}$$

where ϑ_2 is the polar angle relative to the normal to the wall, $0 < \vartheta_2 < \pi/2$, φ_2 is the azimuthal angle relative to the z axis, $0 < \varphi_2 < 2\pi$, and R is a random number, $0 < R < 1$. The polar angle obtained in (3.20) corresponds to the distribution over angle ϑ_2 proportional to $\cos\vartheta_2$. Note, for approximation of the SEE properties of boron nitride ceramics, all three SEE components are emitted according to the distributions (3.20). As an option, the user may select specular scattering of the elastically reflected electrons.

It is important to distinguish between elastically reflected, inelastically backscattered, and true secondary components of the secondary electron flux because they are emitted with different energy distributions. The elastically reflected electrons have the same energy w_{2e} after the collision with the wall as the energy w before the collision:

$$w_{2e} = w \ .$$

The energy of inelastically backscattered electrons w_{2i} is considered to be uniformly

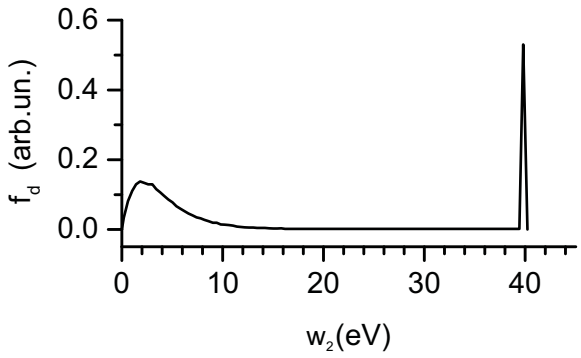

Figure 3.5: The energy spectrum of secondary electrons $f_d(w_2)$ produced by the monoenergetic electron beam with energy $w = 40$ eV and normal angle of incidence $\vartheta = 0$.

distributed between zero and the energy of the backscattered electron before the collision:

$$w_{2i} = Rw \ ,$$

where R is a random number, $0 < R < 1$. The true secondary electrons are emitted with energies corresponding to a half-Maxwellian distribution of temperature T_t

$$f_t(w) = \frac{2w^{1/2}}{\pi^{1/2} T_t^{3/2}} \exp\left(-\frac{w}{T_t}\right) \ .$$

For every true secondary electron emitted, the energy w_{2t} is calculated as a solution of the equation

$$R = \int_0^{w_{2t}} dw f_t(w) \ ,$$

where R is a random number, $0 < R < 1$. An example of the energy spectrum of the total secondary electron flow is presented in Fig. 3.5. This spectrum qualitatively agrees with the energy distribution of electrons presented in Ref. [71].

The emission of secondary current with non-integer emission coefficients is performed statistically – the value of the emission coefficient is treated as probability of emission. A flowchart of the injection algorithm for multiple component SEE with the partial emission coefficients (3.16-3.18) is presented in Fig. 3.6. This algorithm tries to inject either elastically reflected or inelastically backscattered electron first, and only then turns to the possible injection of true secondary electrons. Such ordering prohibits an error from occurring when a primary electron, capable of producing

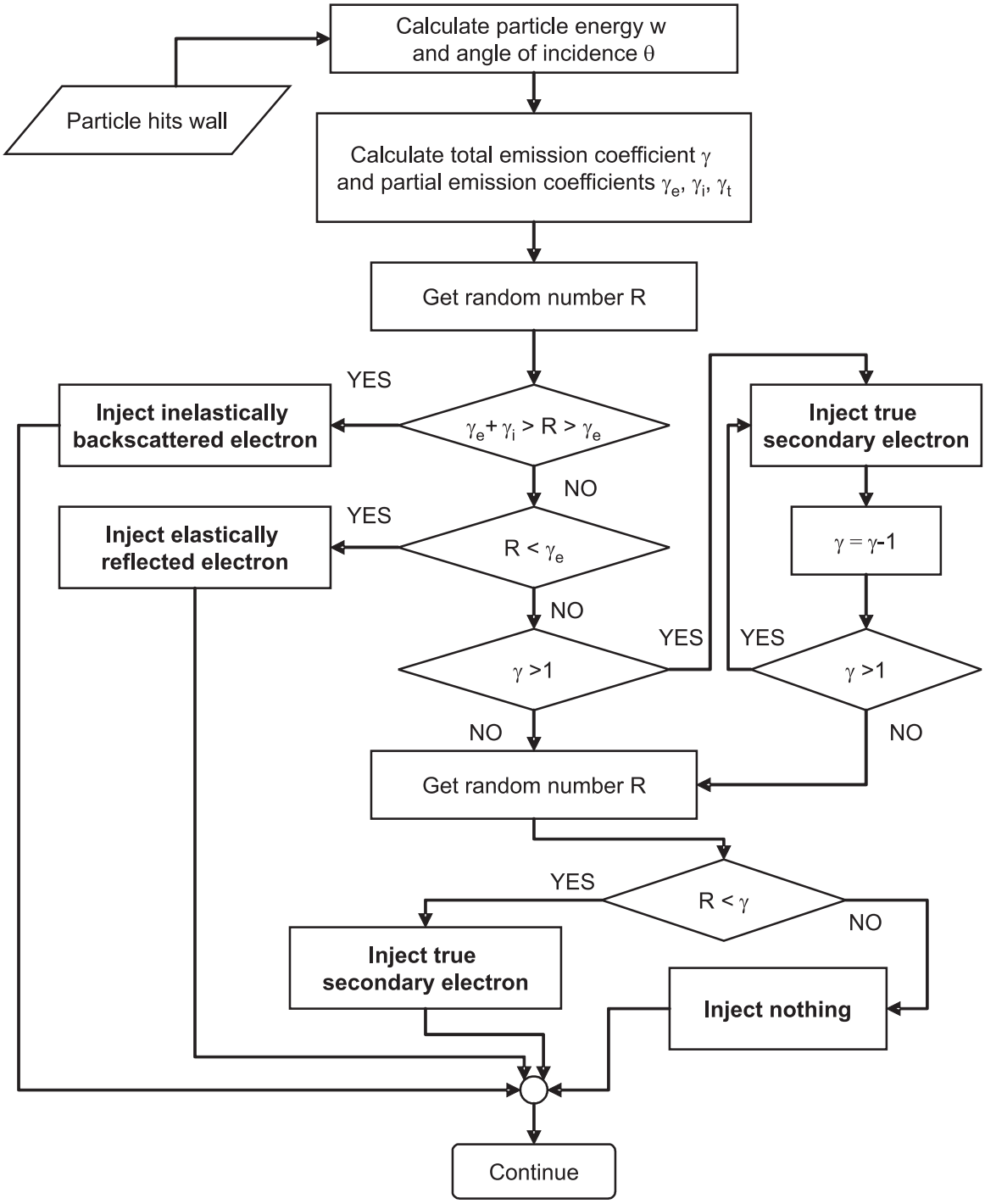

Figure 3.6: The flowchart of the injection algorithm for a multi-component secondary electron current.

more than one secondary electron ($\gamma > 1$), produces some number of *true* secondary electrons first and then scatters back elastically or almost elastically, which may result in a violation of the energy conservation law.

The SEE models similar to the one employed in EDIPIC are implemented in the XPDP1 [114] and in the XOOPIC [115] programs.

3.5 Monte-Carlo model of electron-neutral collisions

3.5.1 The null collision algorithm

The Monte-Carlo model of electron and ion collisions with neutral atoms is based on the null collision algorithm [13], which proposes a highly effective, low numerical cost method of determining the moments of particle collisions (in time). The implemented model assumes that the density of neutral atoms n_a is uniform and constant in time.

When a particle with energy w moves through a set of scatterers with density n_a, the probability that the particle collides during a time interval Δt is

$$P = 1 - \exp\left[-\Delta t \nu(w)\right] ,$$

where $\nu(w) = v\sigma_{sc}(w)n_a$ is the total frequency of all collisions possible for a given particle energy, σ_{sc} is the total cross section of possible collisions, $v = (2w/m)^{1/2}$ is the particle velocity, and m is the particle mass. In simulation, the straightforward way to determine whether a particle collides during the interval Δt is to compare the probability of collision P with a random number R ($0 < R < 1$) – the collision occurs if $R < P$. However, such a method is very expensive numerically, because it requires calculation of an energy and a random number for each particle every time step Δt.

Note, if all particles in the system have the same probability of collision P, then this probability is equal to the relative fraction of particles colliding during the time interval Δt, *i.e.*, $P = N_c/N_{part}$, where N_c is the number of colliding particles and

N_{part} is the total number of particles. Then, instead of comparing probability P with a random number for each particle, one can randomly select $P \times N_{part}$ particles to take part in collisions. The computational savings are significant if $P \ll 1$.

The cross section σ_{sc}, the collision frequency ν, and the collision probability P are functions of particle energy. The probability of collisions is maximal for particles with energy $w_{\max}$, corresponding to the maximum total collision frequency ν, *i.e.*, $\max(\nu) = \nu(w_{\max})$. Introducing the maximal frequency of collisions $\nu_{\max} \equiv \nu(w_{\max})$, the corresponding maximal probability of collisions is

$$P_{\max} = 1 - \exp\left(-\Delta t \nu_{\max}\right) . \tag{3.21}$$

One can consider $P_{\max}$ as an upper limit on the relative fraction of particles, which collide during the time interval Δt.

If a particle can participate in N_{coll} types of collisions, the total frequency of collisions is

$$\nu(w) = \sum_{j=1}^{N_{coll}} \nu_j(w) ,$$

where $\nu_j(w)$ is the frequency of collision type j. The particular collisional frequencies ν_j are calculated via the corresponding cross sections $\sigma_{sc,j}$ as $\nu_j(w) = v\sigma_{sc,j}(w)n_a$, $j = 1, \ldots, N_{coll}$. The null collision method, in addition to the physical collision processes, introduces a collision process, which does not change the velocity of scattered particles – the so-called null collision. The frequency of null collisions ν_{null} is a function of energy that makes the total collision frequency constant and equal to the maximal frequency of physical collisions $\nu_{\max}$:

$$\nu_{null}(w) = \nu_{\max} - \nu(w) .$$

With null collisions introduced as above, the probability of collisions becomes independent of particle energy, $P = P_{\max}$. This value can be precalculated in simulations and used as the relative fraction of particles collided at each time step. Then the collided particles can be selected randomly from the list of particles.

For a colliding particle with energy w, the kind of collision is determined as

follows. A set of values

$$
\begin{aligned}
P_0 &= 0 \ , \\
P_1 &= \frac{\nu_1(w)}{\nu_{\max}} \ , \\
P_2 &= \frac{\nu_1(w) + \nu_2(w)}{\nu_{\max}} \ , \\
&\cdots \\
P_{N_{coll}} &= \sum_{j=1}^{N_{coll}} \frac{\nu_j}{\nu_{\max}}
\end{aligned}
\tag{3.22}
$$

has to be calculated and compared with a random number R, $0 < R < 1$. Collision type j occurs if $P_{j-1} < R < P_j$. With $R > P_{N_{coll}}$ corresponding to the null collision, the particle does not collide. The general flowchart of the selection algorithm for collision particles and types is presented in Fig. 3.7.

In EDIPIC, the values (3.22) are tabulated over the expected energy range of colliding particles before the simulation. During simulation, the values of P_j for each colliding particle are obtained by linear interpolation of the tabulated data.

In the current version of EDIPIC, the following types of collisions between electrons and neutral atoms are implemented: elastic, excitation, and ionization. The realistic cross sections for electron-neutral collisions in xenon are stored in the data files, which are read at the initialization stage. Cross sections for electron-neutral elastic collisions are obtained by averaging and compiling the data presented in Ref. [116] for the electron energy range 0.01 eV − 10 eV, Ref. [117] for 1 eV − 100 eV, and Ref. [118] for 10 eV − 1000 eV (see curve 1 in Fig. 3.8). Cross sections for electron-neutral excitation collisions are presented in Ref. [118] for energies from 8.32 eV to 10000 eV (see curve 2 in Fig. 3.8). Cross sections for electron-neutral ionization collisions are presented in Ref. [119] for energies from 15 eV to 1000 eV (see curve 3 in Fig. 3.8).

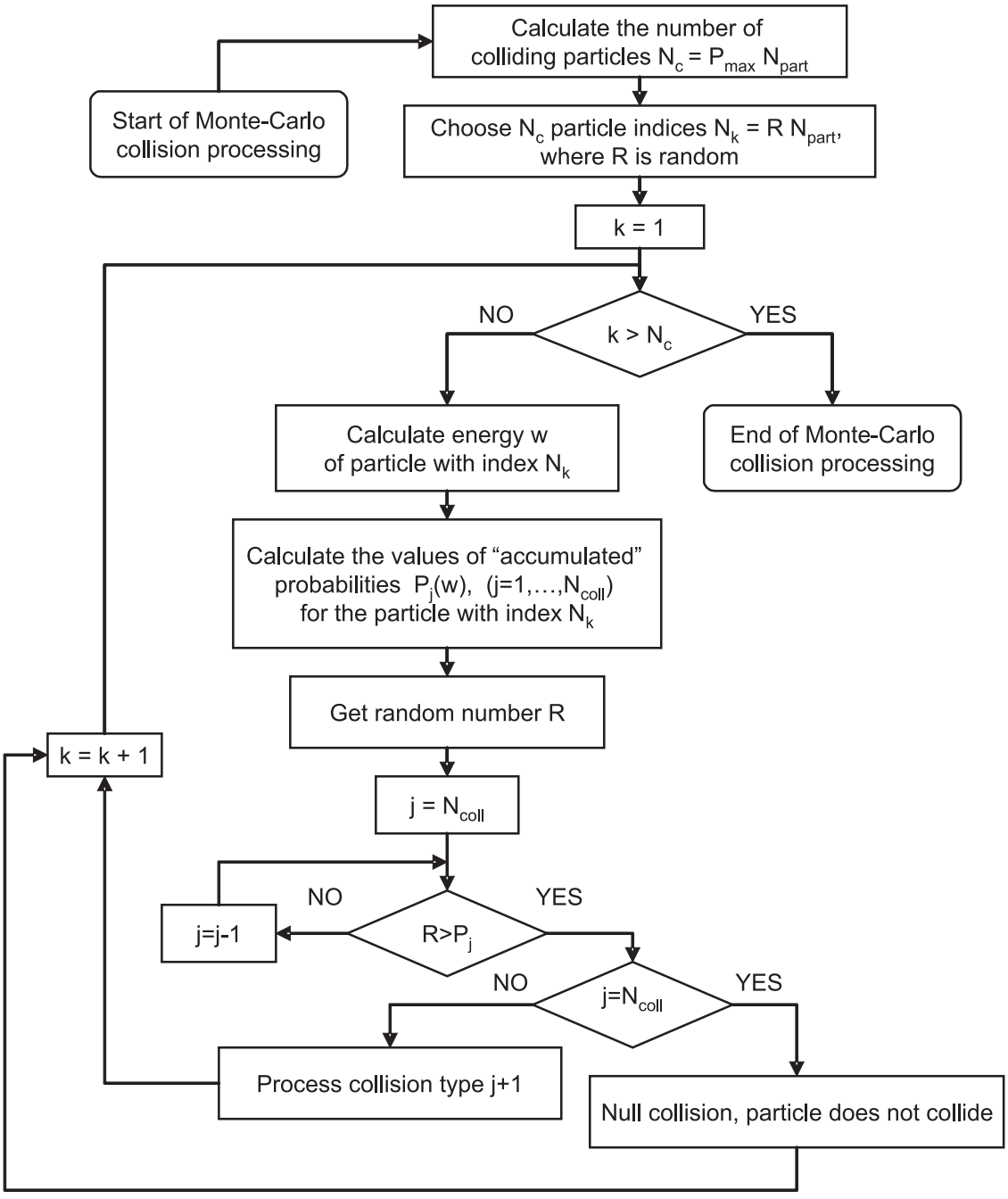

Figure 3.7: The flowchart of the null collision algorithm in the Monte-Carlo collision model. Here N_{part} is the total number of electron macroparticles.

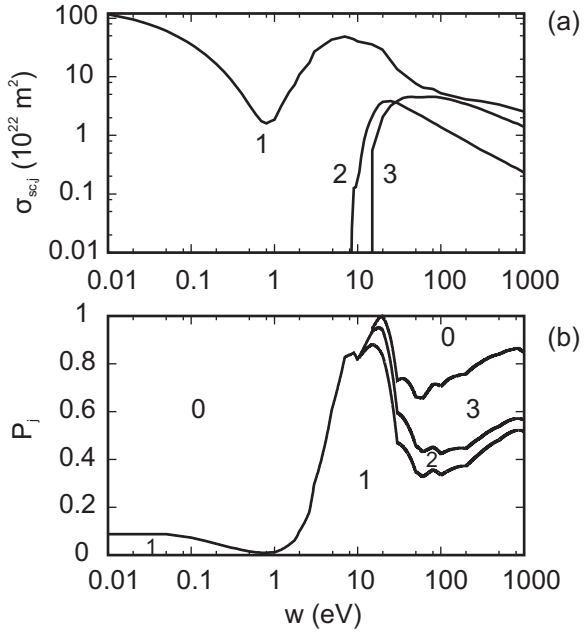

Figure 3.8: (a) The cross sections $\sigma_{sc,j}$ of electron-neutral collisions in xenon versus the colliding electron energy, curve 1 – elastic collisions, curve 2 – excitation collisions, curve 3 – ionization collisions. (b) The corresponding "accumulated" probabilities of collisions P_j versus the energy of colliding electron calculated by (3.22), region 0 corresponds to null collisions, region 1 – elastic collisions, region 2 – excitation collisions, region 3 – ionization collisions.

3.5.2 Elastic collisions. Transformation of the scattered electron velocity

Scattering of electrons in electron-neutral elastic collisions is characterized by the normalized differential cross section in the form [13]

$$\frac{\sigma_{sc}(w,\chi)}{\sigma_{sc}(w)} = \frac{w}{4\pi[1+w\sin^2(\chi/2)]\ln(1+w)} \ , \tag{3.23}$$

where χ is the angle of scattering relative to the initial direction of electron velocity in the laboratory frame (see Fig. 3.9) and w is the electron energy in electronvolts. Normalized differential cross section (3.23) is the differential cross section $\sigma_{sc}(w,\chi)$ divided by the total cross section $\sigma_{sc}(w)$, so that the following condition is satisfied:

$$2\pi \int_0^\pi d\chi \sin\chi \frac{\sigma_{sc}(w,\chi)}{\sigma_{sc}(w)} = 1 \ .$$

The normalized differential cross section defined as above is the probability density of scattering into angle χ, *i.e.*, the distribution function of scattered particles over the scattering angle χ. In simulations the scattering angle corresponding to distribution (3.23) is calculated by

$$\chi = \cos^{-1}\left[\frac{2+w-2(1+w)^R}{w}\right] \ , \tag{3.24}$$

where R is a random number, $0 < R < 1$. It is assumed that scattering is isotropic with respect to the azimuthal angle φ in the plane normal to the initial electron velocity (see Fig. 3.9). This angle is obtained by

$$\varphi = R2\pi \ , \tag{3.25}$$

where R is a random number, $0 < R < 1$. The velocity of an electron scattered through angles χ and ϕ can be expressed by

$$\mathbf{v}_{\rm sc} = \mathbf{v}_{\rm inc}\cos\chi + \frac{\mathbf{v}_{\rm inc}\times\mathbf{k}}{v\sin\theta} v\sin\chi\sin\varphi + \frac{\mathbf{v}_{\rm inc}\times(\mathbf{v}_{\rm inc}\times\mathbf{k})}{v^2\sin\theta} v\sin\chi\cos\varphi \ , \tag{3.26}$$

where $\mathbf{v}_{\rm inc}$ is the vector of electron velocity before scattering, $\mathbf{v}_{\rm sc}$ is the vector of electron velocity after scattering, $v = |\mathbf{v}_{\rm inc}| = |\mathbf{v}_{\rm sc}|$ is the speed, $\mathbf{k}$ is the unity vector

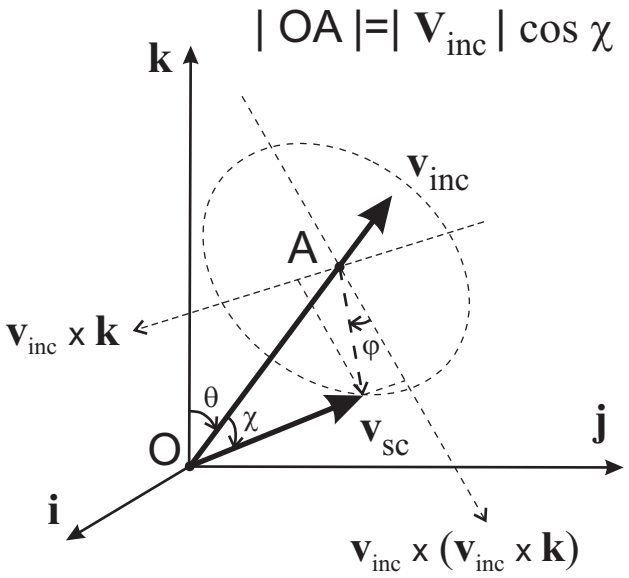

Figure 3.9: Transformation of the electron velocity before scattering on neutral atom $\mathbf{v}_{\rm inc}$ to the velocity after scattering $\mathbf{v}_{\rm sc}$. Angle χ is the angle of scattering relative to the initial direction of electron motion, angle φ is the azimuthal angle of rotation of scattered velocity in the plane normal to $\mathbf{v}_{\rm inc}$, calculated relative to the direction $\mathbf{v}_{\rm inc}\times(\mathbf{v}_{\rm inc}\times\mathbf{k})$. Vectors $\mathbf{i}$, $\mathbf{j}$, and $\mathbf{k}$ are the unit vectors along the x, y, and z directions, respectively.

in the z direction, and θ is the angle between $\mathbf{k}$ and $\mathbf{v}_{\rm inc}$. Note that transformation (3.26) does not change the speed. In Cartesian coordinates, transformation (3.26) is

$$\begin{aligned} v_{{\rm sc},x} &= v_{{\rm inc},x}\cos\chi + \frac{v_{{\rm inc},y}v}{\sqrt{v_{{\rm inc},x}^2+v_{{\rm inc},y}^2}}\sin\chi\sin\varphi + \frac{v_{{\rm inc},x}v_{{\rm inc},z}}{\sqrt{v_{{\rm inc},x}^2+v_{{\rm inc},y}^2}}\sin\chi\cos\varphi\ , \\ v_{{\rm sc},y} &= v_{{\rm inc},y}\cos\chi - \frac{v_{{\rm inc},x}v}{\sqrt{v_{{\rm inc},x}^2+v_{{\rm inc},y}^2}}\sin\chi\sin\varphi + \frac{v_{{\rm inc},y}v_{{\rm inc},z}}{\sqrt{v_{{\rm inc},x}^2+v_{{\rm inc},y}^2}}\sin\chi\cos\varphi\ , \\ v_{{\rm sc},z} &= v_{{\rm inc},z}\cos\chi - \sqrt{v_{{\rm inc},x}^2+v_{{\rm inc},y}^2}\sin\chi\cos\varphi\ , \end{aligned} \tag{3.27}$$

where $v_{{\rm sc},x}$, $v_{{\rm sc},y}$, and $v_{{\rm sc},z}$ are the components of the electron velocity after scattering, $v_{{\rm inc},x}$, $v_{{\rm inc},y}$, and $v_{{\rm inc},z}$ are the components of the electron velocity before scattering, and $v^2 = v_{{\rm inc},x}^2 + v_{{\rm inc},y}^2 + v_{{\rm inc},z}^2$. In elastic scattering, the electron transfers a part

$$\Delta w = \frac{2m}{M}(1-\cos\chi)w_{\rm inc} \tag{3.28}$$

of its energy to the neutral atom, where $w_{\rm inc}$ is the electron energy before scattering, and m and M are the electron and the neutral atom masses. The scattered velocity components must be multiplied after rotation (3.27) by the factor

$$\alpha = \sqrt{1-\frac{\Delta w}{w_{\rm inc}}} \tag{3.29}$$

in order to take into account the energy change (3.28). The energy of the neutral atoms is not followed in the present version of the code. Note that the scattering angle χ is obtained from Eq. (3.24) with $w = w_{\rm inc}$. A flowchart of the process for electron elastic scattering by neutral atoms is presented in Fig. 3.10.

3.5.3 Excitation collisions

Inelastic excitation collisions decrease the energy of scattering electron by the value

$$\Delta w = w_{\rm exc}\ , \tag{3.30}$$

where $w_{\rm exc}$ is the excitation threshold energy, $w_{\rm exc} = 8.32$ eV for xenon [118]. Electrons with an energy below this threshold do not participate in excitation processes. In contrast to the elastic collisions described above, the scattering angle χ is obtained from (3.24) with the modified value of energy $w = w_{\rm inc} - w_{\rm exc}$ [13]. The

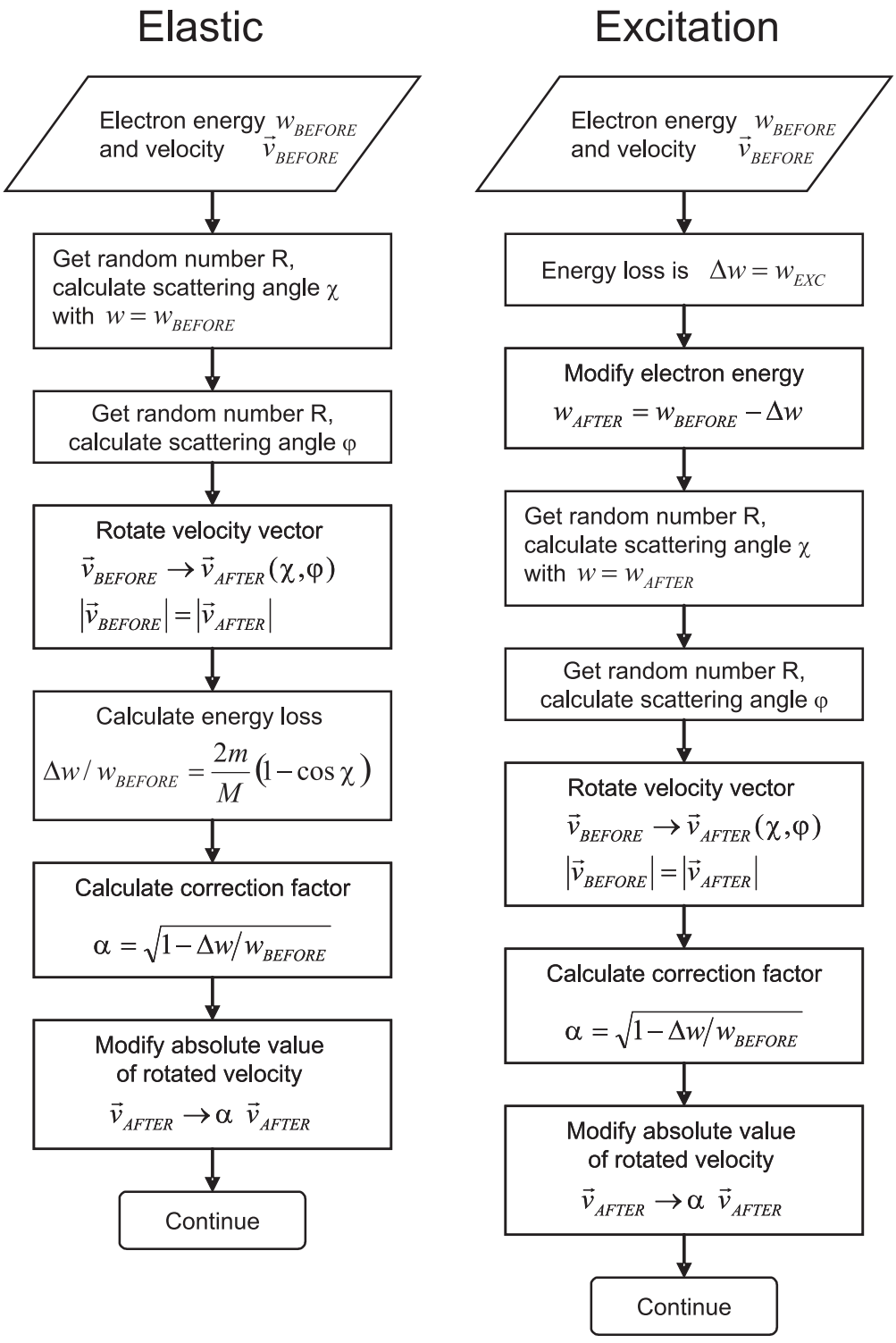

Figure 3.10: Flowcharts of the processes for electrons colliding elastically (left) and inelastically (right) with neutral atoms. Subscripts "before" and "after" denote the values before and after the collision.

azimuthal angle φ is obtained according to (3.25). The velocity components of the scattered particles are calculated with equations (3.27), and then are multiplied by factor (3.29) with Δw from (3.30). A flowchart of the process for electron inelastic excitation collisions with neutral atoms is presented in Fig. 3.10.

3.5.4 Ionization collisions

In the ionization process, an electron collides with a neutral atom and produces one additional electron and an ion. The energy of the product ion is considered to be equal to the energy of the neutral atom participating in the collision. The velocity components of the product ion are obtained corresponding to a Maxwellian velocity distribution function with the temperature of the neutral gas. The energy of the incident electron before the collision w_{inc} must be above the threshold energy of ionization w_{ion}, $w_{\text{inc}} > w_{\text{ion}}$, for xenon $w_{\text{ion}} = 15$ eV [118]. The energy of the electron produced in collision (ejected from the atom) is calculated by

$$w_{\text{ej}} = B(w_{\text{inc}}) \tan\left[R \tan^{-1}\left(\frac{w_{\text{inc}} - w_{\text{ion}}}{2B(w_{\text{inc}})}\right)\right], \tag{3.31}$$

where R is a random number, $0 < R < 1$, $B(w_{\text{inc}})$ is a function of incident electron energy known from experimental measurements, and the energies are given in electronvolts. For xenon $B \sim 8.7$ eV [120]. The energy of the electron that collided with the atom (scattered electron) is obtained from the energy conservation

$$w_{\text{sc}} = w_{\text{inc}} - w_{\text{ion}} - w_{\text{ej}}. \tag{3.32}$$

After the energies of the scattered electron and ejected electron are determined, their velocities $\mathbf{v}_{\text{sc}}$ and $\mathbf{v}_{\text{ej}}$ are obtained via the procedure of scattering, which has to be applied separately for each of these electrons. For both electrons, the velocity vector *to be transformed* is the velocity of the incident electron before the collision $\mathbf{v}_{\text{inc}}$. Scattering angles χ must be calculated by (3.24) with $w = w_{\text{sc}}$ for scattered and $w = w_{\text{ej}}$ for ejected electrons, respectively. Scattering angles φ are obtained randomly by (3.25). The velocity components are calculated with Eqs. (3.27). The ejected electron and the ion have the same coordinate x as the incident/scattered

electron. A flowchart of the process for electron ionization collisions with neutral atoms is presented in Fig. 3.11.

3.5.5 "Turbulent" collisions

Experimentally measured electron mobility in Hall thrusters greatly exceeds the classical collisional mobility. It is believed that in Hall thrusters one of the possible reasons of anomalous electron mobility is the perturbation of $E \times B$ electron drift by fluctuations of azimuthal electric field [57, 59, 64, 66]. If field fluctuations are random, motion of electrons in such fields may be considered as random walk [33]. This process can be described by the Monte Carlo model of collisions, which is why the common approach is to introduce the so-called "anomalous", or "turbulent" collisions [69, 70].

Since scattering by azimuthal electric field occurs in the plane parallel to the walls, "turbulent" collisions randomly scatter particles in this plane and does not affect the electron velocity normal to the walls. The frequency of "turbulent" collisions is the external parameter, which is adjusted to obtain the desired value of electron mobility. The latter value may be known, *e.g.*, from the experimental data. The use of the additional collisional process allows to include the anomalous electron mobility in analytical and numerical models without resolving azimuthal direction of the discharge and field turbulence. The collisional "turbulent" model describes the anomalous electron mobility caused by random field fluctuations.

In EDIPIC the "turbulent" collisions are included as a part of the Monte-Carlo model of collisions. Since the properties of azimuthal field fluctuations causing the anomalous electron mobility are not known, the frequency of "turbulent" collisions ν_t is taken independent on the colliding electron energy. "Turbulent" collisions are processed as follows. First, the angle φ of scattering in the y-z plane is obtained as $\varphi = R2\pi$, where R is a random number, $0 < R < 1$. Second, rotation of the component of the velocity vector in the plane y-z by angle φ is performed by the formulae

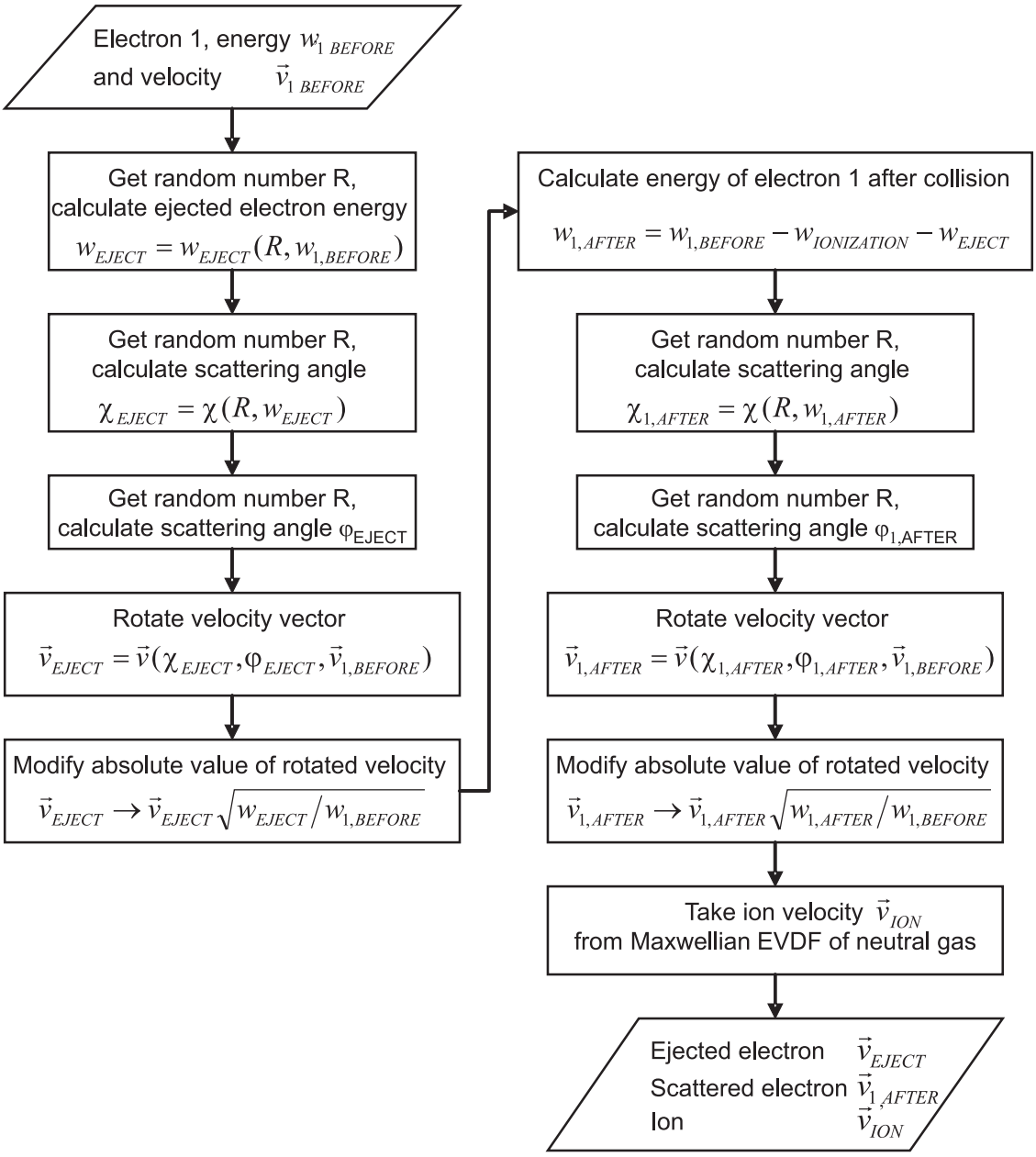

Figure 3.11: Flowchart of the process for ionization of a neutral atom by an electron. Subscripts "1,before" and "1,after" mark the values of the incident electron before and after the collision. Subscripts "eject" and "ion" mark the values of the ejected electron and ion, $w_{ionization}$ is the ionization energy threshold.

$$v_{y,sc} = v_y \cos\varphi - v_z \sin\varphi, \quad v_{z,sc} = v_y \sin\varphi + v_z \cos\varphi,$$

where v_y and v_z are the velocity components before scattering, and $v_{y,sc}$ and $v_{z,sc}$ are the velocity components after scattering.

If one of the objectives of a simulation is to reproduce the experimental electron mobility related to the given axial electric and radial magnetic fields, the value of ν_t is obtained as follows. The neutral gas density determines the frequency of electron-neutral collisions $\langle\nu_{en}\rangle$, where $\langle ...\rangle$ means averaging over all electrons. Then ν_t is adjusted such that the electron mobility μ_e due to both "turbulent" and electron-neutral collisions corresponds to the experimental value of the electron electric current density J_{exp}:

$$J_{exp} = e\overline{n}_e \mu_e E_z = e\overline{n}_e \frac{e\nu_{\text{eff}}}{m(\nu_{\text{eff}}^2 + \omega_c^2)} E_z \tag{3.33}$$

where $\nu_{\text{eff}} = \nu_t + \langle\nu_{en}\rangle$ is the effective collision frequency due to both "turbulent" and electron-neutral collisions, $-e$ and m are the electron charge and mass, $\overline{n}_e$ is the electron density averaged over the width of the plasma slab, and ω_c is the electron cyclotron frequency. With strong plasma-wall interaction, ν_{eff} may also include the electron-wall collision frequency, as it is described in Section 6.2.

3.6 Langevin model of Coulomb collisions

3.6.1 Electron-electron collisions

In contrast to collisions with neutral atoms and "turbulent" collisions, Coulomb collisions are much more frequent and are characterized by predominantly small scattering angles. Because of the long range of the electrostatic force, a scattering charged particle "feels" a large number of scatterers simultaneously, so the direct application of the Monte-Carlo model described above to simulations of collisions between charged particles is, firstly, extremely ineffective numerically, and secondly, physically inappropriate. In PIC simulations, the effect of Coulomb collisions can be

represented as a result of dynamical friction and stochastic diffusion depending on the local EVFD, *i.e.*, scattering on many particles can be substituted by scattering off the grid [112, 121].

The Fokker-Planck equation for electron-electron scattering is

$$\left.\frac{\partial f}{\partial t}\right|_{ee} = -\frac{\partial}{\partial \mathbf{v}}\mathbf{F}_d(\mathbf{v})f(\mathbf{v}) + \frac{1}{2}\frac{\partial^2}{\partial \mathbf{v}\partial \mathbf{v}}\mathbf{D}(\mathbf{v})f(\mathbf{v}) \ , \tag{3.34}$$

where

$$\mathbf{F}_d(\mathbf{v}) = \frac{ne^4}{4\pi\varepsilon_0^2 m^2}\Lambda\frac{\partial}{\partial \mathbf{v}}H(\mathbf{v}) \tag{3.35}$$

is the dynamic friction,

$$\mathbf{D}(\mathbf{v}) = \frac{ne^4}{4\pi\varepsilon_0^2 m^2}\Lambda\frac{\partial^2}{\partial \mathbf{v}\partial \mathbf{v}}G(\mathbf{v}) \tag{3.36}$$

is the velocity diffusion coefficient, n is the density of scatterers, i.e. the electron density,

$$\Lambda = \ln\left(\frac{1}{2}\csc\theta_m\right)$$

is the Coulomb logarithm,

$$\theta_m = 2\tan^{-1}\left(\frac{e^2}{2\pi\varepsilon_0 m v_{th}^2 \lambda_D}\right)$$

is the minimal scattering angle,

$$H(\mathbf{v}) = 2\int d^3\widetilde{v}\frac{f(\widetilde{\mathbf{v}})}{|\mathbf{v}-\widetilde{\mathbf{v}}|} \ , \tag{3.37}$$

and

$$G(\mathbf{v}) = \int d^3\widetilde{v} f(\widetilde{\mathbf{v}})|\mathbf{v}-\widetilde{\mathbf{v}}| \ . \tag{3.38}$$

Coefficients $H(\mathbf{v})$ and $G(\mathbf{v})$ were introduced for the first time by Rosenbluth et al. in [122] and are often called the first and the second Rosenbluth potential. Integration in coefficients $H(\mathbf{v})$ and $G(\mathbf{v})$ is carried out over the velocities of scatterers. The dynamic friction $\mathbf{F}_d(\mathbf{v})$ describes the average rate of change of the electron mean directed velocity due to Coulomb collisions. The velocity diffusion coefficient $\mathbf{D}(\mathbf{v})$ describes the effect of electron spreading in velocity space.

Coefficients $H(\mathbf{v})$ and $G(\mathbf{v})$ must be calculated as grid quantities. The calculation simplifies significantly if the EVDF of scatterers is a function of only the magnitude

of the velocity in the frame where the fluid electron velocity $\mathbf{u}_e$ is zero, $\mathbf{u}_e = 0$. This is a reasonable simplification, since Coulomb collisions tend to make the EVDF more isotropic.

Consider a scattering electron with velocity $\mathbf{v}$ and a scatterer electron with velocity $\widetilde{\mathbf{v}}$ in the laboratory velocity coordinate system. One can introduce a new velocity coordinate system with origin at $\mathbf{u}_e$, and with its third axis directed along $\mathbf{v} - \mathbf{u}_e$. In the new coordinate system the velocity $\mathbf{w}$ of the scattering electron and the velocity $\widetilde{\mathbf{w}}$ of the scatterer electron are

$$\mathbf{w} = \mathbf{v} - \mathbf{u}_e \ ,$$

$$\widetilde{\mathbf{w}} = \widetilde{\mathbf{v}} - \mathbf{u}_e \ .$$

The absolute value of vector $\mathbf{v} - \widetilde{\mathbf{v}}$ can be expressed as

$$|\mathbf{v} - \widetilde{\mathbf{v}}|^2 = |\mathbf{w} - \widetilde{\mathbf{w}}|^2 = w^2 + \widetilde{w}^2 - 2w\widetilde{w}\cos\vartheta \ ,$$

where $\widetilde{w}$ and w are the absolute values of vectors $\widetilde{\mathbf{w}}$ and $\mathbf{w}$, and ϑ is the angle between these vectors. Due to the choice of the third axis of the new frame, angle ϑ is the polar angle of a scatterer electron in that frame, $\vartheta = \widetilde{\vartheta}$. Then

$$\begin{aligned} H(\mathbf{v}) &= 2\int d^3\widetilde{v}\frac{f(\widetilde{\mathbf{v}})}{|\mathbf{v}-\widetilde{\mathbf{v}}|} = 2\int d^3\widetilde{v}\frac{f(|\widetilde{\mathbf{v}}-\mathbf{u}_e|)}{|\mathbf{v}-\widetilde{\mathbf{v}}|} \\ &= 2\int_0^\infty d\widetilde{w}\widetilde{w}^2 f(\widetilde{w})\int_0^{2\pi} d\widetilde{\phi}\int_0^{\pi} d\widetilde{\vartheta}\frac{\sin\widetilde{\vartheta}}{\sqrt{w^2+\widetilde{w}^2-2w\widetilde{w}\cos\widetilde{\vartheta}}} \\ &= \frac{8\pi}{w}\int_0^w d\widetilde{w}\widetilde{w}^2 f(\widetilde{w}) + 8\pi\int_w^\infty d\widetilde{w}\widetilde{w} f(\widetilde{w}) = H(w). \end{aligned} \tag{3.39}$$

Similarly,

$$\begin{aligned} G(\mathbf{v}) &= \int d^3\widetilde{v} f(\widetilde{\mathbf{v}})|\mathbf{v}-\widetilde{\mathbf{v}}| = \int d^3\widetilde{v} f(|\widetilde{\mathbf{v}}-\mathbf{u}_e|)|\mathbf{v}-\widetilde{\mathbf{v}}| \\ &= \int_0^\infty d\widetilde{w}\widetilde{w}^2 f(\widetilde{w})\int_0^{2\pi} d\widetilde{\phi}\int_0^{\pi} d\widetilde{\vartheta}\sin\widetilde{\vartheta}\sqrt{w^2+\widetilde{w}^2-2w\widetilde{w}\cos\widetilde{\vartheta}} \\ &= \frac{4\pi}{3}\int_0^w d\widetilde{w}\widetilde{w}^2\left(\frac{3w^2+\widetilde{w}^2}{w}\right) f(\widetilde{w}) + \frac{4\pi}{3}\int_w^\infty d\widetilde{w}\widetilde{w}\left(w^2+3\widetilde{w}^2\right) f(\widetilde{w}) \\ &= G(w). \end{aligned} \tag{3.40}$$

As one can see, transition from $f(\widetilde{\mathbf{v}})$ to isotropic $f(|\widetilde{\mathbf{v}} - \mathbf{u}_e|)$ made the coefficients H and G functions of the speed of the scattering particle in the frame moving with

electron flow velocity $\mathbf{u}_e$. Substituting (3.39) into (3.35) and allowing for

$$\frac{\partial}{\partial \mathbf{v}} H(w) = \frac{\mathbf{w}}{w} \frac{\partial}{\partial w} H(w) \ ,$$

one obtains the drag force in the form

$$\begin{aligned} \mathbf{F}_d(\mathbf{v}) &= \frac{\mathbf{v}-\mathbf{u}_e}{|\mathbf{v}-\mathbf{u}_e|} n F_d(|\mathbf{v}-\mathbf{u}_e|) \\ &= \frac{\mathbf{v}-\mathbf{u}_e}{|\mathbf{v}-\mathbf{u}_e|} n \left(-\frac{2e^4}{\varepsilon_0^2 m^2} \Lambda \frac{1}{|\mathbf{v}-\mathbf{u}_e|^2} \int_0^{|\mathbf{v}-\mathbf{u}_e|} d\widetilde{w} \widetilde{w}^2 f(\widetilde{w}) \right) \ . \end{aligned} \tag{3.41}$$

Equation (3.41) describes the force directed against the direction of electron motion relative to the electron flow. The dynamic friction force written in the form (3.41) can be readily obtained in the frame where $\mathbf{v}$ and $\mathbf{u}_e$ are given.

To calculate the velocity diffusion, consider tensor $\mathbf{D}(\mathbf{v})$ in the velocity space coordinate system with the third axis directed along $\mathbf{v}-\mathbf{u}_e$. Below, the coordinates and vectors in the new frame will be denoted with a prime, *e.g.*, v'_z or $\mathbf{v}'$. Note that this system is different from the one introduced above for calculation of coefficients H and G — the origin is not shifted to $\mathbf{u}_e$ but *coincides* with that of the laboratory frame. Taking into account that $w = |\mathbf{v}-\mathbf{u}_e| = |\mathbf{v}'-\mathbf{u}'_e| = [(v'_z - u'_{ez})^2]^{1/2}$, in the new coordinate system one obtains

$$\begin{aligned} &\frac{\partial^2}{\partial v_z'^2} G(w) = \frac{\partial^2}{\partial w^2} G(w) \ , \quad \frac{\partial^2}{\partial v_x'^2} G(w) = \frac{\partial^2}{\partial v_y'^2} G(w) = \frac{1}{w} \frac{\partial}{\partial w} G(w) \ , \\ &\frac{\partial^2}{\partial v'_i \partial v'_j} G(w) = 0 \text{ if } i \neq j. \end{aligned} \tag{3.42}$$

Therefore, only the diagonal components of the diffusion coefficient tensor $\mathbf{D}(\mathbf{v}')$ are non-zero. Integration of (3.36) with (3.42) gives

$$\begin{aligned} D_{11}(w) = D_{22}(w) &\equiv n D_1(w) \\ &= n \left\{ \frac{e^4}{3\varepsilon_0^2 m^2} \Lambda \left[\frac{1}{w^3} \int_0^w d\widetilde{w} \widetilde{w}^2 (3w^2 - \widetilde{w}^2) f(\widetilde{w}) + 2 \int_w^\infty d\widetilde{w} \widetilde{w} f(\widetilde{w}) \right] \right\} \ , \\ D_{33}(w) \equiv n D_3(w) &= n \left\{ \frac{2e^4}{3\varepsilon_0^2 m^2} \Lambda \left[\frac{1}{w^3} \int_0^w d\widetilde{w} \widetilde{w}^4 f(\widetilde{w}) + \int_w^\infty d\widetilde{w} \widetilde{w} f(\widetilde{w}) \right] \right\} \ . \end{aligned} \tag{3.43}$$

Transition to the new coordinate system does not modify the speeds, which is why no special notation is introduced for $w = |\mathbf{v}'-\mathbf{u}'_e| = |\mathbf{v}-\mathbf{u}_e|$.

Coefficients $F_d(w)$ and $D_{1,3}(w)$ use the EVDF $f(w)$, which, in fact, has to be determined locally. However, because of statistical fluctuations and finite particle numbers in simulations, it is impossible to calculate the EVDF and the coefficients at every grid point. In Ref. [112], the EVDF during simulation of an ECR discharge was averaged over the magnetic field line (the electrons were magnetized and not supposed to leave the line). In the EDIPIC code, the EVDF $f(w)$ and the fluid velocity $\mathbf{u}_e$ are calculated using all electrons from the region $\delta L < x < L - \delta L$, where δL is larger than the width of the strongly nonuniform near-wall region.

The Fokker-Planck equation (3.34) to first order accuracy in Δt is equivalent to the Langevin equation [112]

$$\Delta \mathbf{v} = \mathbf{F}_d \Delta t + \mathbf{Q} \ , \tag{3.44}$$

where $\mathbf{F}_d$ is the dynamic friction as above and $\mathbf{Q}$ is a random vector responsible for the velocity diffusion. The Langevin equation allows one to obtain corrections for the electron velocity due to Coulomb collisions in simulations.

In the "primed" coordinate system introduced above, coordinates $Q'_{1,2,3}$ of vector $\mathbf{Q}'$ correspond to the distribution

$$\Psi(\mathbf{Q}') = \frac{1}{(2\pi\Delta t)^{3/2} D_{11} D_{33}^{1/2}} \exp\left(-\frac{Q_3'^2}{2D_{33}\Delta t} - \frac{Q_1'^2 + Q_2'^2}{2D_{11}\Delta t} \right) . \tag{3.45}$$

To obtain coordinates of $\mathbf{Q}$ in the laboratory frame, one has to build a transformation matrix using Euler angles [123]. It is convenient to assume that the first axis of the "primed" coordinate system is in the plane $v_x - v_y$ of the laboratory coordinate system – in terms of Euler angles this means that the third angle is zero (see Fig. 3.12). Then the coordinates of vector $\mathbf{Q}$ can be obtained by

$$\begin{pmatrix} Q_x \\ Q_y \\ Q_z \end{pmatrix} = \begin{pmatrix} \cos\phi & -\cos\theta\sin\phi & \sin\theta\sin\phi \\ \sin\phi & \cos\theta\cos\phi & -\sin\theta\cos\phi \\ 0 & \sin\theta & \cos\theta \end{pmatrix} \begin{pmatrix} Q'_1 \\ Q'_2 \\ Q'_3 \end{pmatrix} \ , \tag{3.46}$$

where

$$\begin{aligned} \sin\theta &= \frac{\sqrt{w_x^2 + w_y^2}}{w} \ , \ \cos\theta = \frac{w_z}{w} \ , \\ \sin\phi &= \frac{w_x}{\sqrt{w_x^2 + w_y^2}} \ , \ \cos\phi = -\frac{w_y}{\sqrt{w_x^2 + w_y^2}} \ , \end{aligned} \tag{3.47}$$

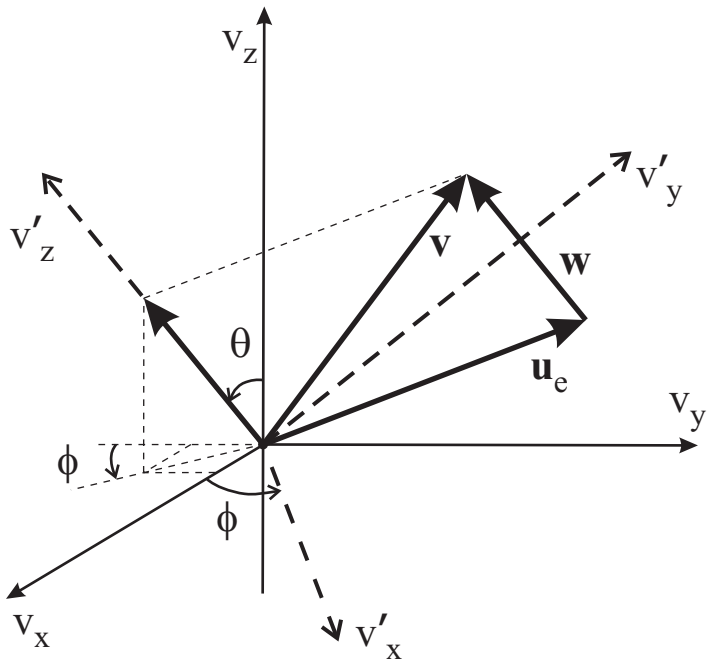

Figure 3.12: The new "primed" coordinate system $\{v'_x, v'_y, v'_z\}$, where the velocity diffusion tensor (3.36) obtains diagonal form. Here $\mathbf{v}$ is the velocity of the scattering electron, $\mathbf{u}_e$ is the electron flow velocity, and $\mathbf{w} = \mathbf{v} - \mathbf{u}_e$. The third axis of the "primed" coordinate system is directed along $\mathbf{w}$, angles θ and ϕ are the first two angles of the Euler transformation. Coordinate system $\{v_x, v_y, v_z\}$ corresponds to the laboratory frame.

and $w_{x,y,z}$ are the components of the velocity of scattering electron relative to the electron flow $\mathbf{w} = \mathbf{v} - \mathbf{u}_e$, determined in the laboratory frame.

The probability function $\Psi(\mathbf{Q}')$ depends on the speed of the electron to be scattered w and the local electron density n (via the coefficients D_{11} and D_{33}). In simulations, a component of vector $\mathbf{Q}'$ corresponding to the distribution (3.45), *e.g.*, the component Q'_3, is the solution of the equation

$$R = \int_{-\infty}^{Q'_3} dy_3 \int_{-\infty}^{\infty} dy_2 \int_{-\infty}^{\infty} dy_1 \Psi(\mathbf{y}) = F_g(Q'_3/\sqrt{2D_3 n \Delta t}) \ ,$$

where R is a random number, $0 < R < 1$, $F_g(\upsilon) = \pi^{-1/2} \int_{-\infty}^{\upsilon} d\tau \exp(-\tau^2)$. Note that the equation $R = F_g(\upsilon)$ with random R has to be solved for υ every time a new value corresponding to the Gaussian distribution $\pi^{-1/2} \exp(-\upsilon^2)$ is required. In addition to the Langevin model of Coulomb collisions, this equation is exploited in the Monte-

Carlo model of electron-neutral collisions for generating a velocity from a Maxwellian EVDF. To reduce the numerical load, before a simulation one must tabulate N_R pairs of values (R_j, υ_j), where $\upsilon_j = \upsilon_0(2j/N_R - 1)$, $R_j = F_g(\upsilon_j)$, $j = 1, ..., N_R$, and N_R is some arbitrary large integer number (in EDIPIC $N_R = 180000$ and $\upsilon_0 = 3$). Then, for a given random number R, the solution of the equation $R = F_g(\upsilon)$ can be found via interpolation over the tabulated values

$$\upsilon = \upsilon_j + (\upsilon_{j+1} - \upsilon_j)\frac{R - R_j}{R_{j+1} - R_j}, \quad R_j < R < R_{j+1} \ .$$

With a given coefficient $D_3(w)$ and density $n(x)$, the component Q'_3 is obtained as $Q'_3 = \upsilon\sqrt{2D_3 n\Delta t}$. Similarly, components $Q'_{1,2}$ are calculated as $Q'_{1,2} = \upsilon\sqrt{2D_1 n\Delta t}$. Note that a new random number has to be taken each time a component of $\mathbf{Q}'$ is calculated.

The general flowchart of the algorithm for electron-electron collisions is presented in Fig. 3.13. At first, the electron flow velocity $\mathbf{u}_e$ is determined and the EVDF $f(w)$ in the electron flow frame is found. Then the drag force coefficient F_d (3.41) and the velocity diffusion coefficients D_1 and D_3 (3.43) are tabulated as functions of w. In the main cycle, the velocity corrections for each electron due to the drag force $\mathbf{F}_d\Delta t$ and the velocity diffusion $\mathbf{Q}$ are calculated by Eqs. (3.41), (3.45), and (3.46); the velocity of every particle is modified by Eq. (3.44). The total energy of electrons before Coulomb scattering W_{before} and after Coulomb scattering W_{after} are accumulated during this stage. Finally, the velocities of all scattered electrons are multiplied by the factor $(W_{before}/W_{after})^{1/2}$ to ensure energy conservation.

3.6.2 Electron-ion collisions

Collisions of electrons with ions are also described by Eqs. (3.34)-(3.36). For single-charged ions of mass M the dynamic friction coefficient $H(\mathbf{v})$ is

$$H(\mathbf{v}) = \frac{m + M}{M}\int d^3\widetilde{v}\frac{f(\widetilde{\mathbf{v}})}{|\mathbf{v} - \widetilde{\mathbf{v}}|} \ , \tag{3.48}$$

and the velocity diffusion coefficient $G(\mathbf{v})$ is determined by (3.38). In calculation of $H(\mathbf{v})$ and $G(\mathbf{v})$ for electron-ion collisions, function $f(\widetilde{\mathbf{v}})$ is the ion velocity distribu-

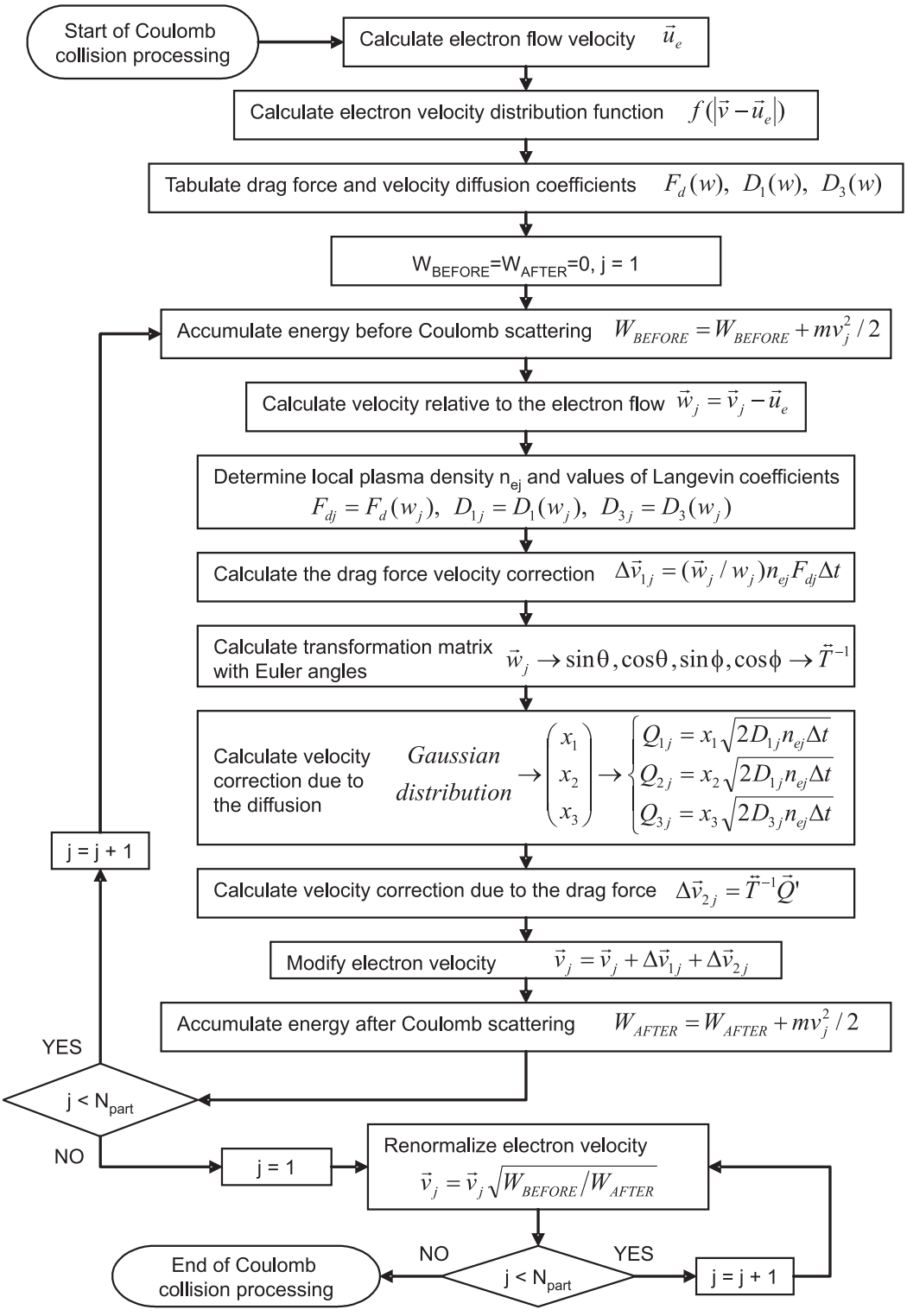

Figure 3.13: Flowchart of the electron-electron collision process. Here N_{part} is the total number of electron macroparticles in simulation.

tion function. Since most of electrons move much faster than ions, one can perform integration in (3.38) and (3.48) assuming $|\mathbf{v}| \gg |\widetilde{\mathbf{v}}|$ and obtain

$$\begin{aligned} H(\mathbf{v}) \equiv H(v) &= \frac{1}{v} \ , \\ G(\mathbf{v}) \equiv G(v) &= v \ , \end{aligned} \tag{3.49}$$

where $v \equiv |\mathbf{v}|$. With (3.49), the drag force (3.35) and the velocity diffusion coefficients (3.36) for the electron-ion collisions are

$$\begin{aligned} \mathbf{F}_d(\mathbf{v}) &= \frac{\mathbf{v}}{|\mathbf{v}|} n F_d(|\mathbf{v}|) = \frac{\mathbf{v}}{|\mathbf{v}|} n \left(-\frac{e^4}{4\pi\varepsilon_0^2 m^2} \Lambda \frac{1}{v^2} \right) \ , \\ D_{11}(v) = D_{22}(v) &\equiv n D_1(v) = n \left(\frac{e^4}{4\pi\varepsilon_0^2 m^2} \Lambda \frac{1}{v} \right) \ , \\ D_{33}(v) &= n D_3(v) = 0 \ . \end{aligned} \tag{3.50}$$

The diffusion coefficients D above are obtained in the coordinate system that has its third axis directed along $\mathbf{v}$, the ion flux velocity is neglected. Note that coefficients (3.50) grow infinitely as v approaches zero. The exact calculation of $H(v)$ and $G(v)$ has to account for the ion velocity distribution function, so that the Langevin coefficients will be finite for slow electrons with $v \sim v_{th,i}$, where $v_{th,i}$ is the ion thermal velocity. However, the number of such electrons is very small. In EDIPIC, all electrons with speed below some threshold, $v < v_{thr}$, are scattered off ions with constant Langevin coefficients $F_{d,thr} = F_d(v_{thr})$ and $D_{1,thr} = D_1(v_{thr})$, independently of the electron energy. The speed threshold v_{thr} is calculated as the electron speed at which the correction due to the drag force is of the order of the speed itself, *i.e.*, $v_{thr} = n\Delta t F_d(v_{thr})$. Then, from (3.50), one obtains

$$v_{thr} = \left(n\Delta t \frac{e^4}{4\pi\varepsilon_0^2 m^2} \Lambda \right)^{1/3} \ . \tag{3.51}$$

This simple algorithm eliminates the appearance of particles with extremely high velocities by preventing unphysically large velocity corrections for slow electrons. To ensure energy conservation, the electron velocity corrections due to electron-ion collisions are calculated and accounted for in conjunction with the corrections due to electron-electron collisions.

3.7 Summary

The parallel, electrostatic PIC code EDIPIC is developed on the basis of the direct implicit algorithm [105, 109]. The objective of EDIPIC is the self-consistent simulation of the plasma-wall interaction in the plane geometry model of the AR of a Hall thruster. The code includes the important physical effects of Hall thruster plasmas: the sheath, the secondary electron emission, the anomalous turbulent electron mobility, the collisions with neutral atoms, and the Coulomb collisions. The use of high-performance massively parallel computers allows spatial scales far less than the electron Debye length to be resolved, thus reproducing the narrow near-wall sheath regions correctly. The probabilistic model of secondary electron emission [110], Monte-Carlo model of electron-neutral collisions [13], and Langevin model of Coulomb collisions for electrons [112, 121] are implemented in the code.

Chapter 4

Testing and verification of the EDIPIC code

Testing is an important and necessary stage in the development of a trusted numerical tool [10]. Parts of the EDIPIC code (the modules responsible for the advance of particles and the solution of the Poisson's equation, the Monte-Carlo model of collisions, the probabilistic SEE model, the Langevin model of Coulomb collisions) were tested separately. These tests showed convincing results. The comprehensive testing of the EDIPIC code has been carried out by simulation of several real physical problems with known numerical or analytical solutions. Here the benchmarks were (i) the problem of sheath formation in the narrow layer between the Maxwellian plasma and the wall [124, 125], and (ii) the two-stream instability of a low-current monoenergetic beam in a cold plasma [126]. Below the details of the verification of the EDIPIC code are presented.

In Section 4.1, the results of the test simulation with two oppositely charged particles are presented. The electric field and the parameters of particle motion are compared with exact values obtained analytically. In Section 4.2, the partial emission coefficients for the three components of SEE (the true secondary, elastically reflected, and inelastically backscattered electrons) obtained in simulations are compared with theoretical curves. Section 4.3 contains a comparison of the EVDF of a monoenergetic electron beam scattered by neutral atoms in simulations with the corresponding theoretically predicted EVDF. The frequencies of elastic, excitation, and ionization electron-neutral collisions obtained in simulations are compared with the values calculated analytically using the known cross sections for xenon.

Section 4.4 describes simulation of the relaxation of the non-Maxwellian EVDF to the Maxwellian one due to the effect of Coulomb collisions. The results of the test simulation are compared with the similar simulation of Ref. [112]. In Section 4.5, the simulations of the semi-infinite plasma bounded by an absorbing or emitting wall is compared with the simulations of Refs. [124, 125]. Section 4.6 compares the simulations of the instability of a cold electron beam in a cold plasma with the predictions of the linear and the nonlinear theories of the two-stream instability [126].

4.1 Two-particle test

The two-particle test [9] is a simple, but powerful method of verification of the major parts of the computational cycle – the modules solving the equations of particle motion (the so-called "mover") and the field equations (the so-called "field solver"). Energy conservation and the diagnostics can also be checked during this test.

Consider a one-dimensional system of two parallel charged sheets with charge Q and $-Q$ per unit area and mass M_Q per unit area. At the moment $t = 0$, the particle positions are $x_1 = x_0$ and $x_2 = -x_0$ with the particles at rest. The charge densities are $\rho_1(x) = Q\delta(x - x_1)$ and $\rho_2(x) = -Q\delta(x - x_2)$, where $\delta(x)$ is the Dirac delta-function. Each charged sheet produces an electric field normal to the sheet surface with absolute value $Q/2\varepsilon_0$. The electrostatic fields of each particle in the region between the particles sum together, while in the outside region they cancel each other. With no external electric field, the field between the particles is

$$E_x = Q/\varepsilon_0 \ , \tag{4.1}$$

while outside the particles it is zero.

The two charged particles described above attract each other with a force $F = \frac{1}{2}QE_x$ which does not depend on the distance between the particles until they change their order. When the particles cross, the direction of the force changes, slowing them down to a complete stop, at which point acceleration towards each other begins again, and the process repeats. Such oscillations are not harmonic oscillations since

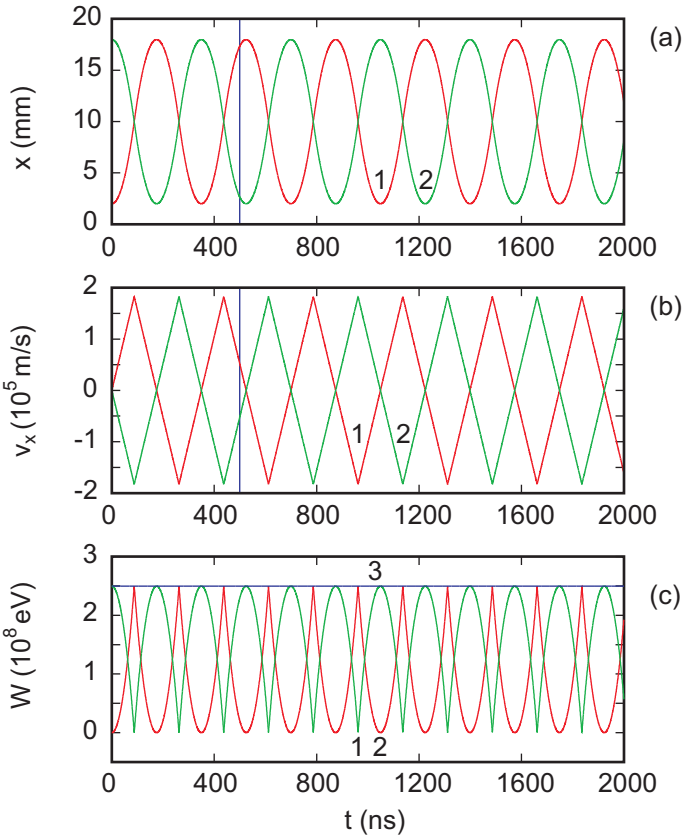

Figure 4.1: Particle dynamics during the two-particle test simulation. The particle coordinates (a) and velocities (b) versus time. In (a) and (b), curves 1 (red) correspond to the negatively charged macroparticle (electron), curves 2 (green) correspond to the positively charged macroparticle (ion); vertical blue lines mark the moment $t = 499.234$ ns when the snapshots presented in Fig. 4.2 were obtained. (c) The potential energy (green curve 1), kinetic energy (red curve 2), and total (kinetic plus potential) energy (blue curve 3) versus time.

the force is not proportional to the displacement. The period of the oscillations T can be calculated as 4 times the interval between the stationary start and the moment when particles meet each other $t_{1/4}$, i.e. $T = 4t_{1/4}$. For motion with constant acceleration a, one obtains $t_{1/4} = \sqrt{2x_0/a}$, where $a = Q^2/2\varepsilon_0 M_Q$. Thus, the period of the non-harmonic oscillations of two particles is

$$T = 8\left(\frac{x_0\varepsilon_0 M_Q}{Q^2}\right)^{1/2} . \tag{4.2}$$

The particles attain their maximal velocity

$$V_{\max} = \left(\frac{x_0 Q^2}{M_Q \varepsilon_0}\right)^{1/2} \tag{4.3}$$

when they cross with each other.

In simulations, the charge of a single macroparticle is

$$Q = \frac{n_0 q \Delta x}{N_{\text{macro}}} , \tag{4.4}$$

where n_0 is the scale density, q is the elementary charge ($q = \pm e$ depending on the species, ions or electrons), Δx is the mesh size, and N_{macro} is the number of macroparticles per cell. The masses of both positive and negative species are set to equal the electron mass m. With (4.4), one obtains

$$\begin{aligned} E_x &= \frac{n_0 q \Delta x}{\varepsilon_0 N_{\text{macro}}} , \\ T &= \frac{2^{3/2}}{\pi}\left(\frac{\Delta L N_{\text{macro}}}{\Delta x}\right)^{1/2} T_{pe} , \\ V_{\max} &= \left(\frac{\Delta L \Delta x}{2N_{\text{macro}}}\right)^{1/2} \omega_{pe} \end{aligned} \tag{4.5}$$

for two-particle simulations, where $\Delta L = 2x_0$ is the maximal distance between the particles, $T_{pe} = 2\pi/\omega_{pe}$ is the period of electron Langmuir plasma oscillations, and $\omega_{pe}^2 = n_0 e^2/\varepsilon_0 m$.

The two-particle test simulation was carried out with a system of length $L =$ 19.975 mm, $N_{\text{macro}} = 1000$, $\Delta L = 0.8L = 15.98$ mm, $\Delta t = 0.8759$ ps, and $\Delta x =$ 0.013141 mm. Floating potential at the walls was taken as a boundary condition. Initially, the two particles with opposite charge are positioned symmetrically relative

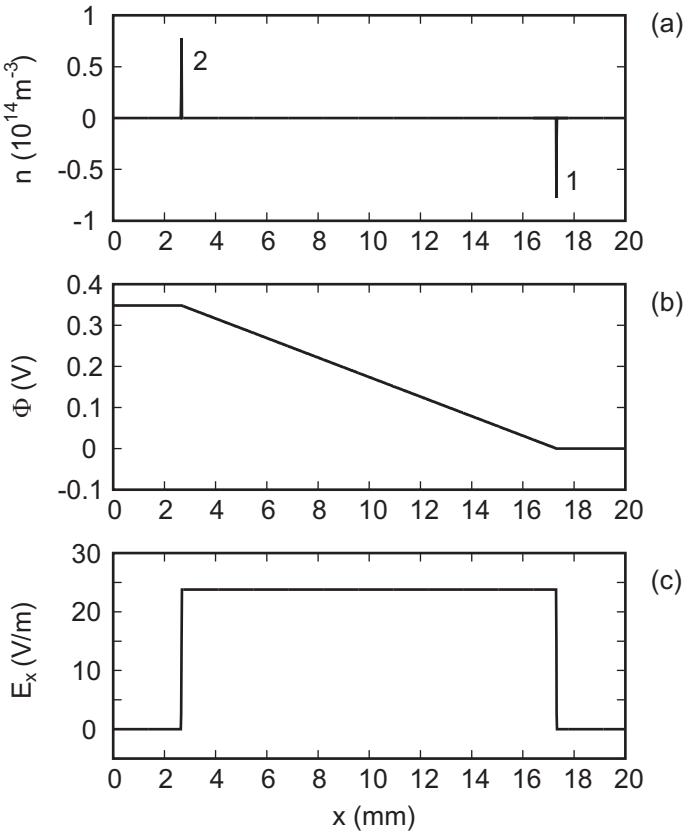

Figure 4.2: Spatial profiles of the charge density (a), the potential (b), and the electric field (c) obtained at $t = 499.234$ ns during the two-particle test simulation. In (a) spike 1 corresponds to the negatively charged macroparticle and spike 2 corresponds to the positively charged macroparticle.

Table 4.1: Comparison of the values calculated during the two-particle test with the values calculated by Eqs. (4.5).

	PIC	Theory	Difference [%]
E_x [V/m]	23.78	23.76	0.084
T [ns]	349.64	349.87	-0.066
$V_{\max}$ [m/s]	$1.827 \cdot 10^5$	$1.8269 \cdot 10^5$	0.005

to the midplane of the system with zero velocities. The two particles oscillate relative to the midplane of the system, showing no drifts in any direction (see Fig. 4.1a). The velocity of each particle changes linearly between turns, as is expected for a position-independent external force (see Fig. 4.1b). The potential energy $W_{pot} = (1/2)\int_0^L dx\rho(x)\Phi(x)$ shown by curve 1 in Fig. 4.1c and the kinetic energy $W_{kin} = \sum_j m_j v_j^2/2$ shown by curve 2 in Fig. 4.1c oscillate with doubled frequency. The total energy $W_{tot} = W_{pot} + W_{kin}$ is constant (see curve 3 in Fig. 4.1c). It is necessary to mention that the total energy is well conserved in simulations with large number of particles, the detailed description of energy evolution during one such simulation is presented in Appendix A.

In Fig. 4.2, the snapshots of spatial profiles of several system parameters obtained at $t = 499.234$ ns are presented. The positions of the two macroparticles are marked by the two spikes of charge density in Fig. 4.2a. The potential $\Phi(x)$ changes linearly in the region between the particles, while in the outside regions it is constant (see Fig. 4.2b). Subsequently, the electric field $E_x(x)$ is constant and finite between the particles and zero in the outside regions (see Fig. 4.2c). Comparison of the results of the two-particle test simulation with theoretical predictions is presented in Table. 4.1. There is very good correspondence between the theoretical values and values obtained in simulations.

4.2 Emission of secondary electrons

The important benchmark of the SEE model is a test of the multi-component emission algorithm (see the flowchart in Fig. 3.6). The objective of the algorithm is to produce fluxes of several components corresponding to the partial emission coefficients for different primary electron incidence angles and energies.

The test of the multi-component emission algorithm was done for case with the following conditions: (i) the external and self-consistent fields, as well as the ion motion, were neglected; (ii) the initial velocity distribution of electrons was taken in the form of a monoenergetic electron beam with energy w_b, beam velocity $\mathbf{v}_b$ was directed at angle ϑ relative to the normal to the wall $x = L$. Evolution of the system was followed for a short period of time $t < 2L/v_b$ to ensure that secondary electrons from the wall $x = 0$ (produced by secondary electrons emitted from the wall $x = L$) do not reach the wall $x = L$ and thus do not modify the energy spectrum of the incident beam.

In Fig. 4.3, the results of such tests are presented for energies of primary electrons from 5 eV to 400 eV and two angles of incidence, $\vartheta = 0$ and $\vartheta = 80^o$. One can see that the markers, which depict the values obtained in simulations, coincide with the solid curves representing the analytically calculated values. The tests reveal very good agreement of the calculated partial emission coefficients with the expected values determined by Eqs. (3.16), (3.17), and (3.18).

4.3 Electron-neutral collisions

Benchmarking the Monte Carlo model of electron-neutral collisions involves testing the velocity distribution of scattered electrons, and testing the null collision algorithm.

For the first test, consider a monoenergetic electron beam with velocity v_b and corresponding energy $w_b = mv_b^2/2$. Let every particle in this beam scatter once according to the differential cross section (3.23). Let the scattering occur isotropically

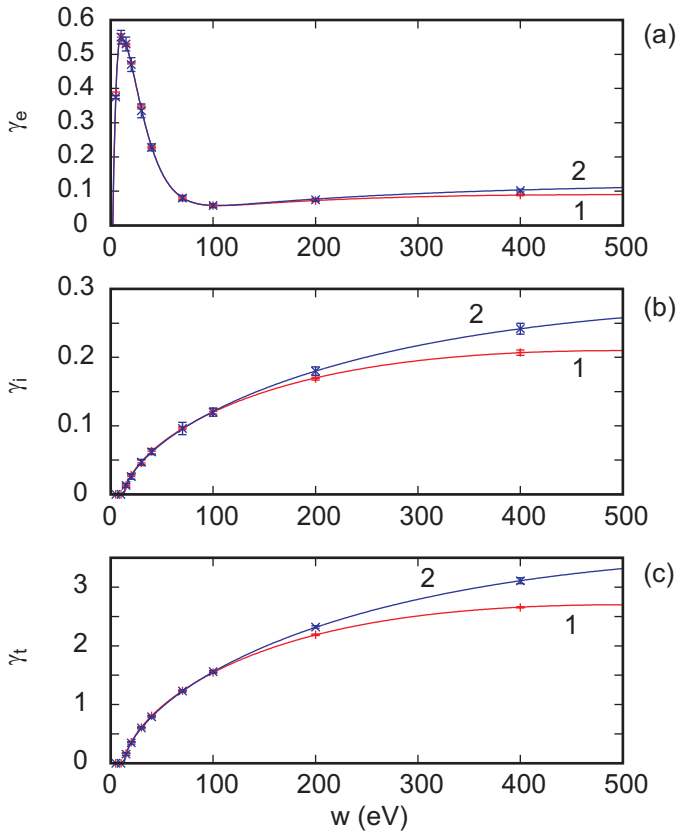

Figure 4.3: The partial emission coefficients versus the primary electron energy for: (a) the elastically reflected electrons, γ_e; (b) inelastically backscattered electrons, γ_i; (c) and true secondary electrons, γ_t. Curves are calculated by (3.16), (3.17), and (3.18). Markers are the values determined in simulations with a monoenergetic beam bombarding the wall. The red markers and curves 1 correspond to normal beam incidence with angle $\vartheta = 0$, and the blue markers and curves 2 correspond to the angle of incidence $\vartheta = 80^o$.

with respect to the azimuthal angle φ. By definition of the differential cross section, the number of particles scattered per unit time into the elementary solid angle $d\Omega = 2\pi \sin\chi d\chi$ is $dN = \Gamma d\sigma_{sc}(w_b) = \Gamma\sigma_{sc}(w_b,\chi)2\pi\sin\chi d\chi$, where Γ is the flux of scattering particles and χ is the pitch angle of scattering. The total number of particles scattered per unit time is $N = \int \Gamma d\sigma_{sc}(w_b) = \Gamma\sigma_{sc}(w_b)$, where integration is performed over the complete scattering cross section $\sigma_{sc}(w_b)$. The relative number of electrons scattered into the elementary solid angle $d\Omega$,

$$\frac{dN}{N} = \frac{\sigma_{sc}(w_b,\chi)}{\sigma_{sc}(w_b)} 2\pi\sin\chi d\chi,$$

is the probability that a single electron will scatter into this solid angle. Then the velocity distribution function of scattered electrons $f(v,\chi,\varphi)$ can be found from

$$\int_0^\infty dv v^2 \int_0^{2\pi} d\varphi \left[f(v,\chi,\varphi)\sin\chi d\chi\right] = \frac{\sigma_{sc}(w_b,\chi)}{\sigma_{sc}(w_b)} 2\pi\sin\chi d\chi \ . \tag{4.6}$$

Assuming that scattering occurs off infinitely massive targets and the energy transfer is zero, so that the speed of scattered electrons does not change, the velocity distribution function must be of the form

$$f(v,\chi,\varphi) \to \delta(v-v_b)\widetilde{f}(\chi) \ , \tag{4.7}$$

where $\delta(x)$ is the Dirac delta-function. Substituting (4.7) into (4.6), one obtains

$$f(v,\chi,\phi) = \delta(v-v_b)\frac{m}{8\pi e\ln(1+w_{be})}\frac{1}{1+\dfrac{w_{be}}{2}(1-\cos\chi)} \ , \tag{4.8}$$

where w_{be} is the electron energy in electronvolts and $w_{be} = w_b/e$. If the beam is initially directed along the z axis, then in Cartesian coordinates the EVDF (4.8) is

$$f\left(\frac{v_x}{v_0},\frac{v_y}{v_0},\frac{v_z}{v_0}\right) = \frac{mv_0^2}{8\pi e\ln(1+w_{be})}\frac{\delta\left[\sqrt{\left(\dfrac{v_x}{v_0}\right)^2+\left(\dfrac{v_y}{v_0}\right)^2+\left(\dfrac{v_z}{v_0}\right)^2}-\dfrac{v_b}{v_0}\right]}{1+\dfrac{w_{be}}{2}\left(1-\dfrac{v_z/v_0}{v_b/v_0}\right)} \ . \tag{4.9}$$

Here v_0 is some scale velocity introduced to simplify comparison with the results of numerical simulations. The EVDF (4.9) is normalized as

$$\int_{-\infty}^{\infty} d\left(\frac{v_x}{v_0}\right)\int_{-\infty}^{\infty} d\left(\frac{v_y}{v_0}\right)\int_{-\infty}^{\infty} d\left(\frac{v_z}{v_0}\right) f\left(\frac{v_x}{v_0},\frac{v_y}{v_0},\frac{v_z}{v_0}\right) = 1 \ .$$

The distribution functions of the scattered electron beam over each velocity component are obtained from (4.9) as follows:

$$f_z\left(\frac{v_z}{v_0}\right) = \int_{-\infty}^{\infty} d\left(\frac{v_y}{v_0}\right) \int_{-\infty}^{\infty} d\left(\frac{v_x}{v_0}\right) f\left(\frac{v_x}{v_0}, \frac{v_y}{v_0}, \frac{v_z}{v_0}\right)$$
$$= \frac{1}{\ln\left(1+w_{be}\right)\left(\frac{v_b}{v_0}\frac{2+w_{be}}{w_{be}} - \frac{v_z}{v_0}\right)} \equiv f_{||}\left(\frac{v_z}{v_0}\right) \ , \tag{4.10}$$

$$f_y\left(\frac{v_y}{v_0}\right) = \int_{-\infty}^{\infty} d\left(\frac{v_z}{v_0}\right) \int_{-\infty}^{\infty} d\left(\frac{v_x}{v_0}\right) f\left(\frac{v_x}{v_0}, \frac{v_y}{v_0}, \frac{v_z}{v_0}\right)$$
$$= \frac{1}{\ln\left(1+w_{be}\right)\sqrt{\frac{4(v_b/v_0)^2}{w_{be}^2}(1+w_{be}) + \left(\frac{v_y}{v_0}\right)^2}} \equiv f_{\perp}\left(\frac{v_y}{v_0}\right) \ , \tag{4.11}$$

$$f_x\left(\frac{v_x}{v_0}\right) = \int_{-\infty}^{\infty} d\left(\frac{v_z}{v_0}\right) \int_{-\infty}^{\infty} d\left(\frac{v_y}{v_0}\right) f\left(\frac{v_x}{v_0}, \frac{v_y}{v_0}, \frac{v_z}{v_0}\right) = f_{\perp}\left(\frac{v_x}{v_0}\right) \ , \tag{4.12}$$

The PIC simulation is carried out with the electrons initially represented as a monoenergetic beam directed along the z axis, neglecting the ion dynamics and the electric and magnetic fields. These assumptions reproduce the conditions that resulted in EVDFs (4.10), (4.11) and (4.12). The simulation is run for only 6 timesteps. After each timestep, all particles are forced to perform elastic scattering without energy exchange, as above. The initial velocity distributions for the velocity components v_z and v_y are represented by narrow spikes 3 in Fig. 4.4. After the first scattering, the velocity distributions f_z and f_y (curve 2 in Fig. 4.4a and Fig. 4.4b, respectively) obtained in simulations exactly coincide with the theoretically obtained functions (4.10) and (4.11) (red markers in Fig. 4.4a and Fig. 4.4b, respectively). Note that after 6 collisions the velocity distribution became almost isotropic (see curve 3 in Fig. 4.4a and Fig. 4.4b). The velocity distributions of inelastic scattering (excitation and ionization) was tested in a similar way and showed good agreement between simulations and theory.

The null-collision algorithm (see flowchart in Fig. 3.7) must reproduce correct frequencies of multiple types of electron-neutral collisions (elastic, excitation, and ionization) in the wide range of electron collision energy. To test this algorithm, several sets of PIC simulations are carried out as follows. The initial plasma EVDF

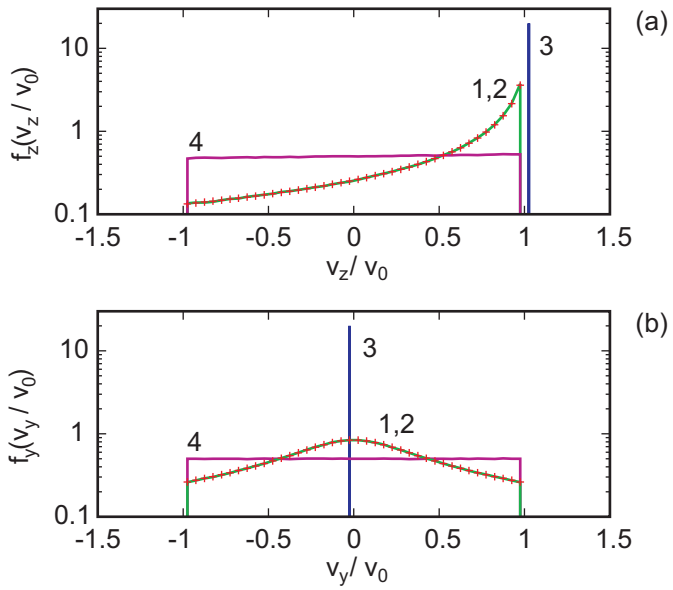

Figure 4.4: (a) The EVDFs over velocity component v_z parallel to the initial direction of beam velocity. (b) The EVDFs over velocity component v_y perpendicular to the initial direction of beam velocity. On both figures markers 1 (red) depict the theoretical EVDF of electrons scattered once; curve 2 (green) is the EVDF obtained in simulations after one scattering; curve 3 (blue) is the initial EVDF; curve 4 (magenta) is the EVDF after six scatterings.

corresponds to a monoenergetic electron beam of energy w_b, directed parallel to the walls, the ion dynamics and the electric and magnetic fields are neglected, the walls absorb particles. The non-zero density of neutral gas is the same for simulations of one set. Two values of neutral atom density are considered: $n_{a1} = 2 \cdot 10^{18}$ m^{-3} and $n_{a2} = 2 \cdot 10^{19}$ m^{-3}. The electron beam energy in one set of simulations is varied from 0.05 eV to 100 eV. The frequencies of the three types of electron-neutral collisions obtained for different electron energies are shown by markers in Fig. 4.5. The values of the frequencies calculated analytically for given electron energies with known cross section for xenon (see Fig. 3.8a) are represented by solid curves in Fig. 4.5, where curves 1 correspond to the lower neutral atom density and curves 2 correspond to the higher neutral atom density. There is good agreement between the frequencies obtained in simulations and the theoretically predicted frequencies for all types of collisions. Note that the drop of elastic collision frequency near 1 eV related to the Ramsauer minimum of cross section [127] is reproduced well (see Fig. 4.5a). For excitation and ionization collisions, the frequency of collisions in simulations is zero if the electron energy is below the corresponding threshold.

4.4 Coulomb collisions

The Langevin model of Coulomb collisions was benchmarked by comparing the results from EDIPIC with the similar simulation described in Ref. [112]. The test PIC simulation was carried out with periodic boundary conditions and strongly non-Maxwellian initial EVDF. The external electric and magnetic fields were set equal to zero. Collisions with neutral atoms were omitted. The initial EVDF is

$$f(v_x, v_y, v_z) = \frac{\Theta(v_x, -v_{0x}, v_{0x})\Theta(v_y, -v_{0y}, v_{0y})\Theta(v_z, -v_{0z}, v_{0z})}{8 v_{0x} v_{0y} v_{0z}} \,, \tag{4.13}$$

where $\Theta(x, a, b) = 1$ if $a < x < b$ and $\Theta(x, a, b) = 0$ otherwise. The electron density is $n_e = 10^{18}$ m^{-3}. In the test simulation, the EVDF (4.13) is characterized by the maximal energy of electron motion in the x, y, and z directions, $mv_{0x}^2/2 = 2$ eV and $mv_{0y,z}^2/2 = 4$ eV. The initial EVDFs are presented in Fig. 4.6b.

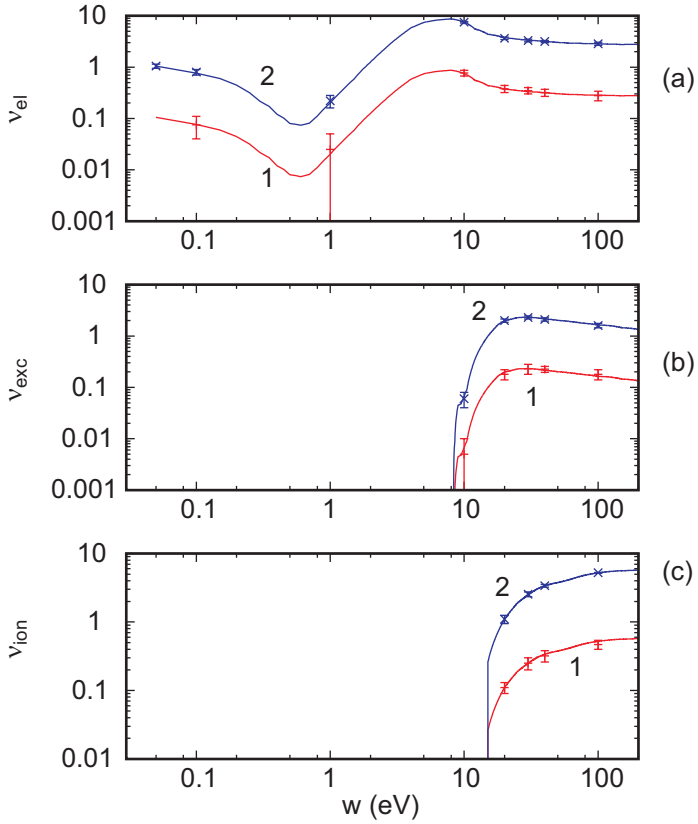

Figure 4.5: Frequencies of electron-neutral collisions versus energy of colliding electrons: (a) elastic, ν_{el}; (b) excitation, ν_{exc}; (c) ionization, ν_{ion}. Curves are calculated with the known values of the cross sections for xenon presented in Fig. 3.8a. Markers are the values determined in simulations with monoenergetic electrons. Everywhere in this figure red curves 1 and red markers correspond to the density of neutral atoms $n_{a1} = 2 \cdot 10^{18}$ m^{-3}, blue curves 2 and blue markers correspond to $n_{a2} = 2 \cdot 10^{19}$ m^{-3}.

The average energy of electron motion in the x direction $\langle w_x \rangle$ is defined as

$$\langle w_x \rangle = \int_{-\infty}^{\infty} dv_x \int_{-\infty}^{\infty} dv_y \int_{-\infty}^{\infty} dv_z \frac{m v_x^2}{2} f(v_x, v_y, v_z) \ .$$

The average energies of electron motion in the y direction $\langle w_y \rangle$ and z direction $\langle w_z \rangle$ are defined similarly. Also, define the average total energy $\langle w \rangle = \langle w_x \rangle + \langle w_y \rangle + \langle w_z \rangle$. For v_{0x} and $v_{0y,z}$ introduced above, one obtains $\langle w_x \rangle = 2/3$ eV, $\langle w_y \rangle = \langle w_z \rangle = 4/3$ eV, $\langle w \rangle = 10/3$ eV.

The Coulomb collisions drive the EVDF towards the isotropic Maxwellian EVDF, so that in the simulation $\langle w_x \rangle$ gradually increases and $\langle w_y \rangle$ and $\langle w_z \rangle$ gradually decrease, approaching the same value (see Fig. 4.6a). The EVDF with initial "rectangular" profiles (Fig. 4.6b) becomes the isotropic Maxwellian EVDF after 400 ns (Fig. 4.6c). The temperature of this Maxwellian EVDF is $T_M = 2.22$ eV $= 2\langle w \rangle/3$. The average total energy remains practically constant, $\langle w \rangle \approx 10/3$ eV, during the simulations, decreasing by less than 1% after 400 ns of evolution (more than $3.6 \cdot 10^5$ time steps). Note that in simulations of Hall thrusters, the plasma density is about 10 times smaller, and therefore, the effects of Coulomb collisions are much weaker.

The isotropization and the Maxwellization of the EVDF due to the Coulomb collisions are well seen on the phase plane $\{v_x, v_y\}$. Initially, all electrons are uniformly distributed inside the rectangle $-v_{x0} < v_x < v_{x0}$, $-v_{y0} < v_y < v_{y0}$ (see Fig. 4.6d). By the end of the simulation, the distribution took a clear isotropic circular shape (see Fig. 4.6e), with more particles in the center than in the outer regions.

Note that the transition from the non-Maxwellian anisotropic EVDF to the Maxwellian isotropic distribution was almost finished after about 150 ns, and during the rest of the time 150 ns $< t <$ 400 ns the evolution of the EVDF involved mostly the slow approach of the high energy tails to the Maxwellian EVDF. For comparison, in Ref. [112], the initial EVDF close to (4.13), with close electron energies and the same electron density, was turned into the isotropic Maxwellian EVDF after 200 ns, which is close to the value of 150 ns mentioned above. Some difference in the times may be attributed to the different initial EVDF in [112].[1] Thus, the

[1]The PIC code in Ref. [112] was developed for simulations of ECR discharges, the electrons were

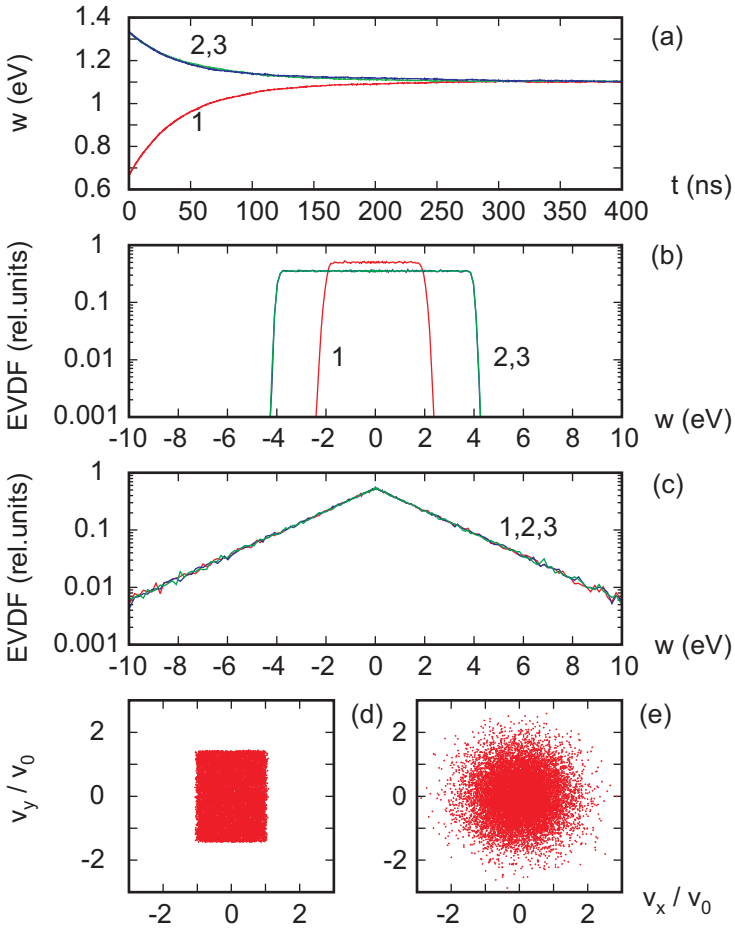

Figure 4.6: Effects of Coulomb collisions on a plasma with initially non-Maxwellian EVDF. (a) The average energies of electron motion along the x, y, and z directions versus time. (b) The initial distribution functions for velocity components, $t = 0$. (c) The distribution functions for velocity components at $t = 400$ ns. In (b) and (c) the distribution functions are plotted in energy coordinates, negative energy values correspond to propagation in negative direction. In (a), (b) and (c) curves 1, 2, and 3 correspond to the x, y, and z directions. (d) The phase plane $\{v_x, v_y\}$ at $t = 0$. (e) The phase plane $\{v_x, v_y\}$ at $t = 400$ ns.

Langevin model of Coulomb collisions implemented in the EDIPIC code qualitatively and quantitatively reproduces the modification of the EVDF due to electron-electron and electron-ion collisions.

4.5 Simulations of the sheath with a Maxwellian plasma source

The comprehensive verification of the EDIPIC code was performed by comparison with the results of sheath dynamics simulations carried out in Refs. [124, 125].

In Ref. [124], the region between a Maxwellian plasma source and an absorbing floating wall is considered analytically and simulated numerically. To reproduce the conditions of Ref. [124], the test simulations with EDIPIC were carried out as follows: (i) the boundary $x = 0$ was the Maxwellian plasma source as described below; (ii) the boundary $x = L$ was purely absorbing; (iii) all collisions between particles were omitted; (iv) no external fields were applied. The plasma slab width was $L = 22\lambda_D$, and the ratio of ion to electron mass was $M/m = 40$, the values of the ratio of ion to electron temperature in the plasma source was $T_i/T_e = 0.1$ or $T_i/T_e = 1$.

The Maxwellian plasma source at $x = 0$ performs injection as follows. First, every time a particle leaves the plasma slab through the source boundary, another particle of the same species is injected into the slab. Second, every time an ion is absorbed by the wall at $x = L$, one electron and one ion are injected. The velocity $v_{x\alpha}$ of a particle of species α emitted by the plasma source is determined as a solution of equation $R = \int_0^{v_{x\alpha}} dv S(v)$ with R the random number, $0 < R < 1$, and the following source function $S(v)$:

$$S(v) = \frac{mv}{T_\alpha} \exp\left(-\frac{mv^2}{2T_\alpha}\right) , \tag{4.14}$$

where $\alpha = e$ for electrons and $\alpha = i$ for ions. Injection with source function (4.14)

considered as firmly attached to the magnetic field lines, only the two electron velocity components were resolved – the one along the magnetic field and the other one perpendicular to the direction of the magnetic field. As a result, the non-Maxwellian EVDF tested in [112] corresponded to a cylinder in the velocity phase space, while the EVDF (4.13) corresponds to a parallelepiped.

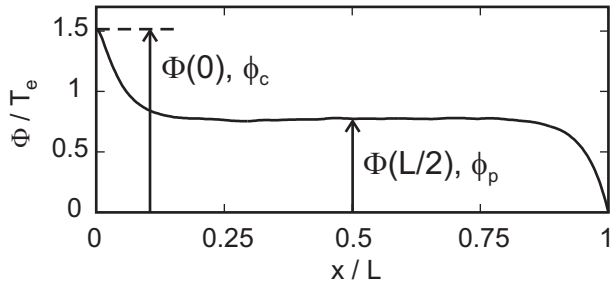

Figure 4.7: Profile of the potential obtained in simulation with EDIPIC code with Maxwellian plasma source and absorbing wall. $M/m = 40$, $T_i/T_e = 0.1$, $L = 22\lambda_D$.

Table 4.2: Comparison of the potential profile parameters calculated with the EDIPIC code [$\Phi(0)$, $\Phi(L/2)$] versus the results of Ref. [118] (ϕ_c, ϕ_p).

	$\frac{\Phi(0)}{T_e}$	$\frac{\phi_c}{T_e}$	$\frac{\Phi(0)-\phi_c}{\phi_c}$	$\frac{\Phi(L/2)}{T_e}$	$\frac{\phi_p}{T_e}$	$\frac{\Phi(L/2)-\phi_p}{\phi_p}$
$T_i/T_e = 0.1$	1.525	1.5	+1.7 %	0.775	0.75	+3.3 %
$T_i/T_e = 1$	1.025	1.0	+2.5 %	0.763	0.75	+1.7 %

produces a half-Maxwellian distribution in a field-free region [128]. Note that simulations described in this Section are one-dimensional both in the configurational and in the velocity space: velocity components v_y and v_z are omitted for all particles.

At the quasi-stationary stage of the test simulation, the plasma potential profile consists of a monotonic drop in potential in the narrow "source sheath" adjacent to the Maxwellian plasma source $x = 0$, a wide region with constant potential, and a monotonic drop of potential in the "collector sheath" adjacent to the absorbing wall $x = L$ (see Fig. 4.7). This qualitative picture agrees with the potential profiles presented in Fig. 6 of Ref. [124]. The potential profile in simulations with EDIPIC is characterized by the values of the potential at the plasma source boundary $\Phi(0)$ and in the midplane $\Phi(L/2)$. In Ref. [124], these parameters are denoted by ϕ_c and ϕ_p, respectively.

Parameters of the potential profile established in the two test simulations with an absorbing wall are presented in Table 4.2. Note that the relative difference between

the values obtained with the EDIPIC code and the values presented in Ref. [124] does not exceed 3.3 %.

In Ref. [125], the region between the Maxwellian plasma source and the wall, which emits secondary electrons, is considered. The secondary emission coefficient is constant and secondary electrons are emitted with a half-Maxwellian distribution of temperature T_2. It is assumed that secondary electrons, if they return to the wall, do not create further secondary electrons, but only decrease the wall surface charge.

In order to reproduce the conditions of Ref. [125] in test simulations, the following adjustments were made:

- The Maxwellian plasma source was introduced at $x = 0$.
- The electron collisions were turned off.
- The elastic and inelastic reflections at the wall were turned off.
- The emission coefficient of the true secondary component γ_t was set equal to a non-zero constant γ_p if the energy of a primary electron at the wall exceeds a threshold value $w_{t,0}$, and zero otherwise.
- The secondary electrons were emitted perpendicular to the wall with the velocities corresponding to a half-Maxwellian distribution with temperature T_2.
- The emission threshold energy was chosen as $w_{t,0} = 10 \times T_2$, this guaranteed that the secondary electrons reflected back to the wall by the nonmonotonic potential in the sheath do not produce secondary emission themselves.
- No external fields were applied.

The test simulations with the EDIPIC code were carried out with $L = 22\lambda_D$, $M/m = 40$, $T_i/T_e = 1$, and $T_2/T_e = 0.01$. The constant secondary emission coefficient was either $\gamma_p = 0.3$ or $\gamma_p = 1.5$. Note that the plasma parameters are the same as in one of test simulations with an absorbing wall considered above (see the last line in Table 4.2).

Table 4.3: Comparison of the potential profile parameters calculated with the EDIPIC code [$\Phi(0)$, $\Phi(L/2)$, and Φ_w] versus the results of Ref. [119] (ϕ_c, ϕ_p, and $\Delta\phi$).

	$\frac{\Phi(0)}{T_e}$	$\frac{\phi_c}{T_e}$	$\frac{\Phi(0)-\phi_c}{\Phi_c}$	$\frac{\Phi(L/2)}{T_e}$	$\frac{\phi_p}{T_e}$	$\frac{\Phi(L/2)-\phi_p}{\phi_p}$
$\gamma = 0.3$	0.668	0.7	-4.6 %	0.383	0.4	-4.3 %
$\gamma = 1.5$	0.575	0.59	-2.5 %	0.283	0.27	+4.8 %

	$\frac{\Phi_w}{T_e}$	$\frac{\Delta\phi}{T_e}$	$\frac{\Phi_w-\Delta\phi}{\Delta\phi}$
$\gamma = 0.3$	n/a	n/a	n/a
$\gamma = 1.5$	0.01775	0.017	+4.4 %

After the stationary stage was established in the simulation with $\gamma = 0.3$, the potential profile was qualitatively similar to the case with an absorbing wall, but the drop of potential across the plasma significantly decreased. In the simulation with $\gamma = 1.5$ the secondary emission is in the SCL regime and the stationary plasma potential profile is nonmonotonic near the emitting wall (see Fig. 4.8). The potential profiles in the test simulations are similar qualitatively to the profiles presented in Fig. 9 of [125].

The nonmonotonic potential profile in the test simulation with high γ_p has the same characteristics as above (see Fig. 4.8a), and one additional characteristic – the depth of the potential well near the emitting wall Φ_w. The corresponding value from Ref. [125] is denoted as $\Delta\phi$ (see Fig. 4.8b).

The parameters of the potential profile obtained in the test simulations with constant SEE are presented in Table 4.3. The maximum relative difference between the potential profiles of the test simulations and of Ref. [125] does not exceed 4.8%. The tests of the EDIPIC code carried out with a Maxwellian plasma source show overall good agreement with the available numerical results.

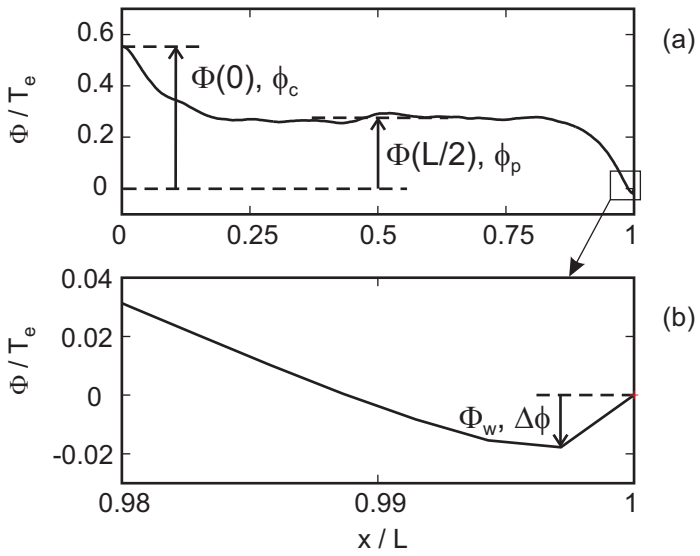

Figure 4.8: Profiles of potential obtained in simulation with EDIPIC code with a Maxwellian plasma source and the emitting wall: the general shape (a) and the enlarged potential well in the sheath adjacent to the wall $x = L$ (b). $M/m = 40$, $T_i/T_e = 1$, $L = 22\lambda_D$, $\gamma_p = 1.5$, $T_2/T_e = 0.01$.

4.6 Instability of a low density cold electron beam in a cold plasma

The beam-plasma instability has been studied extensively since 1949, when it was theoretically predicted independently by Akhiezer, Fainberg [129] and Bohm, Gross [130] (see, *e.g.*, numerous references in the review [131]). The first applications of numerical methods to the solution of this problem were made in the mid 60's [132]. PIC methods have been applied to the study of this instability since the early 70's [133]. Simulation of the beam-plasma instability is considered to be an important benchmark for PIC codes [10].

Consider a one-dimensional cold electron plasma of density n_p with a monoenergetic electron beam of density n_b, $n_b \ll n_p$, and velocity v_b. Oscillations in such a system are described by the dispersion equation [134]

$$1 - \frac{\omega_{pe}^2}{\omega^2} - \frac{\alpha\omega_{pe}^2}{(\omega - kv_b)^2} = 0 \ , \tag{4.15}$$

where k is the wave number parallel to the direction of beam propagation, α is the relative beam density, $\alpha = n_b/n_p \ll 1$. Oscillations with $\omega \simeq kv_b$ are unstable if $k < (\omega_{pe}/v_b)(1+\alpha^{1/3})^{3/2}$. At the linear stage of instability, the beam electrons group in bunches and transfer their energy to the wave, causing the wave amplitude to grow exponentially. At the nonlinear stage [126, 135], the beam particles are trapped in the potential well of the excited wave and oscillate with frequency

$$\Omega \simeq \omega_{pe}\alpha^{1/3}. \tag{4.16}$$

Test simulations of the electron beam instability were carried out with the EDIPIC code with periodic boundary conditions. Initially all plasma (background) electrons had zero velocity, relative density of the beam was $\alpha = 0.001$, the initial beam energy was $w_b = 40$ eV, the beam velocity was $v_b = 3.75 \times 10^6$ m/s, and the plasma density was $n_p = 10^{17}$ m^{-3}. The wave number k of the excited oscillations was determined by the length of the system L as $k = 2\pi/L$.

In simulations, both the linear stage of the beam-plasma instability, with the exponential growth of the wave amplitude, and the subsequent non-linear stage, with the slowly oscillating wave amplitude, have been observed (see Fig. 4.9a). Consider the potential perturbation in the form $\Phi(t,x) = \Phi_A(t)\sin(kx - \mathrm{Re}\ \omega t)$, where $\Phi_A(t)$ is the amplitude. At the linear stage, $\Phi_A(t) \sim \exp(\mathrm{Im}\ \omega t)$, where Im ω is the increment of oscillations, which can be calculated by

$$\mathrm{Im}\ \omega = \left[\frac{d}{dt}\ln\Phi_A(t)\right]^{-1}.$$

The frequencies and increments of the linear instability obtained in the simulations and calculated from Eq. (4.15) for different wave numbers k are presented in Fig. 4.9b. There is very good agreement between the values obtained in the simulations (the red and blue markers in Fig. 4.9b corresponding to Re ω and Im ω) and the exact solutions (complex roots) of Eq. (4.15) (curve 1 for Re ω and curve 2 for Im ω in Fig. 4.9b).

It is instructive to compare the nonlinear stage of the instability of a cold beam with $\alpha = 0.001$ and $kv_b/\omega_{pe} = 1.0053$ observed in the EDIPIC simulation (see

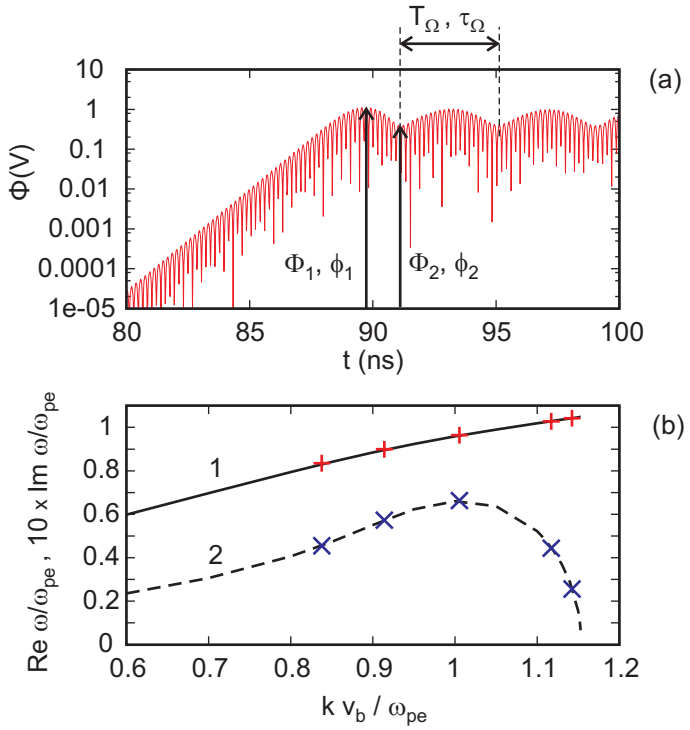

Figure 4.9: Simulations of the instability of a low density, $n_b/n_p = 0.001$, cold electron beam in a cold plasma. (a) Perturbation of the potential versus time for $kv_b/\omega_{pe} = 1.0053$. (b) The theoretical values of frequency (curve 1) and increment (curve 2) of the unstable branch of oscillations versus the wave number; the red vertical crosses and the blue diagonal crosses mark the values of frequency and increment, respectively, obtained in PIC simulations.

Table 4.4: Comparison of the parameters of the nonlinear stage of instability of a low density cold electron beam in a cold plasma obtained with the EDIPIC code (Φ_1, Φ_2, and T_Ω) versus the results of Ref. [120] (ϕ_1, ϕ_2, and τ_Ω).

Φ_1 [V]	ϕ_1 [V]	$\frac{\Phi_1 - \phi_1}{\phi_1}$	Φ_2 [V]	ϕ_2 [V]	$\frac{\Phi_2 - \phi_2}{\phi_2}$	T_Ω [ns]	τ_Ω [ns]	$\frac{T_\Omega - \tau_\Omega}{\tau_\Omega}$
1.1	1.2	-8.3 %	0.4	0.4	0.0 %	4.1	3.8	+7.9 %

Fig. 4.9a) and the nonlinear stage of the instability of the beam with the same density and $kv_b/\omega_{pe} = 1.0$ described in Ref. [126]. It is found numerically in Ref. [126] that at the nonlinear stage the value of the wave amplitude in the first maximum ϕ_1 is

$$\phi_1 \approx \frac{1.5}{k} \left(4\pi n_p m v_b^2 \alpha^{4/3}\right)_{CGS}^{1/2} , \tag{4.17}$$

and the value of the wave amplitude in the first minimum ϕ_2 is

$$\phi_2 \approx \frac{0.5}{k} \left(4\pi n_p m v_b^2 \alpha^{4/3}\right)_{CGS}^{1/2} . \tag{4.18}$$

Eqs. (4.17) and (4.18) are presented in CGS units, as in the original paper [126]. The period of oscillation of the wave amplitude obtained in Ref. [126] is

$$\tau_\Omega \approx \frac{6.7}{\omega_{pe}\alpha^{1/3}} , \tag{4.19}$$

which is close to the value estimated by Eq. (4.16). For the purpose of comparison, the values of ϕ_1, ϕ_2, and τ_Ω were calculated by Eqs. (4.17-4.19) with the values of n_p, v_b, and α used in the test PIC simulation. The calculated values are presented in Table 4.4 and compared with the corresponding values Φ_1, Φ_2, and T_Ω obtained directly from the PIC simulation. Note that the difference between the values of [126] and the values obtained with EDIPIC does not exceed 8.3% and is within the measurement error.[2]

[2]The parameters of the nonlinear stage of instability described in [126] had to be copied from the figure with relatively low resolution (Fig. 1 of [126]).

4.7 Summary

The EDIPIC code has been extensively tested. The two-particle test showed the correct motion of particles and solution of Poisson's equation and demonstrated very good energy conservation. The test of the probabilistic SEE model confirmed that the three components of the SEE are emitted with the correct intensities for various energies and angles of incidence of primary electrons. The test of the Monte-Carlo model of collisions demonstrated (i) that the velocity distribution of scattered particles corresponds to the selected differential cross section, and (ii) that the collisions occur with the correct frequencies in a wide range of the colliding particle energy. The Langevin model of Coulomb collisions ensured that the "rectangular" non-Maxwellian EVDF transforms into the isotropic Maxwellian EVDF within the correct time interval and with good energy conservation. The comprehensive tests included the simulation of the sheath formation with a Maxwellian plasma source and the simulation of the instability of a cold low density electron beam in a cold plasma. All test simulations demonstrated the good agreement with the available analytical and numerical results, therefore, the overall validity of the EDIPIC code is confirmed.

Chapter 5

Electron velocity distribution function in Hall thruster plasmas

The flux of electrons leaving a plasma through the sheath at the wall is determined by the EVDF of the plasma and by the potential barrier formed in the sheath region. The EVDF in low pressure discharges is often far from Maxwellian [4, 5, 6, 7, 46, 85]. However, for the sake of simplicity, in the analytical models of Hall thrusters, the EVDF is often approximated as a Maxwellian, which may give rise to misleading results.

The walls of a Hall thruster channel emit secondary electrons. For a Maxwellian plasma bounded by the wall with SEE, the flux of electrons leaving the plasma at the wall grows considerably with the increase of the electron temperature [75]. The energetic plasma electrons are intensively replaced by the relatively cold secondary electrons, which is an important factor that limits the electron temperature. The fluid theories of a Hall thruster based on the assumption that the EVDF is Maxwellian [69, 76, 81, 82] predict fast electron cooling due to wall losses and saturation of the electron temperature with the growth of discharge voltage. However, in experiments [78, 79] the electron temperature inside the thruster channel (about 40 eV) was several times higher than the maximum value for the electron temperature (18 eV) predicted by some fluid theories [76]. Therefore, the intensity of wall losses in Hall thrusters is lower than it is expected for a Maxwellian plasma.

Kinetic studies of plasmas in Hall thrusters [87] reveal a depletion of the high energy tail of the EVDF and a reduction of the electron losses to the wall compared to the fluid theories. Such depletion is well known for other types of discharges [3, 5].

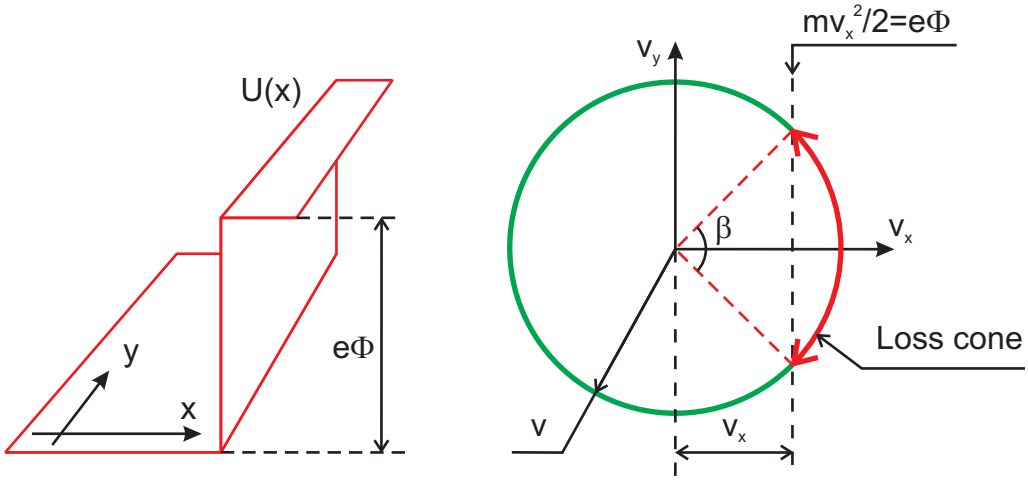

Figure 5.1: The potential barrier $U(x)$ in the two-dimensional configuration space (x,y) (left) and the circle in the corresponding two-dimensional velocity space (v_x,v_y) for particles with energy $w = m(v_x^2 + v_y^2)/2 > e\Phi$. The red section of the circle is the loss cone (right).

It was shown in Ref. [5] for ECR discharges that the EVDF near a wall is far from Maxwellian and is strongly anisotropic in the loss cone. Here the loss cone is defined as follows. Electrons with a given kinetic energy w form a spherical shell in velocity phase space (see Fig. 5.1 for the two-dimensional case). If $w > e\Phi$, where Φ is the plasma potential relative to the wall, then some of these electrons have an energy of motion normal to the wall w_x sufficient to leave the system, $w_x > e\Phi$. In the velocity phase space the vectors of velocities of these electrons are inside the cone with the opening angle $\beta = 2\cos^{-1}(\sqrt{e\Phi/w})$. Note that β depends on the energy w. This cone is called the loss cone.

The EDIPIC code described in Chapter 3 has been applied to simulations of plasmas in the accelerating region of a Hall thruster in the plane geometry approximation. The PIC simulations carried out reveal that there is an essential deviation of the EVDF from the Maxwellian EVDF and, as a result, the plasma-wall interaction in a Hall thruster is different from that of a plasma with a Maxwellian EVDF. The present Chapter contains the analysis of the EVDF in Hall thrusters based on the results of the PIC simulations.

This Chapter is organized as follows. In Section 5.1, the properties of the non-Maxwellian EVDF are described, the reasons for the strong anisotropy and the depletion in the loss cone are discussed, the simulation data are collected in Table 5.1. In Section 5.2, the effects of Coulomb collisions on the EVDF in Hall thruster are described, the corresponding simulation data are collected in Table 5.2. Section 5.3 contains the derivation of the electron wall fluxes, plasma potential, and emission coefficient for an isotropic Maxwellian plasma bounded by the wall with SEE in the SCL regime. The results of Hall thruster simulations are compared with the corresponding properties of Maxwellian plasmas. The major conclusions are given in the Summary Section.

5.1 Properties of the EVDF

5.1.1 Initial parameters of simulations

The initial parameters of Hall thruster simulations described in this Section are presented in Table 5.1. For all simulations, the width of the plasma slab is $L = 2.5$ cm and the neutral gas density is $n_a = 2 \cdot 10^{12}\text{cm}^{-3}$. In simulations 1 and 2, the axial electric field E_z, the radial magnetic field B_x, and the frequency of "turbulent" collisions ν_t correspond to the parameters of the 2 kW Hall thruster at discharge voltages $U_d = 300$ V and $U_d = 350$ V [80], respectively. In these simulations, the values of E_z and B_x were taken at the point of maximal electron temperature, which is inside the thruster channel for the considered discharge voltages. The value of ν_t was estimated by Eq. (3.33), as it is described in Section 3.5.5, without the correction due to the electron-wall collisions. The initial EVDF in simulations 1 and 2 is isotropic Maxwellian with temperatures 46 eV and 53 eV, respectively, these values are the experimentally measured maximal electron temperatures in the 2 kW Hall thruster for $U_d = 300$ V and $U_d = 350$ V [80]. Simulations 3 and 4 are carried out without "turbulent" collisions in order to study the effect of the axial electric field on the EVDF. In these simulations, the initial EVDF is a drifting isotropic Maxwellian

Table 5.1: Initial parameters (constant) and results of Hall thruster simulations with EDIPIC code. Coulomb collisions are omitted. The common parameters are $L = 2.5$ cm and $n_a = 2 \cdot 10^{12}\text{cm}^{-3}$.

Number	1	2	3	4
E_z , [V/cm]	52	200	200	40
B_x , [G]	91	100	100	100
$\langle w_y \rangle$, [eV]	15.3	35.9	22.2	2.6
$\langle w_z \rangle$, [eV]	14.4	24.5	10.8	2.15
$\langle w_x \rangle$, [eV]	4.1	5.75	4.8	1.32
$\widetilde{T}_z$, [eV]	20.1	35.7	22.7	4.2
$\widetilde{T}_x$, [eV]	10.1	12.3	11.8	3.9
Φ_p , [V]	23	22	20	6.2
$\langle \nu_{en} \rangle$, [10^6 s^{-1}]	1.4	1.4	1.4	0.95
ν_t , [10^6 s^{-1}]	7.81	1.46	0	0
$\overline{n}_e$, [10^{11} cm^{-3}]	1.6	3.2	2.0	0.53
γ	0.72	0.97	0.967	0.45
Γ_{1p} , [10^{21} m^{-2}s^{-1}]	0.35	3	1.4	0.09
Γ_1 , [10^{21} m^{-2}s^{-1}]	0.89	20	10.3	0.15

with temperature 10 eV and E_z/B_x drift velocity in the y direction.[1] Since Coulomb collisions are typically considered negligible for plasmas of Hall thrusters [136], in simulations described in this Section the electron-electron and electron-ion collisions were omitted. Other parameters of simulations are given in Table B.1 of Appendix B.

In Table 5.1, the emission coefficient γ, the total primary electron flux Γ_1 and the primary electron flux due to plasma bulk particles Γ_{1p} (see below) are calculated at the wall $x = L$; $\Phi_p = \Phi(L/2)$.

[1]It has been found that such initial EVDF essentially reduces the duration of the transitional period in simulations.

5.1.2 Anisotropy of the electron temperature

The simulations reveal that the average energy of electron motion along the accelerating electric field $\langle w_z \rangle = \langle m v_z^2/2 \rangle$ is several times larger than the average energy of electron motion normal to the walls $\langle w_x \rangle = \langle m v_x^2/2 \rangle$ (see Table 5.1), where averaging $\langle ... \rangle$ is done over all electrons. The average energy of electron motion in the y direction $\langle w_y \rangle = \langle m v_y^2/2 \rangle$ exceeds $\langle w_z \rangle$ by the value related to the $E \times B$ drift motion, $\langle w_y \rangle = \langle w_z \rangle + m V_{dr}^2/2$, where $V_{dr} = E_z/B_x$ is the drift velocity. Thus, the EVDF is strongly anisotropic. Regardless of the $E \times B$ drift, the difference between velocity distributions over v_z and v_y is minor and only the EVDFs for v_x and v_z are discussed below.

Qualitatively, the anisotropy of the EVDF can be explained as follows. The electrons gain their energy from the accelerating electric field E_z as a result of random "turbulent" collisions and collisions with neutral atoms over the period of cyclotron rotation *after* the scattering occurred. The field E_z directly affects only the z-velocity and, therefore, modifies the energy w_z of an electron. However, the cyclotron rotation distributes this energy between the y and z degrees of freedom. As a result, the heating occurs in the direction parallel to the walls (independent of the particular choice of this direction in the $E \times B$ drift frame), while the electron-neutral collisions drive the electron distribution function towards the isotropic EVDF [137]. If the frequency of "turbulent" collisions is much higher than the frequency of collisions with atoms

$$\nu_t \gg \nu_{en} \ , \tag{5.1}$$

the electrons gain kinetic energy parallel to the walls much faster than this energy is transferred by electron-neutral collisions to the motion normal to the walls, resulting in an anisotropic EVDF [5, 138]. Case 1 in Table 5.1 is characterized by a dominating turbulent conductivity (5.1), which corresponds to the low voltage regime of thruster operation [80]. The EVDF in this case is presented in Figs. 5.2 and 5.3. In different energy regions, the EVDF may be approximated by a Maxwellian EVDF with the corresponding temperature. For instance, the EVDF over normal velocity $f_x(v_x)$

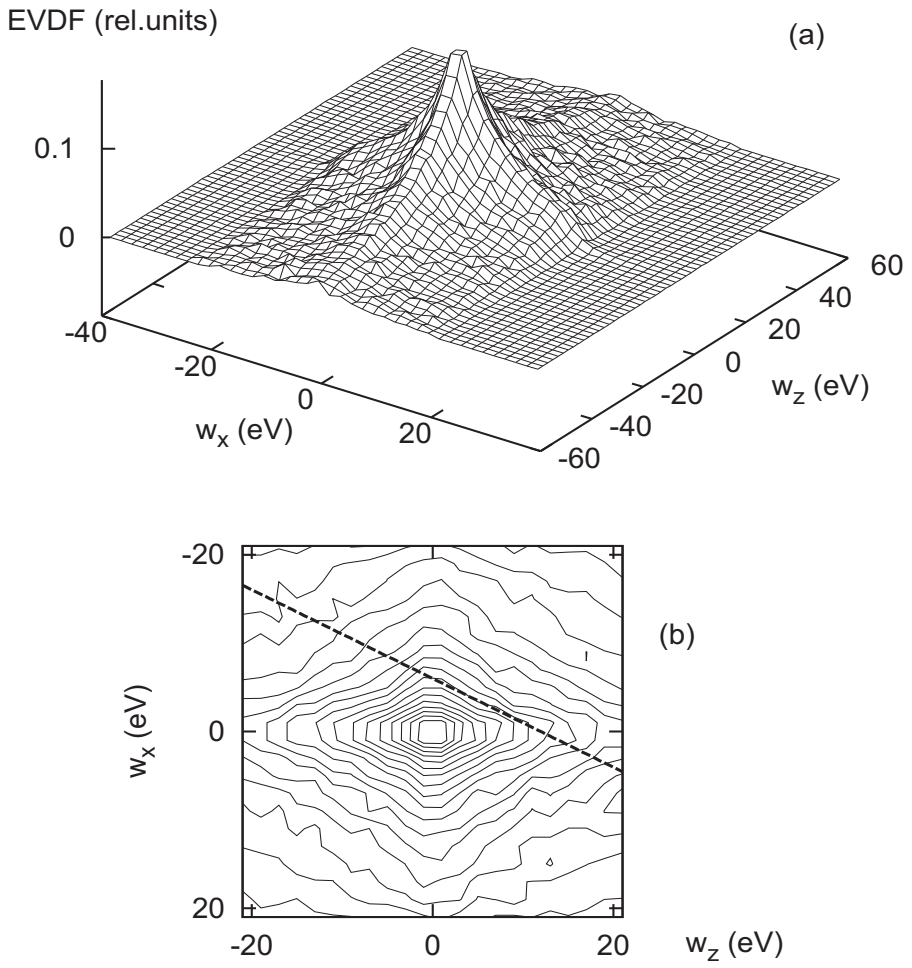

Figure 5.2: For simulation 1 from Table 5.1, the electron velocity distribution over v_x and v_z in the middle of the plasma 10 mm $< x <$ 15 mm plotted in energy coordinates (negative energy values correspond to propagation in the negative direction): (a) the 3D-plot, and (b) the corresponding contour plot of the low energy region $|w_{x,z}| < 20$ eV. Any two neighboring contour lines in (b) have a level difference of 0.01. The plasma potential relative to the wall is $\Phi_p = 23$ V. The dashed bold line in figure (b) is $w_x = w_z \widetilde{T}_x / \widetilde{T}_z + const$.

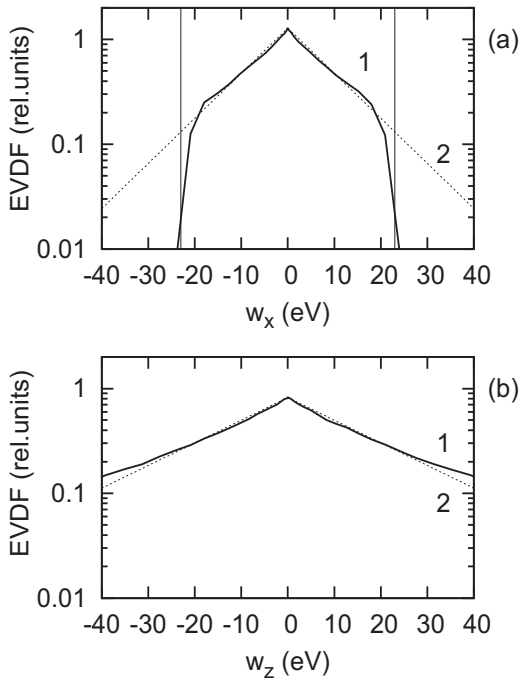

Figure 5.3: For simulation 1 from Table 5.1, the EVDF over v_x (a) and v_z (b) in the middle of the plasma 10 mm $< x <$ 15 mm plotted versus energy (negative energy values correspond to propagation in the negative direction). Curve 1 is the plasma EVDF in simulations. In (a), the two symmetric vertical lines mark the confinement threshold energy $w_x = e\Phi_p$ and straight line 2 has a slope corresponding to $\widetilde{T}_x = 10.1$ eV. In (b), straight line 2 has a slope corresponding to $\widetilde{T}_z = 20.1$ eV.

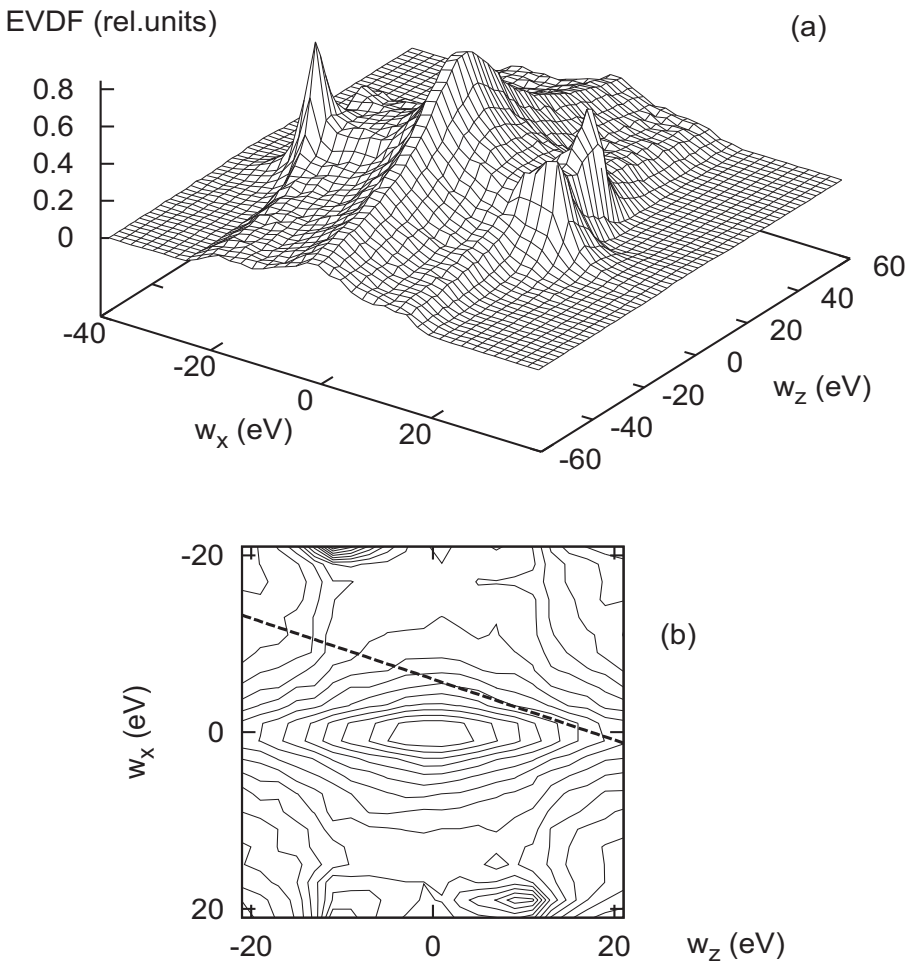

Figure 5.4: For simulation 2 from Table 5.1, the electron velocity distribution over v_x and v_z in the middle of the plasma 10 mm $< x <$ 15 mm plotted in energy coordinates (negative energy values correspond to propagation in the negative direction): (a) the 3D-plot, and (b) the corresponding contour plot of the low energy region $|w_{x,z}| < 20$ eV. Any two neighboring contour lines in (b) have a level difference of 0.05. The plasma potential relative to the wall is $\Phi_p = 22$ V. The dashed bold line in (b) is $w_x = w_z \widetilde{T}_x / \widetilde{T}_z + const$.

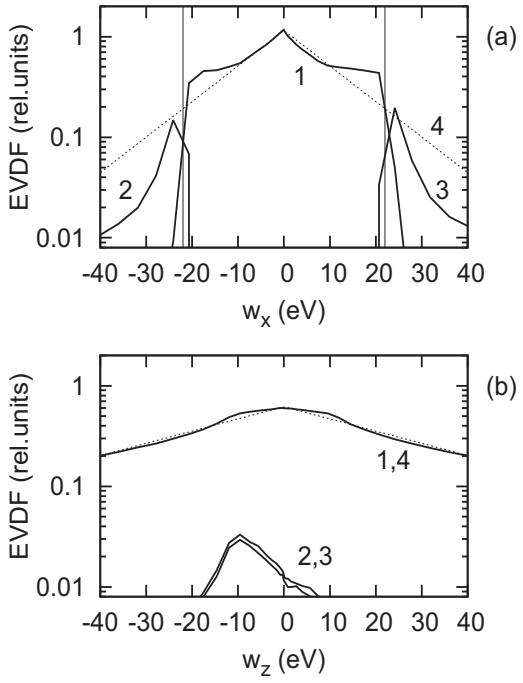

Figure 5.5: For simulation 2 from Table 5.1, the EVDF over v_x (a) and v_z (b) in the middle of the plasma 10 mm $< x <$ 15 mm plotted versus energy (negative energy values correspond to propagation in the negative direction). Curve 1 corresponds to the bulk electrons; curve 2 to the electron beam emitted from the wall $x = L$; curve 3 to the electron beam emitted from the wall $x = 0$. In (a), the two symmetric vertical lines mark the confinement threshold energy $w_x = e\Phi_p$, straight line 4 has a slope corresponding to $\widetilde{T}_x = 12.3$ eV. In (b), straight line 4 has a slope corresponding to $\widetilde{T}_z = 35.7$ eV.

obtained by averaging the three-dimensional EVDF $f(v_x, v_y, v_z)$ is characterized by the effective "normal" temperature T_x defined as

$$T_x(w_x) = -\left[\frac{\partial \ln f_x(v_x)}{\partial w_x}\right]^{-1} , \tag{5.2}$$

where $f_x(v_x) = \int_{-\infty}^{\infty}\int_{-\infty}^{\infty} dv_y dv_z f(v_x, v_y, v_z)$. If f_x is not a Maxwellian EVDF, the temperature T_x is a function of the normal energy w_x. It is instructive to introduce the average temperature as follows:

$$\frac{1}{\widetilde{T}_x} = \frac{\int_0^{\widetilde{w}_x} dw_x \dfrac{1}{T_x(w_x)}}{\int_0^{\widetilde{w}_x} dw_x} , \tag{5.3}$$

where the upper integration limit $\widetilde{w}_x$ is chosen such that $f_x(\sqrt{2\widetilde{w}_x/m})$ is e times less than the maximum $f_x(0)$, here $e = 2.71828\ldots$. Integration of (5.3) with (5.2) gives

$$\widetilde{T}_x = \widetilde{w}_x \ .$$

Similarly, the effective average temperature in the z direction $\widetilde{T}_z$ may be introduced as the energy value at which the EVDF over the z-velocity

$$f_z(v_z) = \int_{-\infty}^{\infty}\int_{-\infty}^{\infty} dv_y dv_z f(v_x, v_y, v_z)$$

is e times less than its maximum value, here $e = 2.71828\ldots$.

The ratio between the average temperatures $\widetilde{T}_x$ and $\widetilde{T}_z$ is a better characteristic of the EVDF anisotropy than the ratio of the average energies $\langle w_x \rangle$ and $\langle w_z \rangle$, (see the description of case 4 below). For a two-dimensional EVDF $f_{xz}(v_x, v_z) = \int_{-\infty}^{\infty} dv_y f(v_x, v_y, v_z)$, the contour lines $f_{xz}(v_x, v_z) = const$ form rhombic structures if the EVDF is Maxwellian, with the ratio of the rhombus diagonals equal to the ratio of temperatures. The contour lines of the two-dimensional EVDF obtained in simulations (*e.g.*, Fig. 5.2b) are similar to rhombi; the linear graph $w_x = w_z\widetilde{T}_x/\widetilde{T}_z + const$ is parallel to the EVDF contour lines in one quadrant of Fig. 5.2b. The smaller the slope of the linear graph – the stronger the anisotropy. The difference from the

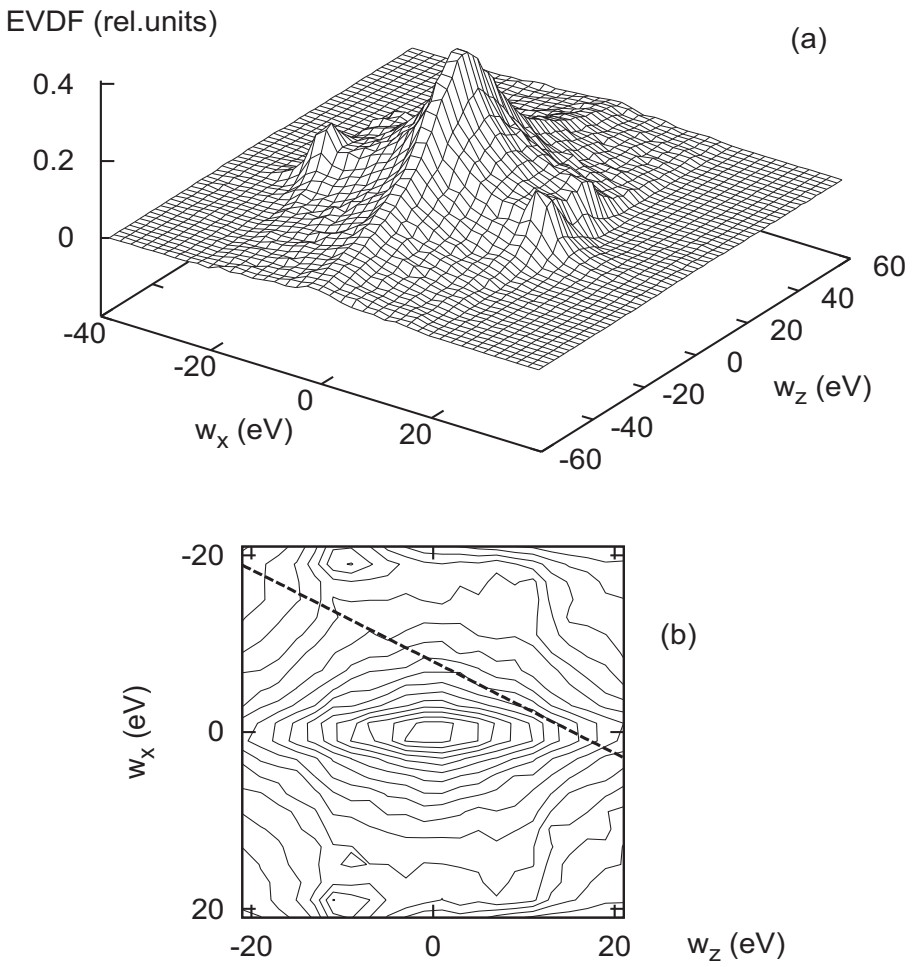

Figure 5.6: For simulation 3 from Table 5.1, the electron velocity distribution over v_x and v_z in the middle of the plasma 10 mm $< x <$ 15 mm plotted in energy coordinates (negative energy values correspond to propagation in the negative direction): (a) the 3D-plot, and (b) the corresponding contour plot of the low energy region $|w_{x,z}| < 20$ eV. Any two neighboring contour lines in (b) have a level difference of 0.025. The plasma potential relative to the wall is $\Phi_p = 20$ V. The dashed bold line in (b) is $w_x = w_z \widetilde{T}_x / \widetilde{T}_z + const.$

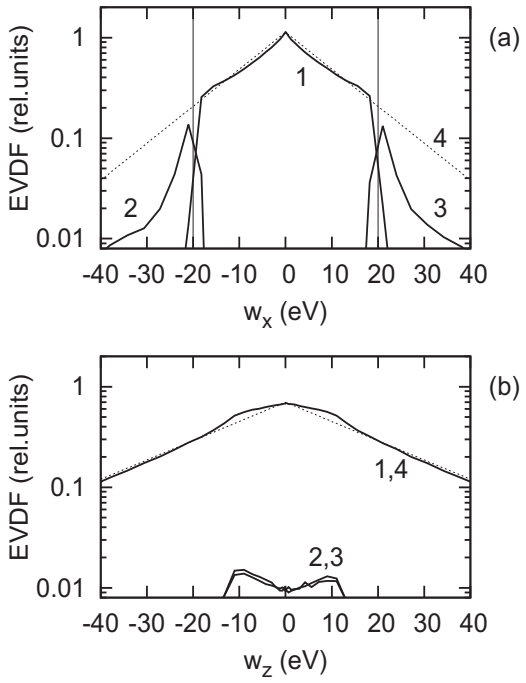

Figure 5.7: For simulation 3 from Table 5.1, the EVDF over v_x (a) and v_z (b) in the middle of the plasma 10 mm $< x <$ 15 mm plotted versus energy (negative energy values correspond to propagation in the negative direction). Curve 1 corresponds to the bulk electrons; curve 2 to the electron beam emitted from the wall $x = L$; curve 3 to the electron beam emitted from the wall $x = 0$. In (a), the two symmetric vertical lines mark the confinement threshold energy $w_x = e\Phi_p$, straight line 4 has a slope corresponding to $\widetilde{T}_x = 11.8$ eV. In (b), straight line 4 has a slope corresponding to $\widetilde{T}_z = 22.7$ eV.

rhombic shape is due to the finite number of velocity boxes used to calculate the EVDF during simulations.

For high discharge voltages, the difference between the classical and the anomalous axial electron mobility decreases so that $\nu_t \sim \nu_{en}$ [79]. In this case, anisotropy may develop if the axial electric field E_z satisfies the criterion

$$eE_z r_L > e\Phi_p \ , \tag{5.4}$$

where r_L is the electron Larmor radius, $\Phi_p = \Phi(L/2)$. If criterion (5.4) is satisfied, the first collision of a low energy electron $mv^2/2 < e\Phi_p$ provides the electron with a significant energy of motion parallel to the walls $\Delta w > e\Phi$, therefore the subsequent electron-neutral collision may scatter this electron into the loss cone and the isotropization does not occur. The corresponding simulation is number 2 in Table 5.1. The 3D-plot of the anisotropic EVDF of such a low-collisional plasma is presented in Fig. 5.4.

In fact, if criterion (5.4) is satisfied, the anisotropy develops even in the absence of "turbulent" collisions, as it is proved by simulation 3 (see Table 5.1 and Fig. 5.6 with Fig. 5.7). Note that the anisotropy decreased compared to the case 2, where the turbulent collision frequency was non-zero (compare the slopes of the bold dashed lines in Fig. 5.4b and Fig. 5.6b).

When criteria (5.1) and (5.2) are not satisfied, the anisotropy practically disappears, see simulation 4 in Table 5.1. The difference in the average energies $\langle w_x \rangle$ and $\langle w_z \rangle$ (see Table 5.1) is determined mostly by the strong depletion of the EVDF over v_x in the loss cone (see Fig. 5.8a and Fig. 5.9a). At the same time, for energies below the plasma potential $w_{x,z} < e\Phi$, the distributions over normal velocity v_x and parallel velocity v_z are characterized by very close values of the effective temperatures $\widetilde{T}_x \simeq \widetilde{T}_z$.

5.1.3 Depletion of the loss cone

The EVDFs of all simulations in Table 5.1 exhibit strong depletion in the region with $w_x > e\Phi_p$, *i.e.*, in the loss cone [3]. This occurs because the MFP between two

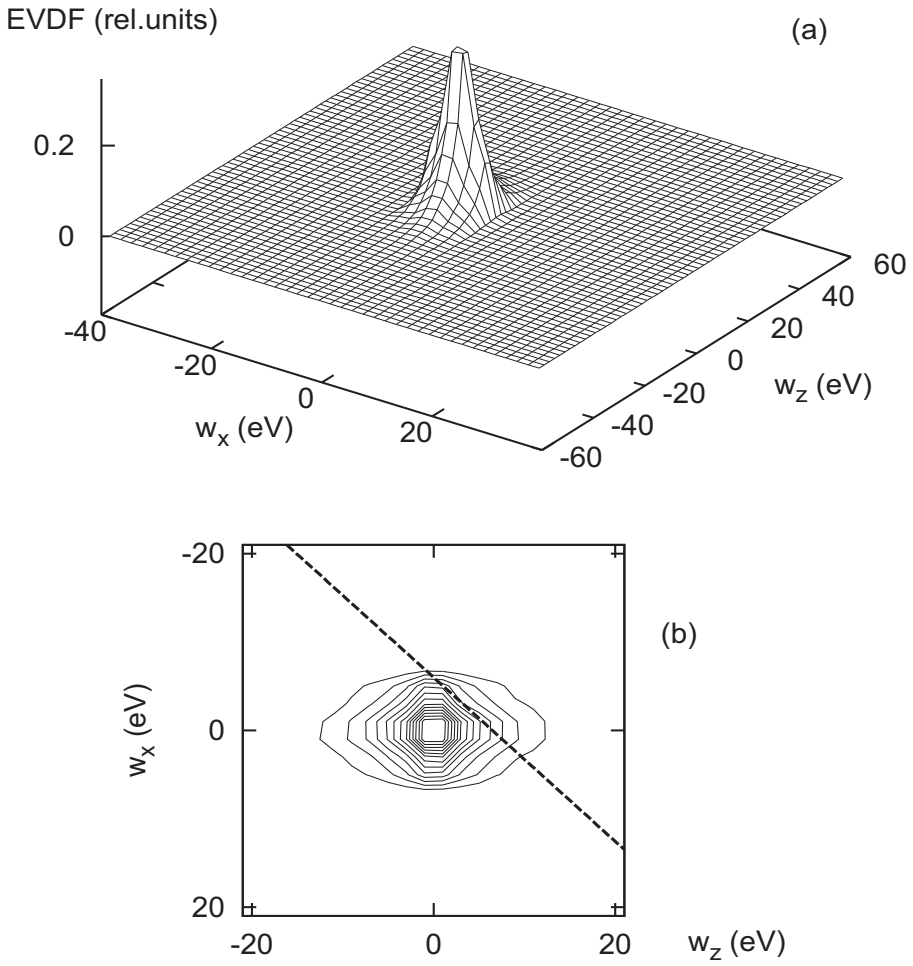

Figure 5.8: For simulation 4 from Table 5.1, the electron velocity distribution over v_x and v_z in the middle of the plasma 10 mm $< x <$ 15 mm plotted in energy coordinates (negative energy values correspond to propagation in the negative direction): (a) the 3D-plot, and (b) the corresponding contour plot of the low energy region $|w_{x,z}| < 20$ eV. Any two neighboring contour lines in (b) have a level difference of 0.025. The plasma potential relative to the wall is $\Phi_p = 6.2$ V. The dashed bold line in (b) is $w_x = w_z \widetilde{T}_x / \widetilde{T}_z + const.$

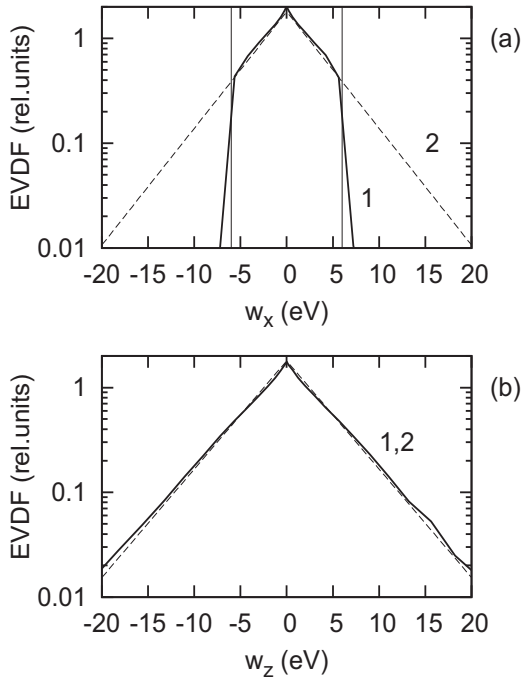

Figure 5.9: For simulation 4 from Table 5.1, the EVDF over v_x (a) and v_z (b) in the middle of the plasma 10 mm $< x <$ 15 mm plotted versus energy (negative energy values correspond to propagation in the negative direction). Curve 1 is the plasma EVDF in simulations. In (a), the two symmetric vertical lines mark the confinement threshold energy $w_x = e\Phi_p$, straight line 2 has a slope corresponding to $\widetilde{T}_x = 3.9$ eV. In (b), straight line 2 has a slope corresponding to $\widetilde{T}_z = 4.2$ eV.

consecutive electron-neutral collisions (which may scatter an electron towards the wall) $l \sim 1$ m is much larger than the width of the plasma slab, $l \gg L$. The EVDF in the loss cone is partially replenished via collisions. The plasma bulk electrons with negative motion integral values $w_x - e\Phi(x) < 0$ are confined by the plasma potential. But a confined electron with the positive total energy $(w_x + w_y + w_z) - e\Phi(x) > 0$ may be scattered to the wall after colliding with a neutral atom or a charged particle.

In the bounded plasma with SEE, there is another source of repopulation of the loss cone. Note that the shape of the EVDFs of simulations 2 and 3 is quite different from that of simulations 1 and 4: in the former two cases the EVDF $f_{xz}(v_x, v_z)$ is non-monotonic in the loss cone (compare Fig. 5.4 and Fig. 5.6 with Fig. 5.2 and Fig. 5.8). This happens because the loss cone is populated not only by the scattered plasma bulk electrons, but also by the secondary electrons emitted from the walls. In Fig. 5.5a for simulation 2, the EVDF over v_x is plotted with contributions from the secondary electrons and from the plasma bulk electrons separated (see also Fig. 5.7 for simulation 3). The secondary electrons form two counter-propagating beams (see curves 2 and 3 in Fig. 5.5a), which travel between the walls almost without collisions. The secondary electron beams may form a major component of the EVDF for $w_x > e\Phi$, and, therefore, compose most of the current to the walls.[2] The EVDFs over v_z of the emitted electron beams may be locally non-symmetric, as shown in Fig. 5.4a and Fig. 5.5b. This asymmetry reflects the motion of the emitted electrons along spiral-like trajectories: the acceleration and deceleration in the x direction is combined with the cyclotron rotation in the y-z plane and $\mathbf{E} \times \mathbf{B}$ drift in the y direction. The detailed dynamics of the secondary electron beams is described in Chapter 6.

[2]Note that in the present thesis the electron flux to the wall created by the *plasma bulk electrons* Γ_{1p} is distinguished from the *total* primary electron flux Γ_1.

5.2 Effects of Coulomb collisions

5.2.1 The effective frequencies of Coulomb collisions in Hall thrusters

Scattering of charged particles by Coulomb forces [139] is a basic physical process, important for many phenomena in space plasmas [140, 141] and laboratory plasmas [7, 142]. Coulomb collisions between particles of the same species, *e.g.*, electron-electron (e-e) collisions, drive the velocity distribution function towards an isotropic Maxwellian distribution. Coulomb collisions between particles with essentially different masses, such as electron-ion (e-i) collisions, are characterized by negligible energy exchange and contribute to the isotropization of the velocity distribution function of the light particles. In bounded plasmas, Coulomb collisions supply electrons to the loss cone and thus play a role similar to the role of collisions with neutral atoms. Coulomb scattering occurs predominantly at small angles. Although scattering through large angles $\theta > \pi/2$ is infrequent, many successive small-angle collisions lead to large-angle scattering. For e-i collisions, the effective frequency of large-angle ($\theta = \pi/2$) deflection after many small-angle collisions ν_{ei}^{dif} is given by [74, 143]

$$\nu_{ei}^{dif} = \frac{n_g v e^4 \ln\Lambda}{2\pi^3 \epsilon_0^2 w^2} \ ,$$

where n_g is the density of target particles (ions), $w = mv^2/2$ is the electron kinetic energy, v is the electron speed, and $\ln\Lambda$ is the Coulomb logarithm. The frequency ν_{ei}^{sgl} of collisions, which scatter electrons by a large angle in a single collision, is much smaller than the effective frequency of cumulative diffusive deflection ν_{ei}^{dif}, $\nu_{ei}^{sgl} = (\pi^2/32\ln\Lambda)\nu_{ei}^{dif} \ll \nu_{ei}^{dif}$ [74]. The difference between the frequencies of large-angle diffusive deflection due to e-i and e-e collisions, ν_{ei}^{dif} and ν_{ee}^{dif}, is a factor of order unity [2]. The effective total frequency of large-angle diffusive deflection ν^{dif} and the effective total frequency of single large-angle scattering ν^{sgl} due to *both* e-i

and e-e collisions are

$$\begin{aligned} \nu^{dif} &= \nu_{ee}^{dif} + \nu_{ei}^{dif} \approx 2\nu_{ei}^{dif} \ , \\ \nu^{sgl} &\approx \frac{\pi^2}{32 \ln \Lambda} \nu^{dif} \ . \end{aligned} \tag{5.5}$$

It is commonly accepted that Coulomb collisions play a minor role [136] in Hall thrusters, as long as the frequencies of Coulomb collision for such plasmas ($\nu^{dif} \sim 10^5$ s^{-1} and $\nu^{sgl} \sim 10^3$ s^{-1}) are much smaller than the frequencies of electron-neutral ($\nu_{en} \sim 10^6$ s^{-1}) and "turbulent" ($\nu_t \sim 10^6 - 10^7$ s^{-1}) collisions. The direct modification of the number of particles in the loss cone due to large-angle Coulomb collisions is about $\nu^{sgl}/\nu_{en} \sim 0.001$ of the unmodified value. The effective frequency ν^{dif} characterizes the rate of isotropization of the EVDF due to Coulomb collisions, and it can be responsible for filling the loss cone with modification of order $\nu^{dif}/\nu_{en} \sim 0.1$. The role of Coulomb collisions for electron heating is small, as long as $(\nu_t + \nu_{en}) \gg \nu^{dif}$.

Note that the collisional frequencies described in the previous paragraph depend crucially on the design and operational regime of a thruster. The frequency of electron-atom collisions ν_{en} is proportional to the neutral gas density n_a, which can be decreased either by reducing the neutral gas flow rate (the so-called throttling regime), or by performing ionization in a different section of the device, as it is in the two-stage thrusters [144]. Additionally, ν_{en} can be decreased if lighter than xenon gases are used (such as argon or hydrogen, with smaller cross sections of electron-neutral collisions). It will be shown below that in some regimes of a conventional thruster, a small modification of the degree of anisotropy $\widetilde{T}_z/\widetilde{T}_x$ due to Coulomb collisions may result in noticeable changes in the SEE intensity, plasma potential, and wall current. Modification of the EVDF by Coulomb scattering is consistently connected with modification of the emission coefficient γ. Since $\Gamma_1 = \Gamma_i/(1-\gamma)$, where Γ_1 and Γ_i are the electron and ion fluxes towards the wall, respectively, the closer γ is to unity, the more sensitive the plasma becomes with respect to small modifications of γ, and therefore, of the EVDF.

5.2.2 Initial simulation parameters

To investigate the modification of the EVDF in a Hall thruster by Coulomb collisions, two sets of simulations with identical initial parameters were carried out with and without Coulomb collisions. Initial parameters and major results of these simulations are presented in Table 5.2. The width of the plasma slab is $L = 2.5$ cm and the neutral gas density is $n_a = 10^{12}$ cm^{-3}. The gas density was reduced compared to the value used in the previous section to enhance the effect of Coulomb collisions, but it is still within the range of experimental parameters. Initially, the electron density is $n_{e0} = 10^{11}$ cm^{-3} and the EVDF is Maxwellian with drift velocity E_z/B_x along the y axis with the electron temperature $T_{e0} = 10$ eV. Duration of the simulations until reaching a quasi-steady state is 8 μs for cases 5 and 6, and 10 μs for cases 7 and 8. Other simulation parameters are given in Table B.1.

In Table 5.2, the effective frequencies of Coulomb collisions ν^{dif} and ν^{sgl} are calculated via Eq. (5.5) for electrons with energy equal to the electron confinement threshold $e\Phi_p$ and $\ln\Lambda = 10$. The emission coefficient γ, the total primary electron flux Γ_1, and the primary electron flux due to plasma bulk electrons Γ_{1p} are calculated at the wall $x = L$.

5.2.3 Coulomb collision effects for weak secondary electron emission

Simulations 5 and 6 of Table 5.2 are characterized by the low axial electric field E_z and the relatively low frequency of "turbulent" collisions ν_t; the effects of modification of secondary emission are minimal in these simulations. Coulomb collisions included in simulation 6 resulted in the following consequences (compare simulations 5 and 6 of Table 5.2):

- The degree of EVDF anisotropy $\widetilde{T}_z/\widetilde{T}_x$ decreases from 1.86 to 1.67, by 10%, the electron temperature $\widetilde{T}_x$ increases.

- The plasma potential Φ_p increases by 37%.

Table 5.2: Initial parameters (constant) and results of Hall thruster simulations with EDIPIC code. Here the simulations with Coulomb collisions are compared with the simulations where Coulomb collisions are omitted. The common parameters are $L = 2.5$ cm, $n_a = 10^{12}\text{cm}^{-3}$.

Number	5	6	7	8
E_z, [V/cm]	50	50	200	200
B_x, [G]	100	100	100	100
Coulomb collisions	off	on	off	on
$\langle w_y \rangle$, [eV]	8.2	7.7	38.2	34.6
$\langle w_z \rangle$, [eV]	7.5	7.0	26.8	23.2
$\langle w_x \rangle$, [eV]	1.9	2.2	4.5	4.9
$\widetilde{T}_z$, [eV]	11.7	11.0	36.7	33.5
$\widetilde{T}_x$, [eV]	6.3	6.6	12.1	14.9
Φ_p, [V]	8.6	11.8	19.4	19.7
$\langle \nu_{en} \rangle$, [10^6 s^{-1}]	0.66	0.66	0.7	0.7
$\langle \nu_t \rangle$, [10^6 s^{-1}]	2.0	2.0	0.7	0.7
ν^{dif}, [10^6 s^{-1}]	n/a	0.09	n/a	0.08
ν^{sgl}, [10^6 s^{-1}]	n/a	0.0028	n/a	0.0024
$\overline{n}_e$, [10^{11} cm^{-3}]	0.59	0.56	1.26	1.1
γ	0.61	0.59	0.957	0.965
Γ_{1p} , [10^{21} m^{-2}s^{-1}]	0.1	0.11	0.7	1
Γ_1 , [10^{21} m^{-2}s^{-1}]	0.25	0.24	4.54	5.44

- The emission coefficient γ decreases. Because a more isotropic EVDF has lower energy of electrons in the loss cone, the decrease is insignificant.
- Due to the higher electron temperature $\widetilde{T}_x$, the flux of plasma bulk particles (ions and electrons) to the wall increases, in this case, by 10%.
- The loss cone of the EVDF over v_x for bulk electrons (line with markers in Fig. 5.10a) is shifted to higher energies corresponding to the increased plasma potential. The transition from the EVDF bulk to the loss cone is smoothed.
- The modification of the EVDF over v_z is insignificant (see Fig. 5.10b).
- The EVDFs over v_x for secondary electron beams (line with markers in Fig. 5.10c for the beam emitted from the wall $x = L$) are shifted to higher energies, consistent with the increased plasma potential.
- There is no significant difference between EVDFs over v_z for secondary electron beams in both cases (see Fig. 5.10d).

5.2.4 Coulomb collisions with strong secondary electron emission

In simulations 7 and 8 of Table 5.2, the electric field E_z is higher than in simulations 5 and 6. The emission coefficient γ is close to unity. In these simulations, the frequency of "turbulent" collisions was reduced according to the correction due to the near-wall conductivity effect, as discussed below in Section 6.2. The Coulomb collisions included in simulation 8 resulted in the following difference from simulation 7, as shown in Table 5.2:

- The degree of anisotropy $\widetilde{T}_z/\widetilde{T}_x$ decreases from 3.03 to 2.25, by 26%.
- The electron temperature $\widetilde{T}_x$ increases by 23%.
- The plasma potential increases insignificantly despite the considerable change in $\widetilde{T}_x$, because the growth of the plasma potential is compensated by the increased intensity of secondary electron emission (see the next item).

- Modification of the plasma potential results in a decreased electron flight time between the walls, which leads to the increased energy of the secondary electron beam at the target wall [94] and, correspondingly, to the enhanced emission coefficient γ (the model of SEE with secondary electron beams is considered in Chapter 6).

- Since γ is close to unity, a small increase of γ results in significant growth of the plasma bulk electron flux to the wall Γ_{1p}, by 43%, and the total primary electron flux Γ_1, by 20%.

- The EVDF over v_x for bulk electrons with Coulomb collisions (curve with markers in Fig. 5.11a) has a smoother transition to the loss cone region and has slightly more particles in this region than the EVDF without Coulomb collisions (curve without markers in Fig. 5.11a).

- The EVDF over v_z for bulk electrons (curve with markers in Fig. 5.11b) has fewer particles in the high energy tail than the same EVDF without Coulomb collisions (curve without markers in Fig. 5.11b).

- The EVDFs over v_x and v_z for secondary electrons changes insignificantly, mainly due to the increase of the secondary electron current (see Fig. 5.11c and Fig. 5.11d).

In simulations 5 and 6, the electron energy is lower than in simulations 7 and 8, but the effect of Coulomb collisions is noticeably stronger for the latter case. The reason is the greater sensitivity of plasma parameters to the intensity of secondary electron emission in regimes with $\gamma \approx 1$.

5.3 Electron fluxes to the wall with space charge limited secondary electron emission

It is instructive to compare the values of the electron flux to the wall, emission coefficient, and plasma potential obtained in PIC simulations of the Hall thruster

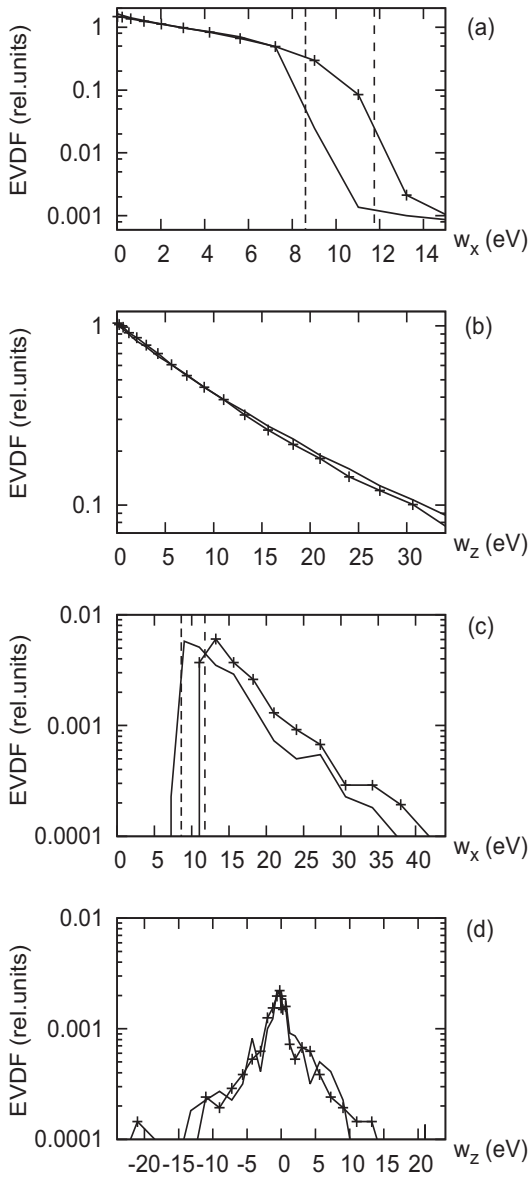

Figure 5.10: The EVDF over v_x (a) and v_z (b) for the bulk plasma, the EVDF over v_x (c) and v_z (d) for the secondary electron beam emitted from the wall $x = 0$. All EVDFs are plotted versus energy, with negative energy values indicating propagation in the negative direction. Curves without markers correspond to simulation 5 (Coulomb collisions turned off) and curves with markers correspond to simulation 6 (Coulomb collisions turned on) from Table 5.2. In (a) and (c), the two vertical lines mark the confinement threshold energies $w_x = e\Phi_p$ corresponding to cases 5 ($w_x = 8.6$ eV) and 6 ($w_x = 11.8$ eV). The EVDFs are calculated in the middle of the plasma 10 mm $< x <$ 15 mm.

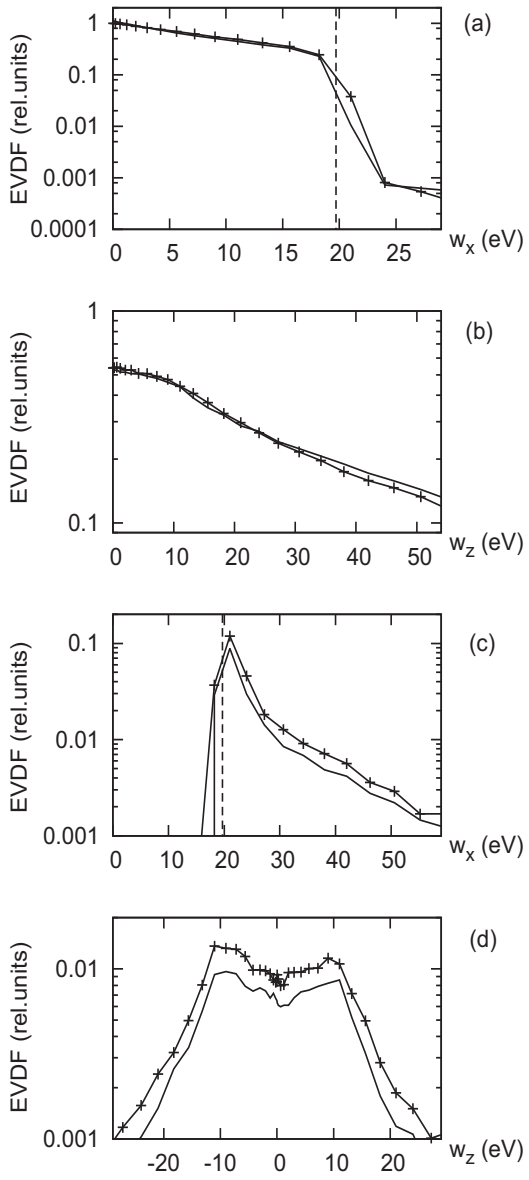

Figure 5.11: The EVDF over v_x (a) and v_z (b) for the bulk plasma, the EVDF over v_x (c) and v_z (d) for the secondary electron beam emitted from the bottom wall. All EVDFs are plotted versus energy, with negative energy indicating propagation in the negative direction. Curves without markers correspond to case 7 (Coulomb collisions turned off) and curves with markers correspond to case 8 (Coulomb collisions turned on) from Table 5.2. In (a) and (c), the vertical line $w_x = 19.7$ eV marks the confinement threshold energy $e\Phi_p$ corresponding to case 8 (case 7 has a close value $e\Phi_p = 19.4$ eV). The EVDFs are calculated in the middle of the plasma 10 mm $< x <$ 15 mm.

model (see Tables 5.1 and 5.2) with the values obtained for a Maxwellian isotropic plasma. The electron temperatures of the Maxwellian plasma corresponding to the EDIPIC simulations can be taken by averaging the effective temperatures as $T_M = (\widetilde{T}_x + 2\widetilde{T}_z)/3$. Note that for simulations 2, 3, 7, and 8, the average temperature T_M exceeds the critical temperature $T_{cr} = 18.3$ eV for boron nitride ceramics, and the Maxwellian plasma will produce space charge limited SEE. Thus, the model of the SCL regime of SEE for a Maxwellian plasma is necessary. Previously, similar model was considered by Schwager [125] in his studies of the plasma layer between the Maxwellian plasma source and emitting wall. The model described below, in contrast to Schwager's approach, (i) considers only the near-wall sheath region and disregards the interface with the plasma source, (ii) allows for emission due to secondary electrons reflected back to the wall by the nonmonotonic sheath, (iii) uses the emission coefficient, which is the realistic function of energy and incidence angle corresponding to the properties of grade HP boron nitride ceramics.

Consider a semi-infinite, uniform plasma bounded by a secondary electron emitting, dielectric wall. The x axis is directed normal to the boundary and the plasma occupies the half-space $x < 0$. The plasma uniformity breaks near the wall, where the plasma is nonuniform and non-neutral in the sheath. If the emission is in the non-SCL regime, the charge density distribution in the sheath is qualitatively similar to that of the case of a non-emitting boundary [74]: the electron density $n_e(x)$ is below the ion density $n_i(x)$ (see orange and green curves in Fig. 5.12), and the potential profile in the sheath $\Phi(x)$ is monotonic (see the black curve in Fig. 5.12). Far from the boundary, the potential and the plasma density are constant: $\lim\limits_{x\to-\infty} \Phi(x) = \Phi_p$, $\lim\limits_{x\to-\infty} n_e(x) = n_p$.

Note that the electron wall fluxes can be calculated without knowing the exact shape of $\Phi(x)$. Introduce the EVDF $f(v_x, v_y, v_z)$ at $x \to -\infty$ that satisfies the condition $\int\limits_{-\infty}^{\infty} dv_x \int\limits_{-\infty}^{\infty} dv_y \int\limits_{-\infty}^{\infty} dv_z f(v_x, v_y, v_z) = n_p$. With a monotonic potential in the sheath, the primary electron flux Γ_1 (red arrow in Fig. 5.12) is:

$$\Gamma_1 = \Gamma_{1p} = \int\limits_{v_*}^{\infty} dv_x v_x \int\limits_{-\infty}^{\infty} dv_y \int\limits_{-\infty}^{\infty} dv_z f(v_x, v_y, v_z) \ , \tag{5.6}$$

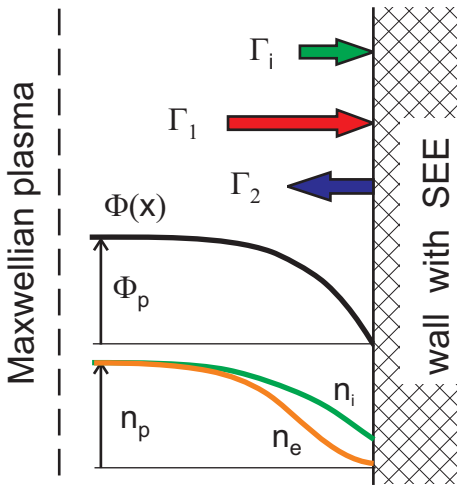

Figure 5.12: Qualitative diagrams of wall fluxes for a semi-infinite plasma bounded by a wall producing secondary electrons in the non space charge limited regime. The black curve is the potential profile. The orange and green curves are the profiles of the electron and ion density, respectively.

where Γ_{1p} is the electron flux to the wall created by plasma bulk electrons, $v_* = (2e\Phi_p/m)^{1/2}$. The primary electron flux (5.6) produces secondary electron flux Γ_2 (blue arrow in Fig. 5.12):

$$\Gamma_2 = \Gamma_{2p} = \int_{v_*}^{\infty} dv_x v_x \int_{-\infty}^{\infty} dv_y \int_{-\infty}^{\infty} dv_z f(v_x, v_y, v_z)\gamma(\sqrt{v_x^2 - 2e\Phi_p/m}, v_y, v_z) \ , \qquad (5.7)$$

where Γ_{2p} is the secondary electron flux produced by the plasma bulk electrons and $\gamma(v_x, v_y, v_z)$ is the emission coefficient of the wall material. The general condition of zero total current at the dielectric wall is

$$\Gamma_i = \Gamma_1 - \Gamma_2 \ , \qquad (5.8)$$

where Γ_i is the ion flux to the wall (green arrow in Fig. 5.12). Assuming a Maxwellian EVDF $f(v_x, v_y, v_z)$ of temperature T_e, and taking the Bohm condition for the ion flow velocity at the sheath boundary, the ion flux is

$$\Gamma_i = n_p \exp(-1/2)\sqrt{\frac{T_e}{M}} \ .$$

Provided $\gamma(v_x, v_y, v_z)$ is known, Eqs. (5.6), (5.7), and (5.8) are sufficient to calculate the plasma potential Φ_p and the fluxes Γ_1 and Γ_2.

If the emission is in the SCL regime, the electron density near the wall exceeds the ion density (see the orange and green curves in Fig. 5.13), forming a double charged layer with a non-monotonic potential profile (see black curve in Fig. 5.13). Denote the potential at the deepest point of the potential well near the wall as $-\Phi_w$, where $\Phi_w > 0$. The flux Γ_{1p} of plasma electrons to the wall (solid red arrow in Fig. 5.13) is calculated by Eq. (5.6) with $v_* = [2e(\Phi_p + \Phi_w)/m]^{1/2}$. These electrons produce the secondary electron flux Γ_{2p} (solid blue arrow in Fig. 5.13), which is calculated by Eq. (5.7) with v_* redefined as above. The flux Γ_{2p} is directed into the plasma, and its value (5.7) is calculated exactly at the wall. Part of this flux (the upper dashed red arrow in Fig. 5.13) is reflected back to the wall by the adjacent potential well. Introduce the reflection coefficient $\kappa < 1$ so that the reflected flux is $\kappa\Gamma_{2p}$. If the emitted electrons have a Maxwellian EVDF $f_2(v_x, v_y, v_z)$ with temperature T_2, then the part of the secondary electron flux Γ_{2p}, which penetrates through the potential well, is $\Gamma_{2p} \exp(-e\Phi_w/T_2)$. Therefore, the reflection coefficient is determined by the depth of the potential well and the secondary electron emission temperature as follows:

$$1 - \kappa = \exp(-e\Phi_w/T_2) \ . \tag{5.9}$$

Assume that the secondary electrons that are reflected by the non-monotonic potential also produce SEE (dashed blue arrow in Fig. 5.13), which is characterized by the average emission coefficient

$$\gamma_2 = \frac{\int_0^{v_w} dv_x v_x \int_{-\infty}^{\infty} dv_y \int_{-\infty}^{\infty} dv_z f_2(v_x, v_y, v_z)\gamma(v_x, v_y, v_z)}{\int_0^{v_w} dv_x v_x \int_{-\infty}^{\infty} dv_y \int_{-\infty}^{\infty} dv_z f_2(v_x, v_y, v_z)} \ , \tag{5.10}$$

where $v_w = (2e\Phi_w/m)^{1/2}$. Here the distribution of the emitted electrons with $|v_x| < v_w$ is used as the distribution of the incident electron flux. Note that

$$\int_0^{\infty} dv_x v_x \int_{-\infty}^{\infty} dv_y \int_{-\infty}^{\infty} dv_z f_2(v_x, v_y, v_z) = \Gamma_{2p} \ .$$

Assume that the temperature of secondary electrons is independent of whether the SEE is caused by the plasma bulk electrons or by the reflected secondary electrons.

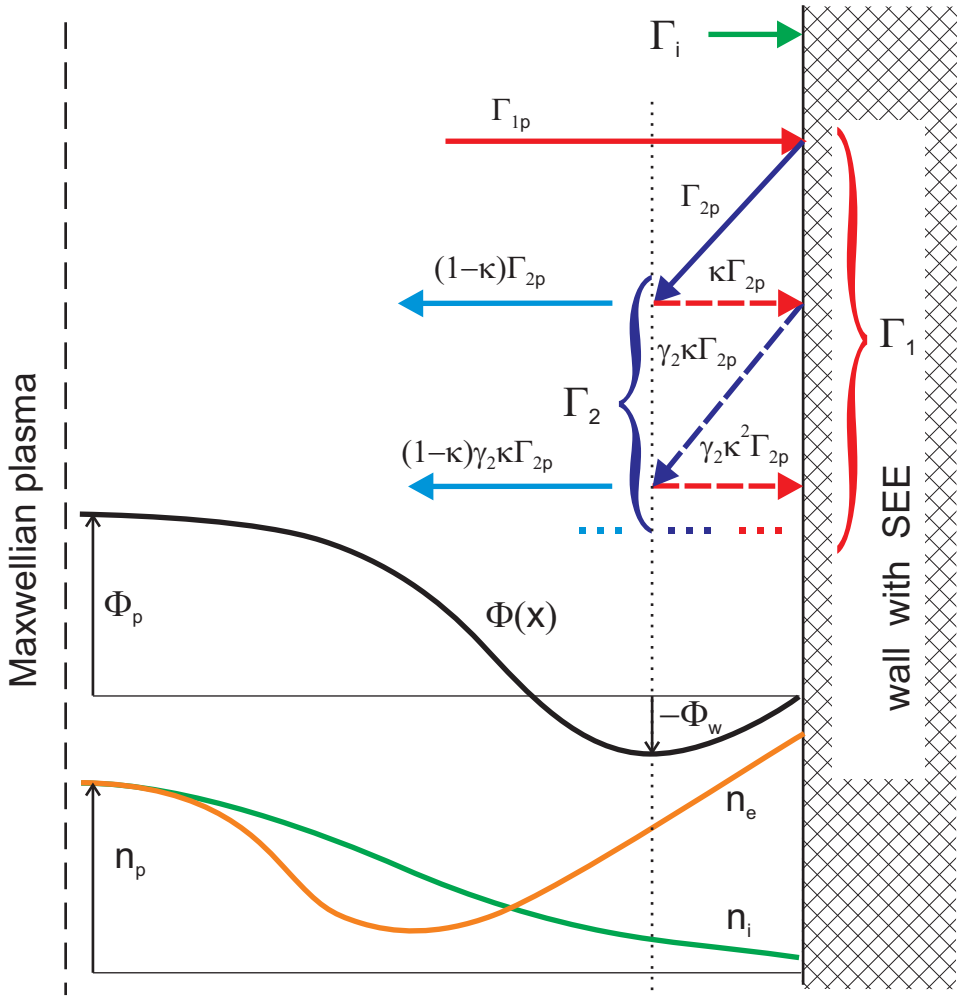

Figure 5.13: Qualitative diagrams of wall fluxes for a semi-infinite plasma bounded by a wall producing secondary electrons in the SCL regime. The black curve is the potential profile. The orange and green curves are the profiles of the electron and ion density, respectively.

Then the total flux of primary electrons may be written as an infinite convergent sum of decreasing components (see also Fig. 5.13):

$$\Gamma_1 = \Gamma_{1p} + \kappa\Gamma_{2p} + \kappa\gamma_2(\kappa\Gamma_{2p}) + \kappa\gamma_2[\kappa\gamma_2(\kappa\Gamma_{2p})] + \dots \ . \tag{5.11}$$

One can reduce (5.11) to the form:

$$\Gamma_1 = \Gamma_{1p}\left[1 + \frac{\kappa\gamma_p}{1-\kappa\gamma_2}\right] \ , \tag{5.12}$$

where γ_p is the average emission coefficient for the plasma bulk electrons

$$\gamma_p = \frac{\Gamma_{2p}}{\Gamma_{1p}} \ . \tag{5.13}$$

Similarly, the total flux of secondary electrons may be written as

$$\Gamma_2 = \Gamma_{2p} + \gamma_2(\kappa\Gamma_{2p}) + \gamma_2[\kappa\gamma_2(\kappa\Gamma_{2p})] + \gamma_2\{\kappa\gamma_2[\kappa\gamma_2(\kappa\Gamma_{2p})]\} + \dots \ , \tag{5.14}$$

which reduces to

$$\Gamma_2 = \Gamma_{1p}\gamma_p\left[1 + \frac{\kappa\gamma_2}{1-\kappa\gamma_2}\right] \ . \tag{5.15}$$

Then the total emission coefficient is

$$\gamma = \frac{\Gamma_2}{\Gamma_1} = \frac{\gamma_p}{1+\kappa(\gamma_p-\gamma_2)} \ . \tag{5.16}$$

Following Hobbs and Wesson [75], and Schwager [125], assume that the total emission coefficient in the SCL regime does not exceed the critical value $\gamma_{cr} < 1$. Condition $\gamma = \gamma_{cr}$ with Eq. 5.16 determine the value of the reflection coefficient

$$\kappa_{cr} = \frac{\gamma_p - \gamma_{cr}}{\gamma_{cr}(\gamma_p - \gamma_2)} \ , \tag{5.17}$$

and, via Eq. 5.9, the depth of the potential well

$$\Phi_w = -\frac{T_2}{e}\ln(1-\kappa_{cr}) \ . \tag{5.18}$$

Note that Schwager [125] obtained a different, though similar, expression for the potential well depth in the case of $\gamma_2 = 0$:

$$\Phi_w = -\frac{T_2}{e}\ln(\gamma_p/\gamma_{cr}) \ .$$

The difference appears because Schwager defined the emission coefficient as the ratio of the secondary current *penetrated* through the sheath to the plasma bulk primary electron current. Hence, in his approach, the *penetrated* secondary current is limited to

$$(1 - \kappa_{cr})\Gamma_{2p} = \gamma_{cr}\Gamma_{1p} \ ,$$

see Eq. 14 in [125]. In the present model and in simulations with EDIPIC, the emission coefficient is determined *at the wall*, in the SCL regime the total primary current *at the wall* increases due to the reflection of emitted electrons in order to limit the total emission coefficient

$$\Gamma_{2p} = \gamma_{cr}(\Gamma_{1p} + \kappa_{cr}\Gamma_{2p}) \ ,$$

which is equivalent to $(1 - \gamma_{cr}\kappa_{cr})\Gamma_{2p} = \gamma_{cr}\Gamma_{1p}$ if $\gamma_2 = 0$. As a result, the critical emission coefficient determined at the wall γ_{cr} is related to the critical emission coefficient determined by Schwager behind the minimum of the potential well γ_{Sch} as

$$\gamma_{cr} = \frac{\gamma_p}{\gamma_p + 1 - \gamma_{Sch}} \ . \tag{5.19}$$

The above expression is valid for $\gamma_2 = 0$ and $\gamma_p \geq \gamma_{Sch}$. Note that $\gamma_{cr} = \gamma_{Sch}$ if $\gamma_p = \gamma_{Sch}$, and $\gamma_{cr} \to 1$ if $\gamma_p \to \infty$.

Eqs. (5.12) and (5.15), together with Eqs. (5.17) and (5.18), combined with Eq. (5.8), are sufficient to find Φ_p, Φ_w, Γ_{1p}, γ_p, and γ, in the SCL regime, $\gamma_p > \gamma_{cr}$, without the self-consistent solution of Poisson's equation (the complete solution can be found, *e.g.*, in [145, 146]).

Calculation of wall fluxes, plasma potentials, and emission coefficients for Maxwellian plasmas with different electron temperatures was carried out as follows. The emission produced by the reflected electrons in the SCL regime was neglected, $\gamma_2 = 0$. The critical emission coefficient for xenon (in Schwager's definition) was $\gamma_{Sch} = 0.983$ calculated by Eq. (1.12). For $\gamma_p < \gamma_{Sch}$, Eqs. (5.6) and (5.7) with $v_* = (2e\Phi_p/m)^{1/2}$, and (5.8) were used. For $\gamma_p > \gamma_{Sch}$, Eqs. (5.12) and (5.15) with $v_* = [2e(\Phi_p + \Phi_w)/m]^{1/2}$, and Eqs. (5.17), (5.18), (5.8) were used. In the latter case the required value of γ_{cr} was determined from (5.19). The plasma density was

$n_p = 10^{17}$ m^{-3}, the ion mass was $M = 131$ u, the SEE emission coefficient approximated the total emission coefficient of boron-nitride ceramics (3.19), and the temperature of the secondary electrons was the same as the temperature of the true secondary electron in PIC simulations, $T_2 = T_t = 2$ eV. The results for Maxwellian plasmas calculated as above are compared with the data of the Hall thruster PIC simulations in Fig. 5.14.

For a Maxwellian plasma, the primary electron flux due to the plasma electrons Γ_{1p} increases exponentially as the electron temperature approaches the critical value $T_{cr} = 18.3$ eV, above this threshold the SEE falls into the SCL regime and the electron flux Γ_{1p} nearly saturates (see black curve in Fig. 5.14a). Transition to the SCL regime is accompanied by the saturation of the total emission coefficient γ at the level $\gamma_{Sch} < \gamma < 1$ (see black curve in Fig. 5.14b). Note that this saturation occurs due to the reflection of part of the secondary current back to the wall and the corresponding increase of Γ_1, as described by Eq. (5.12). The partial emission coefficient due to plasma electrons γ_p defined in (5.13) is not affected by this reflection and continues its increase while $T_e > T_{cr}$ (see dashed blue curve in Fig. 5.14b). The plasma potential changes nonmonotonically with the increase of the electron temperature, it drops considerably when the temperature approaches the transition threshold of the SCL regime (see black curve in Fig. 5.14c).

Note that the average plasma density in Hall thruster simulations $\overline{n}_e$ is different from the density n_p of the Maxwellian plasmas used for the calculations above. For consistent comparison with Maxwellian plasma, the fluxes in the Hall thruster simulations have to be multiplied by a factor of $n_p/\overline{n}_e$.

The properties of the plasmas in Hall thruster simulations presented in Tables 5.1 and 5.2 are quite different from those of Maxwellian plasmas. Due to the depletion of the EVDF in the loss cone, the thruster plasmas are characterized by substantially smaller primary electron fluxes than Maxwellian plasmas with corresponding temperatures. In simulations, the total primary electron flux Γ_1 is about $2 - 10$ times smaller (compare red markers with black curve in Fig. 5.14a), and the primary electron flux due to the plasma bulk electrons Γ_{1p} is about $10 - 50$ times smaller

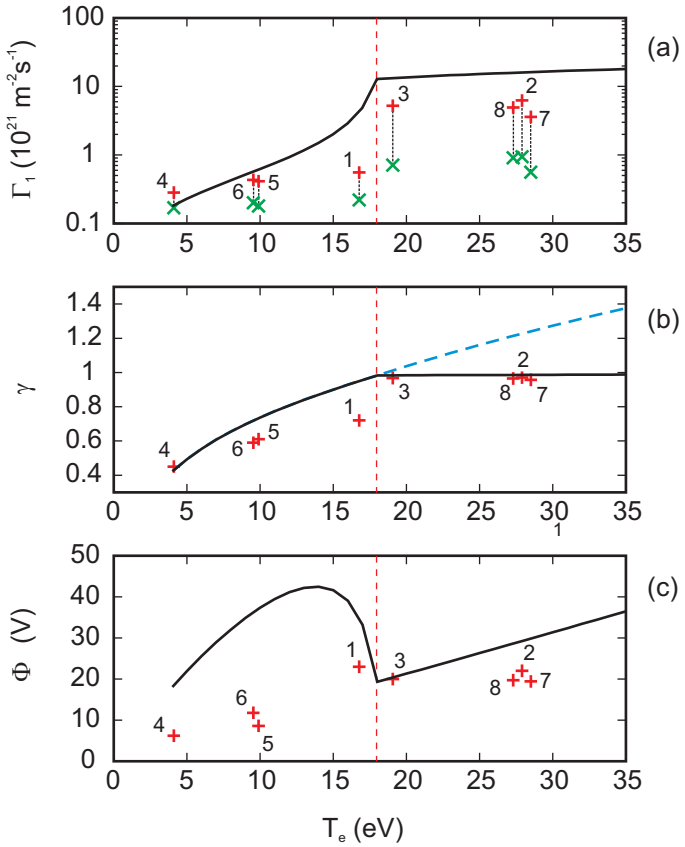

Figure 5.14: Plasma-wall interaction parameters versus the electron temperature. (a) The black curve is the primary electron flux due to the plasma electrons Γ_{1p} calculated from the analytical model of a Maxwellian plasma (5.6); a pair of connected colored markers corresponds to one Hall thruster PIC simulation, here the red vertical cross is the total primary electron flux Γ_1, and the green diagonal cross is the electron flux to the wall created by the plasma bulk electrons Γ_{1p}. (b) The black curve is the total emission coefficient γ in the analytical model of a Maxwellian plasma (5.16); the blue dashed curve is the emission coefficient due to the plasma electrons γ_p in the analytical model (5.13); the red crosses are the total emission coefficients γ in Hall thruster PIC simulations. (c) The black curve is the plasma potential relative to the wall Φ_p obtained in the analytical model of a Maxwellian plasma from the balance of fluxes (5.8); the red crosses are the values of the plasma potential in the midplane Φ_p in Hall thruster PIC simulations. The data for the Hall thruster simulations correspond to those from Tables 5.1 and 5.2. For consistent comparison with a Maxwellian plasma of density n_p, the fluxes are multiplied by the factor $n_p/\overline{n}_e$. The numbers $1-8$ denote the simulation number. The vertical dashed red line separates the regions of non-SCL and SCL SEE for a Maxwellian plasma.

(compare green markers with black curve in Fig. 5.14a).

The huge difference between the wall fluxes *due to the plasma electrons* in Hall thrusters (green markers in Fig. 5.14a) and in Maxwellian plasmas (black curve in Fig. 5.14a) is attributed to the secondary electron beams that constitute most of the primary electron flux in Hall thrusters, this issue is discussed in detail in Chapter 6. Transition to the SCL SEE regime does not occur even for simulations 2, 3, 7, and 8, where the averaged effective temperature T_M exceeds the critical value, $T_M > T_{cr}$ (the markers in Fig. 5.14b are below the saturation level $\gamma = \gamma_{cr}$ of the black curve). The plasma potential in the simulations is usually lower than that of a Maxwellian plasma because of the anisotropy and the strong depletion of the loss cone, compare the markers and the black curve in Fig. 5.14c.

5.4 Summary

PIC simulations of the plane geometry model of a Hall thruster reveal that in the AR the plasma EVDF is non-Maxwellian, anisotropic, and depleted for high energies normal to the walls.

The anisotropy is largely determined by the high frequency of "turbulent" collisions, which are introduced in order to reproduce the anomalous electron mobility across the magnetic field. However, in the limit of strong external accelerating fields, the anisotropy develops even without "turbulent" collisions.

The high-energy tail of the EVDF in the direction normal to the plasma boundaries is depleted because the electron mean free path far exceeds the width of the plasma slab. As a result, the electrons with energy of motion normal to the walls above the plasma potential quickly leave the plasma, forming a loss cone in velocity phase space. The loss cone may be largely populated by secondary electrons emitted from the bounding walls due to SEE. These electrons form two counter-propagating secondary electron beams.

For electrons in Hall thrusters, the frequency of Coulomb collisions is much smaller than the frequency of "turbulent" and electron-neutral collisions. As a re-

sult, the effects of Coulomb collisions on the EVDF are typically weak. Considerable changes occur when the SEE is close to the SCL regime, $\gamma \approx 1$. For typical Hall thruster parameters corresponding to this regime, the electron fluxes to the wall increase by a few tens of percents when Coulomb collisions are included.

The parameters characterizing the interaction of the plasma with the wall (the electron wall fluxes, the plasma potential relative to the wall, and the emission coefficient) obtained in the PIC simulations of Hall thrusters and calculated analytically for isotropic Maxwellian plasmas, exhibit different behavior with the increase of the effective electron temperature.

Due to the depletion of the EVDF in Hall thrusters the primary electron flux is considerably lower than that in a Maxwellian plasma with corresponding temperature. The SCL regime of the SEE does not occur in the considered Hall thruster simulations, even though the averaged effective electron temperature exceeded the critical value $T_{cr} = 18.3$ eV for a Maxwellian plasma.

These results agree with the experimentally observed anomalously high electron temperature inside the ceramic channel of a Hall thruster [78] and the non-SCL regime of the sheath [79] at high discharge voltages.

Chapter 6

Electron dynamics in the model of the accelerating region of a Hall thruster

As it was discussed in the previous Chapter, the EVDF in the AR of a Hall thruster significantly deviates from Maxwellian. It is anisotropic – "cold" along the magnetic field and "hot" in the perpendicular direction – and depleted in the loss cone. The depleted tail of the EVDF leads to a significant reduction of wall losses compared to a Maxwellian plasma. The emission coefficient remains below the critical value (1.12), although the average electron energy of the anisotropic Hall thruster plasma is much higher than the critical electron temperature for a Maxwellian plasma. The difference appears because, contrary to the Maxwellian plasma, the loss cone of the plasma inside the channel of a Hall thruster is largely populated by the secondary electrons with energy quite different from that of the plasma bulk electrons. Simulations with the EDIPIC code show that in Hall thrusters most of secondary electrons emitted from one wall reach the opposite wall, thus forming two counter-propagating secondary electron beams. These beams modify the balance of charged particle fluxes at the walls, and therefore, affect the SEE regime. The secondary electron beams also receive additional energy due to the $E \times B$ motion, which is important because this additional energy is sufficient for secondary emission.

The assumption that the EVDF in a Hall thruster is Maxwellian is equivalent to assuming the complete mixing (or trapping) of emitted electrons inside the plasma.

Recently Ahedo and Parra [147] discussed the effects of partial trapping of secondary electron beams on the SEE regime in Hall thrusters. They showed that the SCL regime may not occur if the beam trapping is weak. In their model, the $E \times B$ effects were omitted and the emission due to the secondary electron beams was not considered.

It was found in simulations with the EDIPIC code that the contribution of the secondary electron beams to the SEE is significant, especially in strong accelerating fields, and cannot be neglected. A model of SEE that includes electron production by the counter-propagating electron beams has been developed. The results of Ref. [147] can be obtained from the theory presented below in the limit of zero emission for the secondary electron beams.

The model of SEE in the AR of a Hall thruster is presented in this Chapter. In Section 6.1, the balance of the electron wall fluxes in the AR is described, allowing for the SEE due to the secondary electron beams. The details of the derivations are given in Appendix C. In Section 6.2, the mechanism for the increase of the secondary electron beam energy and the near-wall conductivity effects are described. The effects of the two-stream instability on the propagation of the secondary electron beams through the plasma slab are discussed in Section 6.3.

6.1 Secondary electron emission with counter - propagating secondary electron beams

In plane geometry, the electron flux to the wall of a Hall thruster channel (or the primary electron flux) consists of several components. Consider the stationary non-SCL regime, when the electrostatic potential $\Phi(x)$ has maximum $\Phi_p = \Phi(L/2)$ in the midplane $x = L/2$ and monotonically decreases towards the walls (red curve in Fig. 6.1b). The plasma bulk electrons with $w_x - e\Phi(x) < 0$ are confined by the plasma potential, but may be scattered to the wall after collision with a neutral atom if $w - e\Phi(x) > 0$. The primary electron flux created by these electrons is called henceforth *the collision-ejected electron flux*, Γ_{1c}. Due to the low frequency

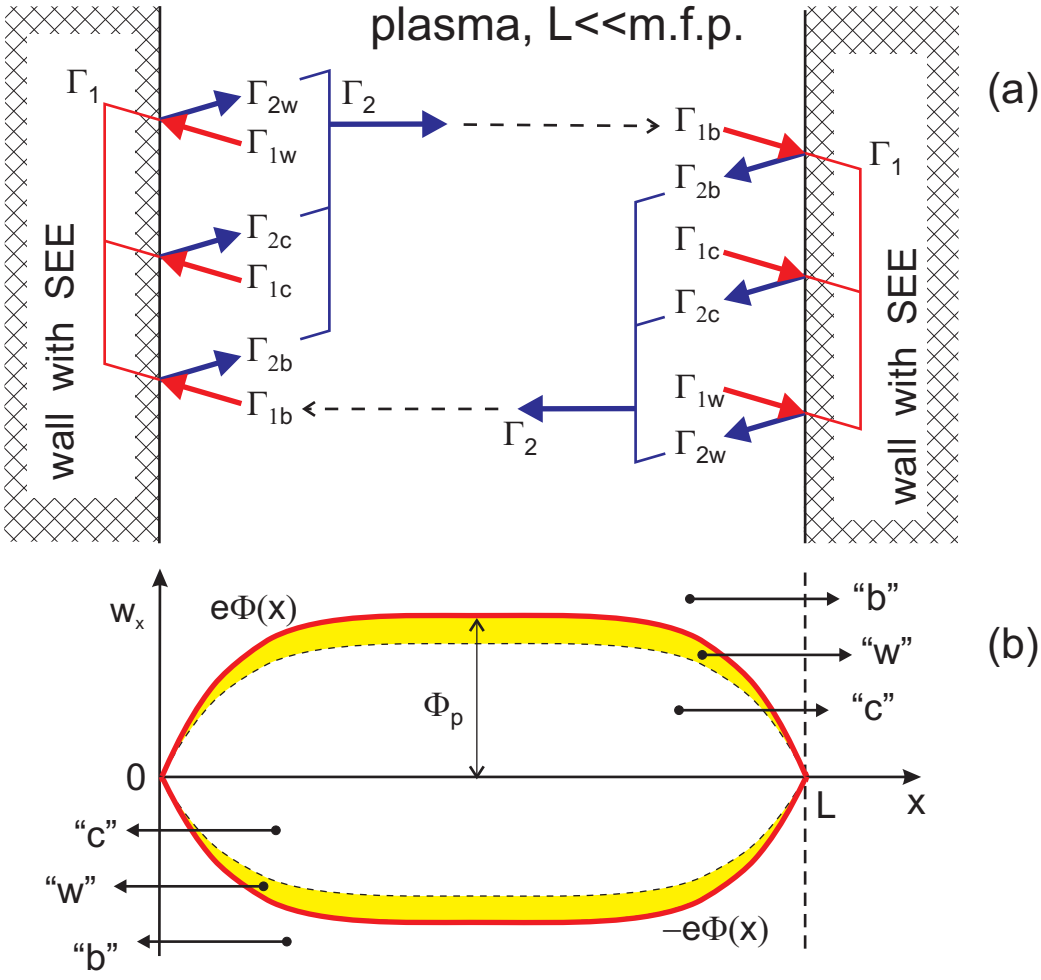

Figure 6.1: (a) Qualitative diagram of the electron wall fluxes in a plasma with large MFP bounded by the walls with SEE: red arrows are the components of the primary electron flux, blue arrows are the corresponding secondary electron fluxes. (b) Qualitative picture of the phase plane $\{x, w_x\}$ of the bounded plasma: arrows "b", "c", and "w" depict secondary electron beams, collision-ejected electrons, and weakly confined electrons, respectively; the red curves are the envelope for the confined electrons in phase space; the yellow bands are the weakly confined electrons. In (b) the electrons moving to the right have $w_x = mv_x^2/2 > 0$, electrons moving to the left have $w_x = -mv_x^2/2 < 0$.

of collisions, the secondary electrons travel between the walls almost freely, forming two counter-propagating electron beams. The electron flux to the wall created by the beam of secondary electrons emitted from the opposite wall is called *the electron beam flux*, Γ_{1b}. In addition to collisions with neutral atoms, the confined electrons with energy slightly below the confinement threshold, $w_x - e\Phi(x) \approx 0$, may be accelerated by plasma waves excited by the secondary electron beams. In the velocity phase space, such electrons form the narrow boundary layer between the secondary electrons accelerated by the plasma potential and the plasma bulk electrons deeply confined by the plasma potential (see yellow bands in Fig. 6.1b). Although the number of these weakly confined electrons is small compared to the total number of electrons in plasma, they need only a small perturbation of motion to leave the plasma, which is why they create a noticeable electron flux to the wall. The primary electron flux due to the electrons accelerated by plasma waves is called *the weakly confined electron flux*, Γ_{1w}.

The total primary electron flux Γ_1 is expressed via the three components as

$$\Gamma_1 = \Gamma_{1b} + \Gamma_{1c} + \Gamma_{1w} \ .$$

The three components of the electron flux to the wall produce respective parts of the secondary electron flux, so that the total secondary electron flux Γ_2 is

$$\Gamma_2 = \Gamma_{2b} + \Gamma_{2c} + \Gamma_{2w} \ .$$

where Γ_{2b}, Γ_{2c}, and Γ_{2w} are the secondary electron fluxes due to the beam electrons, the collision-ejected electrons, and the weakly confined electrons, respectively (see the flux diagram in Fig.6.1a). One can introduce partial emission coefficients corresponding to the three components of the primary electron flux as follows:

$$\gamma_b = \frac{\Gamma_{2b}}{\Gamma_{1b}} \ , \ \gamma_c = \frac{\Gamma_{2c}}{\Gamma_{1c}} \ , \ \gamma_w = \frac{\Gamma_{2w}}{\Gamma_{1w}} \ .$$

A secondary electron beam is emitted at the source wall with the current Γ_2. Some secondary electrons may be decelerated in the direction normal to the walls (see Section 6.3) and be trapped by the plasma potential. As a result, at the other

(target) wall the electron beam current is $\Gamma_{1b} < \Gamma_2$.[1] Quantitatively, the reduction of the secondary electron beam current is characterized by the coefficient of penetration of the secondary electron beam

$$\alpha = \frac{\Gamma_{1b}}{\Gamma_2} \ .$$

With the fluxes and partial emission coefficients defined as above, one obtains a total emission coefficient $\gamma = \Gamma_2/\Gamma_1$ in the form

$$\gamma = \frac{\gamma_p}{1 + \alpha(\gamma_p - \gamma_b)} \ , \tag{6.1}$$

where

$$\gamma_p = \frac{\Gamma_{1c} + \Gamma_{1w}}{\Gamma_{1c} + \Gamma_{1w}} = \frac{\gamma_c + \gamma_w \Gamma_{1w}/\Gamma_{1c}}{1 + \Gamma_{1w}/\Gamma_{1c}} \ , \tag{6.2}$$

is the collective emission coefficient due to all plasma bulk electrons, both collision-ejected and weakly confined. Similarly, one can find the ratio of primary electron fluxes due to the beam and bulk electrons:

$$\frac{\Gamma_{1b}}{\Gamma_{1p}} = \frac{\alpha\gamma_p}{1 - \alpha\gamma_b} \ , \tag{6.3}$$

where $\Gamma_{1p} = \Gamma_{1c} + \Gamma_{1w}$ is the collective primary electron flux due to all plasma bulk electrons, both collision-ejected and weakly confined. The details of the derivation of (6.1) and (6.3) are presented in Appendix C.

Eqs. (6.1) and (6.3) describe the stationary non-SCL SEE in the plane geometry model of a Hall thruster. In general, the emission produced by the plasma bulk and beam electrons depends on the energy of these groups of electrons. Thus, the total emission coefficient (6.1), which determines the regime of the SEE and the sheath potential profile, depends not only on the energy of the plasma bulk electrons, but also on the energy of the secondary electron beams and on the degree of penetration of these beams through the plasma slab. If $\gamma_b < \gamma_p$ then $\gamma < \gamma_p$, *i.e.*, the emission weakens in presence of the low energy secondary electron beams. In the limit $\alpha \to 0$, the total emission coefficient (6.1) becomes equal to the collective emission coefficient of plasma bulk electrons, $\gamma \to \gamma_p$. Eq. (6.3) states that the ratio of the primary

[1]Both bounding walls in Hall thruster simulations produce secondary electrons. Each of these walls are simultaneously a source and a target.

electron fluxes created by the beams and the plasma bulk electrons is determined, in fact, by the flux energies and the coefficient of beam penetration. It is important to know this ratio because, in presence of the secondary electron beams, the total flux of particles and energy to the wall ($\sim \Gamma_{1p} + \Gamma_{1b}$) is different from the losses of the confined plasma ($\sim \Gamma_{1p}$). If $\alpha\gamma_b \sim 1$, then $\Gamma_{1b}/\Gamma_{1p} \gg 1$ and the major part of the total primary electron flux is created by the secondary electron beams. In the limit $\alpha \to 0$, the electron beam flux becomes zero. Eqs. (6.1) and (6.3) are meaningful only if $\alpha\gamma_b < 1$, otherwise the stationary non-SCL SEE is not possible.

In simulations with EDIPIC, various parameters of the three components of the primary electron flux are traced. For simulations 1-8 of Tables 5.1 and 5.2, the values of energy $W_{b,c,w}$, emission coefficient $\gamma_{b,c,w}$, and flux $\Gamma_{1b,c,w}$ of the three components of primary electron flux are given in Table 6.1, as well as the collective plasma bulk values γ_p, Γ_{1p} and the beam penetration coefficient α. The total emission coefficient γ is determined by diagnostics included in the EDIPIC code, the ratio Γ_{1b}/Γ_{1p} must be calculated using the flux data output. Note that when α, γ_p, and γ_b are known, one can use Eqs. (6.1) and (6.3) to calculate the values of the total emission coefficient and the flux ratio, which provides an extra check for the model.

In Table 6.1, the values of the total emission coefficient γ obtained directly in the simulations are given together with the corresponding values calculated by Eq. (6.1) and denoted as $(\gamma)_{calc}$. There is very good agreement between γ and $(\gamma)_{calc}$; the difference does not exceed 2.9%. The flux ratio Γ_{1b}/Γ_{1p} calculated via the flux values is given together with the corresponding ratio calculated by Eq. (6.3) and denoted as $(\Gamma_{1b}/\Gamma_{1p})_{calc}$. Both values of the ratio agree well with each other; the relative difference does not exceed 4.2% (see Table 6.1). Thus, the developed model of the balance of electron fluxes towards the walls of a Hall thruster channel is confirmed by the PIC simulations.

The SCL SEE regime is established if $\gamma > \gamma_{cr}$, and with (6.1) the criterion of the SCL regime is

$$\gamma_p > \gamma_{p,cr}(\gamma_b, \alpha) = \gamma_{cr}\frac{1 - \alpha\gamma_b}{1 - \alpha\gamma_{cr}} \ , \tag{6.4}$$

where $\gamma_{p,cr}(\gamma_b, \alpha)$ is introduced as the threshold value of the collective emission co-

efficient for plasma bulk electrons corresponding to the SCL SEE regime for given secondary electron beam parameters α and γ_b. If $\alpha\gamma_b \ll 1$ while $\alpha\gamma_{cr} \sim 1$, the criterion (6.4) may be satisfied and the SCL SEE may occur only for $\gamma_p \gg \gamma_{cr}$. Note that γ_p is a function of several parameters itself. It is instructive to introduce the threshold value of the emission coefficient for collision-ejected electrons using (6.2) and (6.4) as follows:

$$\gamma_{c,cr}(\gamma_w, \Gamma_{1w}, \Gamma_{1c}, \gamma_b, \alpha) = \gamma_w \frac{\Gamma_{1w}}{\Gamma_{1c}} + \gamma_{cr} \frac{1 - \alpha\gamma_b}{1 - \alpha\gamma_{cr}} \left(1 + \frac{\Gamma_{1w}}{\Gamma_{1c}}\right) . \tag{6.5}$$

Then the SCL SEE regime occurs if $\gamma_c > \gamma_{c,cr}$.

The partial emission coefficients γ_b, γ_c, and γ_w depend on the corresponding electron energy at the moment of impact with the wall: W_b, W_c and W_w. The values of energy and emission coefficient of the three components of primary electron flux may be essentially different from each other (see Table 6.1).

The secondary electrons acquire additional energy while moving in the crossed electric E_z and magnetic B_x fields. This process is discussed below, in Section 6.2.

The collision-ejected electrons usually perform several "turbulent" collisions before they are scattered to the wall by a collision with a neutral atom, as described in Section 5.1.2. The average energy of the collision-ejected electrons, W_c, is proportional to the effective temperature in parallel direction $\widetilde{T}_z$. This energy may be large and the corresponding partial emission coefficient γ_c may substantially exceed unity (see Table 6.1).

The weakly confined electrons come from the region of the EVDF with $w_x \leq e\Phi_p$, which is populated mostly by the former secondary electrons slowed down due to the two-stream instability, as described in Section 6.3. The lifetime of these electrons inside the plasma is usually much shorter than the time between collisions $(\nu_{en}+\nu_t)^{-1}$, which results in $W_w \ll W_c$ and $\gamma_w \ll \gamma_c$. As a result, both the average energy and the emission coefficient of the weakly confined electrons are much smaller than those of the collision-ejected bulk electrons, and the collective plasma bulk emission coefficient γ_p determined by Eq. (6.2) is lower than the emission coefficient of the collision-ejected electrons γ_c (see Table 6.1).

Table 6.1: Plasma-wall interaction parameters for the simulations described in Tables 5.1 and 5.2. Comparison of the values found directly from simulations, γ and Γ_{1b}/Γ_{1p}, with the values $(\gamma)_{calc}$ and $(\Gamma_{1b}/\Gamma_{1p})_{calc}$ calculated by Eqs. (6.1) and (6.3).

Number	1	2	3	4	5	6	7	8
W_2, [eV]	10.8	11.5	11.2	9.5	10.8	10.5	11.6	11.5
W_b, [eV]	13.8	35.46	35.3	10.5	12.5	12.4	34.8	35.9
W_c, [eV]	57.6	99.1	53.1	8.2	22	22	107	94.6
W_w, [eV]	21.8	21	24.9	5.3	12.6	14.1	31.3	32.2
γ_b	0.55	0.961	0.974	0.544	0.545	0.562	0.941	0.969
γ_c	1.18	1.53	1.17	0.44	0.74	0.73	1.59	1.5
γ_w	0.62	0.65	0.777	0.288	0.49	0.515	0.75	0.8
γ_p	0.976	1.022	0.915	0.400	0.690	0.610	1.029	0.936
$\gamma_{p,cr}$	2.845	1.144	1.051	6.703	5.767	4.497	1.279	1.056
$\gamma_{c,cr}$	4.120	1.818	1.558	8.982	7.087	9.562	2.340	2.119
Γ_{1b} , $[10^{20}$ m^{-2}s$^{-1}]$	5.2	179	88.9	0.77	1.37	1.29	38.3	44.5
Γ_{1c} , $[10^{20}$ m^{-2}s$^{-1}]$	2.2	11.5	4.8	0.76	0.84	0.5	2.34	1.93
Γ_{1w} , $[10^{20}$ m^{-2}s$^{-1}]$	1.26	15.7	8.9	0.27	0.21	0.636	4.7	8
Γ_{1p} , $[10^{20}$ m^{-2}s$^{-1}]$	3.46	27.2	13.7	1.03	1.05	1.14	7.04	9.93
α	0.825	0.895	0.898	0.945	0.932	0.908	0.891	0.854
γ	0.722	0.971	0.967	0.45	0.61	0.59	0.957	0.965
$(\gamma)_{calc}$	0.722	0.969	0.966	0.463	0.608	0.584	0.954	0.963
Γ_{1b}/Γ_{1p}	1.50	6.58	6.49	0.75	1.30	1.14	5.44	4.48
$(\Gamma_{1b}/\Gamma_{1p})_{calc}$	1.48	6.54	6.55	0.78	1.31	1.13	5.66	4.64

Note, that simulations 2 and 7 have $\gamma_p > 1$, while the total emission coefficient is below the SCL SEE threshold, $\gamma < \gamma_{cr}$. For all simulations, criteria (6.4) and (6.5) are not satisfied, $\gamma_p < \gamma_{p,cr}$ and $\gamma_c < \gamma_{c,cr}$ (see Table 6.1).

6.2 Dynamics of secondary electron beams in crossed electric and magnetic fields

PIC simulations of thruster plasmas show that the energy of emitted secondary electrons at the moment when they hit the target wall is typically higher than the initial energy of emission. To understand the mechanism of this energy increase, consider a secondary electron emitted from the wall $x = 0$ with initial velocity components (v_{x0}, v_{y0}, v_{z0}). Note that electrons emitted from the wall $x = L$ and propagating towards the wall $x = 0$ can be treated similarly. The equations of motion of the electron are

$$\frac{d}{dt}v_x = \frac{e}{m}\frac{\partial}{\partial x}\Phi(x) \ , \tag{6.6}$$

$$\frac{d}{dt}v_y = -\omega_c v_z \ , \ \frac{d}{dt}v_z = -\frac{e}{m}E_z + \omega_c v_y \ , \tag{6.7}$$

where $\omega_c = eB_x/m$ is the electron cyclotron frequency. Along the x direction (normal to the walls) the electron is accelerated and decelerated by the gradient of the electrostatic potential $\Phi(x)$. Eq. (6.6) has an integral of motion $mv_x^2/2 - e\Phi(x) = mv_{x0}^2/2 = const$, which allows the v_x velocity to be expressed as a function of the x coordinate [here it is assumed that $\Phi(0) = 0$]. Then, for a given potential profile $\Phi(x)$, the electron flight time between the origin and the point with coordinate x can be expressed as the following function of x and v_{x0}:

$$\tau(x, v_{x0}) = \int_0^x \frac{dx'}{v_x(x')} = \int_0^x dx' \left[v_{x0}^2 + \frac{2e\Phi(x')}{m}\right]^{-1/2} \ . \tag{6.8}$$

The solution of Eqs. 6.7 is

$$\begin{aligned} v_y(t) &= V_{dr} + v_{\perp 0}\cos(\omega_c t + \phi) \ , \\ v_z(t) &= v_{\perp 0}\sin(\omega_c t + \phi) \ , \end{aligned} \tag{6.9}$$

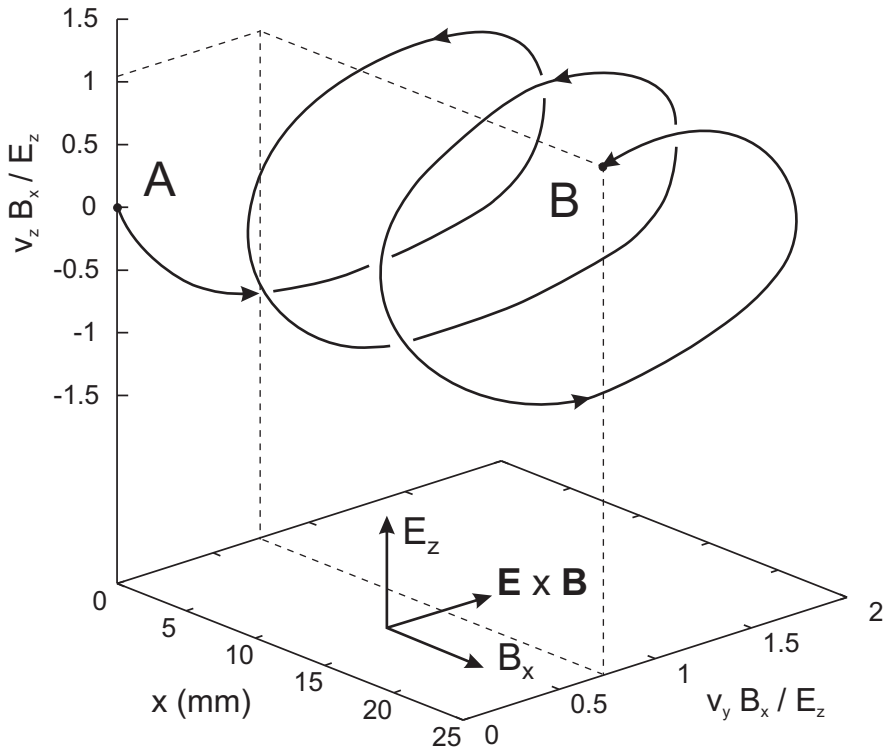

Figure 6.2: Trajectory in phase space $\{x, v_y, v_z\}$ of an electron emitted from the wall $x = 0$ with zero transverse energy $v_{y0}^2 + v_{z0}^2 = 0$. Point A is the start, point B is the end of the trajectory. The walls are at $x = 0$ and $x = 25$ mm.

where $V_{dr} = E_z/B_x$ is the velocity of the $\mathbf{E}\times\mathbf{B}$ drift, $v_{\perp 0} = [v_{z0}^2 + (v_{y0} - V_{dr})^2]^{1/2}$, and $\tan\phi = v_{z0}/(v_{y0} - V_{dr})$. Eqs. (6.9) describe rotation in the y-z plane with frequency ω_c and drift in the y direction with velocity V_{dr}. The electron trajectory in phase space $\{x, v_y, v_z\}$ is a spiral, as seen in Fig. 6.2. Combining (6.9) with (6.8) one obtains the energy w_b of the electron at point x:

$$\begin{aligned} w_b(x, v_{x0}, v_{y0}, v_{z0}) = {} & \frac{m(v_{x0}^2 + v_{y0}^2 + v_{z0}^2)}{2} + e\Phi(x) + mV_{dr}^2 \\ & + mV_{dr}^2 \left\{ \frac{v_{\perp 0}}{V_{dr}} \cos\left[\omega_c \tau(x, v_{x0}) + \phi\right] - \frac{v_{y0}}{V_{dr}} \right\} . \end{aligned} \tag{6.10}$$

The external parameters that affect the energy w_b are (i) the electric E_z and magnetic B_x fields that determine the drift velocity V_{dr}, and (ii) the potential profile $\Phi(x)$ that affects the electron flight time τ.

Introduce $f_2(v_x, v_y, v_z)$ – the initial velocity distribution function of the emitted

secondary electrons. Neglecting the loss of the secondary electron beam current between the walls (associated with the two-stream instability, see Section 6.3), the average energy $W_b(x)$ of the secondary electron beam at the point with coordinate x may be calculated by averaging over the *initial* beam flux, as follows:

$$W_b(x) = \frac{\int_0^\infty dv_x \int_{-\infty}^\infty dv_y \int_{-\infty}^\infty dv_z v_x w_b(x, v_x, v_y, v_z) f_2(v_x, v_y, v_z)}{\int_0^\infty dv_x \int_{-\infty}^\infty dv_y \int_{-\infty}^\infty dv_z v_x f_2(v_x, v_y, v_z)} \tag{6.11}$$
$$= W_2 + e\Phi(x) + mV_{dr}^2 + W_{b,osc}(x) \ .$$

Here

$$W_2 = \frac{\int_0^\infty dv_x \int_{-\infty}^\infty dv_y \int_{-\infty}^\infty dv_z v_x \left[m(v_x^2 + v_y^2 + v_z^2)/2\right] f_2(v_x, v_y, v_z)}{\int_0^\infty dv_x \int_{-\infty}^\infty dv_y \int_{-\infty}^\infty dv_z v_x f_2(v_x, v_y, v_z)}$$

is the average energy of emission, and

$$W_{b,osc}(x) = -mV_{dr}^2 \frac{\int_0^\infty dv_x \int_{-\infty}^\infty dv_y \int_{-\infty}^\infty dv_z v_x \cos\left[\omega_c \tau(x, v_x)\right] f_2(v_x, v_y, v_z)}{\int_0^\infty dv_x \int_{-\infty}^\infty dv_y \int_{-\infty}^\infty dv_z v_x f_2(v_x, v_y, v_z)} \tag{6.12}$$
$$\equiv -mV_{dr}^2 \left\langle \cos\left[\omega_c \tau(x, v_x)\right] \right\rangle$$

is the component that depends on the cyclotron rotation phase $\omega_c \tau(x, v_x)$ of each particle and oscillates in space, $\langle ... \rangle$ means averaging over the flux at the point x. Thus, the average beam energy (6.11) contains a constant part $W_2 + mV_{dr}^2$, the contribution from the plasma potential $e\Phi(x)$, and an oscillating part $W_{b,osc}$. An example of the secondary electron beam energy profile $W_b(x)$ obtained in simulation 7 of Table 6.1 is presented by curve 2 in Fig. 6.3a.

At the target wall, the contribution from the plasma potential to the beam energy vanishes, $\Phi(L) = 0$ (see curve 1 in Fig. 6.3a). As discussed later, the oscillating part at the wall is zero as well, $W_{b,osc}(L) \approx 0$ (see Fig. 6.3b). The contribution of the drift energy mV_{dr}^2 to the constant part of the beam energy (6.11) may be significant. This part determines the intensity of the SEE produced by the electron beam. The values of W_b at the wall $x = L$ and W_2 for the beam emitted at $x = 0$ are given in

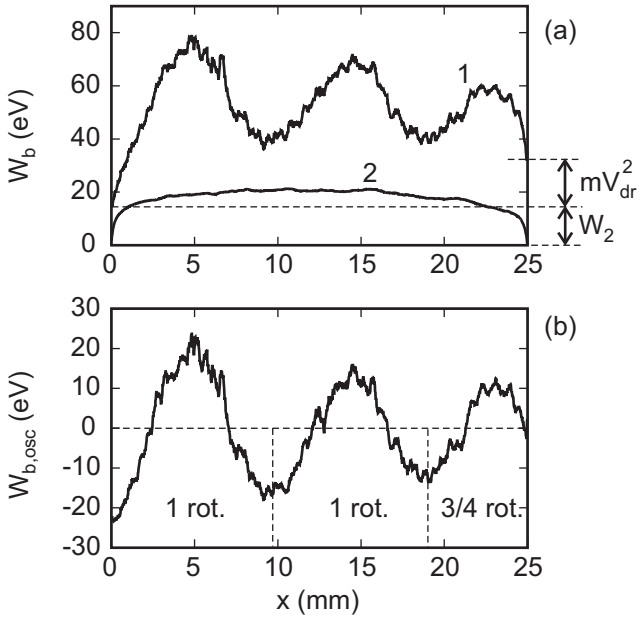

Figure 6.3: (a) The local average energy W_b of the electron beam emitted from the wall $x = 0$ versus the x coordinate (curve 1); the electrostatic potential versus the x coordinate (curve 2). (b) The oscillating part of the beam energy $W_{b,osc}$ versus the x coordinate, the complete and incomplete rotations are marked. The walls are at $x = 0$ and $x = 25$ mm. The results are obtained from simulation 7 of Table 6.1.

Table 6.1. For simulations 2, 3, 7, and 8, the external fields are $E_z = 200$ V/cm and $B_x = 100$ G, the drift velocity is $V_{dr} = 2 \cdot 10^6$ m/s, the average additional energy due to the drift motion $mV_{dr}^2/e = 22.8$ eV $\gg W_2$, and $W_b \approx W_2 + mV_{dr}^2 \gg W_2$. As a result, for these simulations the secondary electron beams produce SEE with the partial emission coefficient in the range $\gamma_b = 0.94 - 0.97$. For simulations 1, 4, 5, and 6, the electric field and the drift velocity are about four times smaller than above, so that the average additional energy is $mV_{dr}^2/e \sim 1$ eV $\ll W_2$, $W_b \approx W_2$, and $\gamma_b = 0.54 - 0.56$.

The oscillating part $W_{b,osc}$ plays an active role in formation of the stationary plasma state, prohibiting certain states and permitting others. It is reasonable to assume that $\gamma_b = \gamma_b(W_b)$ and that $d\gamma_b/dW_b > 0$, here $W_b \equiv W_b(L)$. Then, one may show that the stationary state must satisfy the following criterion

$$\left\langle -mV_{dr}^2 \frac{d}{d\tau} \cos\left[\omega_c \tau(x, v_x)\right] \right\rangle \Bigg|_{x=L} < 0 \ . \tag{6.13}$$

The criterion above is, in fact, the result of differentiation of the oscillating energy (6.12) with respect to the flight time of the beam electrons.

Consider a plasma with a small perturbation of the amplitude Φ_p of the potential profile $\Phi(x)$. If criterion (6.13) is satisfied, then the variation of the plasma potential modifies the total beam energy $W_b(L)$ [via the electron flight times τ and the oscillating part $W_{b,osc}(L)$] such that the variation of the emission coefficient γ [via γ_b, see (6.1)] compensates the plasma potential variation [75] (see left flowchart in Fig. 6.4 for a positive potential perturbation). The state, which does not satisfy criterion (6.13), is unstable, because the modification of the emission coefficient amplifies the perturbation of the plasma potential (see right flowchart in Fig. 6.4).

The form (6.13) of the stability criterion is exact, but it contains derivatives with respect to the flight time of electrons with different energies and is difficult to analyze. It is instructive to introduce a simplified criterion, where the individual flight times are replaced with the average electron flight time. Most secondary electrons have close values of the flight time because (i) they are emitted with an initial energy much lower than the energy provided by the plasma potential, and (ii) the plasma

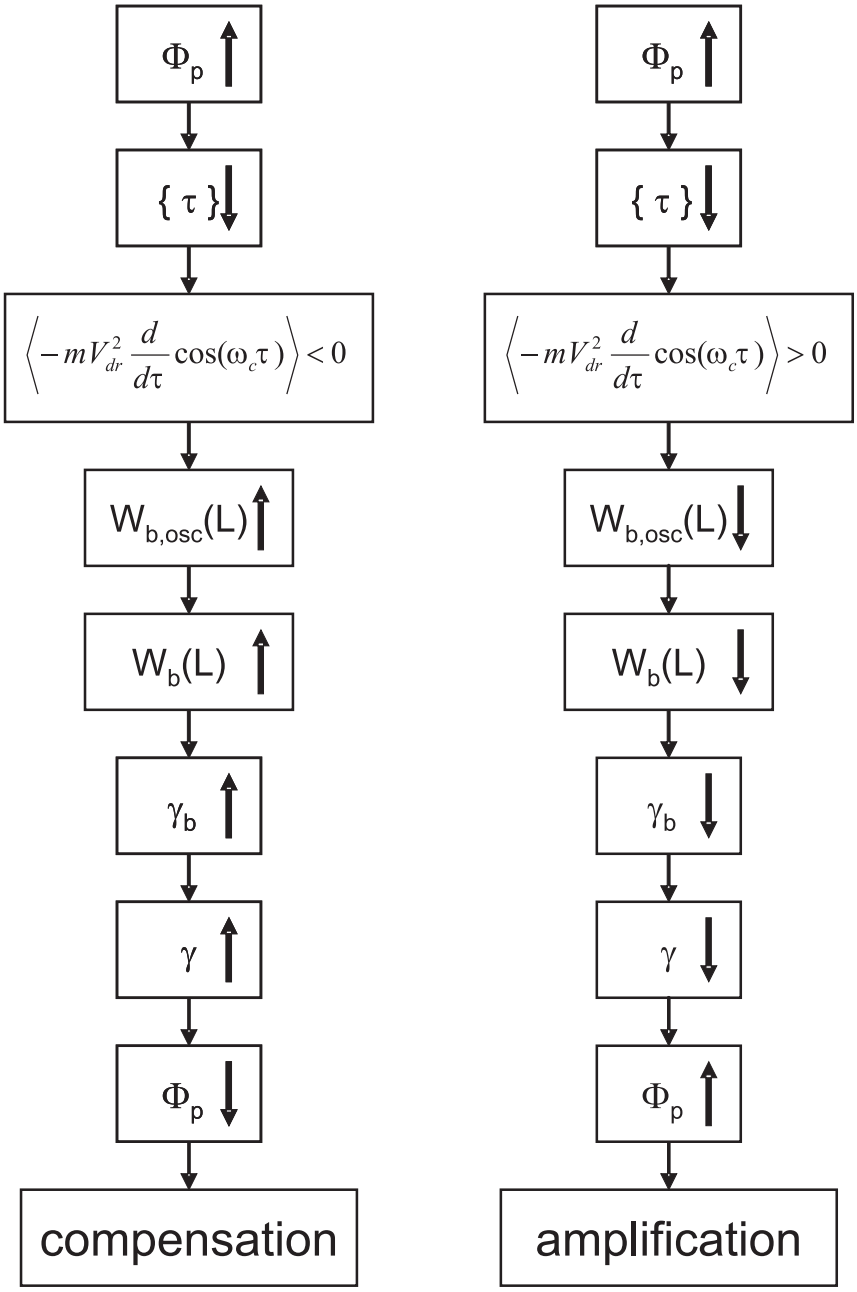

Figure 6.4: Qualitative flowchart of the plasma response to a small positive perturbation of plasma potential. Left column – perturbation is compensated by the increased emission if criterion (6.13) is satisfied. Right column – perturbation is amplified by the decreased emission if criterion (6.13) is not satisfied.

gap is narrow. If the average electron flight time T_L is defined as

$$\cos \omega_c T_L = \langle \cos [\omega_c \tau(x, v_x)] \rangle|_{x=L} ,$$

then the oscillating part of the beam energy at the target wall (6.12) is

$$W_{b,osc}(L) = -mV_{dr}^2 \cos (\omega_c T_L) . \tag{6.14}$$

With the average electron flight time introduced as above, the simplified stability criterion is

$$\frac{dW_{b,osc}(L)}{dT_L} < 0 , \quad \text{or} \quad \omega_c m V_{dr}^2 \sin (\omega_c T_L) < 0 . \tag{6.15}$$

Similar to (6.13), criterion (6.15) states that, in the stationary state, variations of the average electron flight time (increase or decrease) cause opposite variations of the beam energy (decrease or increase, respectively). The most probable stable states correspond to the minima of the derivative in (6.15) and are attained when $\sin(\omega_c T_L) = -1$:

$$\omega_c T_L = (2n + 3/2)\pi, \quad n = 0, 1, \dots . \tag{6.16}$$

Thus, the stationary potential profile must ensure that the emitted electrons, on average, perform some number of full rotations and 3/4 of a rotation during their flight between the walls. In particular, the electron in Fig. 6.2 performs $2\frac{3}{4}$ rotations, the profile of the oscillating energy in Fig. 6.3b has $2\frac{3}{4}$ periods, both figures correspond to the same simulation. Substituting (6.16) into (6.14), one obtains that at the stationary state the oscillating part of beam energy at the wall is zero, $W_{b,osc}(L) = 0$, which is confirmed by Fig. 6.3b.

Note that the electron flight time depends on the distance between the walls L. Modification of L changes the range of stable parameters. Recently, it was observed that the channel width had a strong effect on thruster operation [80], which may be related to the dependence of the secondary electron beam energy on the width of the channel.

Scattering of electrons by the wall is commonly considered as a source of the increased electron mobility across the magnetic field in Hall thrusters. This is the so-called near-wall conductivity (NWC) effect, described, *e.g.*, in Ref. [68]. The NWC

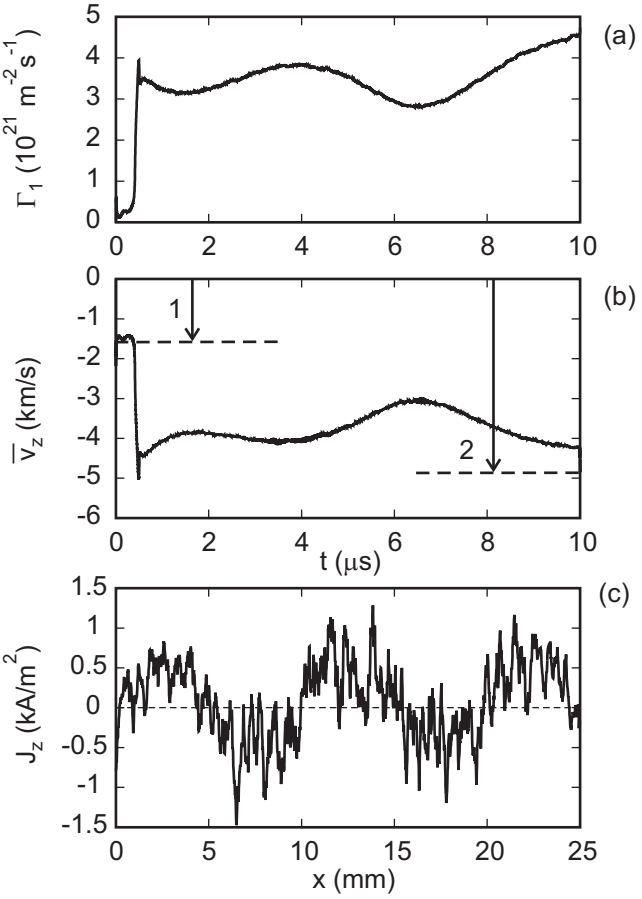

Figure 6.5: The near-wall conductivity effect. (a) The total primary electron flux Γ_1 to the wall $x = L$ versus time. (b) The average electron flow velocity $\overline{v}_z$ versus time, arrow 1 marks the value of the flow velocity due to collisions with neutral atoms and turbulent collisions, arrow 2 marks the value of the flow velocity allowing for the electron-wall collisions. (c) The profile of the electron current density $J_z(x)$. The walls are at $x = 0$ and at $x = 25$ mm. The results are obtained from simulation 7 of Table 6.1.

effect is observed in simulations with the EDIPIC code. In Fig. 6.5b, the temporal evolution of the electron flow velocity in the z direction

$$\overline{v}_z = L^{-1} \int_0^L dx \int d^3v v_z f(v_x, v_y, v_z, x) \ ,$$

where $f(v_x, v_y, v_z, x)$ is the plasma EVDF, is presented for simulation 7 of Table 6.1. The simulation starts with the plasma occupying the region $0.05L < x < 0.95L$. At the initial stage $0 < t < 0.5$ μs, until the ion background reaches the walls, the electron flux to the wall is small (see Fig. 6.5a). At this stage the electron mobility is determined mostly by collisions with neutral atoms and "turbulent" collisions, the corresponding electron flow velocity is

$$\overline{v}_z = \frac{e(\nu_t + \nu_{en})}{m[(\nu_t + \nu_{en})^2 + \omega_c^2]} E_z \ .$$

The value $\overline{v}_z$ calculated by the above expression with ν_{en}, ν_t, and E_z of simulation 7 from Table 5.2 is presented by arrow 1 in Fig. 6.5b and corresponds well to the actual value of electron flow velocity (the red curve). After the ions reach the wall, at $t > 0.5$ μs, both the electron flux to the wall (see Fig.6.5a) and the electron flow velocity (see Fig.6.5b) increase significantly. Introducing the frequency of electron-wall collisions as

$$\nu_w = \frac{2\Gamma_1}{\overline{n}_e L} \tag{6.17}$$

and using $\nu_{eff} = \nu_t + \nu_{en} + \nu_w$ as the effective frequency for calculation of the electron flow velocity, one obtains the increased value marked by arrow 2 in Fig. 6.5b. Note that this simple estimation produces a value close to the actual electron flow velocity in simulations that include the strong NWC effect.

It is interesting that the profile of the electron current $J_z(x)$ is modulated (see Fig. 6.5c) as it was predicted in Ref. [68]. The modulated current profile is formed by the counter-propagating secondary electron beams that rotate around the magnetic force lines. Note that the number of positive half-periods of the current profile $J_z(x)$ in Fig. 6.5c exceeds the number of the negative half-periods (three to two). It is evident that if the secondary electron beams performed an integer number of rotations, then the number of positive and negative half-periods of the current profile

would have been equal to each other and the total current due to the NWC effect would have been zero. If such a situation was possible, then the strong emission would have been combined with low axial electron mobility, modifying the regimes of a Hall thruster operation at high voltages [79]. However, the condition (6.16) on the electron flight time in a steady state prohibits an integer number of rotations and ensures that the NWC effect *will* contribute to the axial electron mobility as long as the wall collision frequency is sufficiently large, $\nu_w \geq \nu_t + \nu_{en}$.

6.3 Penetration of an electron beam through a non-Maxwellian plasma slab

In Section 6.1, the coefficient of the secondary electron beam penetration α was introduced phenomenologically as the ratio of the beam current reaching the wall to the current emitted from the opposite wall. In PIC simulations, the penetration coefficient is usually high, $\alpha = 80 - 90\%$ (see Table 6.1), even at high emission currents. The process of the penetration of the electron beam through the plasma slab is discussed below.

Due to the low frequency of collisions with neutral atoms, the main mechanism that decreases the energy of beam electrons and the beam current through the plasma is the two-stream instability [129, 130]. Consider simulation 2 of Tables 6.1 and 5.1, where the penetration coefficient is $\alpha = 0.895$. In the midplane $x = L/2$, the plasma density is $n_e = 4.2 \cdot 10^{17}$ m^{-3}, the plasma potential is $\Phi_p = 22$ V, and therefore, the beam velocity is $v_b = 2.7 \cdot 10^6$ m/s (here the initial energy of beam emission is neglected compared to the energy acquired from the plasma potential). With these parameters, the beam density is $n_b = \Gamma_{1b}/v_b = 7.4 \cdot 10^{15}$ m^{-3} and the relative beam density is $n_b/n_e = 0.018$.

The EVDF over v_x of the beam emitted at $x = 0$ is represented by curve 3 in Fig. 5.5a. The beam has significant velocity dispersion, $\Delta v_b/v_b \approx (T_t/e\Phi_p)^{1/2} \approx 0.3$, where $T_t = 2$ eV is the temperature of the true secondary electrons (the major component of the emitted current). Since $(n_b/n_e)^{1/3} \approx 0.26 \sim \Delta v_b/v_b$, the beam cannot

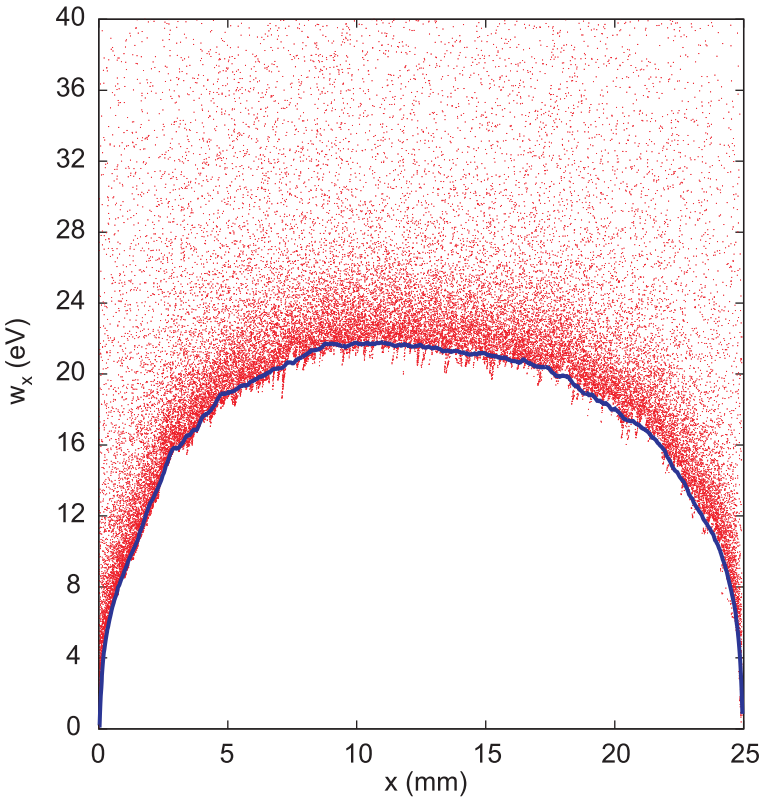

Figure 6.6: For simulation 2 of Table 6.1, the phase plane $\{x, w_x\}$ of the secondary electron beam emitted from the wall $x = 0$. The other wall is at $x = 25$ mm. Red points mark the beam particles, the blue line is the plasma potential profile averaged over the plasma period. The phase plane is obtained at $t = 6.83$ μs.

be considered as a cold one [1] and the growth rate of the instability is much smaller than the growth rate of the instability of a cold beam $\gamma_{cold} = 3^{1/2}2^{-4/3}(n_b/n_e)^{1/3}\omega_p \approx 0.18\omega_p$. The phase plane $\{x, v_x\}$ of the secondary electron beam emitted from the wall $x = 0$ (see Fig. 6.6) shows that a small number of beam electrons lose energy (signified by the "threads" with a period of about $\lambda = 0.3$ mm), however, trapping of the beam particles by the excited electrostatic wave does not occur (the "threads" do not exhibit twisting). The instability does not develop into the nonlinear stage, and the number of beam particles with energy w_x below the local value of potential $e\Phi(x)$ (these particles cannot penetrate through the sheath near the target wall) is much smaller than the number of particles with $w_x > e\Phi(x)$.

The criterion of plasma stability with respect to the two-stream instabilities is

the decreasing EVDF [134]:

$$\frac{\partial}{\partial(v^2)} f(v) < 0 \quad \text{for all } v \ . \tag{6.18}$$

For the considered case, although the two-dimensional distribution $f_{xz}(v_x, v_z) = \int_{-\infty}^{\infty} dv_y f(v_x, v_y, v_z)$ presented in Fig. 5.5 is nonmonotonic, the total EVDF over velocity normal to the walls $f_x(v_x) = \int_{-\infty}^{\infty} dv_y \int_{-\infty}^{\infty} dv_z f(v_x, v_y, v_z)$ is very close to the stability condition (6.18) (red curve in Fig. 6.7a). The total EVDF is a decreasing function of v_x because of the non-Maxwellian EVDF of the plasma bulk electrons, which is depleted in the loss cone $w_x > e\Phi_p$ but "enriched" in the weakly confined zone $e\Phi_p > w_x > e(\Phi_p - \Delta\Phi)$, where $\Delta\Phi \ll \Phi_p$ (blue curve in Fig. 6.7a). If one takes a Maxwellian EVDF for the bulk electrons with the same electron temperature as the effective electron temperature $\widetilde{T}_x$ found for the thruster plasma (blue curve in Fig. 6.7b), and combines it with the secondary electron beam EVDF (green curve in Fig. 6.7b, identical to that in Fig. 6.7a), then the total EVDF will have an increasing part (red curve in Fig. 6.7b) and may produce a strong two-stream instability.

The "enrichment" of the EVDF by the weakly-confined electrons is important for good beam penetration. This "enrichment" occurs similar to the formation of the plateau on the EVDF at the non-linear saturation stage of the two-stream instability [1]. To study the modification of the bulk EVDF during the beam propagation through the plasma slab, the symmetric injection of electron beams with constant current into the bounded plasma has been simulated in the following way. Initially, a uniform Maxwellian plasma occupies the whole space $0 < x < L$, boundaries $x = 0$ and $x = L$ have fixed potential $\Phi = 0$ and absorb electrons. No external fields are applied. It is assumed that the plasma is collisionless and the ions form a uniform immobile background. The initial plasma parameters are close to that of plasmas in Hall thruster simulations – the plasma density is $n_e = 10^{17}$ m^{-3}, the initial electron temperature is $T_{e0} = 10$ eV, and the system width is $L = 2.5$ cm. After the system is released, the electrons with the highest energy leave the system, the narrow sheath regions form at the boundaries, and the plasma acquires some potential Φ_p (see Fig. 6.8b for $t < 20$ ns). The potential $\Phi(x)$ is uniform outside of

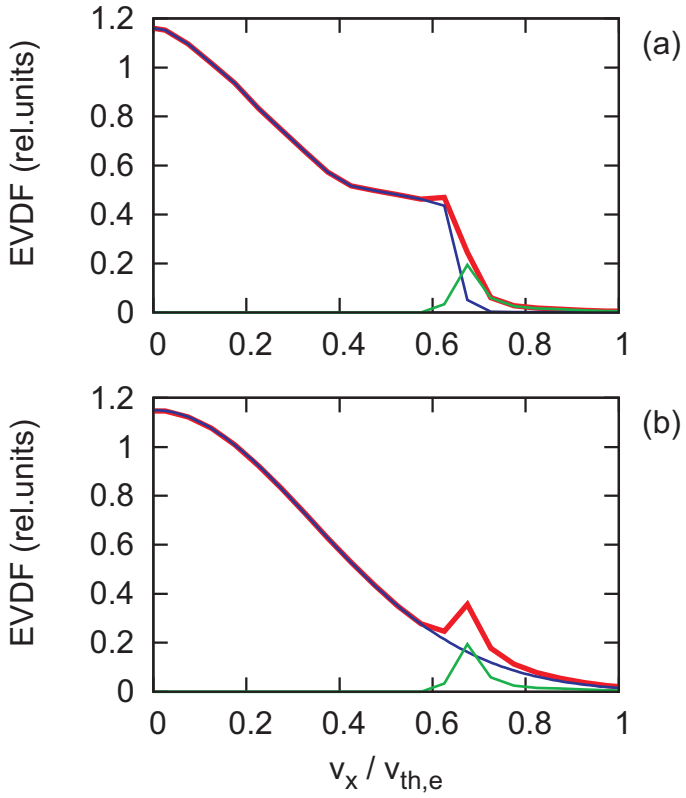

Figure 6.7: (a) The EVDF over velocity normal to the walls for all electrons (the red curve), for plasma bulk electrons (the blue curve), and for the secondary electron beam emitted from the wall $x = 0$ (the green curve); the EVDFs are obtained in the midplane for case 2 of Table 5.1. (b) The blue curve is the Maxwellian EVDF with temperature $T_e = 12.3$ eV equal to the effective electron temperature $\widetilde{T}_x$ in case 2 of Table 5.1; the green curve is the EVDF of the secondary electron beam, identical to that in figure (a); the red curve is the total EVDF formed by the Maxwellian and the beam EVDFs. The velocity is given in units of $v_{th,e} = (2eT_{e0}/m)^{1/2}$, where $T_{e0} = 53$ eV is the initial electron temperature in simulation 2 of Table 5.1.

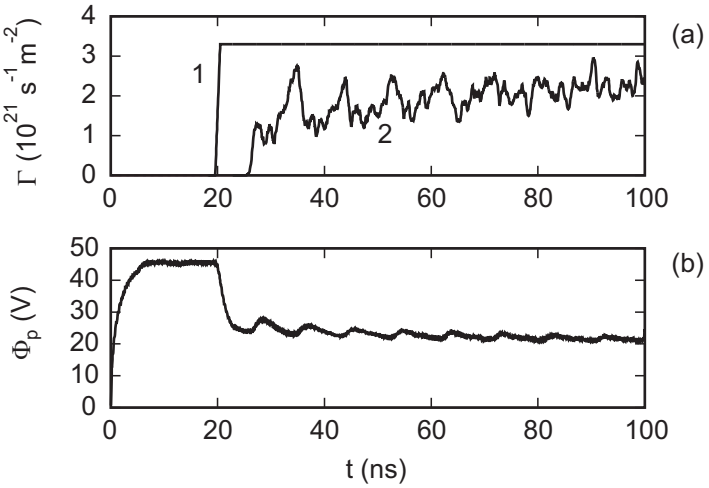

Figure 6.8: Simulation of the symmetric injection of constant electron current into a collisionless Maxwellian plasma slab with immobile ions. (a) Curve 1 is the electron flux emitted at wall $x = 0$ versus time, curve 2 is the corresponding penetrated flux detected at the boundary $x = L$. (b) The plasma potential in the midplane versus time. The electron injection is started at $t = 20$ ns.

the sheath regions, it has a Π-shaped profile. The EVDF is a cutoff Maxwellian, with $|v_x| < (2e\Phi_p/m)^{1/2}$. After 20 nanoseconds of system evolution, the symmetric injection of electrons with constant current is started from both boundaries (see curve 1 in Fig. 6.8a). The electrons are injected normal to the walls, with a half-Maxwellian EVDF of temperature $T_b = 2$ eV (the true SEE component in Hall thruster simulations has the same temperature). The injection decreases the plasma potential (see Fig. 6.8b) for $t > 20$ ns, similar to the SEE effect. The injected electrons are accelerated by the drop of potential across the narrow sheath and then propagate through the plasma slab. Eventually, at each boundary the current of the electrons emitted from the *opposite* boundary is registered (see curve 2 in Fig. 6.8a).

At first, after the injection is started, the bulk EVDF remains a cutoff Maxwellian (blue curve in Fig. 6.9a), with the cutoff velocity corresponding to the new plasma potential. The total EVDF (red curve in Fig. 6.9a) does not satisfy stability criterion (6.18). Thus, the two-stream instability develops, many beam electrons are slowed down by the excited electrostatic wave and cannot penetrate through the sheath

at the target wall, the average beam penetration is low, about 50% (Fig. 6.8a for 27 ns $< t <$ 50 ns). The slowed down beam electrons become part of the group of weakly confined electrons. Accumulation of these electrons results in the total EVDF, which nearly satisfies stability criterion (6.18) (red curve in Fig. 6.9b). Then the two-stream instability weakens and the beam penetration increases (Fig. 6.8a for $t >$ 80 ns). Note that the plasma bulk EVDF (blue curve in Fig. 6.9b) at the stage of enhanced beam penetration deviates from the Maxwellian EVDF (dashed magenta curve in Fig. 6.9b) for $1.2v_{th,e} < v_x < 1.45v_{th,e}$.

In the simulation described above, the relative electron density is $n_b/n_0 = 0.01$ and the beam penetration coefficient is about $\alpha = 0.66$, which is lower than in Hall thruster simulation 2 of Table 6.1, where the value of beam penetration is $\alpha = 0.895$ for a more dense beam $n_b/n_0 = 0.018$. The two-stream instability is strong in simulations with constant injection and immobile ions because in such simulations (i) the beam accelerates only in the narrow sheath region, and (ii) the beam interacts with a uniform plasma, which maintains the resonance between the beam and excited wave and supports the instability. In Hall thruster simulations, the ions are mobile, so the plasma density and the electrostatic potential are not uniform across any portion of the plasma gap, which disturbs the resonance between the beam particles and the wave and suppresses the instability [148]. In such simulations, the width of the region in the midplane, where the plasma potential and the plasma density may be considered uniform, is typically about $L/3$ (see Fig. 6.6), *i.e.*, less than 1 cm. One-dimensional simulations of the two-stream instability with periodic boundary conditions were undertaken to find (i) the distance a half-Maxwellian beam can travel before it loses part of its current, and (ii) its final current loss. These simulations are described below.

The simulated system consists of a plasma and an electron beam. Initially, the plasma electrons of density n_e have a cutoff Maxwellian velocity distribution function:

$$f_p(v_x) = \frac{n_e}{N} \exp\left(-\frac{mv_x^2/2}{T_e}\right),$$

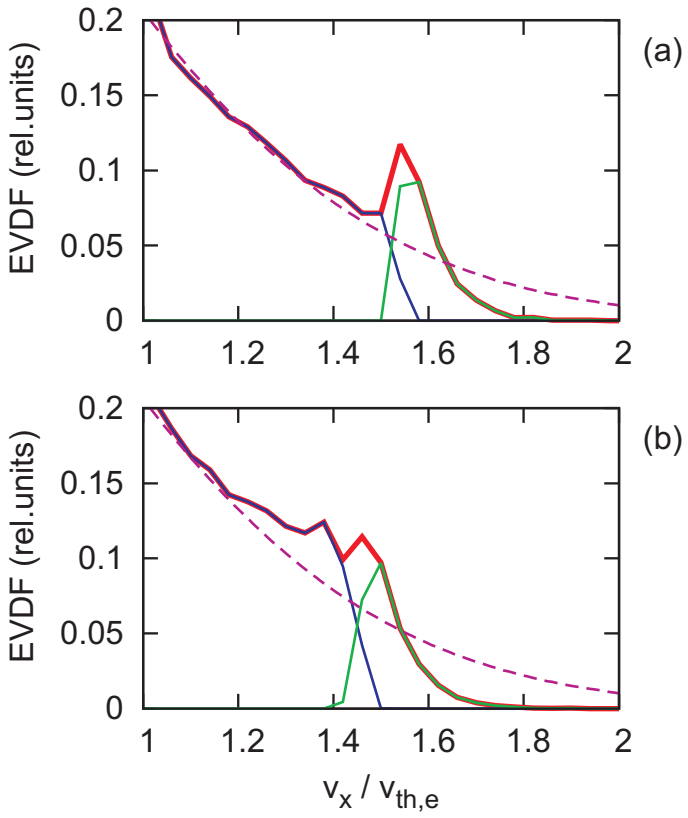

Figure 6.9: Simulation of the symmetric injection of constant electron current into a collisionless Maxwellian plasma slab with immobile ions. (a) The EVDF over velocity normal to the walls for all electrons (red curve), for plasma bulk electrons (blue curve), and for the injected electron beam emitted from the wall $x = 0$ (green curve) at the moment $t = 27$ ns. (b) Same as above, at the moment $t = 90$ ns. The EVDFs are averaged over the region 1 mm $< x <$ 2 mm. The velocity is given in units of $v_{th,e} = (2T_{e0}/m)^{1/2}$, where $T_{e0} = 10$ eV is the initial electron temperature. The dashed magenta line is the Maxwellian EVDF with temperature T_{e0}.

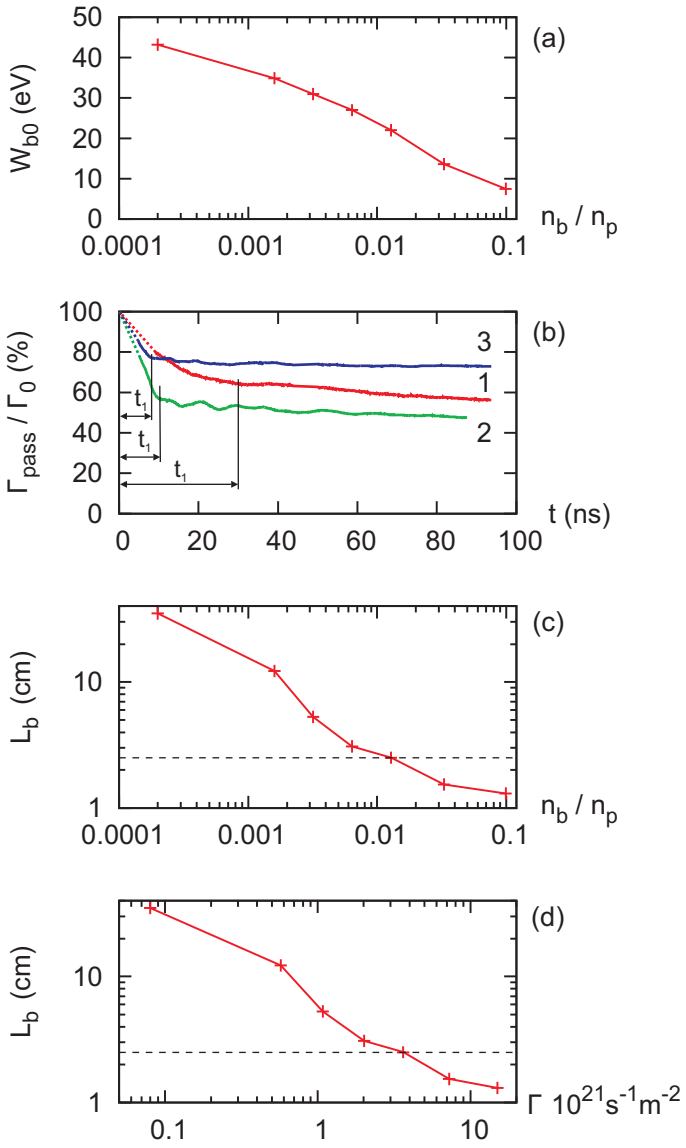

Figure 6.10: Simulations with periodic boundaries of propagation of a half-Maxwellian electron beam through a cutoff Maxwellian plasma. (a) The cutoff energy (the minimal initial energy of beam particles) versus the relative density of the electron beam. (b) Temporal evolution of the penetration coefficient calculated by (6.19), curves 1, 2, and 3 correspond to the relative beam densities $n_b/n_0 = 0.0016$, 0.0064, and 0.099. (c) The length of beam relaxation versus the relative beam density. (d) The length of beam relaxation versus the initial beam flux. The dashed line in (c) and (d) marks $L = 2.5$ cm – the width of the plasma gap in Hall thruster simulations. The plasma density $n_e = 10^{17}$ m^{-3}, the plasma temperature $T_e = 10$ eV, and the beam temperature $T_b = 2$ eV.

where $|v_x| < v_0$, v_0 is the cutoff velocity, T_e is the electron temperature, and

$$N = \int_{-v_0}^{v_0} dv_x \exp\left(-\frac{mv_x^2/2}{T_e}\right) .$$

The EVDF of the electron beam of density n_b is

$$f_{b0}(v_x) = n_b \left(\frac{2m}{\pi T_b}\right)^{1/2} \exp\left(-\frac{mv_x^2/2 - W_0}{T_b}\right) ,$$

where $v_x > v_0$, $mv_0^2/2 = W_0$, and T_b is the beam temperature. The plasma temperature is $T_e = 10$ eV and the beam temperature is $T_b = 2$ eV. The cutoff energy W_0 equals the plasma potential $e\Phi_p$ that forms in the simulation with immobile ions and two symmetrically injected constant current electron beams with the same relative beam density n_b/n_p. This energy decreases for beams with higher density, as shown in Fig. 6.10a. The period of the system is chosen much larger than the plasma wavelength, $L = 2$ cm, $L \gg 2\pi v_0/\omega_p$, to decrease the effects of longitudinal wavenumber detuning on the instability. The ions form an immobile uniform background with density $n_p + n_b$. No external fields are applied. The plasma is collisionless. During the evolution of the system, the two-stream instability develops, some of the beam electrons lose energy and the beam EVDF $f_b(v_x)$ deviates from the initial form $f_{b0}(v_x)$. The coefficient of beam penetration in this case is defined as the ratio of the current Γ_{pass} of beam electrons with energy $w_x > W_0$ to the initial beam current Γ_0:

$$\alpha = \frac{\Gamma_{pass}}{\Gamma_0} = \frac{\int_{v_0}^{\infty} dv_x v_x f_b(v_x)}{\int_{v_0}^{\infty} dv_x v_x f_{b0}(v_x)} . \tag{6.19}$$

In simulations, the beam energy loss and current reduction occur in two stages (see Fig. 6.10b). Most of the current reduction takes place in the first stage. During the much longer second stage, the current Γ_{pass} decreases insignificantly, slowly approaching a stationary value. The first stage finishes at the moment t_1, when trapping of the beam particles by the excited electrostatic wave begins. The length of the beam relaxation L_b is introduced as the distance the beam travels until the particle trapping begins. The value of t_1 is obtained directly in simulations (see Fig. 6.10b), from which the beam relaxation length is calculated as $L_b = v_0 t_1$. In Figs. 6.10c and d, the length of the beam relaxation is given as a function of the

electron beam density and current, respectively. One can see that for $n_b/n_p < 0.01$, *i.e.*, for $\Gamma_0 < 3 \cdot 10^{21}$ s^{-1}m^{-2} with $n_p = 10^{17}$ m^{-3}, the beam relaxation length exceeds the width of the plasma gap $L = 2.5$ cm in Hall thrusters. In simulations with typical Hall thruster parameters, presented in Table 6.1, the relative density of secondary electron beams in the midplane is $n_b/n_p < 0.02$. The corresponding beam relaxation length L_b exceeds the width of the middle quasi-uniform region, which is about 1 cm. Therefore, the two-stream instability may not reach its saturation level. This agrees with the linear behavior of the two-stream instability represented in Fig. 6.6 and the overall high level of penetration of the secondary electron beams in Hall thruster simulations.

6.4 Summary

It is found from EDIPIC simulations that the total primary electron flux towards the wall of a Hall thruster channel consists of three components that are characterized by essentially different energy: (i) the secondary electrons emitted from the opposite wall (in Hall thruster the secondary electrons form the two counter-propagating electron beams), (ii) the electrons from the plasma bulk with anisotropic EVDF scattered to the wall after collisions with neutral atoms, and (iii) the so-called weakly confined electrons from the boundary layer on the phase plane $\{x, w_x\}$ between the electrons of the plasma bulk (deeply confined by the plasma potential) and the secondary electron beams (accelerated by the plasma potential). These three electron groups produce SEE with different partial emission coefficients corresponding to the energy of the group.

The model of SEE with multi-component primary and secondary electron fluxes inside the ceramic channels of Hall thrusters is developed. The model reveals that the total average emission coefficient contains contributions from the secondary electron beams, the collision-ejected electrons, and the weakly confined electrons. It is important that the total emission coefficient is no longer the function of the energy of the plasma bulk electrons only. The modified criterion of the SCL SEE is obtained.

The criterion shows that, in presence of the low-energy primary electron fluxes of secondary and weakly confined electrons, the SCL regime only occurs if the emission due to the plasma bulk electrons is much more intense than in the case when the plasma bulk is the only source of primary electrons. As a result, in simulations, the average energy of plasma bulk electrons exceeds the threshold value of the SCL SEE for a Maxwellian plasma by several times, yet the emission remains in the non-SCL regime. This result agrees with the experimental observation of the anomalously high electron temperature inside Hall thrusters [78, 79].

It is found in simulations that secondary electrons acquire additional energy related with the $E \times B$ drift motion *after* the emission. The average energy of the emitted electrons at the moment when they impact the target wall exceeds the average initial energy of emission by $m(E_z/B_x)^2$. In strong external electric fields, the final secondary electron beam energy is sufficient to produce equally strong SEE. In this case, most of the primary electron current is created by electrons emitted from the walls, not by electrons from the confined plasma. This is the other mechanism that reduces plasma electron cooling due to wall losses, in addition to the depletion of the EVDF loss cone discussed in Chapter 5.

It is found that the energy of the secondary electron beam contains the important component $W_{b,osc}$, which is an oscillating function of the average electron flight time T_L. It is shown that a stable stationary state must satisfy the criterion $dW_{b,osc}(L)/dT_L < 0$ and that the emitted electrons must perform $n + 3/4$ rotations before they reach the target wall (here n is an integer).

The increase of the axial electron mobility due to the NWC effect under the condition of intense SEE is observed in simulations. A modulated profile of the axial electron current qualitatively similar to that described by Morozov and Savel'ev in Ref [68] is obtained. Physically, the oscillating behavior of the secondary electron beam energy with respect to the electron flight time (and the distance from the emitting wall) and the modulated profile of the axial electron current are based on the same effect of cyclotron rotation.

PIC simulations show that the two-stream instability results in minor losses of

the secondary electron beam current during its propagation between the walls. The bulk EVDF (depleted in the loss cone and enriched in the region of weakly confined electrons), when combined with the EVDFs of secondary electron beams (close to a half-Maxwellian EVDF), forms a velocity distribution, which is a decreasing function of the electron velocity normal to the walls and is stable with respect to the two-stream instability. Additionally, simulations with periodic boundary conditions show that for the typical parameters of Hall thruster plasmas, *i.e.*, the plasma density and the secondary electron beam current and energy, the width of the plasma gap in Hall thrusters is too short for the two-stream instability to develop to the nonlinear saturation level. Under such conditions the two-stream instability is weak, and most of emitted electrons penetrate through the plasma slab.

Chapter 7

Relaxation oscillations of the sheath

Morozov [149] pointed out that in Hall thrusters the sheath structure can be much more complicated than predicted by simple theories. He showed that the sheath potential solution is unstable if it is characterized by negative conductivity, which is possible for a non-Maxwellian EVDF. Basing on experiments that revealed electrons randomly scattered by the walls with energy much lower than the expected plasma potential, Morozov formulated the idea that an unstable potential profile may flicker, dipping to zero and thus enhancing plasma-wall interaction.

The sheath at the interface between a Maxwellian plasma and a secondary electron emitting wall switches to the SCL regime if the plasma temperature exceeds the critical value [76]. In bounded plasmas with non-Maxwellian EVDF, where the counter-propagating beams of secondary electrons constitute part of the primary electron fluxes to the walls (see Chapter 6), the critical value of the partial emission coefficient for the plasma bulk electrons (6.4) is substantially larger than the critical emission coefficient (1.12) for a Maxwellian plasma [75]. Thus, the SCL regime in the bounded plasma requires the energy of the bulk plasma electrons to be much higher than that of a Maxwellian plasma with critical temperature.

In simulations with the EDIPIC code, the SCL regime was not observed for the plasma parameters corresponding to the experimental values. However, in some simulations with an artificially increased frequency of "turbulent" collisions (*i.e.*, the heating intensity), a new regime of sheath operation with quasi-periodic oscillations has been observed, which qualitatively corresponds to Morozov's predictions. In this regime, the sheath becomes space-charge limited for only short periods of time, and most of the time stays in the non-SCL regime.

The period of these oscillations ($0.1 - 1$ μs) is in the same range as the period of ion plasma oscillations $T_i = 2\pi\omega_{pi}^{-1} \simeq 0.1 - 0.2$ μs. Therefore, the ion plasma oscillations were considered a probable reason for such oscillations. Indeed, the ion plasma oscillations may perturb the sheath structure and allow the anisotropic energetic electrons of the plasma bulk to reach the walls, which results in the SCL regime. Hernqvist [150] observed oscillations with a frequency corresponding to the ion plasma oscillations in ion-neutralized electron beams. The mechanism supporting these oscillations involved interaction of the secondary electron current (from the bounding walls around the beam) with the AC electric field of ion oscillations. Low frequency oscillations in beam-plasma systems have been observed, *e.g.*, in Refs. [151, 152], and the excitation of the oscillations was attributed to the relative drift of electrons and ions [153, 154]. In a gas discharge, the plasma ion oscillations were observed with a negatively biased probe in [155]. The spectrum of the ion oscillations extending from ion acoustic waves to ion plasma oscillations was measured in [156].

In the simulated plasma system, motion of the electrons relative to the ions in the direction normal to the plasma boundary is observed only in the narrow sheath region, thus the Buneman instability cannot be the reason for the excitation of oscillations. It was found that the frequency of the observed sheath oscillations is not proportional to the ion plasma frequency. Moreover, the frequency of the sheath oscillations may significantly vary during the evolution of the simulated system.

Such behavior corresponds to the oscillations of nonlinear systems. For example, in a one-dimensional low pressure thermionic converter, multiple electron DC states are possible for the same ion DC state [157]. These states produce different potential profiles and are responsible for low-frequency relaxation-type oscillations [158]. The current-voltage characteristic of a thermionic discharge is nonlinear, with hysteresis corresponding to the negative resistance; the oscillations in this system may become irregular and chaotic [159, 160]. The sudden jumps in the behavior of a discharge with negative conductivity may be described as a cusp catastrophe [161].

The negative resistance may be caused by different reasons. The negative differential resistance of the electron sheath caused by electron inertia results in high

frequency sheath oscillations being generated around a positively biased current-carrying electrode immersed in a Maxwellian plasma [162]. The instability with the low frequency of the order of the ion plasma frequency, which occurs in the current-carrying sheath around the negatively biased grid in double-plasma devices, is related with the negative sheath resistance due to ion inertia [163, 164]. In Hall thruster simulations, the negative resistance of the sheath appears due to the non-Maxwellian velocity distribution of confined electrons and SEE from the walls.

This Chapter is organized as follows. In Section 7.1, the evolution of plasma parameters during one period of relaxation oscillations is described. Section 7.2 explains the mechanism of the stepwise transition from the non-SCL to the SCL regime, also the current-voltage characteristics of the sheath with negative conductivity are presented. Section 7.3 contains the qualitative criterion of the oscillating regime and the results of parametric studies of this regime. Conclusion are given in the Summary Section.

7.1 Evolution of plasma parameters during the relaxation sheath oscillations

A PIC simulation of a thruster-like system was carried out with most of the parameters close to those used in simulation 7 described in Tables 5.2 and 6.1: the distance between the dielectric walls was $L = 2.5$ cm, the external electric field was $E_z = 200$ V/cm, the magnetic field was $B_x = 100$ Gauss, the neutral gas density was $n_a = 10^{12}$ cm^{-3}, the initial plasma density was $n_{e0} = 10^{11}$ cm^{-3}, the initial EVDF was a drifting Maxwellian with temperature $T_{e0} = 10$ eV and drift velocity in the y direction $V_{dr} = E_z/B_x$. The "turbulent" collision frequency was increased by 4 times compared to simulation 7 to $\nu_t = 2.8 \cdot 10^6$ s^{-1}. The simulation parameters were not chosen so as to reproduce some regime of a real Hall thruster, but rather to investigate the plasma-wall interaction and the regime of the sheath with SEE while under the condition of intense turbulent heating. In particular, the SCL SEE regime with $\gamma > \gamma_{cr}$ and a nonmonotonic potential profile in the sheath regions was

expected.

In the simulation, the plasma became strongly anisotropic: $\langle w_y \rangle = 53$ eV, $\langle w_z \rangle = 42$ eV, $\langle w_x \rangle = 4.2$ eV, $\langle w_{y,z} \rangle \gg \langle w_x \rangle$, where averaging $\langle ... \rangle$ is done over all particles. The total average energy of motion parallel to the walls $\langle w_y \rangle + \langle w_z \rangle \sim 95$ eV significantly exceeds the critical electron temperature $T_{cr} \approx 18$ eV for the SEE properties of the chosen wall material.

The SCL SEE regime was observed in the simulation, but a stationary SCL state was not observed. Instead, it was found that the system "switches" quasi-periodically between the SCL and non-SCL regimes. The SCL state lasts for a short time, while the non-SCL state lasts much longer (the width of the spikes in Fig. 7.1a is much smaller than the intervals between the spikes). In the SCL state, the primary electron flux grows abruptly and is several times higher than during the non-SCL state (see Fig. 7.1b) and the plasma potential decreases (see Fig. 7.1c). A typical nonmonotonic potential profile from the SCL state with $\gamma > \gamma_{cr}$ is shown in Fig. 7.2a,b,c. The monotonic potential profile from the non-SCL state is presented in Fig. 7.2d. In the SCL state, the electron energy losses at the walls are significantly enhanced compared to the non-SCL state, which strongly limits the electron energy. Note that the dependence of the average electron energy versus time shown in Fig. 7.1d has a sawtooth shape, where the abrupt drops at the SCL state are followed by gradual increases during the non-SCL state. The observed global oscillations of the plasma parameters are strongly nonlinear, below they are referred to as the relaxation sheath oscillations (RSO).

The SCL SEE requires the plasma electrons to have significant energy. Consider the typical RSO period described in Fig. 7.3. The system accumulates the energy in the non-SCL state due to collisional heating. Then, during the SCL state, this energy is rapidly spent on intense emission (see Fig. 7.3a and Fig. 7.3e). The transition from the non-SCL to SCL state occurs when the total emission coefficient γ approaches the critical value, $\gamma \to \gamma_{cr}$. Consider the evolution of the components of the primary electron flux preceding the transition. For the secondary electron beam, the average energy W_b (curve 1 in Fig. 7.3c) and the partial emission coefficient γ_b (curve 1 in

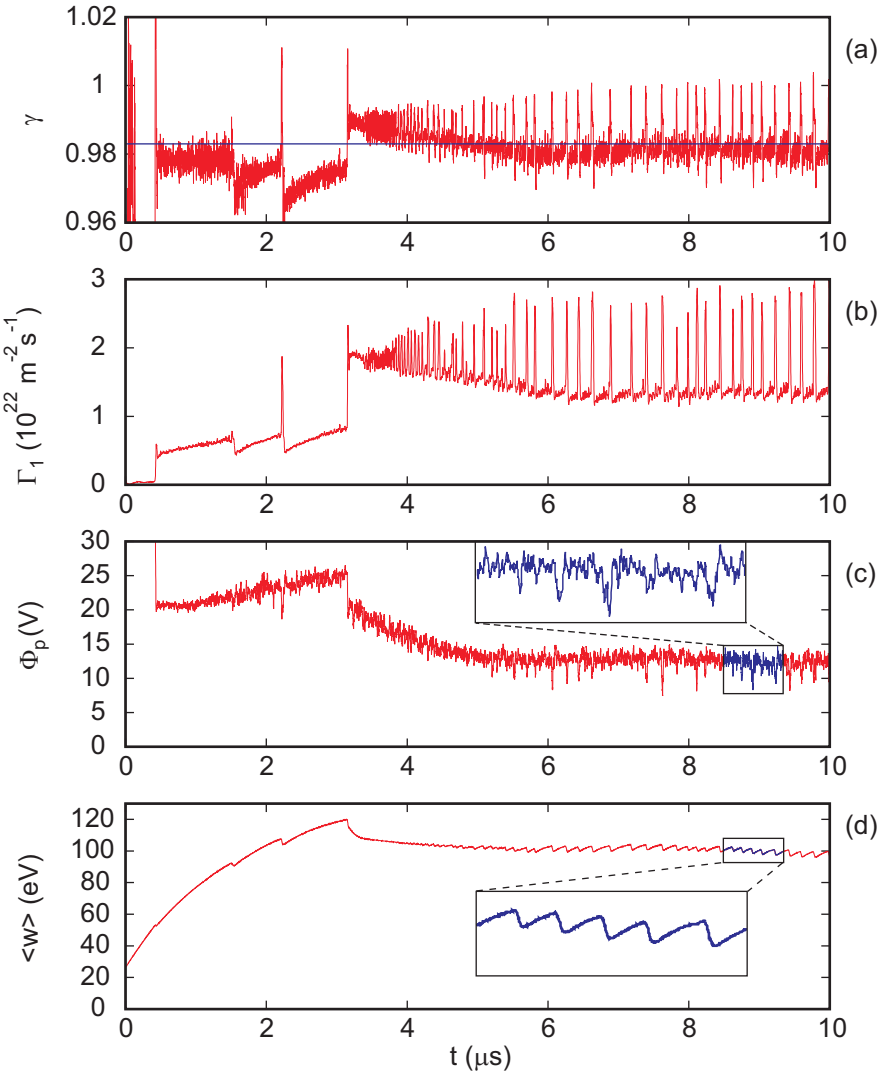

Figure 7.1: Evolution of general plasma parameters with time in the RSO regime. (a) Total emission coefficient γ at the wall $x = L$ (red curve) and the threshold emission coefficient for the SCL SEE (blue line). (b) Total primary electron flux Γ_1 to the wall $x = L$. (c) Electrostatic potential in the middle of the plasma Φ_p. (d) Average electron energy $\langle w \rangle$.

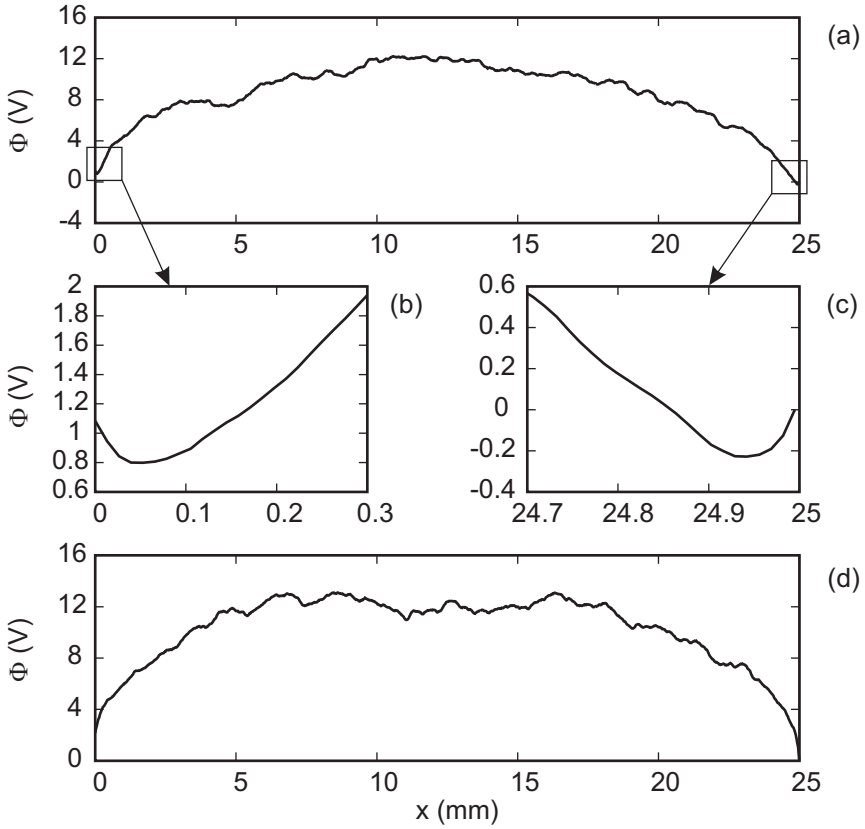

Figure 7.2: The nonmonotonic spatial profile of the electrostatic potential in the SCL state at the moment $t = 9222.7$ ns: (a) the entire domain, (b) and (c) the fine scale plots of the potential wells near the walls $x = 0$ and $x = L$, respectively. (d) The monotonic spatial profile of the potential in the non-SCL state at the moment $t = 9415.4$ ns. The profiles correspond to the simulation presented in Fig. 7.1.

Fig. 7.3d) change insignificantly. For the collision-ejected electrons, the changes of W_c (curve 2 in Fig. 7.3c) and γ_c (curve 2 in Fig. 7.3d) are more intense, however, the contribution of this component is minor because of its very low flux Γ_c (curve 2 in Fig. 7.3b). The most noticeable changes occur for the weakly confined electrons. While the system is in the non-SCL state, the energy of this group W_w grows from about 25 eV to about 40 eV (curve 3 in Fig. 7.3c) and the partial emission coefficient γ_w changes from 0.67 to about 1.0 (curve 3 in Fig. 7.3d). Since γ_w grows, the total emission coefficient γ increases, asymptotically approaching the value $\gamma = 0.98$ (follow the red arrow in Fig. 7.3e). The stepwise transition to the SCL state occurs at the moment marked by the vertical dashed line B in Fig. 7.3 despite $\gamma < \gamma_{cr} = 0.983$. The reason for such a jump is the unstable plasma state discussed below in Section 7.2.

Simulations show that the transition to SCL SEE starts at one of the walls, either $x = 0$ or $x = L$. At the other wall, the SCL SEE occurs with a delay of about the electron flight time between the walls. Consider the evolution of the components of electron flux towards both walls during the SCL state shown in Fig. 7.4. Important events at consecutive moments t_A, t_B, t_C, and t_D are marked by vertical dashed lines with respective indices in Fig. 7.4. For this particular case, the SCL regime starts at moment t_A at the wall $x = L$, resulting in a rapid increase of the primary electron flux to this wall (curve 1 in Fig. 7.4a). Transition to the SCL regime is accompanied by a decrease of the plasma potential relative to the wall, $\Phi_p - \Phi(L)$, so the electrons moving towards this wall and previously confined by the higher plasma potential at the non-SCL state suddenly become part of the primary electron flux (curve 1 in Fig. 7.4b).[1] By time t_B, the fastest secondary electrons emitted from the wall $x = L$ have crossed the plasma gap to reach the opposite wall $x = 0$. These electrons carry a large energy (curve 2 in Fig. 7.4d), which initiates the SCL regime there. Then

[1]The diagnostics of the EDIPIC code considers all primary electrons, which are not the secondary beam electrons or the electrons scattered to the wall after collision with a neutral atom, as the weakly confined electrons. As a result, in Fig. 7.4b, the primary electron flux due to the electrons that became untrapped after the decrease of the plasma potential is contained in the weakly confined electron flux.

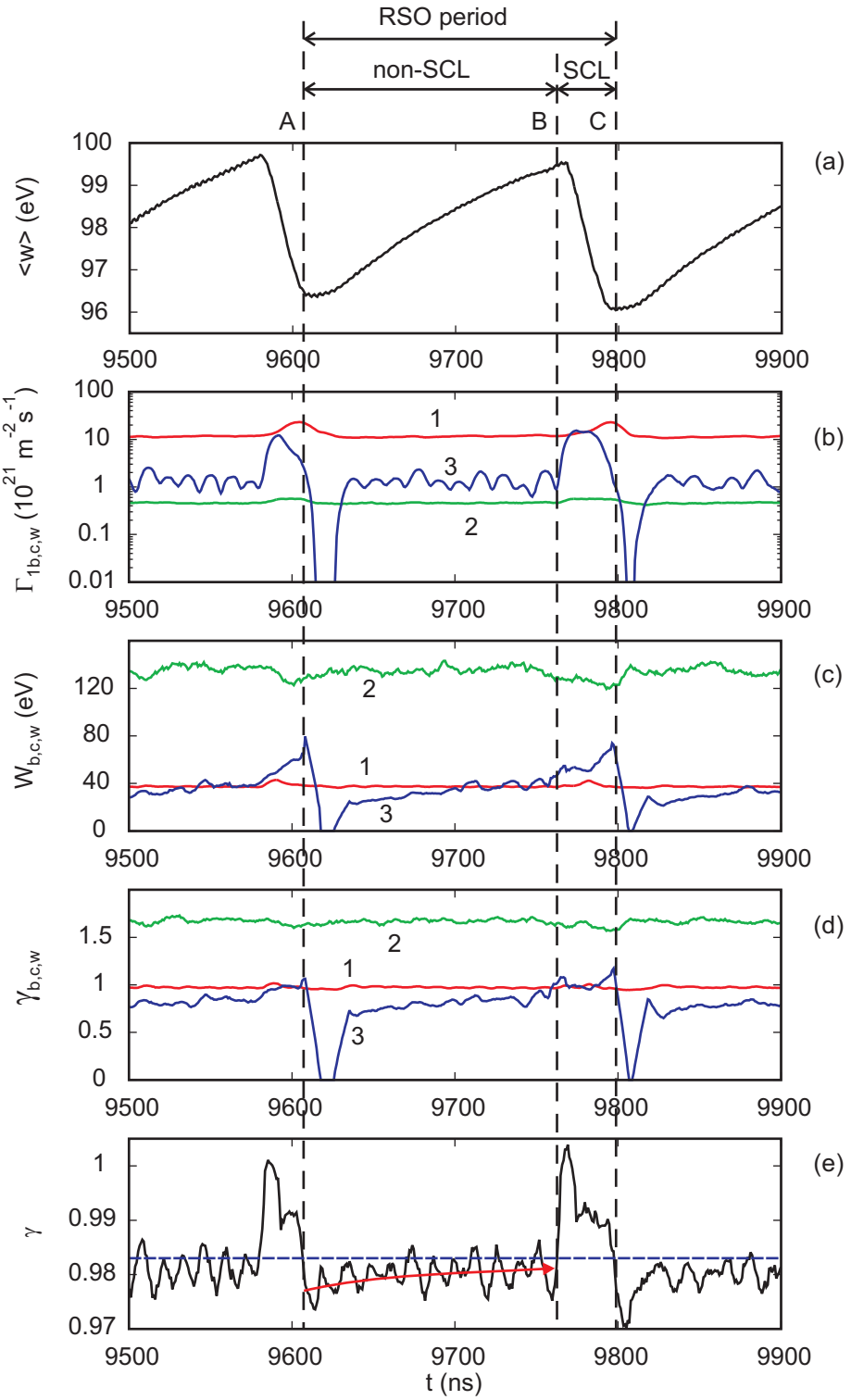

Figure 7.3: Evolution of parameters during one RSO period. (a) The average electron energy. (b) The flux, (c) the average energy, and (d) the partial emission coefficient of the components of the primary electron flux. Curves 1,2, and 3 correspond to the secondary electron beam, collision-ejected, and weakly confined electrons. (e) The total emission coefficient.

the plasma potential relative to the wall $x = 0$, $\Phi_p - \Phi(0)$, decreases, the primary flux of the untrapped plasma bulk electrons (curve 2 in Fig. 7.4b) and the total primary electron flux to the wall $x = 0$ increase (curve 2 in Fig. 7.4a). By times t_C and t_D, the major parts of the secondary electron fluxes (Fig. 7.4c) have reached the walls $x = 0$ and $x = L$, respectively. These large fluxes have relatively low energy (Fig. 7.4d) and extinguish the SCL emission, first at the wall $x = 0$, and then at the wall $x = L$. The delay between moments t_D and t_C (when the SCL regimes were terminated) is approximately the same as the delay between moments t_B and t_A (when the SCL regimes were started). While the system is in the SCL state, with the potential depressed, the confined plasma exchanges some of its electrons, which have accumulated significant energy after several turbulent collisions, for secondary beam electrons with lower energy. As a result, when the system leaves the SCL regime, it must accumulate the energy again in order to return to the SCL state.

7.2 Reason for the stepwise transition to the space charge limited regime

The final stage of the transition to the SCL state (marked by the vertical dashed line B in Fig. 7.3e) occurs in a stepwise manner, with the emission coefficient changing abruptly from a value below the threshold γ_{cr} to a value above the threshold. Simulations reveal that the processes immediately before the transition to the SCL state and the processes that occur during the SCL state happen on time scales of the order of the electron flight time between the walls. Under such conditions, the formalism developed in Section 6.1 is not applicable since it considers the stationary state and assumes that the SEE occurs symmetrically on both walls. As it is described above, the SCL state lasts until the intense emitted secondary electron fluxes with low energy reach the walls. It will be shown below that a similar delay may result in instability and the transition to the SCL state.

In Ref. [149], the stability of the sheath of a semi-infinite plasma with SEE was attributed to the electron conductivity of the sheath – the sheath was unstable if the

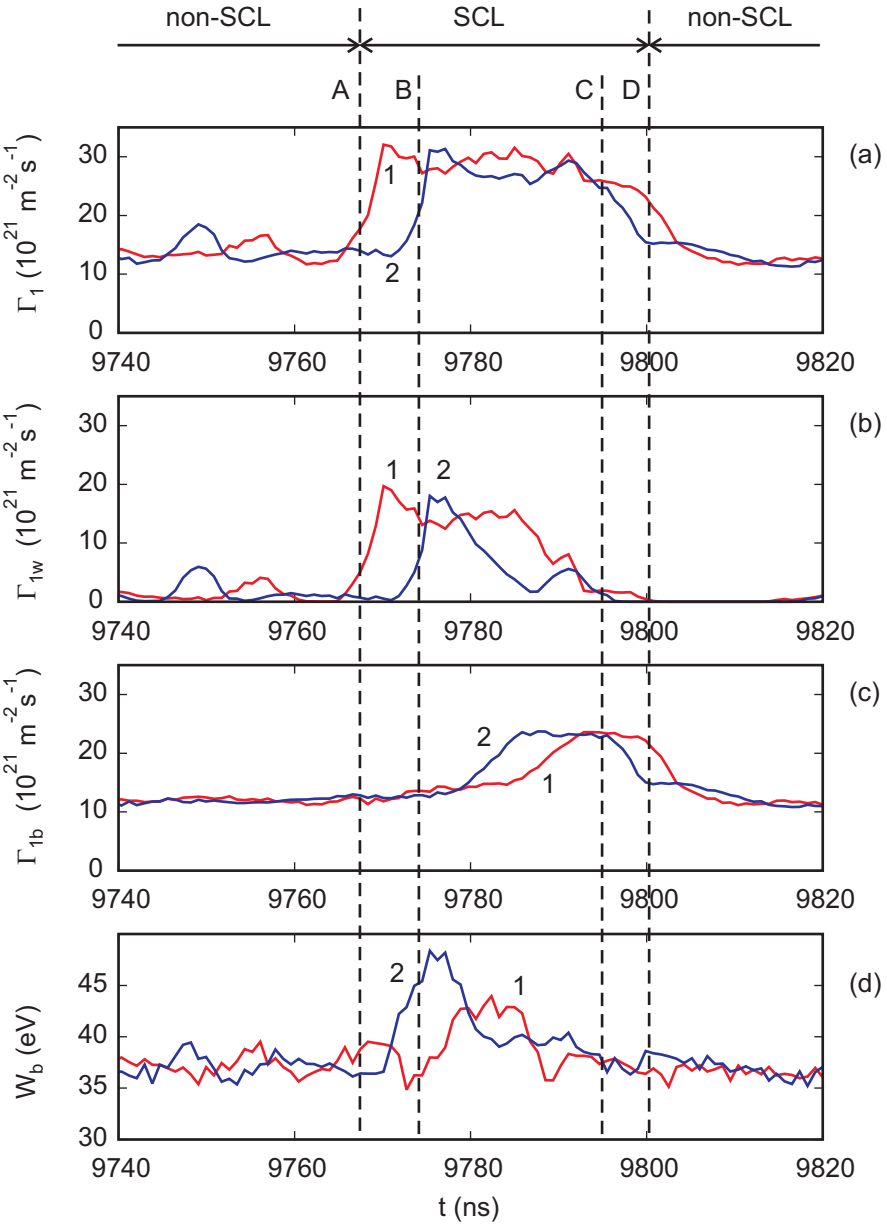

Figure 7.4: Evolution of parameters in the SCL state. (a) The total primary electron flux. (b) The flux of the weakly confined and untrapped plasma electrons. (c) The secondary electron beam flux. (d) The average energy of the secondary electron beam at the target wall. Curves 1 (red) correspond to the wall $x = L$, curves 2 (blue) to the wall $x = 0$.

conductivity was negative:

$$\frac{dJ_{ex}}{d\Phi_p} < 0 \ , \tag{7.1}$$

where J_{ex} is the electric current created by electrons at the wall (includes contributions of both primary and secondary electron fluxes) and Φ_p is the potential of plasma relative to the wall. The stability of the plasma in the model of the AR of a Hall thruster may be studied using a similar approach. Consider the plasma in the stationary state, with equal SEE intensity and electron fluxes at both walls. Let, due to some fluctuation, the potential of the plasma relative to one wall start changing, correspondingly modifying the flux of the plasma electrons towards that wall. The electron beam flux to this wall remains unchanged, $\Gamma_{1b} = const$, during the period equal to the electron flight time between the walls, $\tau \approx L/(2e\Phi_p/m)^{1/2}$. With respect to a short-time (compared to τ) perturbation, the bounded plasma does not differ from a semi-infinite plasma with the same EVDF. Then, considering the EVDF in the middle of the plasma $x = L/2$ as a constant source EVDF, one may investigate the dependence of the electron flux to the wall versus the potential of the source relative to the wall (*i.e.*, the current-voltage characteristic), and make conclusions about the stability of the plasma state depending on the sign of the conductivity.

The total electric current J_{ex} created by electrons at the wall $x = L$ for a given EVDF in the midplane $f(v_x, v_y, v_z, L/2)$ and potential profile $\Phi(x)$ is

$$\begin{aligned} J_{ex}(L) &= e[\Gamma_2(L) - \Gamma_1(L)] \\ &= e\int_{v_*}^{\infty} dv_x v_x \int_{-\infty}^{\infty} dv_y \int_{-\infty}^{\infty} dv_z f(v_x, v_y, v_z, L/2) \left\{\gamma\left[w_x(L), w_{yz}(L)\right] - 1\right\} \ , \end{aligned} \tag{7.2}$$

where $v_*^2 = 2e\Phi_p/m$, $\gamma\left[w_x(L), w_{yz}(L)\right]$ is the emission coefficient, $w_x(L) = w_x(L/2) - e\Phi_p$ is the energy of motion of an incident electron in the direction normal to the wall, and $w_{yz}(L) \equiv w_y(L) + w_z(L)$ is the energy of motion of an incident electron parallel to the walls. The latter energy is a function of the phase of cyclotron rotation in crossed fields E_z and B_x. Similar to (6.10), one obtains

$$w_{yz}(L) = \frac{m(v_y^2 + v_z^2)}{2} + mV_{dr}^2 \left[\left(1 - \frac{v_y}{V_{dr}}\right)\left(1 - \cos\omega_c T_{L/2}\right) - \frac{v_z}{V_{dr}} \sin\omega_c T_{L/2}\right] \ ,$$

where $T_{L/2}$ is the duration of the electron flight from the midplane $x = L/2$ to the wall $x = L$, calculated similar to (6.8) as

$$T_{L/2} = \int_{L/2}^{L} dx \left[v_x^2 + \frac{2e\Phi(x)}{m} \right]^{-1/2} ,$$

where v_x, v_y and v_z are the velocity components of an electron in the midplane, $x = L/2$.

The current-voltage characteristic of the sheath is obtained in the following procedure. The EVDF in the midplane $f(v_x, v_y, v_z, L/2)$ and the initial potential profile $\Phi(x)$ corresponding to one point of the current-voltage characteristic are obtained self-consistently, in PIC simulations, for a stationary non-SCL state. Below, this point is referred to as *the operating point*. The potential profile is expressed in the form $\Phi(x) = \Phi_p \times f(x)$, where $f(x)$ is the profile shape function, $f(L/2) = 1$. Then the total electron current at the wall is calculated for different values of Φ_p by Eq. (7.2). Such a procedure is partially non-self-consistent, because it uses a prescribed monotonic potential profile with variable amplitude Φ_p, without solving Poisson's equation. The results obtained with this approach are meaningful only if the emission coefficient

$$\gamma = \frac{\int_{v_*}^{\infty} dv_x v_x \int_{-\infty}^{\infty} dv_y \int_{-\infty}^{\infty} dv_z f(v_x, v_y, v_z, L/2) \gamma \left[w_x(L), w_{yz}(L) \right]}{\int_{v_*}^{\infty} dv_x v_x \int_{-\infty}^{\infty} dv_y \int_{-\infty}^{\infty} dv_z f(v_x, v_y, v_z, L/2)} , \qquad (7.3)$$

is below the critical value, $\gamma < \gamma_{cr}$.

The current-voltage characteristics at the beginning (marked by line A in Fig. 7.5a) and at the end (marked by line B in Fig. 7.5a) of the non-SCL state are substantially different from each other (compare green and red curves in Fig. 7.5c). At the beginning of the non-SCL state, the operating point is in the region of the current-voltage characteristic with $dJ_{ex}/d\Phi_p > 0$ (see marker 1 and the slope of the corresponding tangent line in Fig. 7.5c). Thus, the non-SCL state is initially stable. The operating point at the end of the non-SCL state, immediately before the transition to the SCL state, is in the region of the current-voltage characteristic with negative conductivity, $dJ_{ex}/d\Phi_p < 0$ (see marker 2 and the negative slope of the black tangent line passing through this marker in Fig. 7.5c). Thus, the non-SCL state becomes unstable

with time and at this stage a small fluctuation of potential may result in the rapid transition to the SCL state.

Note that the stable state satisfying criterion (7.1) is characterized by the positive $d\gamma/d\Phi_p$ (see marker 1 and the slope of the tangent line passing through this marker in Fig. 7.5b). The condition

$$\frac{d\gamma}{d\Phi_p} > 0 \tag{7.4}$$

is qualitatively different from stability condition (6.13). Condition (7.4) characterizes the stability of a plasma with a given EVDF with respect to the short-time potential perturbations that do not modify the EVDF, *i.e.*, when perturbation near one wall occurs independently of emission at the other wall. Condition (6.13) characterizes the stability of a plasma with respect to gradual modifications of the whole potential profile affecting the electron flight time, such perturbation does not violate the symmetry of emission at the walls.

Differentiation of the electron current at the wall in the form $J_{ex} = e\Gamma_1(\gamma - 1)$ with respect to the plasma potential Φ_p gives

$$\frac{dJ_{ex}}{d\Phi_p} = e\frac{d\Gamma_1}{d\Phi_p}(\gamma - 1) + e\Gamma_1\frac{d\gamma}{d\Phi_p} \ .$$

Since $d\Gamma_1/d\Phi_p < 0$ and $\gamma < \gamma_{cr} < 1$, the negative conductivity $dJ_{ex}/d\Phi_p < 0$ may appear only if condition (7.4) is violated, $d\gamma/d\Phi_p < 0$. The corresponding increase of the emission coefficient for a plasma potential below the operating point potential occurs because of the high energy of plasma electrons confined by the operating point potential. These electrons accumulate energy due to anisotropic heating in the non-SCL state. Thus, the negative conductivity of the sheath and the unstable plasma state, which results in the transition to the SCL state, are induced by intense anisotropic heating.

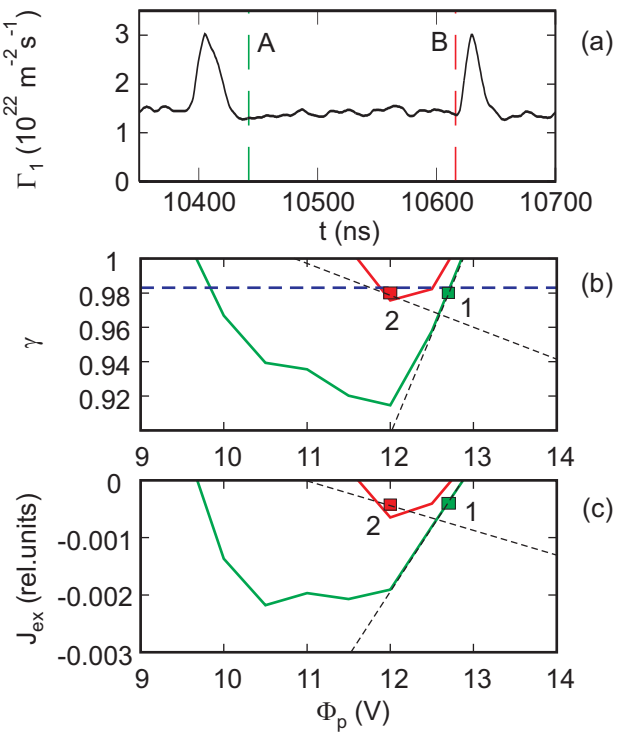

Figure 7.5: (a) The primary electron flux to the wall $x = L$ during one RSO period, vertical lines A and B mark the beginning and the end of the non-SCL state. (b) The emission coefficient at the wall $x = L$ versus the plasma potential, calculated by (7.3); the blue line is $\gamma = \gamma_{cr}$. (c) The total electron current at the wall $x = L$ versus the plasma potential, calculated by (7.2). In (b) and (c), the green and the red curves correspond to the moments A and B in (a), respectively. Squares 1 and 2 mark the operating points at the moments A and B in (a), respectively. The black dashed lines are the tangent lines at the operating points. Parameters of the simulation are the same as in Figs. 7.1– 7.4.

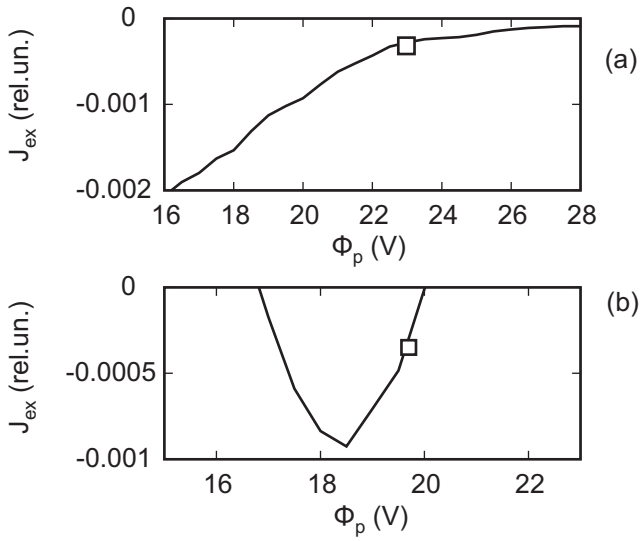

Figure 7.6: Current-voltage characteristics of simulations without RSO: (a) simulation 1 of Table 5.1, and (b) simulation 7 of Table 5.2. The white square marks the operating point.

7.3 Effects of plasma parameters on the relaxation sheath oscillations

The exact criterion of the RSO regime is not clear yet. Qualitatively, the RSO regime requires the presence of (i) the negative conductivity branch of the current-voltage characteristic of the sheath, and (ii) the mechanism that "moves" the unstable branch towards the operating point.

Simulations show that RSO do not occur if the current-voltage characteristic satisfies criterion (7.1) for all values of the plasma potential, as it is shown in Fig. 7.6a for simulation 1 of Table 5.1. Such a stable state is formed in low energy plasmas, when the heating is weak. However, RSO may not occur even if the heating is sufficient to maintain the high average electron energy and to form the branch of the current-voltage characteristic with $dJ_{ex}/d\Phi_p < 0$ (see Fig. 7.6b). In the latter case, corresponding to simulation 7 of Table 5.2, the operating point (white square in Fig. 7.6b) remains in the stable branch of the current-voltage characteristic, prohibiting the transition to the SCL regime.

The unstable branch of the current-voltage characteristic approaches the operating point with potential Φ_p if the electrons with $e(\Phi_p - \Delta\Phi) < w_x < e\Phi_p$, which are confined by the plasma potential at the stationary state, reach some threshold level of energy of motion parallel to the walls, $\langle w_y + w_z \rangle > w_{thr}$, sufficient to violate condition (7.4). Here averaging $\langle ... \rangle$ is performed over the electrons of the group, $\Delta\Phi$ is the amplitude of potential perturbations in the system, $\Delta\Phi \ll \Phi_p$ (potential perturbations may appear, *e.g.*, due to the two-stream instability). Qualitatively, the maximal level of energy $\langle w_y + w_z \rangle$, which may be attained by the aforementioned electron group, is determined by (i) the average energy a particle obtains from a collision, $w_{coll} \sim mV_{dr}^2$, and (ii) by the ratio between the lifetime of electrons of this group τ_{life} and the period between collisions $\tau_{coll} \sim \nu_t^{-1}$ (it is assumed that $\nu_t \gg \nu_{en}$). The group is comprised of the weakly confined electrons as well as some of the plasma bulk electrons, the lifetime τ_{life} may be estimated as $\tau_{life} \sim n_{eff} L/(\Gamma_{1p} + \Gamma_{1b})$, where n_{eff} is the density of the electrons of the group. Finally, $\langle w_y + w_z \rangle \sim mV_{dr}^2 [n_{eff} L/(\Gamma_{1p} + \Gamma_{1b})]\nu_t \sim E_z^2 L \nu_t$, so the qualitative criterion of the RSO regime $\langle w_y + w_z \rangle > w_{thr}$ is equivalent to the condition that

$$E_z^2 L \nu_t > \left(E_z^2 L \nu_t\right)_{thr} \ , \tag{7.5}$$

where the right hand side is a threshold value.

The effects of collision frequency ν_t and the distance between the walls L on the RSO were investigated. First, a set of simulations was carried out with different values of "turbulent" collision frequency, keeping the other simulation parameters the same as those of simulation 7 of Table 5.2. In these tests, the relaxation oscillations did not appear for $\nu_t = 0.7 \times 10^6$ s^{-1} and $\nu_t = 1.4 \times 10^6$ s^{-1}, but were present when $\nu_t = 2.8 \times 10^6$ s^{-1} (shown in Fig. 7.1). Second, a set of simulations was carried out with different values of the plasma gap width L. The common parameters were the same as in the simulation presented in Fig. 7.1. The RSO did not occur when $L = 1.5$ cm and smaller (see Fig. 7.7a), but did when $L = 2$ cm and larger (see Fig. 7.7b,c,d). The period of oscillations is not regular, typically decreasing for the wider plasma gaps (see Fig. 7.7e). Quenching of the RSO regime in the case of low

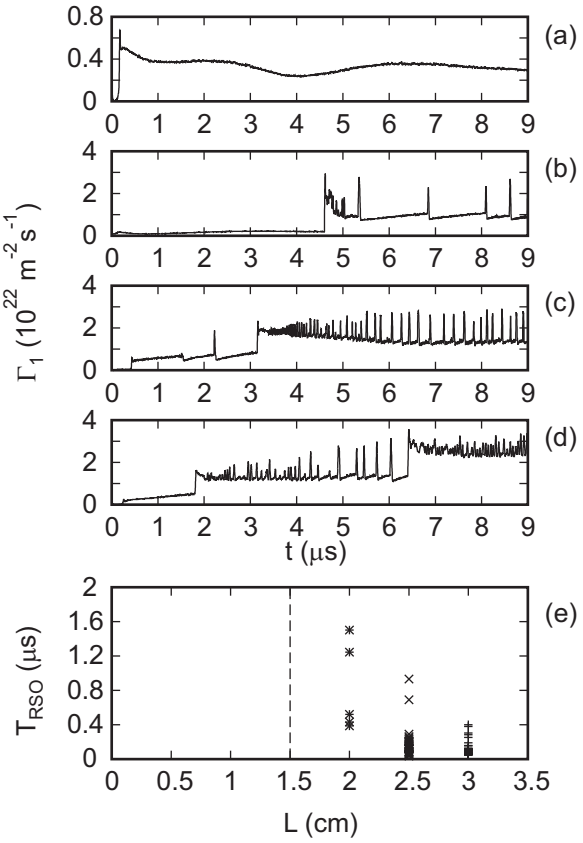

Figure 7.7: Primary electron fluxes to the wall $x = L$ versus time for different sizes of plasma gap: (a) $L = 1.5$ cm, (b) $L = 2$ cm, (c) $L = 2.5$ cm, and (d) $L = 3$ cm. (e) The relaxation oscillation period T_{osc} versus plasma gap L; markers in each vertical set correspond to different oscillation periods for the same plasma gap width. The common simulation parameters are those of simulation 7 of Table 5.2.

ν_t and small L agrees with the qualitative criterion (7.5).

The ion plasma oscillations, in principle, may result in sheath disturbance and possible transition to the SCL regime, which is why the effect of the ion mass on the frequency of relaxation oscillations was studied (see Fig. 7.8). A set of simulations was carried out with $E_z = 100$ V/cm, $B_x = 100$ G, $n_a = 2 \cdot 10^{12}$ cm^{-3}, $\langle \nu_{en} \rangle = 1.4 \cdot 10^6$ s^{-1}, $\nu_t = 2.2 \cdot 10^7$ s^{-1}, and different values of ion mass M. The period of oscillations was non-regular (see Fig. 7.8a-d) and significantly exceeded the ion plasma period (see Fig. 7.8e). In simulations with variable plasma gap width (see Fig. 7.7) and constant ion mass, some RSO periods were even smaller than the ion

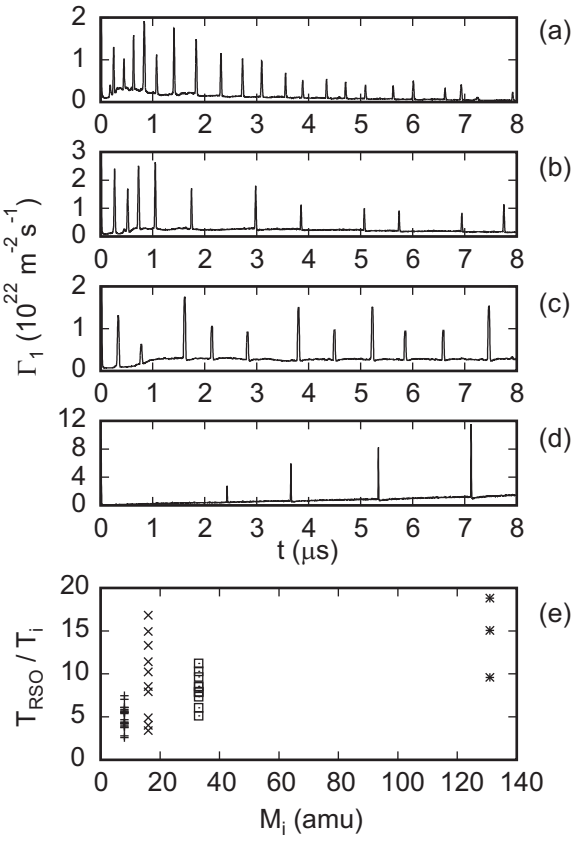

Figure 7.8: Primary electron fluxes to the wall $x = L$ versus time for different values of ion mass: (a) $M = 8$ amu; (b) $M = 16$ amu; (c) $M = 32$ amu; (d) $M = 131$ amu. (e) The ratio of the RSO period to the corresponding average ion plasma period $T_i = 2\pi(\varepsilon_0 M/\langle n\rangle e^2)^{1/2}$ versus the ion mass; markers in each vertical set correspond to different oscillation periods in a single simulation with a given ion mass.

plasma period. Thus, it is unlikely that the ion plasma oscillations are responsible for the observed RSO. Modification of the average RSO period in simulations with different ion masses is attributed to the difference in ion wall fluxes and corresponding difference in position of the operating point on the current-voltage characteristic relative to the minimum of the characteristic.

7.4 Summary

A new regime with relaxation sheath oscillations is observed in simulations of a bounded thruster-like plasma system. During one period of RSO the plasma spends a long time in the non-SCL state with monotonic potential profile in the sheath, and then switches to the SCL state with nonmonotonic potential profile in the sheath for a short time. In the SCL state, the electron wall losses are several times greater than the losses in the non-SCL state, significantly depleting the EVDF and decreasing the average electron energy. The energy required for the intense emission at the SCL state is accumulated during the long non-SCL state. Transition to the SCL state occurs in a stepwise manner, when the non-SCL state becomes unstable with respect to potential perturbations, which are short compared to the electron flight time between the walls. This instability is related to the negative conductivity of the sheath near the secondary electron emitting wall, which [conductivity] appears from strong SEE due to the intense anisotropic heating. The SCL state is essentially non-stationary, it starts with intense emission and quenches as soon as the emitted electrons fly through the plasma gap and reach the walls.

It is found that the oscillations have a non-regular period, which may vary significantly during system evolution in one simulation. Such behavior is related to the mechanism of transition between the non-SCL and the SCL states, which depends on the existing perturbations affecting the moment of exit from the unstable non-SCL state.

The qualitative criterion of the RSO regime (7.5) shows that the oscillations may not occur if the plasma gap is narrow or if the heating is not sufficient (the heating is determined by both the axial electric field and the turbulent collision frequency). This criterion agrees with the parametric studies of the RSO. Although the RSO regime requires a significant level of heating, several times higher than the available experimental parameters, this regime agrees with the prediction of Ref. [149] that the sheath in Hall thrusters may be non-stationary and flickering.

Chapter 8

Conclusions

Plasma behavior in low pressure discharges, where the electron mean free path exceeds the dimensions of the device, is often far from a simple fluid picture. The absorption of energy may occur in a nonlocal manner, independently for different groups of electrons, and as a result, the electron velocity distribution function (EVDF) may deviate from Maxwellian [3, 4, 5, 6, 7, 87]. The physics of such plasmas is rich in kinetic and nonlinear effects. In the present thesis, the two classes of such phenomena are analyzed. In inductively coupled plasmas (ICP), the penetration of radio-frequency (RF) electromagnetic (EM) fields and the nonlinear ponderomotive force (PMF) become affected by electron thermal motion. In Hall thrusters, the losses of electron energy to the walls with secondary electron emission (SEE) appear to be substantially smaller than predicted by fluid theories, which assume a Maxwellian EVDF. The description of such plasmas must be kinetic, and because of the complexity of the problem, the straightforward approach is to use particle-in-cell (PIC) simulations. Several PIC codes have been developed by the author to study kinetic effects in ICP and in Hall thrusters. The most important results of these studies are presented in this thesis.

The 1d3v fully electromagnetic, quasineutral, collisionless PIC code simulating propagation of a plane EM wave through an overdense plasma slab is applied to investigate the effects of the electron thermal motion on the PMF in ICP. The standard approach of the linear theory of the anomalous skin-effect [18, 25] assumes that the electron trajectories are not affected by the RF magnetic field. The PMF obtained analytically in Ref. [35] with this assumption is strongly reduced in warm plasmas. In low frequency ICP, the RF magnetic field is significant and the elec-

tron trajectories are far from linear. The nonlinear electron trajectories can hardly be accounted for in an analytical description. However, in PIC simulations these trajectories are naturally implemented. Here are the major results found in PIC simulations of ICP [53, 51, 52]:

- At high electron temperatures, the nonlinear electron trajectories result in a PMF several times larger than predicted by linear theory.

- The trajectories of electrons, whose Larmor radius is smaller than or comparable to the skin layer depth, are strongly modified. The ICP dynamics can be nonlinear due to these low energy electrons, even when the trajectories of thermal electrons are weakly perturbed. PIC simulations show that the small linear PMF can be expected only at very low amplitudes of RF field, typically much smaller than the RF field amplitudes in operating ICP discharges.

The practical importance of the obtained results is that the PMF, which contributes to the formation of the density profile in low frequency ICP, is essentially a nonlinear phenomenon and is stronger than predicted by the nonlocal linear theory. The range of applicability of linear approximation appears to be much smaller than one could expect from simple qualitative considerations.

Future investigations of the kinetic and nonlinear effects in ICP should include (1) simulations with mobile ions, (2) implementation of electron-neutral and Coulomb collisions in the electromagnetic PIC code, (3) simulations of cylindrical plasmas. The latter two issues are related with the necessity to include in the PMF theory the nonlinear convective term $(\mathbf{u} \cdot \nabla)\mathbf{u}$, which is important in curvilinear geometry [39, 40], and the nonlinearly modified plasma viscosity [165].

One of the most significant results of the present work is the development of the 1d3v electrostatic direct implicit PIC code (EDIPIC) for kinetic studies of plasmas inside the channel of a Hall thruster. The important physical effects in such plasmas are (i) the collisions with neutral atoms and Coulomb collisions, (ii) the anomalous electron mobility across the magnetic field, (iii) the secondary electron emission, and (iv) the non-neutral narrow sheath regions near the walls. Note that the frequency

of collisions in Hall thrusters remains sufficiently low that the kinetic effects play a significant role in such plasmas.

The EDIPIC code simulates a plasma slab bounded by secondary electron emitting dielectric walls. The external magnetic field is applied normal to the walls and the electric field is directed parallel to the walls. The SEE model describes the properties of grade HP boron nitride ceramics. The Monte-Carlo model of electron-neutral and "turbulent" collisions and the Langevin model of Coulomb collisions are included in the code. The simulated system is the plane geometry approximation of the acceleration region (AR) of a Hall thruster. The code resolves both the sheath regions and the plasma bulk. For effective simulation speed, the code has been parallelized. The validity of the code has been confirmed in numerous tests. The EDIPIC code is applied to study the effects of SEE on plasma-wall interaction in Hall thrusters.

Operation of a Hall thruster depends crucially on the electron temperature and the SEE from the thruster's channel walls. Fluid theories assume that the EVDF is Maxwellian and predict fast electron cooling due to high wall losses and saturation of the electron temperature [69, 81, 82]. However, recent experiments [78, 79] show that the plasma-wall interaction is less intense than predicted by fluid theories – the measured electron temperatures are higher and the electron wall collision frequencies are smaller than the values possible for a Maxwellian EVDF. Available kinetic studies of Hall thrusters do not resolve the distribution over velocity components and use simplified models of the sheath [87, 88]. In the model of the AR of a Hall thruster considered in the present thesis, the EVDF and the potential profile are formed self-consistently, depending on the applied external fields, collisions, width of plasma gap, and SEE properties of wall material. The major results found in PIC simulations of the considered model are [90, 91, 92, 93, 94, 95]:

- The EVDF of plasmas in the AR of Hall thrusters is non-Maxwellian, anisotropic, and depleted in the region of high energy of electron motion normal to the walls. The anisotropy is largely determined by the high frequency of "turbulent" collisions, which are introduced in order to reproduce the anomalous elec-

tron mobility across the magnetic field. However, in the limit of strong external accelerating fields, the anisotropy develops even without the "turbulent" collisions. The depletion of the high-energy tail occurs because the electron mean free path far exceeds the width of the plasma slab, so electrons with energy of motion normal to the walls larger than the plasma potential quickly leave the plasma. Such electrons form the loss cone in velocity space. The depletion of the loss cone results in a significant, of about one order of magnitude, decrease of the electron wall losses compared to plasmas with Maxwellian EVDF.

- For Hall thruster plasmas, the frequency of Coulomb collisions is much smaller than the frequency of "turbulent" collisions and collisions with neutral atoms. Usually the effect of Coulomb collisions on EVDF in Hall thrusters is weak. Considerable changes occur when the SEE is close to the SCL regime. For typical Hall thruster parameters corresponding to such a regime, Coulomb collisions increase the electron flux to the wall by a few tens of percents.

- PIC simulations show that the loss cone is populated by (i) the secondary electrons, which form two counter-propagating beams, (ii) the electrons from the plasma bulk scattered into the loss cone after collisions with neutral atoms, and (iii) the weakly confined electrons from the narrow boundary layer in phase space between the plasma bulk electrons and the secondary electron beams. These three electron groups form the three components of the primary electron flux to the walls, with different characteristic energies and partial emission coefficients.

- The new model of SEE in a bounded plasma is developed, which considers the three components of the electron flux to the wall – the secondary electron beams, the collision-ejected electrons, and the weakly confined electrons – and the secondary emission produced by each of the components. The total emission coefficient obtained in this model is no longer simply a function of the plasma bulk electron energy. The modified criterion for SCL SEE is obtained. The criterion shows that, when the primary electron flux of the collided elec-

trons is combined with the low-energy primary electron fluxes of secondary and weakly confined electrons, the SCL regime occurs if the emission due to the plasma bulk electrons is much more intense than in the case when the plasma bulk is the only source of primary electrons. This explains why the experiments show that the SEE is in the non-SCL regime for electron temperatures several times higher than the critical threshold for Maxwellian plasmas [78, 79]. The proposed model of SEE in bounded plasmas is more general than the recent model of Ref. [147], where the important effect of SEE emission due to the secondary electron beams was not considered.

- It is found that secondary electrons may significantly increase their energy during the travel between the walls. The axial electric field inside the AR of a Hall thruster contributes to the energy of motion of secondary electrons in the plane parallel to the walls when the electrons are taken up by the $E \times B$ drift. The value of this additional energy depends on the external electric and magnetic fields, as well as on the time of electron flight between the walls. The latter parameter is determined by the potential profile in the plasma and by the plasma gap width. Note that changing the width of the thruster channel results in significant modification of discharge properties [80]. The additional energy acquired by secondary electron beams may be much larger than the initial energy of emission, and SEE produced by these beams may be significant. These secondary electrons may contribute considerably to the electron current to the walls.

- The important parameter in the SEE model with counter-propagating secondary electron beams is the coefficient of beam penetration through the plasma slab, α. Due to the low collision frequency, the dominant obstruction to beam penetration is the electron deceleration caused by the two-stream instability. PIC simulations show that in Hall thruster plasmas the beam penetration is high and the current losses due to the two-stream instability are not significant. The total EVDF of both plasma bulk and beam electrons is a

decreasing function of the electron velocity normal to the walls and is stable with respect to the two-stream instability. Simulations with periodic boundary conditions show that for the typical parameters of the secondary electron beams in Hall thruster plasmas, the width of the plasma gap in Hall thrusters is too small for the two-stream instability to reach the nonlinear saturation level. Under such conditions the two-stream instability is weak and most of the emitted electrons penetrate through the plasma slab.

- A new regime, which contains relaxation sheath oscillations (RSO), is identified from PIC simulations. In this regime, the plasma is in the non-SCL state most of the time, but quasi-periodically, for a short periods of time, it switches to the state of SCL SEE. In the SCL state, the electron wall losses increase considerably, which limits the quasistationary level of the average plasma electron energy. It is found that in the RSO regime, the current-voltage characteristic of the sheath has an unstable branch with negative conductivity. This branch appears due to intense anisotropic heating. Transition from the non-SCL to the SCL state of the plasma occurs in a stepwise manner, when the negative conductivity branch approaches the point corresponding to the non-SCL plasma state. The frequency of relaxation oscillations may vary significantly during the system evolution. The qualitative criterion for the RSO regime shows that it may not occur if the plasma gap width is small or if the heating is low. Although the RSO regime requires a level of heating, which is several times higher than that in ordinary Hall thrusters, the existence of such a regime may be important for the physics of Hall thrusters. Some experimental data [149] suggest that the sheath structure inside the thruster channel may be non-uniform or a "mosaic", and that the plasma potential relative to the wall may locally become zero.

The practical importance of this kinetic study of the plane geometry Hall thruster model is that the results provide an explanation of the anomalously high electron temperature inside the Hall thrusters and show that the use of Maxwellian EVDF

leads to a significant overestimation of the intensity of plasma-wall interaction. These results emphasize a limited ability of fluid models to describe the wall losses.

Future study of kinetic effects in Hall thrusters must clarify the following issues: (1) the functional dependence of the degree of EVDF anisotropy on collision frequencies and the applied electric and magnetic fields; (2) the effects of different initial energy distributions of SEE – the secondary electron beam penetration may decrease if this energy distribution is not half-Maxwellian; (3) the effects of other possible models of the anomalous electron mobility, *e.g.*, approximating the electric field of the azimuthal turbulence in Hall thrusters with an externally applied oscillating electric field [64, 66]; (4) the quantitative criterion for the occurrence of the relaxation oscillation regime; (5) the effect of cylindrical geometry on the EVDF anisotropy. A most ambitious project would be to perform kinetic simulations resolving at least two spatial dimensions.

References

[1] L. Artsimovich. *A Physicist's ABC on Plasma.* Moscow : Mir Publishers, 1978.

[2] Robert J. Goldston and Paul H. Rutherford. *Introduction to Plasma Physics.* Institute of Physics Publishing, Bristol and Philadelphia, 1995.

[3] L. D. Tsendin. Electron energy distribution in transversly inhomogeneous current-carrying plasma. *Sov. Phys. JETP*, 39:805–810, 1974.

[4] R. R. Arslanbekov and A. A. Kudravtsev. Modeling of nonlocal electron kinetics in a low-pressure afterglow plasma. *Phys. Rev. E*, 58:7785–7798, 1998.

[5] I. Kaganovich, M. Misina, S. V. Berezhnoi, and R. Gijbels. Electron Boltzmann kinetic equation averaged over fast electron bouncing and pitch-angle scattering for fast modeling of electron cyclotron resonance discharge. *Phys. Rev. E*, 61:1875–1889, 2000.

[6] V. A. Godyak, B. M. Alexandrovich, and V. I. Kolobov. Lorentz force effects on the electron energy distribution in inductively coupled plasmas. *Phys. Rev. E*, 64:026406, 2001.

[7] Alex V. Vasenkov and Mark J. Kushner. Electron energy distributions and anomalous skin depth effects in high-plasma-density inductively coupled discharges. *Phys. Rev. E*, 66:066411, 2002.

[8] A. Mangeney, F. Califano, C. Cavazzoni, and P. Travnicek. A numerical scheme for the integration of the Vlasov - Maxwell system of equations. *J. Comput. Phys.*, 179:495–538, 2002.

[9] Roger W. Hockney and James W. Eastwood. *Computer Simulation Using Particles.* McGraw-Hill Inc., 1981.

[10] C. K. Birdsall and A. B. Langdon. *Plasma Physics via Computer Simulations.* Bristol and Philadelphia : IOP Publishing, 1991.

[11] J. P. Verboncoeur. Particle simulation of plasmas: review and advances. *Plasma Phys. Control. Fusion*, 47, 2005.

[12] D. V. Romanov, V. Yu. Bychenkov, W. Rozmus, C. E. Capjack, and R. Fedosejevs. Self-organization of a plasma due to 3d evolution of the Weibel instability. *Phys. Rev. Lett.*, 93, 2004.

[13] V. Vahedi and M. Surendra. A Monte Carlo collision model for the particle-in-cell method: applications to argon and oxygen discharges. *Comput. Phys. Commun.*, 87:179–198, 1995.

[14] W. Hittorf. Ueber die electricitätsleitung der gase. *Wiedemanns Ann. Phys.*, 21:90–139, 1884.

[15] J. Hopwood. Review of inductively coupled plasmas for material processing. *Plasma Sources Sci. Technol.*, 1:109–116, 1992.

[16] V. A. Godyak. Radio frequency light sources. In *Proceedings of IEEE IAS Annual Meeting, Rome, Italy*, pages 3281–3288. IEEE, New York, 2000, 2000.

[17] Michel Tuszewski. Planar inductively coupled plasmas operated with low and high radio frequencies. *IEEE Trans. Plasma Sci.*, 27:68–69, 1999.

[18] E. S. Weibel. Anomalous skin effect in a plasma. *Phys. Fluids*, 10:741–748, 1967.

[19] H. London. The high-frequency resistance of superconducting tin. *Proc. R. Soc. London A*, 176:522–533, 1940.

[20] R. A. Demirkhanov, I. Ya. Kadysh, and Yu. S. Khodyrev. Skin effect in a high frequency ring discharge. *Sov. Phys. JETP*, 19:791–796, 1964.

[21] A. B. Pippard. The surface impedance of superconductors and normal metals at high frequencies. 2. The anomalous skin effect in normal metals. *Proc. R. Soc. London A*, 191:385–399, 1947.

[22] V. I. Kolobov and D. J. Economou. The anomalous skin effect in gas discharge plasmas. *Plasma Sources Sci. Technol.*, 6:R1–R17, 1997.

[23] G. E. H. Reuter and E. H. Sondheimer. The theory of the anomalous skin effect in metals. *Proc. R. Soc. London A*, 195:336–364, 1948.

[24] V. A. Godyak, R. B. Piejak, B. M. Alexandrovich, and V. I. Kolobov. Hot plasma and nonlinear effects in inductive discharges. *Phys. Plasmas*, 6:1804–1812, 1999.

[25] K. C. Shaing. Electron heating in inductively coupled discharges. *Phys. Plasmas*, 3:3300–3303, 1996.

[26] V. Vahedi, M. A. Lieberman, G. DiPeso, T. D. Rognlien, and D. Hewett. Analytic model of power deposition in inductively coupled plasma sources. *J. Appl. Phys.*, 78:1446–1458, 1995.

[27] Yu. M. Aliev, I. D. Kaganovich, and H. Schluter. Quasilinear theory of collisionless electron heating in radio frequency gas discharge. *Phys. Plasmas*, 4:2413–2421, 1997.

[28] V. A. Godyak, R. B. Piejak, B. M. Alexandrovich, and V. I. Kolobov. Experimental evidence of collisionless power absorption in inductively coupled plasmas. *Phys. Rev. Lett.*, 80:3264–3267, 1998.

[29] G. Cunge, B. Crowley, D. Vender, and M. M. Turner. Anomalous skin effect and collisionless power dissipation in inductively coupled discharges. *J. Appl. Phys.*, 89:3580–3589, 2001.

[30] A. I. Smolyakov, V. A. Godyak, and Y. O. Tyshetskiy. Nonlinear effects in inductively coupled plasmas. *Phys. Plasmas*, 10:2108–2116, 2003.

[31] V. Godyak, R. Piejak, B. Alexandrovich, and A. Smolyakov. Observation of the ponderomotive effect in an inductive plasma. *Plasma Sources Sci. Technol.*, 10:459–462, 2001.

[32] A. V. Gaponov and M. A. Miller. Potential wells for charged particles in high-frequency electromagnetic field. *Sov. Phys. JETP*, 7:168–169, 1958.

[33] Francis F. Chen. *Introduction to plasma physics*. Plenum Press, New York, 1974.

[34] G. W. Kentwell and D. A. Jones. The time-dependent ponderomotive force. *Phys. Reports*, 145:319–403, 1987.

[35] A. I. Smolyakov, V. Godyak, and Y. A. Tyshetskiy. Effect of the electron thermal motion on the ponderomotive force in inductive plasma. *Phys. Plasmas*, 8:3857–3860, 2001.

[36] R. H. Cohen and T. D. Rognlien. Electron kinetics in radio-frequency magnetic fields of inductive plasma sources. *Plasma Sources Sci. Technol.*, 5:442–452, 1996.

[37] R. H. Cohen and T. D. Rognlien. Induced magnetic field effects in inductively coupled plasmas. *Phys. Plasmas*, 3:1839–1847, 1996.

[38] V. Godyak. Nonlinear effects in inductive discharges. *Bulg. J. Phys.*, 27:13–19, 2000.

[39] A. Smolyakov, V. Godyak, and A. Duffy. On nonlinear effects in inductively coupled plasmas. *Phys. Plasmas*, 7:4755–4762, 2000.

[40] Francis F. Chen. Collisional, magnetic, and nonlinear skin effect in radio-frequency plasmas. *Phys. Plasmas*, 8:3008–3017, 2001.

[41] M. Tuszewski. Enhanced radio frequency field penetration in an inductively coupled plasma. *Phys. Rev. Lett.*, 77:1286–1289, 1996.

[42] M. Tuszewski. Inductive electron heating revisited. *Phys. Plasmas*, 4:1922–1928, 1997.

[43] M. Tuszewski. Particle and heat transport in a low-frequency inductively coupled plasma. *Phys. Plasmas*, 5:1198–1205, 1998.

[44] O. I. Lyubimov, N. N. Makarov, and V. A. Yampolskii. Nonlinear skin effect in metals. *Sov. Phys. JETP*, 58:1253–1259, 1983.

[45] Richard S. Wise, Dimitris P. Lymberopoulos, and Demetre J. Economou. Rapid two-dimensional self-consistent simulation of inductively coupled plasma and comparison with experimental data. *Appl. Phys. Lett.*, 68:2499–2501, 1996.

[46] U. Kortshagen, I. Pukropski, and L. D. Tsendin. Experimental investigation and fast two-dimensional self-consistent kinetic modeling of a low-pressure inductively coupled rf discharge. *Phys. Rev. E*, 51:6063–6078, 1995.

[47] M. M. Turner. Simulation of kinetic effects in inductive discharges. *Plasma Sources Sci. Technol.*, 5:159–165, 1996.

[48] Peter L. G. Ventzek, Robert J. Hoekstra, and Mark J. Kushner. Two-dimensional modeling of high plasma density inductively coupled sources for materials processing. *J. Vac. Sci. Technol. B*, 12:461–477, 1994.

[49] M. M. Turner. Collisionless electron heating in an inductively coupled discharge. *Phys. Rev. Lett.*, 71:1844–1847, 1993.

[50] N. S. Yoon, S. S. Kim, C. S. Chang, and Duk-In Choi. One-dimensional solution for electron heating in an inductively coupled plasma discharge. *Phys. Rev. E*, 54:757–767, 1996.

[51] D. Y. Sydorenko, A. I. Smolyakov, Y. O. Tyshetskiy, and V. A. Godyak. Ponderomotive force in warm plasma. *Bull. Am. Phys. Soc.*, 48:KP1.059, 2003.

[52] D. Sydorenko and A. Smolyakov. Simulations of nonlinear ponderomotive effects in an inductively coupled plasma slab. *Bull. Am. Phys. Soc.*, 49:187, 2004.

[53] D. Y. Sydorenko, A. I. Smolyakov, Y. O. Tyshetskiy, and V. A. Godyak. Simulations of ponderomotive effects in inductively coupled plasmas. *Phys. Plasmas*, 12:033503, 2005.

[54] A. I. Morozov. The conceptual development of stationary plasma thrusters. *Plasma Phys. Reports*, 29:235–250, 2003.

[55] V. V. Zhurin, H. R. Kaufman, and R. S. Robinson. Physics of closed drift thrusters. *Plasma Sources Sci. Technol.*, 8:R1–R20, 1999.

[56] K. N. Kozubskii, V. M. Murashko, Yu. P. Rylov, Yu. V. Trifonov, V. P. Khodnenko, V. Kim, G. A. Popov, and V. A. Obukhov. Stationary plasma thrusters operate in space. *Plasma Phys. Reports*, 29:251–266, 2003.

[57] G. S. Janes and R. S. Lowder. Anomalous electron diffusion and ion acceleration in a low-density plasma.

[58] D. Bohm, E. H. S. Burshop, and H. S. W. Massey. *The characterictics of electrical discharges in magnetic fields*. McGraw-Hill, New York, 1949. p. 13.

[59] S. Yoshikawa and D. J. Rose. Anomalous diffusion of a plasma across a magnetic field. *Phys. Fluids*, 5:334–340, 1962.

[60] A. B. Mikhailovskii and V. S. Tsypin. High-frequency instability of plasma situated in the radial electric and longitudinal magnetic fields. *Sov. Phys. JETP Lett.*, 3:158–160, 1966.

[61] I. Alexeff, K. Estabrook, A. Hirose, W. D. Jones, R. V. Neidigh, J. N. Olsen, F. R. Scott, W. L. Stirling, M. M. Widner, and W. R. Wing. Understanding turbulent ion heating in the oak ridge mirror machine, "Burnout V". *Phys. Rev. Lett.*, 25:848–851, 1970.

[62] A. Hirose and I. Alexeff. Electrostatic instabilities driven by currents perpendicular to an external magnetic field. *Nucl. Fusion*, 12:315–323, 1972.

[63] M. A. Capelli, N. Meezan, and N. Gascon. Transport physics in Hall thrusters. In *40th AIAA Aerospace Science Meeting and Exhibit.*, Nevada, 2002. AIAA-2002-0485.

[64] M. Hirakawa and Y. Arakawa. Particle simulation of plasma phenomena in Hall thrusters. In *Proceedings of the 24th International Electric Propulsion Conference*, Moscow, Russia, September 1995. IEPC paper 95-164.

[65] M. Hirakawa and Y. Arakawa. Numerical simulation of plasma particle behavior in a Hall thruster. In *Proceedings of the 32nd AIAA Joint Propulsion Conference*, Lake Buena Vista, FL, 1996. AIAA paper 96-3195.

[66] J. C. Adam, A. Heron, and G. Laval. Study of stationary plasma thrusters using two-dimensional fully kinetic simulations. *Phys. Plasmas*, 11:295–305, 2004.

[67] A. I. Morozov. Effect of near-wall conductivity in a strongly magnetized plasma. *Zh. Prikl. Mekh. Tekh. Fiz.*, 3:19, 1968. Journal of Applied Mechanics and Technical Physics, in Russian.

[68] A. I. Morozov and V. V. Savel'ev. Theory of the near-wall conductivity. *Plasma Phys. Reports*, 27:570–575, 2001.

[69] M. Keidar, I. D. Boyd, and I. I. Beilis. Plasma flow and plasma-wall transition in Hall thruster channel. *Phys. Plasmas*, 8:5315–5322, 2001.

[70] A. Smirnov, Y. Raitses, and N. Fisch. Electron cross-field transport in a low power cylindrical Hall thruster. *Phys. Plasmas*, 11:4922–4933, 2004.

[71] H. Seiler. Secondary electron emission in the scanning electron microscope. *J. Appl. Phys.*, 54:R1–R18, 1983.

[72] Lewi Tonks and Irving Langmuir. A general theory of the plasma in an arc. *Phys. Rev.*, 34:876–922, 1929.

[73] N. Hershkowitz. Sheath: More complicated than you think. *Phys. Plasmas*, 12:055502, 2005.

[74] M. A. Lieberman and A. J. Lichtenberg. *Principles of plasma discharges and materials processing.* New York : Wiley, 1994.

[75] G. D. Hobbs and J. A. Wesson. Heat flow through a Langmuir sheath in the presence of electron emission. *Plasma Phys.*, 9:85–87, 1967.

[76] E. Y. Choueiri. Fundamental difference between the two Hall thruster variants. *Phys. Plasmas*, 8:5025–5033, 2001.

[77] Y. Raitses, D. Staack, L. Dorf, and N. J. Fisch. Experimental study of acceleration region in a 2 kw Hall thruster. In *39th AIAA/ASME/SAE/ASEE Joint Propulsion Conf. and Exhibit.*, Huntsville, Alabama, 20-23 July 2003. AIAA-2003-5153.

[78] D. Staack, Y. Raitses, and N. J. Fisch. Temperature gradient in Hall thrusters. *Appl. Phys. Lett.*, 84:3028–3030, 2004.

[79] Y. Raitses, D. Staack, A. Smirnov, and N. J. Fisch. Space charge saturated sheath regime and electron temperature saturation in Hall thrusters. *Phys. Plasmas*, 12:073507, 2005.

[80] Y. Raitses, D. Staack, M. Keidar, and N. J. Fisch. Electron-wall interaction in Hall thrusters. *Phys. Plasmas*, 12:057104, 2005.

[81] E. Ahedo, J. M. Gallardo, and M. Martinez-Sanchez. Effects of the radial plasma-wall interaction on the Hall thruster discharge. *Phys. Plasmas*, 10:3397–3409, 2003.

[82] S. Barral, K. Makowski, Z. Peradzynski, N. Gascon, and M. Dudeck. Wall material effects in stationary plasma thrusters. II. Near-wall and in-wall conductivity. *Phys. Plasmas*, 10:4137–4152, 2003.

[83] A. V. Zharinov and Yu. S. Popov. Acceleration of plasma by a closed Hall current. *Sov. Phys. Tech. Phys.*, 12:208–211, 1967.

[84] E. Ahedo. Presheath/sheath model with secondary electron emission from two parallel walls. *Phys. Plasmas*, 9:4340–4347, 2002.

[85] V. A. Godyak. Abnormally low electron-energy and heating-mode transition in a low-pressure argon rf discharge at 13.56 MHz. *Phys. Rev. Lett.*, 65:996–999, 1990.

[86] V. Yu. Fedotov, A. A. Ivanov, G. Guerrini, A. N. Vesselovzorov, and M. Bacal. On the electron energy distribution function in a Hall-type thruster. *Phys. Plasmas*, 6:4360–4365, 1999.

[87] N. B. Meezan and M. A. Cappelli. Kinetic study of wall collisions in a coaxial Hall discharge. *Phys. Rev. E*, 66:036401, 2002.

[88] V. Latocha, L. Garrigues, P. Degond, and J.-P. Boeuf. Numerical simulation of electron transport in the channel region of a stationary plasma thruster. *Plasma Sources Sci. Technol.*, 11:104–114, 2002.

[89] Francesco Taccogna, Savino Longo, and Mario Capitelli. Plasma sheaths in Hall discharge. *Phys. Plasmas*, 12:093506, 2005.

[90] D. Sydorenko and A. Smolyakov. Simulation of secondary electron emission effects in a plasma slab in crossed electric and magnetic fields. *Bull. Am. Phys. Soc.*, 49:261, 2004.

[91] D. Sydorenko, A. Smolyakov, I. Kaganovich, and Y. Raitses. Modification of electron velocity distribution in bounded plasmas by secondary electron emission. In *Workshop "Nonlocal Collisionless Phenomena in Plasmas"*, Princeton Plasma Physics Laboratory, Princeton, NJ, August 2-4 2005.

[92] D. Sydorenko, A. Smolyakov, I. Kaganovich, and Y. Raitses. Particle-in-cell simulation of plasma-wall interaction in presence of a strong secondary electron emission. *Bull. Am. Phys. Soc.*, 50:175, 2005.

[93] D. Sydorenko, A. Smolyakov, I. Kaganovich, and Y. Raitses. Kinetic simulation of effects of secondary electron emission on electron temperature in Hall thrusters. In *29th International Electric Propulsion Conference*, Princeton University, Princeton, NJ, October 31 - November 4 2005. IEPC-2005-078.

[94] D. Sydorenko, A. Smolyakov, Y. Tyshetskiy, and V. Godyak. Kinetic simulation of secondary electron emission effects in Hall thrusters. *Phys. Plasmas*, 13:014501, 2006.

[95] D. Sydorenko, A. Smolyakov, I. Kaganovich, and Y. Raitses. Modification of electron velocity distribution in bounded plasmas by secondary electron emission. *to be published in IEEE Trans. Plasma Sci.*, 2006.

[96] T. W. Johnston. Time-averaged effects on charged particles in a-c fields. *RCA Rev.*, 21:570–610, 1960.

[97] R. E. Aamodt and M. C. Vella. Kinetic description of ponderomotive effects in a plasma. *Phys. Rev. Lett.*, 39:1273–1276, 1977.

[98] P. Mora and R. Pellat. Ponderomotive effects and magnetic field generation in radiation plasma interaction. *Phys. Fluids*, 22:2408–2417, 1979.

[99] A. N. Kondratenko. *Field penetration into plasmas*. Atomizdat, Moscow, 1979. in Russian.

[100] A. B. Langdon and J. M. Dawson. Investigations of a sheet model for a bounded plasma field and radiation. In *Proceedings of the First Conf. Num. Sim. Plasmas*, page 39, Williamsburg, VA, April 1967. College of William and Mary.

[101] Bruce I. Cohen, Michael A. Mostrom, Dwight R. Nicholson, Allan N. Kaufman, Claire E. Max, and A. Bruce Langdon. Simulation of laser beat heating of a plasma. *Phys. Fluids*, 18:470–474, 1975.

[102] B. B. Godfrey. Numerical Cherenkov instabilities in electromagnetic particle codes. *J. Comput. Phys.*, 15:504–521, 1974.

[103] Glenn Joyce, Martin Lampe, Steven P. Slinker, and Wallace M. Manheimer. Electrostatic particle-in-cell simulation technique for quasineutral plasma. *J. Comput. Phys.*, 138:540–562, 1997.

[104] J. D. Evans and F. F. Chen. Nonlocal power deposition in inductively coupled plasmas. *Phys. Rev. Lett.*, 86:5502–5505, 2001.

[105] A. B. Langdon, B. I. Cohen, and A. Friedman. Direct implicit large time-step particle simulation of plasmas. *J. Comput. Phys.*, 51:107–138, 1983.

[106] Bruce I. Cohen, A. Bruce Langdon, and Dennis W. Hewett. Performance and optimization of direct implicit particle simulations. *J. Comput. Phys.*, 81:151–168, 1989.

[107] A. Friedman, S. E. Parker, S. L. Ray, and C. K. Birdsall. Multi-scale particle-in-cell plasma simulation. *J. Comput. Phys.*, 96:54–70, 1991.

[108] S. E. Parker, A. Friedman, S. L. Ray, and C. K. Birdsal. Bounded multi-scale plasma simulation: Application to sheath problems. *J. Comput. Phys.*, 107:388–402, 1993.

[109] M. R. Gibbons and D. W. Hewett. The Darwin direct implicit particle-in-cell (DADIPIC) method for simulation of low frequency plasma phenomena. *J. Comput. Phys.*, 120:231–247, 1995.

[110] V. P. Gopinath, J. P. Verboncoeur, and C. K. Birdsall. Multipactor electron discharge physics using an improved secondary emission model. *Phys. Plasmas*, 5:1535–1540, 1998.

[111] A. Dunaevsky, Y. Raitses, and N. J. Fisch. Secondary electron emission from dielectric materials of a Hall thruster with segmented electrodes. *Phys. Plasmas*, 10:2574–2577, 2003.

[112] Wallace M. Manheimer, Martin Lampe, and Glenn Joyce. Langevin representation of Coulomb collisions in PIC simulations. *J. Comp. Phys.*, 138:563–584, 1997.

[113] J. R. M. Vaughan. A new formula for secondary emission yield. *IEEE Trans./ Elecron Devices*, 36:1963–1967, 1989.

[114] J. P. Verboncoeur, M. V. Alves, V. Vahedi, and C. K. Birdsall. Simultaneous potential and circuit solution for 1d bounded plasma particle simulation code. *J. Comp. Phys.*, 104:321–328, 1993.

[115] J. P. Verboncoeur, A. B. Langdon, and N. T. Gladd. An object-oriented electromagnetic PIC code. *Comp. Phys. Comm.*, 87:199–211, 1995.

[116] R. P. McEachran and A. D. Stauffer. Relativistic low-energy elastic and momentum transfer cross sections for electron scattering from xenon. *J. Phys. B: At. Mol. Phys.*, 20:3483–3486, 1987.

[117] D. F. Register, L. Vuskovic, and S. Trajmar. Elastic electron scattering cross sections for Xe in the 1-100 eV impact energy region. *J. Phys. B: At. Mol. Phys.*, 19:1685–1697, 1986.

[118] Makoto Hayashi. Determination of electron-xenon total excitation cross sections, from threshold to 100 eV, from experimental values of Townsend's α. *J. Phys. D: Appl. Phys.*, 16:581–589, 1983.

[119] E. Krishnakumar and S. K. Srivastava. Ionization cross sections of rare-gas atoms by electron impact. *J. Phys. B: At. Mol. Opt. Phys.*, 21:1055–1082, 1988.

[120] C. B. Opal, W. K. Peterson, and E. C. Beaty. Measurements of secondary-electron spectra produced by electron impact ionization of a number of simple gases. *J. Chem. Phys.*, 55:4100–4106, 1971.

[121] Michael E. Jones, Don S. Lemons, Rodney J. Mason, Vincent A. Thomas, and Dan Winske. A grid-based Coulomb collision model for PIC codes. *J. Comput. Phys.*, 123:169–181, 1996.

[122] Marshall N. Rosenbluth, William M. MacDonald, and David L. Judd. Fokker-Planck equation for an inverse-square force. *Phys. Rev.*, 107:1–6, 1957.

[123] Herbert Goldstein. *Classical mechanics*. Reading, Mass. ; Don Mills, Ont. : Addison-Wesley Pub. Co., 1980.

[124] L. A. Schwager and C. K. Birdsall. Collector and source sheaths of a finite ion temperature plasma. *Phys. Fluids B*, 2:1057–1068, 1990.

[125] L. A. Schwager. Effects of secondary and thermionic electron emission on the collector and source sheaths of a finite ion temperature plasma using kinetic theory and numerical simulation. *Phys. Fluids B*, 5:631–645, 1993.

[126] N. G. Matsiborko, I. N. Onishchenko, V. D. Shapiro, and V. I. Shevchenko. On non-linear theory of instability of a mono-energetic electron beam in plasma. *Plasma Phys.*, 14:591–600, 1972.

[127] C. Ramsauer and R. Kollath. The cross section effect of noble gase molecules against electrons under 1 Volt. *Ann. Phys.*, 3:536–564, 1929.

[128] R. J. Procassini, C. K. Birdsall, and E. C. Morse. A fully kinetic, self-consistent particle simulation model of the collisionless plasma-sheath region. *Phys. Fluids B*, 2:3191–3205, 1990.

[129] Akhiezer A. I. and Fainberg Ya. B. On interaction of a charged particle beam with an electron plasma. *Dokl. Akad. Nauk SSSR*, 69:555–556, 1949. in Russian.

[130] D. Bohm and E. P. Gross. Theory of plasma oscillations. b. Excitation and damping of oscillations. *Phys. Rev.*, 75:1864–1876, 1949.

[131] B. N. Brejzman and D. D. Ryutov. Powerful relativistic electron beams in a plasma and in a vacuum (theory). *Nucl. Fusion*, 14:873–907, 1974.

[132] K. V. Roberts and H. L. Berk. Nonlinear evolution of a two-stream instability. *Phys. Rev. Lett*, 19:297–301, 1967.

[133] Selig Kainer, John Dawson, and Ramy Shanny. Interaction of a highly energetic electron beam with a dense plasma. *Phys. Fluids*, 15:493–501, 1972.

[134] A. B. Mikhailovskii. *Theory of plasma instabilities.*, volume 1. New York : Consultants Bureau, 1974.

[135] T. M. O'Neil, J. H. Winfrey, and J. H. Malmberg. Nonlinear interaction of a small cold beam and a plasma. *Phys. Fluids*, 14:1204–1212, 1971.

[136] J. P. Boeuf and L. Garrigues. Low frequency oscillations in a stationary plasma thruster. *J. Appl. Phys.*, 84:3541–3554, 1998.

[137] I. D. Kaganovich and L. D. Tsendin. The space-time-averaging procedure and modeling of the rf discharge. Part II: Model of collisional low-pressure rf discharge. *IEEE Trans. Plasma Sci.*, 20:66–75, 1992.

[138] I. Kaganovich. Modeling of collisionless and kinetic effects in thruster plasmas. In *29th International Electric Propulsion Conference*, Princeton University, Princeton, NJ, October 31 - November 4 2005. IEPC-2005-096.

[139] Michal Gryzinski. Two-particle collisions. II. Coulomb collisions in the laboratory system of coordinates. *Phys. Rev. A*, 138:A322–A335, 1965.

[140] C. Y. Ma and D. Summers. Formation of power-law energy spectra in space plasmas by stochastic acceleration due to whistler-mode waves. *Geophys. Res. Lett.*, 25:4099–4102, 1998.

[141] B. Abel and R. M. Thorne. Electron scattering loss in Earth's inner magnetosphere - 1. Dominant physical processes. *J. Geophys. Res. Space Phys.*, 103:2385–2396, 1998.

[142] U. Kortshagen and H. Schluter. On the influence of Coulomb collisions on the electron-energy distribution function of surface-wave produced argon plasmas. *J. Phys. D*, 25:644–651, 1992.

[143] Lyman Spitzer. *Physics of fully ionized gases.* New York, Interscience Publishers, 1962. Chapter 5.

[144] A. I. Morozov, A. I. Bugrova, A. V. Desyatskov, and et. al. ATON-thruster plasma accelerator. *Plasma Phys. Reports*, 23:587–597, 1997.

[145] C. A. Ordonez. Boundary conditions including sheath effects at a plasma-facing surface. *Phys. Rev. E*, 55:1858–1871, 1997.

[146] S. Takamura, N. Ohno, M. Y. Ye, and T. Kuwabara. Space-charge limited current from plasma-facing material surface. *Contrib. Plasma Phys.*, 44:126–137, 2004.

[147] E. Ahedo and F. I. Parra. Partial trapping of secondary-electron emission in a Hall thruster plasma. *Phys. Plasmas*, 12:073503, 2005.

[148] V. A. Nemchinskii. Stabilization of the two-stream instability in an inhomogeneous plasma. *Sov. Phys. Tech. Phys.*, 16:332–333, 1971.

[149] A. I. Morozov. Steady-state uniform Debye sheaths. *Sov. J. Plasma Phys.*, 17:393–397, 1991.

[150] K. G. Hernqvist. Plasma ion oscillations in electron beams. *J. Appl. Phys.*, 26:544–548, 1955.

[151] K. Kato, K. Matsuura, and M. Yoseli. Plasma ion oscillation in a plasma-beam system. *J. Phys. Soc. Japan*, 20:443–448, 1965.

[152] S. Iizuka, K. Saeki, N. Sato, and Y. Hatta. Buneman instability, Pierce instability, and double-layer formation in a collisionless plasma. *Phys. Rev. Lett.*, 43:1404–1407, 1979.

[153] O. Buneman. Dissipation of currents in ionized media. *Phys. Rev.*, 115:503–517, 1959.

[154] Burton D. Fried and Roy W. Gould. Longitudinal ion oscillations in a hot plasma. *Phys. Fluids*, 4:139–147, 1961.

[155] M. D. Gabovich, L. L. Pasechnik, and V. G. Yazeva. Observation of ion oscillations in a plasma. *Sov. Phys. JETP*, 11:1033–1035, 1960.

[156] H. Tanaca, M. Koganei, and A. Hirose. Dispersion relation of ion waves in mercury-vapor discharges. *Phys. Rev. Lett.*, 16:1079–1081, 1966.

[157] Peter Burger. Theory of large-amplitude oscillations in the one-dimensional low-pressure cesium thermionic converter. *J. Appl. Phys.*, 36:1938–1943, 1965.

[158] F. Greiner, T. Klinger, H. Klostermann, and A. Piel. Experimental and particle-in-cell simulations on self-oscillations and period doubling in thermionic discharges at low pressure. *Phys. Rev. Lett.*, 70:3071–3074, 1993.

[159] P. Y. Cheung and A. Y. Wong. Chaotic behavior and period doubling in plasmas. *Phys. Rev. Lett.*, 59:551–554, 1987.

[160] P. Y. Cheung, S. Donovan, and A. Y. Wong. Observations of intermittent chaos in plasmas. *Phys. Rev. Lett.*, 61:1360–1363, 1988.

[161] G. Knorr. Hysteresis phenomena in plasmas and catastrophe theory. *Plasma Phys. Controlled Fusion*, 26:949–953, 1984.

[162] R. L. Stenzel. Instability of the sheath-plasma resonance. *Phys. Rev. Lett.*, 60:704–707, 1988.

[163] N. Ohno, A. Komori, M. Tanaka, and Y. Kawai. Instabilities associated with a negative rf resistance in current-carrying ion sheaths. *Phys. Fluids B*, 3:228–235, 1991.

[164] A. Rohde, A. Piel, and H. Klostermann. Simulation of the nonlinear dynamics of grid sheath oscillations in double plasma devices. *Phys. Plasmas*, 4:3933–3942, 1997.

[165] V. I. Perel and Ya. M. Pinskii. Stress tensor for a plasma in a high frequency electromagnetic field with account of collisions. *Sov. Phys. JETP*, 27:1014, 1968.

Appendix A

Conservation of energy in Hall thruster simulations

The energy conservation law in Hall thruster simulations is

$$\frac{dW_{tot}}{dt} = \left(\frac{dW}{dt}\right)_{heat} + \left(\frac{dW}{dt}\right)_{coll} + \left(\frac{dW}{dt}\right)_{emit} + \left(\frac{dW}{dt}\right)_{wall} , \qquad (A.1)$$

where $W_{tot} = W_{kin} + W_{pot}$ is the total system energy. The right hand side of (A.1) is the sum of rates of energy change due to the following processes: the Joule heating $\left(\frac{dW}{dt}\right)_{heat} = \int_0^L dx J_z(x) E_z$, the inelastic collisions with neutral atoms $\left(\frac{dW}{dt}\right)_{coll}$, the injection of secondary electrons $\left(\frac{dW}{dt}\right)_{emit}$, and the losses of particles at the walls $\left(\frac{dW}{dt}\right)_{wall}$. Rates $\left(\frac{dW}{dt}\right)_{coll}$ and $\left(\frac{dW}{dt}\right)_{wall}$ describe energy loss and are negative, rates $\left(\frac{dW}{dt}\right)_{heat}$ and $\left(\frac{dW}{dt}\right)_{emit}$ describe energy gain and are positive. Introduce

$$\begin{aligned} W_{heat}(t) &= \int_0^t dt \left(\frac{dW}{dt}\right)_{heat} , \quad W_{coll}(t) = \int_0^t dt \left(\frac{dW}{dt}\right)_{coll} , \\ W_{emit}(t) &= \int_0^t dt \left(\frac{dW}{dt}\right)_{emit} , \quad W_{wall}(t) = \int_0^t dt \left(\frac{dW}{dt}\right)_{wall} , \end{aligned} \qquad (A.2)$$

where $W_{heat}(t)$ is the energy gained by the system due to the Joule heating, $W_{coll}(t)$ is the energy lost by the system due to the inelastic collisions with neutral atoms, $W_{emit}(t)$ is the energy introduced into the system by the emitted secondary electrons, $W_{wall}(t)$ is the energy carried out of the system by particles (electrons and ions) collided with the walls by the time t. The example of evolution of quantities (A.2) during simulation is presented in Fig. A.3a. With (A.2), the energy conservation law (A.1) can be expressed in the form

$$W_{tot}(t) - W_{tot}(0) = W_{heat}(t) + W_{coll}(t) + W_{emit}(t) + W_{wall}(t) . \qquad (A.3)$$

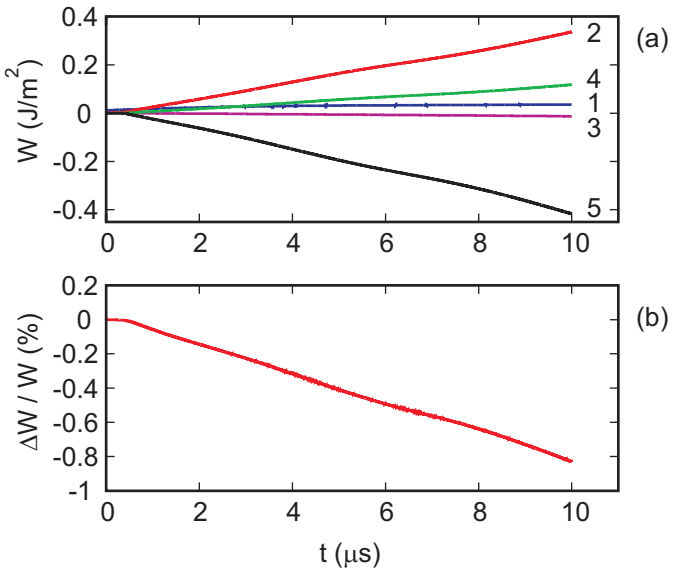

Figure A.1: For simulation 7 of Table 5.2: (a) Curve 1 is the total energy (kinetic plus potential), curve 2 is the energy gained due to the Joule heating, curve 3 is the energy lost by electrons in inelastic collisions with neutral atoms, curve 4 is the energy of injection of secondary electrons, curve 5 is the energy of particles collided with the walls versus time, here the negative energy value correspond to the energy loss. (b) The relative deviation from the energy conservation law versus time.

One can use the following ratio as a quantitative characteristic of energy conservation in simulations:

$$\frac{\Delta W}{W} = \frac{W_{tot}(t) - W_{heat}(t) - W_{coll}(t) - W_{emit}(t) - W_{wall}(t) - W_{tot}(0)}{W_{tot}(t)} \,. \qquad \text{(A.4)}$$

In simulations with EDIPIC code this relative deviation from the energy conservation law typically does not exceed 1% after about 10^7 timesteps (see Fig. A.1b).

Appendix B

Parameters of Hall thruster simulations with EDIPIC code

In Table B.1, T_{sc} and n_{sc} are the values of electron temperature and density used for scaling in simulations. These scale values are chosen within the range of typical Hall thruster parameters. The size of the mesh of the computational grid is $\Delta x = \lambda_{sc}/16$, where $\lambda_{sc} = (2T_{sc}\varepsilon_0/n_{sc}e^2)^{1/2}$ is the electron Debye length for T_{sc} and n_{sc}. The time step is $\Delta t = \Delta x/4v_{sc}$, where $v_{sc} = (2T_{sc}/m)^{1/2}$ is the electron thermal velocity for T_{sc}. The number of cells in the computational grid is $N_{cell} = L/\Delta x$, where $L = 2.5$ cm is the plasma gap width common for all simulations. The number of macroparticles per cell N_{macro} is found empirically. On one hand, it is large enough to provide overall convergence of simulations. On the other hand, it is limited to ensure reasonable simulation run time. Spatially uniform distribution with N_{macro} macroparticles per cell produces plasma density equal to n_{sc}.

Table B.1: Parameters of EDIPIC simulations (complementary to Tables 5.1 and 5.2).

Simulation number	1	2	3	4	5	6	7	8
T_{sc} , [eV]	46	53	40	40	40	40	40	40
n_{sc} , [10^{11} cm^{-3}]	1	1	1	1	1	1	1	1
Δx, [10^{-6} m]	14.09	15.13	13.14	13.14	13.14	13.14	13.14	13.14
Δt, [10^{-12} s]	0.876	0.876	0.876	0.876	0.876	0.876	0.876	0.876
N_{cell}	1760	1648	1902	1902	1902	1902	1902	1902
N_{macro}	500	2000	1000	1000	1000	1000	1000	1000

Appendix C

Derivation of the emission coefficient and the ratio of primary electron flux components

It is convenient to combine the weakly confined and the collision-ejected plasma bulk electrons into a single group of plasma bulk electrons, as follows:

$$\Gamma_{1p} = \Gamma_{1c} + \Gamma_{1w} \ , \ \Gamma_{2p} = \Gamma_{2c} + \Gamma_{2w} \ , \ \gamma_p = \frac{\Gamma_{2p}}{\Gamma_{1p}} = \frac{\gamma_c + \gamma_w \Gamma_{1w}/\Gamma_{1c}}{1 + \Gamma_{1w}/\Gamma_{1c}} \ , \tag{C.1}$$

where Γ_{1p}, Γ_{2p} and γ_p are, respectively, the primary and secondary electron fluxes and the general emission coefficient due to all electrons coming from the plasma bulk (collision-ejected and weakly confined). Then the total primary electron flux is

$$\Gamma_1 = \Gamma_{1p} + \Gamma_{1b} = \Gamma_{1p} + \alpha\Gamma_2 \ , \tag{C.2}$$

and the total emission coefficient can be found as

$$\gamma = \frac{\Gamma_2}{\Gamma_1} = \frac{1}{\Gamma_{1p}/\Gamma_2 + \alpha} \ . \tag{C.3}$$

The total secondary electron flux is

$$\Gamma_2 = \Gamma_{2p} + \Gamma_{2b} = \gamma_p\Gamma_{1p} + \gamma_b\Gamma_{1b} = \gamma_p\Gamma_{1p} + \gamma_b\alpha\Gamma_2 \ , \tag{C.4}$$

which gives the ratio

$$\frac{\Gamma_{1p}}{\Gamma_2} = \frac{1 - \alpha\gamma_b}{\gamma_p} \ . \tag{C.5}$$

Substituting (C.5) into (C.3), one obtains the total emission coefficient in the form

$$\gamma = \frac{\gamma_p}{1 + \alpha(\gamma_p - \gamma_b)} \ . \tag{C.6}$$

Combining Eqs. (C.2) and (C.4) with Eq. (C.6), one obtains

$$\frac{\gamma_p\Gamma_{1p} + \gamma_b\Gamma_{1b}}{\Gamma_{1p} + \Gamma_{1b}} = \frac{\gamma_p}{1 + \alpha(\gamma_p - \gamma_b)} \ ,$$

then the ratio of primary electron fluxes due to beam and bulk electrons is given by

$$\frac{\Gamma_{1b}}{\Gamma_{1p}} = \frac{\alpha\gamma_p}{1 - \alpha\gamma_b} \ . \tag{C.7}$$